Research Topics

Predictive and diagnostic approaches for systemic disorders using ocular assessment

Edited by
Kai Jin, Jiong Zhang and Andrzej Grzybowski

Published in
Frontiers in Medicine

May 2025

ISSN 1664-8714
ISBN 978-2-8325-6307-6
DOI 10.3389/978-2-8325-6307-6

About Frontiers

Frontiers is more than just an open access publisher of scholarly articles: it is a pioneering approach to the world of academia, radically improving the way scholarly research is managed. The grand vision of Frontiers is a world where all people have an equal opportunity to seek, share and generate knowledge. Frontiers provides immediate and permanent online open access to all its publications, but this alone is not enough to realize our grand goals.

Frontiers journal series

The Frontiers journal series is a multi-tier and interdisciplinary set of open-access, online journals, promising a paradigm shift from the current review, selection and dissemination processes in academic publishing. All Frontiers journals are driven by researchers for researchers; therefore, they constitute a service to the scholarly community. At the same time, the *Frontiers journal series* operates on a revolutionary invention, the tiered publishing system, initially addressing specific communities of scholars, and gradually climbing up to broader public understanding, thus serving the interests of the lay society, too.

Dedication to quality

Each Frontiers article is a landmark of the highest quality, thanks to genuinely collaborative interactions between authors and review editors, who include some of the world's best academicians. Research must be certified by peers before entering a stream of knowledge that may eventually reach the public - and shape society; therefore, Frontiers only applies the most rigorous and unbiased reviews. Frontiers revolutionizes research publishing by freely delivering the most outstanding research, evaluated with no bias from both the academic and social point of view. By applying the most advanced information technologies, Frontiers is catapulting scholarly publishing into a new generation.

What are Frontiers Research Topics?

Frontiers Research Topics are very popular trademarks of the *Frontiers journals series*: they are collections of at least ten articles, all centered on a particular subject. With their unique mix of varied contributions from Original Research to Review Articles, Frontiers Research Topics unify the most influential researchers, the latest key findings and historical advances in a hot research area.

Find out more on how to host your own Frontiers Research Topic or contribute to one as an author by contacting the Frontiers editorial office: frontiersin.org/about/contact

Predictive and diagnostic approaches for systemic disorders using ocular assessment

Topic editors
Kai Jin — Zhejiang University, China
Jiong Zhang — University of Southern California, United States
Andrzej Grzybowski — University of Warmia and Mazury in Olsztyn, Poland

Citation
Jin, K., Zhang, J., Grzybowski, A., eds. (2025). *Predictive and diagnostic approaches for systemic disorders using ocular assessment*. Lausanne: Frontiers Media SA.
doi: 10.3389/978-2-8325-6307-6

Table of contents

Frontiers | Frontiers in Medicine

TYPE Editorial
PUBLISHED 11 December 2024
DOI 10.3389/fmed.2024.1529861

OPEN ACCESS

EDITED AND REVIEWED BY
Jodhbir Mehta,
Singapore National Eye Center, Singapore

*CORRESPONDENCE
Kai Jin
✉ jinkai@zju.edu.cn

RECEIVED 17 November 2024
ACCEPTED 22 November 2024
PUBLISHED 11 December 2024

CITATION
Jin K, Zhang J and Grzybowski A (2024) Editorial: Predictive and diagnostic approaches for systemic disorders using ocular assessment. *Front. Med.* 11:1529861. doi: 10.3389/fmed.2024.1529861

Editorial: Predictive and diagnostic approaches for systemic disorders using ocular assessment

Kai Jin[1]*, Jiong Zhang[2] and Andrzej Grzybowski[3]

[1]Eye Center, The Second Affiliated Hospital, School of Medicine, Zhejiang University, Hangzhou, China, [2]Laboratory of Advanced Theranostic Materials and Technology, Ningbo Institute of Materials Technology and Engineering, Chinese Academy of Sciences, Ningbo, Zhejiang, China, [3]Institute for Research in Ophthalmology, Foundation for Ophthalmology Development, Poznan, Poland

KEYWORDS

ocular assessment, systemic diseases, retinal imaging, optical coherence tomography, artificial intelligence

Editorial on the Research Topic
Predictive and diagnostic approaches for systemic disorders using ocular assessment

Introduction

The human eye is not just a window to the soul but also a critical portal through which medical professionals can glean information about a patient's overall health. Advances in technology and research over recent decades have underscored the eye's value as a diagnostic tool for detecting systemic diseases. This editorial explores how ocular assessments can be leveraged for predictive and diagnostic purposes in systemic disorders, underlining the scientific basis and clinical applications of such practices.

Ocular manifestations of systemic diseases

Systemic diseases often manifest in the eye due to their unique vasculature and neural composition. The retina, for instance, shares similar embryological origins with the brain and is supplied by a rich vascular network. This makes it an ideal site for detecting vascular and neurological changes that reflect systemic conditions. Conditions such as diabetes, hypertension, and autoimmune diseases frequently display characteristic ocular signs, which, when detected early, can facilitate timely interventions.

For example, diabetic retinopathy remains a prominent example of how ophthalmic examinations can reveal the severity and progression of systemic diabetes. Retinal imaging enables the identification of microaneurysms, hemorrhages, and neovascularization, all hallmark features of the disease (1). The presence of these signs not only confirms the diagnosis but can also predict the potential for systemic complications (2).

Ocular imaging technologies

Advancements in optical coherence tomography (OCT), fundus photography, and retinal angiography have improved the diagnostic capabilities for systemic disorders (3). OCT, with its non-invasive cross-sectional imaging, has been instrumental in assessing macular edema and optic nerve health. It can reveal subtle changes that might correspond to early signs of systemic diseases, including multiple sclerosis and Alzheimer's disease (4). The technique's high resolution enables clinicians to observe changes in the retinal nerve fiber layer (RNFL) thickness, which is crucial in neurological assessments (5).

Artificial intelligence (AI) has also been a game-changer in ocular diagnostics (6). By applying deep learning algorithms to retinal images, researchers have developed predictive models capable of assessing cardiovascular risk factors, such as age, gender, and blood pressure, based solely on retinal scans (7, 8). Such models can transform the way systemic risk stratification is conducted, making assessments more accessible and less invasive.

Cardiovascular and neurological insights

The retinal microvasculature is often reflective of the broader systemic vascular system. Conditions such as hypertensive retinopathy can reveal not only the presence of high blood pressure but also its duration and impact on vascular health (9). Retinal vascular changes like arteriolar narrowing and arteriovenous nicking are indicative of chronic hypertension and are predictive of an increased risk of stroke (10). Furthermore, studies have shown that monitoring the retinal vessel calibers can serve as an indicator for coronary artery disease, suggesting that ocular assessments could be included as part of a cardiovascular risk assessment protocol (11).

In the realm of neurological disorders, the eye has shown remarkable promise in providing early diagnostic markers. Changes in the optic nerve head and RNFL have been associated with diseases such as Alzheimer's disease and Parkinson's disease. Retinal imaging has demonstrated a thinning of the RNFL in patients with neurodegenerative conditions, correlating with cognitive decline and disease severity (12). This association opens pathways for non-invasive monitoring and early detection, potentially preceding significant brain pathology visible on standard neuroimaging.

Autoimmune and inflammatory conditions

Autoimmune diseases like systemic lupus erythematosus (SLE) and rheumatoid arthritis (RA) often exhibit ocular manifestations such as uveitis, scleritis, or retinal vasculitis. Ocular assessment not only aids in diagnosing these diseases but can also monitor disease activity and guide treatment (13). Regular eye exams can serve as a practical adjunct to systemic inflammatory markers, providing real-time insight into disease progression.

Challenges and future directions

While the potential of ocular assessments for systemic disease diagnosis is immense, there are challenges. The integration of eye exams into general medical practice requires enhanced interdisciplinary collaboration between ophthalmologists and other healthcare providers. Additionally, the development and standardization of AI algorithms must ensure reproducibility and fairness across diverse populations to avoid biases that could affect diagnostic accuracy.

Looking ahead, further research should focus on validating ocular biomarkers and integrating these findings into routine clinical practice. Studies exploring the longitudinal relationship between ocular changes and systemic disease outcomes will strengthen the clinical utility of these assessments.

Conclusion

Ocular assessments hold tremendous promise as a non-invasive, cost-effective means of diagnosing and predicting systemic disorders. As imaging technologies advance and AI becomes more sophisticated, the role of the eye as a diagnostic gateway to broader health assessments will undoubtedly expand. The convergence of ophthalmology with general medicine is an exciting frontier that promises to enhance patient care through earlier detection, more accurate risk stratification, and improved management of systemic diseases.

Author contributions

KJ: Conceptualization, Writing – original draft. JZ: Writing – review & editing. AG: Writing – review & editing.

Conflict of interest

The authors declare that the research was conducted in the absence of any commercial or financial relationships that could be construed as a potential conflict of interest.

Publisher's note

References

1. Ting DSW, Cheung CY, Lim G, Tan GSW, Quang ND, Gan A, et al. Development and validation of a deep learning system for diabetic retinopathy and related eye diseases using retinal images from multiethnic populations with diabetes. *J Am Med Assoc.* (2017) 318:2211–23. doi: 10.1001/jama.2017.18152

2. Zhou J, Song S, Zhang Y, Jin K, Ye J. OCT-based biomarkers are associated with systemic inflammation in patients with treatment-naïve diabetic macular edema. *Ophthalmol Ther.* (2022) 11:2153–67. doi: 10.1007/s40123-022-00576-x

3. Grzybowski A, Barboni P. *OCT and Imaging in Central Nervous System Diseases: The Eye as a Window to the Brain*. Berlin: Springer (2020).

4. Zhang Y, Wang Y, Shi C, Shen M. Advances in retina imaging as potential biomarkers for early diagnosis of Alzheimer's disease. *Transl Neurodegener.* (2021) 10:6. doi: 10.1186/s40035-021-00230-9

5. Ko F, Muthy ZA, Gallacher J, Sudlow C, Rees G, Yang Q, et al. Association of retinal nerve fiber layer thinning with current and future cognitive decline: a study using optical coherence tomography. *J Am Med Assoc Neurol.* (2018) 75:1198–205. doi: 10.1001/jamaneurol.2018.1578

6. Grzybowski A. *Artificial Intelligence in Ophthalmology: Promises, Hazards and Challenges*. Berlin: Springer (2021).

7. Poplin R, Varadarajan AV, Blumer K, Liu Y, McConnell MV, Corrado GS, et al. Prediction of cardiovascular risk factors from retinal fundus photographs via deep learning. *Nat Biomed Eng.* (2018) 2:158–64. doi: 10.1038/s41551-018-0195-0

8. Rim TH, Lee CJ, Tham YC, Cheung N, Yu M, Lee G, et al. Deep-learning-based cardiovascular risk stratification using coronary artery calcium scores predicted from retinal photographs. *Lancet Digit Health.* (2021) 3:e306–16. doi: 10.1016/S2589-7500(21)00043-1

9. Chew EY, Burns SA. Standardization and clinical applications of retinal imaging biomarkers for cardiovascular disease: a Roadmap from an NHLBI workshop. *Nat Rev Cardiol.* (2024). doi: 10.1038/s41569-024-01060-8. [Epub ahead of print].

10. Cheung CY, Tay WT, Ikram MK, Ong YT, De Silva DA, Chow KY, et al. Retinal microvascular changes and risk of stroke: the Singapore Malay Eye Study. *Stroke.* (2013) 44:2402–8. doi: 10.1161/STROKEAHA.113.001738

11. Wong TW, Klein R, Sharrett AR, Manolio TA, Hubbard LD, Marino EK, et al. The prevalence and risk factors of retinal microvascular abnormalities in older persons: the Cardiovascular Health Study. *Ophthalmology.* (2003) 110:658–66. doi: 10.1016/S0161-6420(02)01931-0

12. Ge YJ, Xu W, Ou YN, Qu Y, Ma YH, Huang YY, et al. Retinal biomarkers in Alzheimer's disease and mild cognitive impairment: a systematic review and meta-analysis. *Ageing Res Rev.* (2021) 69:101361. doi: 10.1016/j.arr.2021.101361

13. Meng L, Wang Y, Yang Z, Lin S, Wang Y, Chen H, et al. Ocular fundus changes and association with systemic conditions in systemic lupus erythematosus. *Front Immunol.* (2024) 15:1395609. doi: 10.3389/fimmu.2024.1395609

frontiers | Frontiers in Medicine

TYPE Mini Review
PUBLISHED 16 January 2024
DOI 10.3389/fmed.2023.1349571

OPEN ACCESS

EDITED BY
Kai Jin,
Zhejiang University, China

REVIEWED BY
Zhi-Qin Huang,
Capital Medical University, China

*CORRESPONDENCE
Joanne Thomas
✉ joanne.jess.thomas@emory.edu
Steven Yeh
✉ syeh@unmc.edu

†These authors have contributed equally to this work and share first authorship

RECEIVED 04 December 2023
ACCEPTED 27 December 2023
PUBLISHED 16 January 2024

CITATION
Curran EH, Devine MD, Hartley CD, Huang Y, Conrady CD, Debiec MR, Justin GA, Thomas J and Yeh S (2024) Ophthalmic implications of biological threat agents according to the chemical, biological, radiological, nuclear, and explosives framework.
Front. Med. 10:1349571.
doi: 10.3389/fmed.2023.1349571

Ophthalmic implications of biological threat agents according to the chemical, biological, radiological, nuclear, and explosives framework

Emma H. Curran[1†], Max D. Devine[2†], Caleb D. Hartley[3†], Ye Huang[4], Christopher D. Conrady[3,5], Matthew R. Debiec[6], Grant A. Justin[6], Joanne Thomas[7]* and Steven Yeh[3,8,9]*

[1]Creighton University School of Medicine, Omaha, NE, United States, [2]College of Medicine, University of Nebraska Medical Center, Omaha, NE, United States, [3]Department of Ophthalmology and Visual Sciences, Stanley M. Truhlsen Eye Institute, University of Nebraska Medical Center, Omaha, NE, United States, [4]Department of Ophthalmology, University of Illinois-Chicago, Chicago, IL, United States, [5]Department of Microbiology and Pathology, University of Nebraska Medical Center, Omaha, NE, United States, [6]Walter Reed National Military Medical Center, Bethesda, MD, United States, [7]Department of Ophthalmology, Emory University School of Medicine, Atlanta, GA, United States, [8]Global Center for Health Security, University of Nebraska Medical Center, Omaha, NE, United States, [9]National Strategic Research Institute, University of Nebraska Medical Center, Omaha, NE, United States

As technology continues to evolve, the possibility for a wide range of dangers to people, organizations, and countries escalate globally. The United States federal government classifies types of threats with the capability of inflicting mass casualties and societal disruption as Chemical, Biological, Radiological, Nuclear, and Energetics/Explosives (CBRNE). Such incidents encompass accidental and intentional events ranging from weapons of mass destruction and bioterrorism to fires or spills involving hazardous or radiologic material. All of these have the capacity to inflict death or severe physical, neurological, and/or sensorial disabilities if injuries are not diagnosed and treated in a timely manner. Ophthalmic injury can provide important insight into understanding and treating patients impacted by CBRNE agents; however, improper ophthalmic management can result in suboptimal patient outcomes. This review specifically addresses the biological agents the Center for Disease Control and Prevention (CDC) deems to have the greatest capacity for bioterrorism. CBRNE biological agents, encompassing pathogens and organic toxins, are further subdivided into categories A, B, and C according to their national security threat level. In our compendium of these biological agents, we address their respective CDC category, systemic and ophthalmic manifestations, route of transmission and personal protective equipment considerations as well as pertinent vaccination and treatment guidelines.

KEYWORDS

ophthalmic, biological agents, CBRNE, management, public health

1 Introduction

Recent outbreaks of Ebola virus disease, monkeypox, and the COVID-19 pandemic, which are public health emergencies of international concern (PHEIC) per World Health Organization (WHO) criteria, have provided insights into the clinical impact, socioeconomic implications, and widespread disruption of society (1–3). Identifying and understanding these infectious disease threats could be extended to potential engineered pathogens as well.

As technology evolves, a wide range of threats to service members, diplomats, and United States (US) citizens emerges. The US federal government classifies types of threats with the capability of inflicting mass casualties and societal disruption as Chemical, Biological, Radiological, Nuclear, and Energetics/Explosives (CBRNE) (4, 5). These incidents include accidental events like chemical waste spills to intentional use of technology like weapons of mass destruction (5, 6). CBRNE events have the potential to inflict death or severe disabilities in the absence of accurate diagnosis and timely treatment. There are various echelons of CBRNE initiatives within the US aimed to prevent, prepare for, respond to, and recover from these incidents (4–6). However, to date, we are unaware of a centralized resource for CBRNE incidents as they pertain to ophthalmic disease and countermeasures. Ophthalmic injury can provide key insight into understanding and treating patients impacted by CBRNE agents, while improper diagnosis and management can lead to debilitating implications for patients' vision and quality of life.

CBRNE biological agents encompass pathogens and toxins from microbes and plants. The Center for Disease Control and Prevention (CDC) classifies biological agents into categories A, B, and C according to their national security threat level using the following elements: ease of dissemination; mortality and morbidity rates; capacity for inciting public panic and social disruption; and requirements for special public health preparations (Table 1) (7). Category A agents are of highest priority, Category B of moderate importance, and Category C agents are emerging in nature and require further research for detection, diagnosis and treatment (8).

This is a comprehensive summary of the biological agents with special focus in relation to CBRNE preparation and management as identified by the CDC. We address the CDC category, the clinical manifestations and ophthalmic findings, the route of transmission and personal protective equipment (PPE) considerations, and the current vaccination and treatment guidelines for each identified biological agent in this review.

TABLE 1 Biological agent characteristics by threat category.

Agent characteristic	Category		
	A	B	C
Priority level	Highest	Second highest	Third highest
Ease of dissemination	High	Moderate	High
Associated mortality	High	Low	High
Associated morbidity	High	Moderate	High
Other	May cause large scale panic and social disruption	Require enhanced diagnostic and surveillance measures	Emergent in nature

Overview of biological agent characteristics according to Centers for Disease Control and Prevention threat category.

2 Viruses

A wide array of viruses is found in biological agent Categories A, B, and C. Proper hand washing and surface disinfection practices aid in prevention of nosocomial dissemination (9). Since a considerable number of viral infections are zoonotic, general preventative measures involve limiting contact with vectors and reducing direct and indirect contact with natural reservoirs and intermediate hosts. For example, removal of standing water sources when handling mosquito-borne infections reduces vector propagation, thus reducing disease burden (10).

Multiple viruses may be shed in the tear film and subsequently pose additional risk to eye care providers; therefore, ophthalmologic environmental interventions may include transparent shields on slit lamps, disinfection of potentially contaminated surfaces and instruments between patients, and implementation of telemedicine initiatives. Awareness of potential aerosol generation such as air puff-like tonometry is also critical to risk mitigation (11, 12). Appendix 1 summarizes key viruses according to the CDC categories.

2.1 Category A

Category A viruses encompass viral hemorrhagic fevers (VHFs) including arenaviruses (Lassa and Machupo viruses) and filoviruses (Marburg and Ebola viruses), and smallpox (variola major) (7).

2.1.1 Arenaviruses: Lassa fever and Machupo virus

Arenaviruses cause zoonotic hemorrhagic diseases via rodents and include Lassa fever and Machupo viruses (13). Rodent-to-human transmission occurs through contact with urine, feces, and saliva in contaminated food, aerosolized particles, and epidermal barrier lesions. Human-to-human transmission occurs through direct contact with infectious body fluids and contaminated fomites (14). Lassa fever is an arenavirus endemic to Africa and transmitted by the *Mastomys natalensis* mouse (13). Systemic manifestations include fever, exudative pharyngitis, proteinuria, emesis, sensorineural hearing loss, and other neurologic complications. Patients may progress into acute hemorrhagic fever and multi-organ failure. Ophthalmic findings of Lassa fever are conjunctivitis and subconjunctival hemorrhage in an acute disease state, with potential for visual acuity decline over time due to anterior and posterior segment pathology (15).

Machupo virus is the etiologic agent of Bolivian Hemorrhagic Fever and is transmitted by the *Calomys callosus* vesper mouse (16, 17). Systemic manifestations are a flu-like syndrome (16). Less than one third of cases may progress to neurologic and hemorrhagic syndromes culminating in multi-organ failure and death. Ophthalmic findings include conjunctivitis, conjunctival congestion, and periorbital edema. Current treatment is supportive care. Some early animal trials and *per os* administration suggest potential benefits of ribavirin and favipiravir as treatment and prophylaxis for Lassa fever and Machupo viral infections (13, 16).

2.1.2 Filoviruses: Marburg and Ebola virus diseases

Marburg and Ebola virus diseases are caused by members of the *Filoviridae* family—Marburg virus (MARV) and Ebola virus (EBOV), respectively (18). MARV is transmitted from its reservoir host, the African fruit bat, to humans and nonhuman primates (NHPs) through infectious body fluids and contaminated fruits (19). Infected NHPs can also serve as intermediate hosts for MARV transmission to humans through direct contact and bushmeat consumption while human-to-human transmission occurs via body fluids and contaminated fomites. High-risk populations for filovirus infection include health care workers and those involved in the burial of infected human corpses (19, 20). Systemic MARV manifestations are grouped into three phases: Phase 1: flu-like illness and fever; Phase 2: neurological and hemorrhagic symptoms; and Phase 3: prolonged phase of restoration or multi-organ failure and death (19). There have been reports of acute anterior uveitis three months after initial disease onset (21, 22). Current treatment is supportive care with no effective vaccines or therapeutics available (19).

EBOV is highly fatal and demonstrates similar human-to-human transmission mechanisms as MARV especially in instances of accidental needlesticks by healthcare workers (20, 23). Although EBOV's natural reservoir is unknown, bats are often implicated (20). Systemic manifestations are divided into three phases: Phase 1: Nonspecific symptoms and fever that progresses to intractable vomiting and watery diarrhea; Phase 2: Illness peaks with meningoencephalitis, acute kidney injury, adrenal insufficiency, pulmonary vascular leakage, pericarditis, and pancreatitis; and Phase 3: development of late-onset sequelae including ophthalmic and otologic complications, cognitive difficulties, and musculoskeletal pain and weakness (24). Ophthalmic findings during acute infection are conjunctival hemorrhages and vision loss, and after convalescence patients may present with anterior uveitis followed by posterior uveitis (25–27). Other ophthalmic sequelae include eye pain, redness, photophobia with acute or chronic unilateral vision loss, episcleritis, interstitial keratitis, and cataracts. A slit lamp exam may reveal nonspecific signs of active or old inflammation, as well as retinal and peripapillary lesions (Figure 1). Like MARV, current treatment is supportive care with no effective vaccines or therapeutics available.

2.1.3 Variola major: smallpox

Variola major virus, the etiological agent of smallpox, is an *Orthopoxvirus* that significantly impacted human populations for centuries until vaccination efforts globally eradicated this notorious pathogen in 1980 (28). Changes in global population health, vaccination hesitance, and increased intercontinental contact portend risks for pandemics and bioterrorism (28, 29). Transmission of variola virus involves inhalation of microdroplets from the respiratory tract, skin, and body fluids of infected patients. Systemic manifestations include a nonspecific prodromal phase followed by a rash of characteristic small cutaneous lesions that synchronously progress to scabs and pock scars (28). Vaccination with the vaccinia virus, a live attenuated poxvirus like smallpox and treatment with cidofovir are used to prevent and manage systemic infection (28, 29). Ophthalmic findings include pustular rash, edema, discharge, and dried secretions of the eyelids; conjunctival pustules that induce pain, photophobia, and lacrimation; corneal ulceration and perforation, iris prolapse, hypopyon, staphyloma, and endophthalmitis (9). Additional ophthalmic findings may include iritis, iridocyclitis, secondary glaucoma, and disciform keratitis, among others (9, 30–32). Subsequent treatments may involve topical antivirals, vaccinia immunoglobulins, and combination therapy with antivirals and topical steroids.

2.2 Category B

2.2.1 Togaviruses: Venezuelan encephalomyelitis and Western equine encephalomyelitis

Category B viruses consist of three alphaviruses from the Togaviridae family with severe morbidity and mortality—Venezuelan encephalomyelitis (VEEV) and Eastern and Western Equine encephalomyelitides (EEEV, WEEV) (7, 33, 34). Although primarily transmitted by mosquitos between equine, the natural reservoir, and humans, these viruses have been aerosolized as highly infectious virions employed in biowarfare (34, 35). Shared systemic manifestations for all three encephalomyelitides includes an asymptomatic febrile incubation period, symptomatic phase encephalopathy, and high case fatalities, especially with EEEV (50–75%) (33). Severe neurologic sequelae present in survivors (VEEV 4–14%, EEEV 50–90%, WEEV 15–30%) include emotional instability, seizures, and cognitive, sensory, and motor deficits (10, 33).

Ophthalmic findings in addition to those seen in encephalitis with papilledema from elevated intracranial pressure involve occasional optic neuritis and/or cranial nerve (CN) palsies (CN-VI, CN-VII) affecting vision (10). Those with VEEV and WEEV may also exhibit conjunctivitis, eye pain, and photophobia. Current treatment is supportive care. Although several vaccine candidates are under investigation, none have been approved for use in humans (34, 35). Preventive methods entail vector control by thorough elimination of standing water sources, bed nets, insect repellents and mosquito-repellent clothing (10).

2.3 Category C

Category C agents include Nipah virus (NiV) and Hantaviruses (7).

2.3.1 Hantavirus

Hantaviruses are rodent-carried viruses transmitted by aerosols of excreta, saliva, and urine; however, they are rarely transmitted human-to-human (36, 37). These viruses are subdivided according to their geographic distribution and unique systemic manifestations following a nonspecific symptom phase. 'New World' hantaviruses, predominately in the Americas, present with cardiopulmonary syndrome (HCPS) that progresses to organ failure. 'Old World' hantaviruses are endemic to Europe and Asia and present as hemorrhagic fever with renal syndrome (HFRS) and potential renal failure (36, 38). The first ophthalmic finding is acute, transient myopia, which is primarily associated with the HFRS-causing Puumala hantavirus (39, 40). One case reported a co-presentation of assumed hantavirus necrotizing retinitis and HFRS (41). Additional manifestations include anterior segment changes such

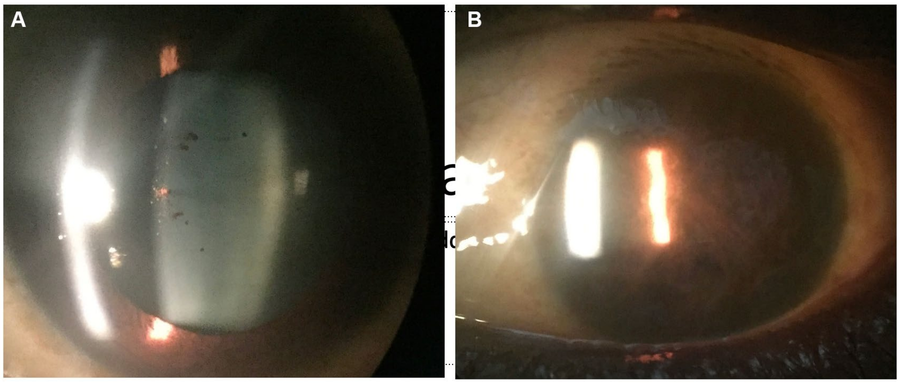

FIGURE 1
Anterior segment photograph of an Ebola virus disease survivor shows pigment on the lens capsule **(A)**, indicative of prior uveitis. In a West African survivor who was seen late in the uveitis disease course, complete seclusion of the pupil from extensive posterior synechiae and chronic inflammation is observed **(B)**.

as conjunctival chemosis, lens thickening, vitreous length shallowing, and macular features such as intraretinal hemorrhages, in addition to disc streak hemorrhages (42). Current treatment is supportive care with no effective vaccines or therapeutics available (43).

2.3.2 Nipah virus

Nipah virus (NiV), a member of the *Paramyxoviridae* family, is a zoonotic disease naturally found in fruit bats with spillover into intermediate hosts (pigs and horses) and humans (44). Reported transmission from bats was associated with bat-bitten fruit and bat saliva- and excreta-contaminated date palm sap (44–47). Human-to-intermediate hosts and human-to-human NiV transmission has been recorded in association with urine, saliva and respiratory secretions in addition to direct contact, fomites, and aerosols (45, 46, 48, 49). Severe respiratory and neurologic systemic manifestations encompass acute respiratory distress syndrome pneumonia, encephalitis, meningitis, seizures, and multiple organ dysfunction syndrome with a 40–70% case fatality (44–47). Several small studies report the following ophthalmic findings: nystagmus, CN-VI palsy and transient blindness during the acute phase of the illness; branch retinal artery occlusion, CN-VI palsy and Horner's syndrome upon follow up with a higher mortality associated with doll's eye reflex and pin-point pupils (50, 51). Current treatment is supportive care with no effective vaccines or therapeutics available (47).

3 Bacteria

Many bacteria are noted in the CDC's tripartite partitioning of biological agents within the CBRNE framework. Appendix 2 contains a summary of the bacteria and toxins according to CDC categories.

3.1 Category A

Category A bacteria include *Bacillus anthracis*, *Yersinia pestis*, and *Francisella tularensis*, and the botulinum toxin of *Clostridium botulinum* (7).

3.1.1 *Bacillus anthracis*: anthrax

Bacillus anthracis is a spore-forming, aerobic, Gram-positive rod that rose to public notoriety following the 2001 Anthrax letters (52, 53). Produced by the Soviet Union in at least one military research facility in 1979 (54), the bacterium is capable of cutaneous, respiratory, and gastrointestinal forms, which arise from the entrance of endospores into the body via breaks in the skin, by inhalation, or by ingestion. The vast majority of reported cases are cutaneous, and the gastrointestinal form is quite rare (55). Inhalational anthrax, also known as wool sorter's disease, is the cause of bioterror potential and involves germination of endospores in the lungs (55). Systemic manifestations of the disease include an early phase of fever, malaise, headache, and a nonproductive cough followed by a secondary phase of dyspnea and hypoxemia that can progress to septic shock (55). Ophthalmic findings of anthrax are limited and seen in the cutaneous form, with the characteristic black eschar seen on the eyelids (56). Current treatment of inhalational anthrax includes two months of intravenous antimicrobial combination therapy of at least one bactericidal drug and one protein synthesis inhibitor, an antitoxin, and postexposure prophylactic vaccination (57–59).

3.1.2 Botulinum toxin (*Clostridium botulinum*): botulism

The botulinum toxin, produced by *Clostridium botulinum*, can be spread via foodborne vectors (consumption of spores in children or preformed toxin in adults), direct wound colonization and toxin production by *C. botulinum*, inhalation of aerosolized toxin, or an iatrogenic route via exposure to injectable therapeutic toxin (60). Regardless of the mode of transmission, infection from botulinum toxin results in a characteristic bilateral, symmetric, flaccid paralysis that can lead to respiratory failure. Ophthalmic manifestations include photophobia, ptosis, diplopia, mydriasis, and extraocular/eyelid paralysis (61). Treatment of botulism includes antitoxin administration and supportive care, and intubation may be required in instances of airway protection and respiratory failure (60, 62).

3.1.3 *Francisella tularensis*: tularemia

Francisella tularensis, like *Yersinia pestis,* is a poorly staining Gram-negative coccobacillus that can be transmitted by ingestion or inhalation and via tick bites (63). Studied by several countries in the 20th century and probably used to some degree in World War II (WWII), Tularemia presents with six forms – ulceroglandular, glandular, oculoglandular, oropharyngeal, typhoidal and respiratory (64–66). Each of these forms begins with a nonspecific, flu-like phase of headache, fever, fatigue, chills, and myalgias (64). Given the scope of this article, the focus will be on the oculoglandular form. As the only ophthalmic form of tularemia, this localized form manifests with symptoms of photophobia, lacrimation, conjunctivitis, yellow conjunctival ulcers, chemosis, and eyelid edema (10, 63, 67). These symptoms coincide with the formation of regional pre-auricular or submandibular lymphadenopathy, and treatment should include 10–21 days of tetracycline, aminoglycoside, or fluoroquinolone antibiotics (10).

3.1.4 *Yersinia pestis*: plague

Yersinia pestis, commonly known as plague, is a Gram-negative coccobacillus transmitted by flea bites, infected animal contact, and inhalation (68). Plague can manifest in bubonic, septicemic, and pneumonic forms, with pneumonic being the most likely bioterror threat due to the potential for particles to be aerosolized. In WWII, the Japanese military used plague on prisoners at Manchuria, and even deployed plague-infected fleas in a number of cities in China (69, 70). This form begins with a sudden onset of headache, chills, fever, tachypnea, tachycardia, and a cough that progresses from dry to hemoptysis (68, 71). Ocular plague has been described in mule deer, but no cases have been reported in humans (72). Infections can be successfully treated with an aminoglycoside, such as streptomycin (68, 71, 73).

3.2 Category B

The CDC has designated the following ten bacteria and two bacterial toxins as Category B agents.

3.2.1 *Brucella* spp.: brucellosis

Brucellosis is the clinical disease caused by species of the *Brucella* genus. Like many bacteria, Brucella can be transmitted by ingestion of contaminated food, inhalation, or contact with mucous membranes (74). The clinical manifestations of brucellosis are both numerous and nonspecific. Patients may present with flu-like illness, abdominal pain, hepatomegaly and splenomegaly, or arthralgia, with more severe cases reporting endocarditis, motor and cranial nerve deficits, meningitis, seizures, bronchopneumonia, and pleural adhesion (75). Despite the many clinical manifestations reported, ophthalmic manifestation is infrequent. One 26-year study in Peru described 52 patients with ocular brucellosis, with uveitis being the most common presentation although keratitis and conjunctivitis were also reported (76). Treatment of brucellosis is difficult, requiring a combination therapy of doxycycline plus streptomycin/gentamicin or doxycycline plus rifampin (77).

3.2.2 *Burkholderia mallei*: glanders

Burkholderia mallei is a Gram-negative intracellular bacterium, and the causative agent of glanders. While glanders is rarely seen in developed countries today, it was one of the first biological agents used in warfare during the World War I and employed to impact adversarial transport animals (78). Transmission and human infection can occur through direct contact with damaged skin or mucosal membranes and inhalation (79, 80). Clinical presentation of glanders can range from a localized infection to septicemia. Generalized symptoms include fever, fatigue, headache, myalgias, and lymphadenopathy, and localized infections characterized by focal areas of suppuration that may ulcerate. Ophthalmic symptoms are generally due to localized eye infection of the conjunctiva, resulting in photophobia and excessive lacrimation (80). Pulmonary infection due to inhalation can cause a productive cough, dyspnea, and chest pain with pneumonia, pleuritis, or abscess formation. Dissemination of infection to the bloodstream can lead to bacterial colonization and abscess formation in nearly any organ (79, 80). Due to the lack of recent human glanders cases, treatment options have not been well described, but *B. mallei* has been shown to be susceptible to doxycycline, imipenem, ceftazidime, ciprofloxacin, piperacillin, and aminoglycosides (81).

3.2.3 *Burkholderia pseudomallei*: melioidosis

Despite being from the same genus, *Burkholderia pseudomallei* causes a separate clinical disease known as Melioidosis. Unlike glanders, human melioidosis cases are still known to occur in tropical and subtropical regions with endemic areas including Australia, southeast Asia, and India (82). Human infection typically occurs via inhalation or contact with contaminated water or soil (83). Pneumonia is the most common presentation and is associated with subsequent bacteremia. These patients typically present with a productive cough and dyspnea with fever and abscess formation following dissemination like glanders. Melioidosis can also present with a localized ulcerative infection (79, 83). Ocular melioidosis is rare but may present with symptoms such as orbital cellulitis, endophthalmitis, corneal ulceration, and dacryocystitis (84). Current regimens include ceftazidime or a carbapenem followed by trimethoprim-sulfamethoxazole (81, 83). Employment of biosafety level 3 precautions for laboratory workers has been suggested by some researchers (82, 83).

3.2.4 *Chlamydia psittaci:* psittacosis

Psittacosis is considered an atypical pneumonia caused by the Gram negative, intracellular bacterium *Chlamydia psittaci* (85, 86). The bacterium commonly infects both domestic and wild birds and can be transmitted to humans via inhalation of aerosolized feces or feather dust (85, 86). Systemic signs of psittacosis include an abrupt onset flu-like illness of fever, headache, chills, myalgias, fatigue, and cough, with less common manifestations of hepatosplenomegaly and peri-, endo-, or myocarditis (86, 87). The most commonly reported ophthalmic symptom of psittacosis is keratoconjunctivitis although this is still rare and typically reported in bird fanciers or laboratory workers (88). An association between psittacosis and ocular adnexal lymphoma has been described although this is still contested (89). Treatment of psittacosis with oral doxycycline is effective, and a macrolide such as azithromycin is considered a second line agent (85, 87).

3.2.5 *Coxiella burnetii*: Q fever

Coxiella burnetii, the causative agent of Q fever, is a Gram-negative, obligate intracellular bacterium that spreads via inhalation of aerosolized body fluids or consumption of contaminated food material (90). In humans, the clinical disease begins with a sudden onset of flu-like symptoms with pneumonia and hepatitis (91). Q fever can progress to a chronic form which can involve endocarditis. In pregnant women, Q fever has been linked to both spontaneous abortion and stillbirth (92). Ophthalmic manifestations of Q fever are limited to case reports and include acute multifocal retinitis, optic neuritis, and bilateral exudative retinal detachment (93–95). Both acute (2–3 weeks) and chronic (18–24 months) Q fever should be treated with doxycycline and hydroxychloroquine (91). Due to the aerosolized nature of transmission, PPE should include respirators (96).

3.2.6 Enterotoxin B (*Staphylococcus* spp.)

Comparable to *C. botulinum, Staphylococcus* species can produce a Category B toxin known as Enterotoxin B. It was previously studied for use as an aerosol biological weapon, but the toxin can also spread via contaminated food (97, 98). The toxin is a superantigen that causes widespread stimulation of the immune system, inducing fever, hypotension, pulmonary edema, acute respiratory distress syndrome, or septic shock (97–99). Ophthalmic symptoms are typically not well characterized, although purulent conjunctivitis following exposure to the toxin has been reported (100). The rapid and widespread onset of symptoms from Enterotoxin B make treatment difficult, and there are currently no approved antitoxins for clinical use (97–99).

3.2.7 Epsilon toxin (*Clostridium perfringens*)

The capacity for aerosolization of the epsilon toxin produced by *Clostridium perfringens* makes it a possible biowarfare agent (101). Despite this, little is known about the clinical manifestations, with only two cases ever being reported, both from 1955 (102, 103). One of the patients presented with only profuse diarrhea while the other developed a peritoneal effusion with a gangrenous ileum (102, 103). No ophthalmic symptoms have been reported. Moreover, there is currently no known treatment for infection with epsilon toxin (101).

3.2.8 Food safety threats: non-typhoid *Salmonella* spp., *Shigella dysenteriae*, *Escherichia coli* O157:H7

Non-typhoid *Salmonella* species, *Shigella dysenteriae*, and *Escherichia coli* O157:H7 together are classified as food safety threats by the CDC (7). Each bacterium is spread via the fecal-oral route through the consumption of contaminated food or water (*Salmonella* can also be transmitted via contact with reptiles) (104–106). While these pathogens exhibit shared clinical manifestations, *Salmonella* has some pertinent differences. *Salmonella* infection has a nonspecific presentation that may include fever, diarrhea, or pneumonia with hepatosplenomegaly common with bacteremia (105, 107). *Shigella* and *E. coli* O157:H7 can cause a watery diarrhea that progresses to a bloody diarrhea, or, in severe cases, hemolytic uremic syndrome (HUS) (104, 106). Infection of *Shigella* has been linked to reactive arthritis, previously known as Reiter's syndrome, which is a rare presentation of infection-induced arthritis that can cause conjunctivitis, among other non-ocular symptoms (108). Non-typhoidal *Salmonella* species have also been implicated in reactive arthritis, causing keratitis, uveitis and conjunctivitis (109, 110). While some strains of *E.coli* are known to impact the eye, the O157:H7 strain is not known to cause ocular disease. Unless immunocompromised, *Salmonella* infections are typically self-limited and should be treated supportively (111). The recommendation for *E. coli* treatment is similar, with antibiotic treatment demonstrating increased potential for developing HUS (104). *Shigella*, however, should be treated in both children and adults with ciprofloxacin or ceftriaxone (112, 113).

3.2.9 *Rickettsia prowazekii*: typhus fever

Rickettsia prowazekii is a Gram-negative bacilli and the causative agent of typhus fever. The disease is spread to humans via deposition of louse feces into bites or mucosal surfaces, or inhalation of aerosolized feces (114, 115). Clinical onset includes high fever, headache, and a rash due to hematogenous dissemination of *R. prowazekii*. Other symptoms can include nausea, vomiting, pneumonia, myocarditis, thrombocytopenia, jaundice, seizures, confusion, or even coma (114). Despite the numerous potential clinical manifestations of typhus fever, ophthalmic manifestations have not been described. Treatment of typhus fever is tetracyclines, with doxycycline being the preferred agent (115). Due to the louse-borne transmission of typhus fever, proper use of gowns, gloves, and caps should be used to prevent louse spread.

3.2.10 Water safety threats: *Vibrio cholerae* and *Cryptosporidium parvum*

Akin to the previous bacteria, *Vibrio cholerae* is designated by the CDC as a water safety threat, along with the protozoan *Cryptosporidium parvum* (7). Despite its eukaryotic classification, this review includes *C. parvum* here due to the CDC grouping with *V. cholerae*. While the classical transmission route of both organisms is the consumption of contaminated water, both can also be acquired via contaminated food, and *C. parvum* is capable of respiratory transmission (116–118). Infection from either organism leads to a watery diarrhea. *V. cholerae* causes pathognomonic "rice water" stool that leads to severe dehydration and electrolyte imbalances (116). In contrast, *C. parvum* infection typically presents with less severe diarrhea along with abdominal pain, nausea, flatulence, anorexia, and fatigue. If inhaled, one may also demonstrate a productive cough (117).

While neither are widely known for ophthalmic manifestations, some cases have been reported including a single case report of keratitis with corneal scraping cultures that grew *V. cholerae* after the patient was struck in the right eye by a marine shrimp (119). It should be noted that this infection was presumably caused by the direct contact of *V. cholerae* to the mucosal surface of the eye, and not the typical water-borne route. One study also reported that 9% of patients reported eye pain one-year post infection with *C. parvum*, but the protozoan is otherwise not linked to any other ophthalmic disease (120). The hallmark of cholera treatment is volume replacement and rehydration therapy with doxycycline indicated in severe cases (116). *C. parvum* infection should be treated with nitazoxanide (117).

4 Miscellaneous

4.1 Category B

4.1.1 Ricin toxin (*Ricinus communis*)

The ricin toxin is the only bioterrorism agent classified by the CDC that is neither viral, nor bacterial (or designated as a specific threat with a bacterium, as is the case with *C. parvum*) (Appendix 3). The toxin is produced by *Ricinus communis*, the castor bean, and when extracted, it can be disseminated by a number of modalities including aerosol, injection, or ingestion pathways (121). Physical symptoms vary by route of intoxication.

If ricin is aerosolized, the inhaled toxin can cause dyspnea, fever, cough, nausea, chest tightness, pulmonary edema, and skin erythema. If injected, myalgias and circulatory collapse are common. Ingested ricin typically causes abdominal pain, diarrhea, cramping, and dehydration (121). Ophthalmic implications of ricin toxin have yet to be described other than conjunctival injection. An antitoxin has been shown to be an effective countermeasure against ricin toxin in swine models (122).

5 COVID-19

Although not included in the CBRNE framework, response efforts to novel agents such as SARS-CoV-2 involve principles shared with other biological pathogens. The WHO COVID-19 Dashboard shows that estimates of COVID-19 has exceeded 770 million affected individuals and nearly 7 million deaths (123). Transmission is variable and includes SARS-CoV-2 particles landing on or otherwise coming into contact with the eyes, mouth, or nose, as well as inhalation of aerosol particles or droplets that contain the virus (124). Those infected may experience a range of symptoms, including those that are mild, moderate, and severe, but asymptomatic infection and transmission may also occur. Reported symptoms include malaise, fever or chills, cough, new loss of taste or smell, muscle or body aches, and difficulty breathing (125).

Ophthalmic manifestations associated with COVID-19 have been reported and include findings involving both the anterior and posterior segments of the eye. Reported findings include conjunctival hyperemia and injection, eye pain and redness, photophobia, cotton wool spots, retinal artery occlusion, retinal hemorrhage, and retinopathy (126–131). In addition to these ophthalmic findings, SARS-CoV-2 RNA has been previously detected in the tear film of 25% of patients in a hospitalized COVID-19 cohort (126). These ocular findings may provide insight into the physiologic changes of COVID-19, as well as the behavior of SARS-CoV-2 on the ocular surface.

6 Personal protective equipment

Due to the variable nature of the above biological agents, PPE decision-making relies on an understanding of the agent(s) of interest including the specific route(s) of transmission (e.g., respiratory, aerosolized droplets, contact), and the potential for spread during asymptomatic or presymptomatic infection. Agencies within the United States federal government, such as the National Institute for Occupational Safety and Health (NIOSH) and the Occupational Safety and Health Administration (OSHA), among others, have developed specific guidelines for CBRNE incident response that consider transmission routes (132–134).

Droplets of variola major virus, for example, can be spread through a respiratory route and guidance from the CDC indicates appropriate PPE as: eye protection, a NIOSH-certified N95 respirator, and disposable gown and gloves (135). Alternatively, contact transmission has been implicated in a number of VHFs so the CDC and WHO advocate for transmission-specific PPE provisions, such as a disposable facemask, full face shield, fluid-resistant gown, and two pairs of gloves (136, 137). Other key factors related to PPE include the specific tasks to be performed, duration of PPE wear, and the environmental conditions where patient care activities occur (e.g., forward, resource-austere settings vs. high resource settings).

7 Conclusion

Biologic agents can precipitate great ophthalmic injury and cause significant morbidity. With overlapping or limited ophthalmic findings, further investigations and close clinical monitoring of impacted patients are critical. As the global public health community continues to learn more about these agents, the CBRNE biological agent list and associated classification framework will require subsequent reevaluation, including potential revision of PPE guidance. Additionally, the appearance of emerging infectious diseases, especially zoonoses, necessitates continual pathogen surveillance, investigation, characterization, and assessment of merit for CBRNE status. Several zoonotic agents described here also require vector and/or source control measures for biohazard containment, and although an in-depth review of vector control is out of scope for this work, its importance should not be minimized. Future research to improve understanding of known pathogens will require reevaluation of the current CBRNE biological agent list and pathogen classification.

As globalization continues to expand, the risk for CBRNE incidents increases and subsequently prompts the need for progressive, vigilant surveillance and timely response to incidents to ensure a healthy global health community. Improving healthcare response and outcomes starts with accurate diagnosis, agent control, and treatment. This paper summarizes the clinical and ophthalmic manifestations, transmission routes and PPE considerations, as well as the current management guidelines for the biologic agents the CDC deems to be most dangerous to public health.

Author contributions

EC: Writing – original draft, Writing – review & editing. MDD: Writing – original draft, Writing – review & editing. CH: Writing – review & editing. YH: Writing – review & editing. CC: Writing – review & editing. MRD: Writing – review & editing. GJ: Writing – review & editing. JT: Supervision, Writing – review & editing. SY: Conceptualization, Supervision, Writing – review & editing.

Funding

The author(s) declare financial support was received for the research, authorship, and/or publication of this article. This project was supported by the National Eye Institute of the National Institutes of Health under award number R01 EY029594 (SY). Grant support was also provided by the Macula Society Retina Research Foundation, ARVO Mallinckrodt Young Investigator Grant, and the Stanley M. Truhlsen Family Foundation, Inc. CC was supported in part by a Knights Templar Eye Foundation career development award and competitive renewal, IDeA-CTR career development award, and National Eye Institute of the National Institutes of Health award number K08 EY034892.

Conflict of interest

The authors declare that the research was conducted in the absence of any commercial or financial relationships that could be construed as a potential conflict of interest.

Publisher's note

Author disclaimer

The content is solely the responsibility of the authors and does not necessarily represent official views of the National Institutes of Health or the views or policies of the Department of Health and Human Services, nor does mention of trade names, commercial products, or organizations imply endorsement by the U.S. Government.

Supplementary material

The Supplementary material for this article can be found online at: https://www.frontiersin.org/articles/10.3389/fmed.2023.1349571/full#supplementary-material

References

1. The lancet infectious D. Ebola Pheic is over but emergency continues. *Lancet Infect Dis*. (2016) 16:507. doi: 10.1016/s1473-3099(16)30013-5

2. Shadmi E, Chen Y, Dourado I, Faran-Perach I, Furler J, Hangoma P, et al. Health equity and COVID-19: global perspectives. *Int J Equity Health*. (2020) 19:104. doi: 10.1186/s12939-020-01218-z

3. Tambo E, Al-Nazawi AM. Combating the global spread of poverty-related monkeypox outbreaks and beyond. *Infect Dis Poverty*. (2022) 11:80. doi: 10.1186/s40249-022-01004-9

4. U.S. Department of Homeland Security. (2022). Cbrne Program. Available at: https://www.dhs.gov/hazardous-response-program (Accessed October 8, 2023).

5. U.S. Department of Homeland Security. (2022). National Strategy for Chemical, Biological, Radiological, Nuclear, and Explosives (Cbrne) Standards. Available at: https://www.dhs.gov/national-strategy-chemical-biological-radiological-nuclear-and-explosives-cbrne-standards (Accessed October 8, 2023).

6. U.S. Department of Homeland Security. (2023). Office of Emerging Threats. Available at: https://www.fema.gov/about/offices/response-recovery/emerging-threats (Accessed October 8, 2023).

7. Centers for Disease Control and Prevention. (2018). Emergency preparedness and response-bioterrorism agents/diseases: U.S. Department of Health & Human Services. Available at: https://emergency.cdc.gov/agent/agentlist-category.asp#catdef (Accessed March 22, 2023).

8. Mushtaq A, El-Azizi M, Khardori N. Category C potential bioterrorism agents and emerging pathogens. *Infect Dis Clin N Am*. (2006) 20:423–41, x. doi: 10.1016/j.idc.2006.03.003

9. Semba RD. The ocular complications of smallpox and smallpox immunization. *Arch Ophthalmol*. (2003) 121:715–9. doi: 10.1001/archopht.121.5.715

10. Karesh JW, Mazzoli RA, Heintz SK. Ocular manifestations of mosquito-transmitted diseases. *Mil Med*. (2018) 183:450–8. doi: 10.1093/milmed/usx183

11. Walker DH, McCormick JB, Johnson KM, Webb PA, Komba-Kono G, Elliott LH, et al. Pathologic and virologic study of fatal Lassa fever in man. *Am J Pathol*. (1982) 107:349–56.

12. Britt JM, Clifton BC, Barnebey HS, Mills RP. Microaerosol formation in noncontact 'Air-Puff' tonometry. *Arch Ophthalmol*. (1991) 109:225–8. doi: 10.1001/archopht.1991.01080020071046

13. Aloke C, Obasi NA, Aja PM, Emelike CU, Egwu CO, Jeje O, et al. Combating Lassa fever in West African sub-region: Progress, challenges, and future perspectives. *Viruses*. (2023) 15:146. doi: 10.3390/v15010146

14. Centers for Disease Control and Prevention. (2021). Viral hemorrhagic fevers (Vhfs) – arenaviruses (Arenaviridae): U.S. Department of Health & Human Services. Available at: https://www.cdc.gov/vhf/virus-families/arenaviridae.html (Accessed July 31, 2023).

15. Li AL, Grant D, Gbakie M, Kanneh L, Mustafa I, Bond N, et al. Ophthalmic manifestations and vision impairment in Lassa fever survivors. *PLoS One*. (2020) 15:e0243766. doi: 10.1371/journal.pone.0243766

16. Frank MG, Beitscher A, Webb CM, Raabe V. South American hemorrhagic fevers: a summary for clinicians. *Int J Infect Dis*. (2021) 105:505–15. doi: 10.1016/j.ijid.2021.02.046

17. Silva-Ramos CR, Faccini-Martínez ÁA, Calixto OJ, Hidalgo M. Bolivian hemorrhagic fever: a narrative review. *Travel Med Infect Dis*. (2021) 40:102001. doi: 10.1016/j.tmaid.2021.102001

18. Centers for Disease Control and Prevention. (2021). Viral hemorrhagic fevers (Vhfs) – filoviruses (filoviridae): U.S. Department of Health & Human Services. Available at: https://www.cdc.gov/vhf/virus-families/filoviridae.html (Accessed April 14, 2023).

19. Abir MH, Rahman T, Das A, Etu SN, Nafiz IH, Rakib A, et al. Pathogenicity and virulence of Marburg virus. *Virulence*. (2022) 13:609–33. doi: 10.1080/21505594.2022.2054760

20. Baseler L, Chertow DS, Johnson KM, Feldmann H, Morens DM. The pathogenesis of Ebola virus disease. *Annu Rev Pathol*. (2017) 12:387–418. doi: 10.1146/annurev-pathol-052016-100506

21. Gear JS, Cassel GA, Gear AJ, Trappler B, Clausen L, Meyers AM, et al. Outbreake of Marburg virus disease in Johannesburg. *Br Med J*. (1975) 4:489–93. doi: 10.1136/bmj.4.5995.489

22. Kuming BS, Kokoris N. Uveal involvement in Marburg virus disease. *Br J Ophthalmol*. (1977) 61:265–6. doi: 10.1136/bjo.61.4.265

23. Vingolo EM, Messano GA, Fragiotta S, Spadea L, Petti S. Ocular manifestations of Ebola virus disease: an Ophthalmologist's guide to prevent infection and panic. *Biomed Res Int*. (2015) 2015:487073. doi: 10.1155/2015/487073

24. Beeching NJ, Fenech M, Houlihan CF. Ebola virus disease. *BMJ*. (2014) 349:g7348. doi: 10.1136/bmj.g7348

25. Varkey JB, Shantha JG, Crozier I, Kraft CS, Lyon GM, Mehta AK, et al. Persistence of Ebola virus in ocular fluid during convalescence. *N Engl J Med*. (2015) 372:2423–7. doi: 10.1056/NEJMoa1500306

26. Shantha JG, Crozier I, Hayek BR, Bruce BB, Gargu C, Brown J, et al. Ophthalmic manifestations and causes of vision impairment in Ebola virus disease survivors in Monrovia, Liberia. *Ophthalmology*. (2017) 124:170–7. doi: 10.1016/j.ophtha.2016.10.011

27. Mattia JG, Vandy MJ, Chang JC, Platt DE, Dierberg K, Bausch DG, et al. Early clinical sequelae of Ebola virus disease in Sierra Leone: a cross-sectional study. *Lancet Infect Dis*. (2016) 16:331–8. doi: 10.1016/s1473-3099(15)00489-2

28. Meyer H, Ehmann R, Smith GL. Smallpox in the post-eradication era. *Viruses*. (2020) 12:2. doi: 10.3390/v12020138

29. Centers for Disease Control and Prevention. (2017). Smallpox: U.S. Department of Health & Human Services Available at: https://www.cdc.gov/smallpox/index.html (Accessed April 15, 2023).

30. Patton J. Small-pox keratitis. *Trans Am Acad Ophthalmol Otolaryngol*. (1922) 27:270–80.

31. Smith CL. Disciform keratitis following smallpox. *Am J Ophthalmol*. (1922) 5:32–4. doi: 10.1016/S0002-9394(22)91025-6

32. Fleck HK. Disciform keratitis secondary to smallpox. *Am J Ophthalmol*. (1921) 4:573–9. doi: 10.1016/S0002-9394(21)90487-2

33. Ronca SE, Dineley KT, Paessler S. Neurological sequelae resulting from encephalitic alphavirus infection. *Front Microbiol*. (2016) 7:959. doi: 10.3389/fmicb.2016.00959

34. Kehn-Hall K, Bradfute SB. Understanding host responses to equine encephalitis virus infection: implications for therapeutic development. *Expert Rev Anti-Infect Ther*. (2022) 20:1551–66. doi: 10.1080/14787210.2022.2141224

35. Sharma A, Knollmann-Ritschel B. Current understanding of the molecular basis of Venezuelan equine encephalitis virus pathogenesis and vaccine development. *Viruses*. (2019) 11:164. doi: 10.3390/v11020164

36. Wells RM, Sosa Estani S, Yadon ZE, Enria D, Padula P, Pini N, et al. An unusual hantavirus outbreak in southern Argentina: person-to-person transmission? Hantavirus pulmonary syndrome study Group for Patagonia. *Emerg Infect Dis*. (1997) 3:171–4. doi: 10.3201/eid0302.970210

37. Enría D, Padula P, Segura EL, Pini N, Edelstein A, Posse CR, et al. Hantavirus pulmonary syndrome in Argentina. Possibility of person to person transmission. *Medicina (B Aires)*. (1996) 56:709–11.

38. Krüger DH, Schönrich G, Klempa B. Human pathogenic hantaviruses and prevention of infection. *Hum Vaccin*. (2011) 7:685–93. doi: 10.4161/hv.7.6.15197

39. Theiler G, Langer-Wegscheider B, Zollner-Schwetz I, Valentin T, Hönigl M, Schnedl W, et al. Blurred vision and myopic shift in Puumala virus infections are independent of disease severity. *Clin Microbiol Infect*. (2012) 18:E435–7. doi: 10.1111/j.1469-0691.2012.03997.x

40. Kontkanen M, Puustjärvi T, Lähdevirta J. Myopic shift and its mechanism in Nephropathia Epidemica or Puumala virus infection. *Br J Ophthalmol*. (1994) 78:903–6. doi: 10.1136/bjo.78.12.903

41. Cao Y, Zhao X, Yi J, Tang R, Lei S. Hantavirus retinitis and concurrent hemorrhagic fever with renal syndrome. *Can J Ophthalmol*. (2017) 52:e41–4. doi: 10.1016/j.jcjo.2016.09.017

42. Mehta S, Jiandani P. Ocular features of hantavirus infection. *Indian J Ophthalmol*. (2007) 55:378–80. doi: 10.4103/0301-4738.33827

43. Singh S, Numan A, Sharma D, Shukla R, Alexander A, Jain GK, et al. Epidemiology, virology and clinical aspects of hantavirus infections: an overview. *Int J Environ Health Res*. (2022) 32:1815–26. doi: 10.1080/09603123.2021.1917527

44. Bruno L, Nappo MA, Ferrari L, Di Lecce R, Guarnieri C, Cantoni AM, et al. Nipah virus disease: epidemiological, clinical, diagnostic and legislative aspects of this unpredictable emerging zoonosis. *Animals (Basel)*. (2022) 13:159. doi: 10.3390/ani13010159

45. Luby SP, Hossain MJ, Gurley ES, Ahmed BN, Banu S, Khan SU, et al. Recurrent zoonotic transmission of Nipah virus into humans, Bangladesh, 2001-2007. *Emerg Infect Dis*. (2009) 15:1229–35. doi: 10.3201/eid1508.081237

46. Chua KB. Nipah Virus Outbreak in Malaysia. *J Clin Virol*. (2003) 26:265–75. doi: 10.1016/s1386-6532(02)00268-8

47. Singh RK, Dhama K, Chakraborty S, Tiwari R, Natesan S, Khandia R, et al. Nipah virus: epidemiology, pathology, immunobiology and advances in diagnosis, vaccine designing and control strategies – a comprehensive review. *Vet Q*. (2019) 39:26–55. doi: 10.1080/01652176.2019.1580827

48. Luby SP. The pandemic potential of Nipah virus. *Antivir Res*. (2013) 100:38–43. doi: 10.1016/j.antiviral.2013.07.011

49. Islam MS, Sazzad HM, Satter SM, Sultana S, Hossain MJ, Hasan M, et al. Nipah virus transmission from bats to humans associated with drinking traditional liquor made from date palm sap, Bangladesh, 2011-2014. *Emerg Infect Dis*. (2016) 22:664–70. doi: 10.3201/eid2204.151747

50. Goh KJ, Tan CT, Chew NK, Tan PS, Kamarulzaman A, Sarji SA, et al. Clinical features of Nipah virus encephalitis among pig farmers in Malaysia. *N Engl J Med*. (2000) 342:1229–35. doi: 10.1056/nejm200004273421701

51. Lim CC, Lee WL, Leo YS, Lee KE, Chan KP, Ling AE, et al. Late clinical and magnetic resonance imaging follow up of Nipah virus infection. *J Neurol Neurosurg Psychiatry*. (2003) 74:131–3. doi: 10.1136/jnnp.74.1.131

52. Dixon TC, Meselson M, Guillemin J, Hanna PC. Anthrax. *N Engl J Med*. (1999) 341:815–26. doi: 10.1056/nejm199909093411107

53. Bush LM, Abrams BH, Beall A, Johnson CC. Index case of fatal inhalational anthrax due to bioterrorism in the United States. *N Engl J Med*. (2001) 345:1607–10. doi: 10.1056/NEJMoa012948

54. Meselson M, Guillemin J, Hugh-Jones M, Langmuir A, Popova I, Shelokov A, et al. The Sverdlovsk anthrax outbreak of 1979. *Science*. (1994) 266:1202–8. doi: 10.1126/science.7973702

55. Kamal SM, Rashid AK, Bakar MA, Ahad MA. Anthrax: an update. *Asian Pac J Trop Biomed*. (2011) 1:496–501. doi: 10.1016/s2221-1691(11)60109-3

56. Amraoui A, Tabbara KF, Zaghloul K. Anthrax of the eyelids. *Br J Ophthalmol*. (1992) 76:753–4. doi: 10.1136/bjo.76.12.753

57. Hendricks KA, Wright ME, Shadomy SV, Bradley JS, Morrow MG, Pavia AT, et al. Centers for Disease Control and Prevention expert panel meetings on prevention and treatment of anthrax in adults. *Emerg Infect Dis*. (2014) 20:e130687. doi: 10.3201/eid2002.130687

58. Pillai SK, Huang E, Guarnizo JT, Hoyle JD, Katharios-Lanwermeyer S, Turski TK, et al. Antimicrobial treatment for systemic anthrax: analysis of cases from 1945 to 2014 identified through a systematic literature review. *Health Secur*. (2015) 13:355–64. doi: 10.1089/hs.2015.0033

59. Chateau A, Van der Verren SE, Remaut H, Fioravanti A. The *Bacillus Anthracis* cell envelope: composition, physiological role, and clinical relevance. *Microorganisms*. (2020) 8:1864. doi: 10.3390/microorganisms8121864

60. Rao AK, Sobel J, Chatham-Stephens K, Luquez C. Clinical guidelines for diagnosis and treatment of botulism, 2021. *MMWR Recomm Rep*. (2021) 70:1–30. doi: 10.15585/mmwr.rr7002a1

61. Caya JG. Clostridium botulinum and the ophthalmologist: a review of botulism, including biological warfare ramifications of botulinum toxin. *Surv Ophthalmol*. (2001) 46:25–34. doi: 10.1016/s0039-6257(01)00227-2

62. Yu PA, Lin NH, Mahon BE, Sobel J, Yu Y, Mody RK, et al. Safety and improved clinical outcomes in patients treated with new equine-derived heptavalent botulinum antitoxin. *Clin Infect Dis*. (2017) 66:S57. doi: 10.1093/cid/cix816

63. Wawszczak M, Banaszczak B, Rastawicki W. Tularaemia – a diagnostic challenge. *Ann Agric Environ Med*. (2022) 29:12–21. doi: 10.26444/aaem/139242

64. World Health Organization. *Who Guidelines on Tularaemia; Epidemic and Pandemic Alert and Response*. Geneva: World Health Organization (2007).

65. Hirschmann JV. From squirrels to biological weapons: the early history of tularemia. *Am J Med Sci*. (2018) 356:319–28. doi: 10.1016/j.amjms.2018.06.006

66. Croddy E, Krčálová S. Tularemia, biological warfare, and the Battle for Stalingrad (1942–1943). *Mil Med*. (2001) 166:837–8. doi: 10.1093/milmed/166.10.837

67. Kantardjiev T, Padeshki P, Ivanov IN. Diagnostic approaches for Oculoglandular tularemia: advantages of Pcr. *Br J Ophthalmol*. (2007) 91:1206–8. doi: 10.1136/bjo.2007.117523

68. Rosario-Acevedo R, Biryukov SS, Bozue JA, Cote CK. Plague prevention and therapy: perspectives on current and future strategies. *Biomedicine*. (2021) 9:1421. doi: 10.3390/biomedicines9101421

69. Bellamy RJ, Freedman AR. Bioterrorism. *QJM*. (2001) 94:227–34. doi: 10.1093/qjmed/94.4.227

70. Dennis DT. Plague as a biological weapon. *Bioterror Infect Agents*. (2009):37–70. doi: 10.1007/978-1-4419-1266-4_2

71. Kool JL. Risk of person-to-person transmission of pneumonic plague. *Clin Infect Dis*. (2005) 40:1166–72. doi: 10.1086/428617

72. Edmunds DR, Williams ES, O'Toole D, Mills KW, Boerger-Fields AM, Jaeger PT, et al. Ocular plague (*Yersinia Pestis*) in mule deer (*Odocoileus Hemionus*) from Wyoming and Oregon. *J Wildl Dis*. (2008) 44:983–7. doi: 10.7589/0090-3558-44.4.983

73. Inglesby TV, Dennis DT, Henderson DA, Bartlett JG, Ascher MS, Eitzen E, et al. Plague as a biological weapon: medical and public health management. Working Group on Civilian Biodefense. *JAMA*. (2000) 283:2281–90. doi: 10.1001/jama.283.17.2281

74. de Figueiredo P, Ficht TA, Rice-Ficht A, Rossetti CA, Adams LG. Pathogenesis and immunobiology of brucellosis: review of brucella-host interactions. *Am J Pathol*. (2015) 185:1505–17. doi: 10.1016/j.ajpath.2015.03.003

75. Dean AS, Crump L, Greter H, Hattendorf J, Schelling E, Zinsstag J. Clinical manifestations of human brucellosis: a systematic review and meta-analysis. *PLoS Negl Trop Dis*. (2012) 6:e1929. doi: 10.1371/journal.pntd.0001929

76. Rolando I, Olarte L, Vilchez G, Lluncor M, Otero L, Paris M, et al. Ocular manifestations associated with brucellosis: a 26-year experience in Peru. *Clin Infect Dis*. (2008) 46:1338–45. doi: 10.1086/529442

77. Solera J, Martínez-Alfaro E, Espinosa A. Recognition and optimum treatment of brucellosis. *Drugs*. (1997) 53:245–56. doi: 10.2165/00003495-199753020-00005

78. Wheelis M. First shots fired in biological warfare. *Nature*. (1998) 395:213. doi: 10.1038/26089

79. Johns Hopkins Center for Health Security. (2011). *Burkholderia Mallei* (Glanders) and Burkholderia (Melioidosis) Fact Sheet: Johns Hopkins Bloomberg School of Public Health. Available at: https://www.centerforhealthsecurity.org/our-work/publications/glanders-and-melioidosis-fact-sheet (Accessed March 26, 2023).

80. Van Zandt KE, Greer MT, Gelhaus HC. Glanders: an overview of infection in humans. *Orphanet J Rare Dis*. (2013) 8:131. doi: 10.1186/1750-1172-8-131

81. Estes DM, Dow SW, Schweizer HP, Torres AG. Present and future therapeutic strategies for melioidosis and glanders. *Expert Rev Anti-Infect Ther*. (2010) 8:325–38. doi: 10.1586/eri.10.4

82. Currie BJ, Dance DA, Cheng AC. The global distribution of Burkholderia Pseudomallei and melioidosis: an update. *Trans R Soc Trop Med Hyg*. (2008) 102:S1–4. doi: 10.1016/s0035-9203(08)70002-6

83. Gassiep I, Armstrong M, Norton R. Human Melioidosis. *Clin Microbiol Rev*. (2020) 33:2. doi: 10.1128/cmr.00006-19

84. Yaisawang S, Asawaphureekorn S, Chetchotisakd P, Wongratanacheewin S, Pakdee P. Ocular involvement in melioidosis: a 23-year retrospective review. *J Ophthalmic Inflamm Infect*. (2018) 8:5. doi: 10.1186/s12348-018-0147-6

85. Basarab M, Macrae MB, Curtis CM. Atypical pneumonia. *Curr Opin Pulm Med*. (2014) 20:247–51. doi: 10.1097/mcp.0000000000000048

86. Knittler MR, Sachse K. *Chlamydia Psittaci*: update on an underestimated zoonotic agent. *Pathog Dis*. (2015) 73:1–15. doi: 10.1093/femspd/ftu007

87. West A. A brief review of *Chlamydophila Psittaci* in birds and humans. *J Exotic Pet Med*. (2011) 20:18–20. doi: 10.1053/j.jepm.2010.11.006

88. Dean D, Shama A, Schachter J, Dawson CR. Molecular identification of an avian strain of *Chlamydia Psittaci* causing severe keratoconjunctivitis in a bird fancier. *Clin Infect Dis*. (1995) 20:1179–85. doi: 10.1093/clinids/20.5.1179

89. Raderer M, Kiesewetter B, Ferreri AJ. Clinicopathologic characteristics and treatment of marginal zone lymphoma of mucosa-associated lymphoid tissue (malt lymphoma). *CA Cancer J Clin*. (2016) 66:153–71. doi: 10.3322/caac.21330

90. Van Leuken JPG, Swart AN, Brandsma J, Terink W, Van de Kassteele J, Droogers P, et al. Human Q fever incidence is associated to spatiotemporal environmental conditions. *One Health*. (2016) 2:77–87. doi: 10.1016/j.onehlt.2016.03.004

91. Ullah Q, Jamil T, Saqib M, Iqbal M, Neubauer H. Q fever-a neglected zoonosis. *Microorganisms*. (2022) 10:8. doi: 10.3390/microorganisms10081530

92. Kampschreur L, Dekker S, Hagenaars JCJP, Lestrade P, Renders NHM, de Jager-Leclercq MGL, et al. Identification of risk factors for chronic Q fever, the Netherlands. *Emerg Infect Dis J*. (2012) 18:563–70. doi: 10.3201/eid1804.111478

93. Mahmoud A, Abid F, Khairallah M, Affes S, Mbarek S, Amor HH, et al. Acute multifocal retinitis in a patient with Q fever (*Coxiella Burnetii* infection) with endocarditis. *J Ophthalmic Inflamm Infect*. (2022) 12:19. doi: 10.1186/s12348-022-00295-1

94. Ong C, Ahmad O, Senanayake S, Buirski G, Lueck C. Optic neuritis associated with Q fever: case report and literature review. *Int J Infect Dis*. (2010) 14:e269–73. doi: 10.1016/j.ijid.2009.11.010

95. Udaondo P, Garcia-Delpech S, Salom D, Garcia-Pous M, Diaz-Llopis M. Q fever: a new ocular manifestation. *Clin Ophthalmol*. (2011) 5:1273–5. doi: 10.2147/opth.S18771

96. Ganter M. Zoonotic risks from small ruminants. *Vet Microbiol*. (2015) 181:53–65. doi: 10.1016/j.vetmic.2015.07.015

97. Pinchuk IV, Beswick EJ, Reyes VE. Staphylococcal enterotoxins. *Toxins (Basel)*. (2010) 2:2177–97. doi: 10.3390/toxins2082177

98. Fries BC, Varshney AK. Bacterial toxins-staphylococcal enterotoxin B. *Microbiol Spectr*. (2013) 1:2. doi: 10.1128/microbiolspec.AID-0002-2012

99. Krakauer T. Therapeutic Down-modulators of staphylococcal superantigen-induced inflammation and toxic shock. *Toxins (Basel)*. (2010) 2:1963–83. doi: 10.3390/toxins2081963

100. Rusnak JM, Kortepeter M, Ulrich R, Poli M, Boudreau E. Laboratory exposures to staphylococcal enterotoxin B. *Emerg Infect Dis*. (2004) 10:1544–9. doi: 10.3201/eid1009.040250

101. Alves GG, Machado de Ávila RA, Chávez-Olórtegui CD, Lobato FC. *Clostridium Perfringens* epsilon toxin: the third Most potent bacterial toxin known. *Anaerobe*. (2014) 30:102–7. doi: 10.1016/j.anaerobe.2014.08.016

102. Gleeson-White MH, Bullen JJ. Clostridium Welchii epsilon toxin in the intestinal contents of man. *Lancet*. (1955) 268:384–5. doi: 10.1016/s0140-6736(55)91275-7

103. Kohn J, Warrack GH. Recovery of clostridium Welchii type D from man. *Lancet*. (1955) 268:385. doi: 10.1016/s0140-6736(55)91276-9

104. Rahal EA, Kazzi N, Nassar FJ, Matar GM. *Escherichia Coli* O157:H7-clinical aspects and novel treatment approaches. *Front Cell Infect Microbiol*. (2012) 2:138. doi: 10.3389/fcimb.2012.00138

105. Crump JA, Sjölund-Karlsson M, Gordon MA, Parry CM. Epidemiology, clinical presentation, laboratory diagnosis, antimicrobial resistance, and antimicrobial Management of Invasive Salmonella Infections. *Clin Microbiol Rev*. (2015) 28:901–37. doi: 10.1128/cmr.00002-15

106. Pakbin B, Brück WM, Brück TB. Molecular mechanisms of shigella pathogenesis; recent advances. *Int J Mol Sci*. (2023) 24:2448. doi: 10.3390/ijms24032448

107. Gilchrist JJ, MacLennan CA. Invasive nontyphoidal salmonella disease in Africa. *EcoSal Plus*. (2019) 8:2018. doi: 10.1128/ecosalplus.ESP-0007-2018

108. Hannu T, Mattila L, Siitonen A, Leirisalo-Repo M. Reactive arthritis attributable to shigella infection: a clinical and epidemiological Nationwide study. *Ann Rheum Dis*. (2005) 64:594–8. doi: 10.1136/ard.2004.027524

109. Collins NE, Fitzgerald O, Murphy CC. Clinical image: keratitis in reactive arthritis. *Arthritis Rheum*. (2011) 63:2522. doi: 10.1002/art.30397

110. Saari KM, Vilppula A, Lassus A, Leirisalo M, Saari R. Ocular inflammation in Reiter's disease after salmonella enteritis. *Am J Ophthalmol*. (1980) 90:63–8. doi: 10.1016/s0002-9394(14)75077-9

111. Onwuezobe IA, Oshun PO, Odigwe CC. Antimicrobials for treating symptomatic non-typhoidal salmonella infection. *Cochrane Database Syst Rev*. (2012) 11:CD001167. doi: 10.1002/14651858.CD001167.pub2

112. Christopher PRH, David KV, John SM, Sankarapandian V. Antibiotic therapy for shigella dysentery. *Cochrane Database Syst Rev*. (2009):4. doi: 10.1002/14651858.CD006784.pub2

113. Traa BS, Walker CL, Munos M, Black RE. Antibiotics for the treatment of dysentery in children. *Int J Epidemiol*. (2010) 39 Suppl 1:i70–4. doi: 10.1093/ije/dyq024

114. Angelakis E, Bechah Y, Raoult D. The history of epidemic typhus. *Microbiol Spectr*. (2016) 4, 2–3. doi: 10.1128/microbiolspec.PoH-0010-2015

115. Blanton LS. The rickettsioses: a practical update. *Infect Dis Clin N Am*. (2019) 33:213–29. doi: 10.1016/j.idc.2018.10.010

116. Chowdhury F, Ross AG, Islam MT, McMillan NAJ, Qadri F. Diagnosis, management, and future control of cholera. *Clin Microbiol Rev*. (2022) 35:e0021121. doi: 10.1128/cmr.00211-21

117. Helmy YA, Hafez HM. Cryptosporidiosis: from prevention to treatment, a narrative review. *Microorganisms*. (2022) 10:2456. doi: 10.3390/microorganisms10122456

118. DuPont HL, Chappell CL, Sterling CR, Okhuysen PC, Rose JB, Jakubowski W. The infectivity of *Cryptosporidium Parvum* in healthy volunteers. *N Engl J Med*. (1995) 332:855–9. doi: 10.1056/NEJM199503303321304

119. Chen WD, Lai LJ, Hsu WH, Huang TY. *Vibrio Cholerae* non-O1 – the first reported case of keratitis in a healthy patient. *BMC Infect Dis*. (2019) 19:916. doi: 10.1186/s12879-019-4475-4

120. Stiff RE, Davies AP, Mason BW, Hutchings HA, Chalmers RM. Long-term health effects after resolution of acute *Cryptosporidium Parvum* infection: a 1-year follow-up of outbreak-associated cases. *J Med Microbiol*. (2017) 66:1607–11. doi: 10.1099/jmm.0.000609

121. Rasetti-Escargueil C, Avril A. Medical countermeasures against ricin intoxication. *Toxins (Basel)*. (2023) 15:2. doi: 10.3390/toxins15020100

122. Falach R, Sapoznikov A, Evgy Y, Aftalion M, Makovitzki A, Agami A, et al. Post-exposure anti-ricin treatment protects swine against lethal systemic and pulmonary exposures. *Toxins (Basel)*. (2020) 12:354. doi: 10.3390/toxins12060354

123. World Health Organization. (2023). Who coronavirus (COVID-19) dashboard: World Health Organization. Available at: https://covid19.who.int/ (Accessed December 13, 2023).

124. Centers for Disease Control and Prevention. (2023). COVID-19 overview and infection prevention and control priorities in non-U.S. healthcare settings: Centers for Disease Control and Prevention. Available at: https://www.cdc.gov/coronavirus/2019-ncov/hcp/non-us-settings/overview/index.html#r1 (Accessed December 14, 2023).

125. Centers for Disease Control and Prevention. (2022). Symptoms of COVID-19: Centers for Disease Control and Prevention. Available at: https://www.cdc.gov/coronavirus/2019-ncov/symptoms-testing/symptoms.html (Accessed December 13, 2023).

126. Shantha JG, Fashina T, Stittleburg V, Randleman C, Ward L, Regueiro M, et al. COVID-19 and the eye: systemic and laboratory risk factors for retinopathy and detection of tear film Sars-Cov-2 Rna with a triplex rt-Pcr assay. *PLoS One*. (2022) 17:e0277301. doi: 10.1371/journal.pone.0277301

127. Shantha JG, Auld SC, Anthony C, Ward L, Adelman MW, Maier CL, et al. Retinopathy and systemic disease morbidity in severe COVID-19. *Ocul Immunol Inflamm*. (2021) 29:743–50. doi: 10.1080/09273948.2021.1952278

128. Guan WJ, Ni ZY, Hu Y, Liang WH, Ou CQ, He JX, et al. Clinical characteristics of coronavirus disease 2019 in China. *N Engl J Med*. (2020) 382:1708–20. doi: 10.1056/NEJMoa2002032

129. Gangaputra SS, Patel SN. Ocular symptoms among nonhospitalized patients who underwent COVID-19 testing. *Ophthalmology*. (2020) 127:1425–7. doi: 10.1016/j.ophtha.2020.06.037

130. Ma N, Li P, Wang X, Yu Y, Tan X, Chen P, et al. Ocular manifestations and clinical characteristics of children with laboratory-confirmed COVID-19 in Wuhan, China. *JAMA Ophthalmol*. (2020) 138:1079–86. doi: 10.1001/jamaophthalmol.2020.3690

131. Invernizzi A, Torre A, Parrulli S, Zicarelli F, Schiuma M, Colombo V, et al. Retinal findings in patients with COVID-19: results from the Serpico-19 study. *EClinicalMedicine*. (2020) 27:100550. doi: 10.1016/j.eclinm.2020.100550

132. Brown CK, Matthews DL, Thomas RJ, Edens AL. Developing a personal protective equipment selection matrix for preventing occupational exposure to Ebola virus. *Health Secur*. (2019) 17:213–28. doi: 10.1089/hs.2019.0014

133. National Institute for Occupational Safety and Health. Guidance on emergency responder personal protective equipment (Ppe) for response to Cbrn terrorism incidents. *Ctr Dis Control Prev*. (2008) 1–13.

134. Occupational Safety and Health Administration. *Chemical-biological-radiological-nuclear (CBRN) personal protective equipment selection matrix for emergency responders: U.S. Department of Labor*. Occupational Safety & Health Administration, U.S. Department of Labor, Washington, DC, USA (2005).

135. Centers for Disease Control and Prevention. *Smallpox: Prevent Spread of Disease: U.S. Department of Health and Human Services*. Centers for Disease Control and Prevention, Atlanta, GA, USA (2017).

136. World Health Organization. *Infection control for viral Haemorrhagic fevers in the African health care setting*. Geneva: World Health Organization (1998).

137. Centers for Disease Control and Prevention. (2023). Guidance on personal protective equipment (Ppe) in U.S. healthcare settings for evaluating patients suspected to have selected viral hemorrhagic fevers who are clinically stable and do not have bleeding, vomiting, or diarrhea: U.S. Department of Health and Human Service. Available at: https://www.cdc.gov/vhf/ebola/healthcare-us/ppe/guidance-clinically-stable-puis.html (Accessed November 14, 2023).

frontiers | Frontiers in Medicine

TYPE Original Research
PUBLISHED 04 March 2024
DOI 10.3389/fmed.2024.1367900

Effect of PCI on ophthalmic artery hemodynamics in patients with acute coronary syndrome

Wen-long Liu, Lan-ting Wu, Jia-lin Wang, Jiao Sun, Xue-ru Cheng, Zhuo-hua Zhou, Jia-xin Guan, Yan-ling Wang*† and Zhao-yang Meng*†

Department of Ophthalmology, Beijing Friendship Hospital, Capital Medical University, Beijing, China

Purpose: We aimed to explore the effects of percutaneous coronary intervention (PCI) on the ophthalmic artery (OA) hemodynamics in patients with acute coronary syndrome (ACS).

Methods: A total of 73 participants (Group0: healthy controls, Group1: Patients with ACS underwent PCI < 3 months, Group2: Patients with ACS underwent PCI ≥ 3 months) were enrolled. Computed tomographic angiography images were used to construct three-dimensional models of participants' OAs. Numerical simulations based on computational fluid dynamics were used to acquire hemodynamic parameters.

Results: The angle between the OA and internal carotid artery in Group2 was significantly larger compared with Group0 and Group1 ($P = 0.003$ and $P = 0.044$). Hemodynamic simulation showed a significantly slower OA blood velocity in Group1 than in the control ($P < 0.001$) and Group2 ($P = 0.033$). Lower wall shear stress was found in Group1 than that in control ($P = 0.040$). Patients after PCI had a higher wall pressure than healthy controls ($P = 0.012$ and $P = 0.004$). Mass flow ratios were decreased in Group1 and Group2 ($P = 0.021$ and $P = 0.002$). The hemodynamic parameters of OA were correlated with several clinical indicators.

Conclusions: The OA blood flow velocity of patients with ACS after PCI initially slowed down, which increased the risk of plaque formation, and then showed an increasing trend. There was a correlation between OA hemodynamic parameters and clinical indexes related to cardiac stress. Ischemia-reperfusion injury and changes in blood flow status after PCI may affect OA morphology and hemodynamics, leading to ocular lesions.

Trial registration: ChiCTR2100050428.

KEYWORDS

percutaneous coronary intervention, ophthalmic artery, computational fluid dynamics, hemodynamic numerical simulation, three-dimensional reconstruction

OPEN ACCESS

EDITED BY
Kai Jin,
Zhejiang University, China

REVIEWED BY
Ludwig M. Heindl,
University Hospital of Cologne, Germany
Bojun Zhao,
Shandong Provincial Hospital, China

*CORRESPONDENCE
Yan-ling Wang
✉ wangyanl@ccmu.edu.cn
Zhao-yang Meng
✉ mm1526@ccmu.edu.cn

†These authors have contributed equally to this work

RECEIVED 09 January 2024
ACCEPTED 19 February 2024
PUBLISHED 04 March 2024

CITATION
Liu W-l, Wu L-t, Wang J-l, Sun J, Cheng X-r, Zhou Z-h, Guan J-x, Wang Y-l and Meng Z-y (2024) Effect of PCI on ophthalmic artery hemodynamics in patients with acute coronary syndrome. *Front. Med.* 11:1367900. doi: 10.3389/fmed.2024.1367900

Introduction

Cardiovascular disease is the leading cause of death worldwide. Despite the initial results, the treatment of up to 197 million patients with ischemic heart disease worldwide still faces significant challenges (1). Percutaneous coronary intervention (PCI) is currently an important treatment for myocardial revascularization in patients with acute coronary syndrome (ACS), reducing the risk of death and improving the long-term prognosis. Advances in technology and development of antiplatelet therapy are increasing the safety of the procedure (2). However, significant complications can still occur during and after PCI that may be related to the puncture site, the oral catheterization of the coronary artery, or the intervention itself. Moreover, myocardial ischemia-reperfusion injury (IRI) after PCI should not be ignored (3). Different organs, including the kidney, brain, eyes, and gastrointestinal system, may be targets of thromboembolic events after PCI (4). Since 1985, cases of ocular complications after PCI have been reported from around the world (5–7). Ophthalmic complications of PCI include a wide range of clinical manifestations, from transient visual impairment to permanent and devastating conditions. Most cases describe retinal artery occlusion (RAO) after PCI. The incidence of new retinal embolism after PCI was 6.33% (8). Therefore, it is of great significance to explore the changes of ocular blood flow after PCI for the prevention and treatment of ocular diseases such as RAO.

Our previous study found that ophthalmic artery (OA) can reflect changes in ocular blood supply earlier than retinal vessels (9). Using computational fluid dynamics (CFD), we found that OA in patients with ACS had a slower blood flow velocity (10). The numerical simulation technology based on CFD has solved the difficult problem of OA observation and measurement, and provided an effective means for exploring the relationship between OA and ischemic heart disease. However, there is a lack of research on retrobulbar blood flow changes after PCI. Therefore, the purpose of this study was to investigate the effects of PCI on the OA hemodynamics in patients with ACS.

Methods

Study design and participants

This study (ChiCTR2100050428) included patients with ACS who underwent head and neck computed tomographic angiography (CTA) examination after PCI at Beijing Friendship Hospital between September 2021 and January 2023, as well as healthy controls (HCs) who received CTA for other reasons. The study protocol was approved by the local ethics committee of the Beijing Friendship Hospital (2020-P2-008-01) and conformed to the tenets of the Declaration of Helsinki. All participants provided written informed consent. Three groups were defined, prior to recruitment: HCs (Group 0), patients with ACS underwent PCI $<$ 3 months (Group 1), and patients with ACS underwent PCI $\geq$ 3 months (Group 2).

A detailed ophthalmic examination was performed on each participant, including best-corrected visual acuity, intraocular pressure and slit-lamp examination. The slit-lamp examination was performed by two experienced ophthalmologists. Patients with significant ocular lesions such as glaucoma, orbital space-occupying diseases, and optic neuritis, as well as those caused by systemic diseases such as diabetic retinopathy, were excluded. The electronic medical records were collected retrospectively to record general information, laboratory parameters, echocardiogram results, coronary angiography results, and concomitant medications.

Ophthalmic artery computational fluid dynamics simulation

Based on our previous research method (10), the original head and neck CTA images of all participants were obtained, and the three-dimensional OA models were reconstructed. Import the CTA DICOM image into Mimics 21.0 (Materialize, Ann Arbor, MI, USA). An image segmentation technique was used to reconstruct one of the OAs visible on the CTA image for each participant. Manually edit model boundaries to eliminate adjacent interference structures. A solid blood vessel model was obtained after smoothing the surface of the model in Geomagic Studio 14.0 (3D Systems, Rock Hill, SC, USA).

Based on CFD, the finite-volume method was adopted and ANSYS Fluent 15.0 (ANSYS, Inc., Canonsburg, PA, USA) was used for hemodynamic numerical simulation. The blood vessels were assumed to be rigid and non-slipped, and the simulated blood was considered to be a steady-state, laminar, incompressible Newtonian fluid. The governing equations for the numerical simulation were the Navier-Stokes equation and mass conservation equation (Equations 1, 2):

$$\rho\left(\vec{u}\cdot\nabla\right)\vec{u}+\nabla p-\mu\Delta\vec{u}=0 \tag{1}$$

$$\nabla\cdot\vec{u}=0 \tag{2}$$

In the formula, $\vec{u}$ represents the velocity vector, p is the pressure, ρ is the blood density, and μ is blood viscosity. The blood viscosity and density were set to 3.5×10^{-3} kg/ms and 1,050 kg/m^3, respectively. Based on the literature (11), we adopted a systolic and diastolic mean flow velocity of 0.34 m/s as the inlet velocity (velocity of the internal carotid artery [ICA] siphon). All models were set to the same boundary conditions.

Quantitative assessment

We measured the morphological data of the OA models. The centerline of each model was generated to obtain the best-fit diameter of the initial OA and the angle between the OA and ICA centerline. The initial OA was defined as the region where OA originates from ICA. Two experienced ophthalmologists collected all the data.

After successful simulation, the OA hemodynamic data were obtained by using the Ansys Fluent post-processing software. The blood flow velocity, wall shear stress (WSS), and initial OA pressure were obtained quantitatively. The mass flow of the OA and ICA in flux reports was obtained. Additionally, the mass flow ratio, defined as the mass flow of the OA accounted for ipsilateral ICA mass flow, was calculated.

Statistical analysis

Statistical analyses were performed using SPSS Statistics 26.0 (IBM, Armonk, NY, USA). The Shapiro-Wilk test was used to test the normality of the variables. Data for normal distribution are expressed as mean ± standard deviation, and descriptive data for non-normal distribution are expressed as median (25–75%). In the multi-group comparison, one-way ANOVA with Bonferroni correction was used for continuous variables with normal distribution, and Kruskal-Wallis H test was used for variables with non-normal distribution. Depending on normality, comparisons between the two groups were made using either the t-test or Mann-Whitney U test. Categorical variables were expressed as numbers and percentages and analyzed using χ^2 or Fisher's exact

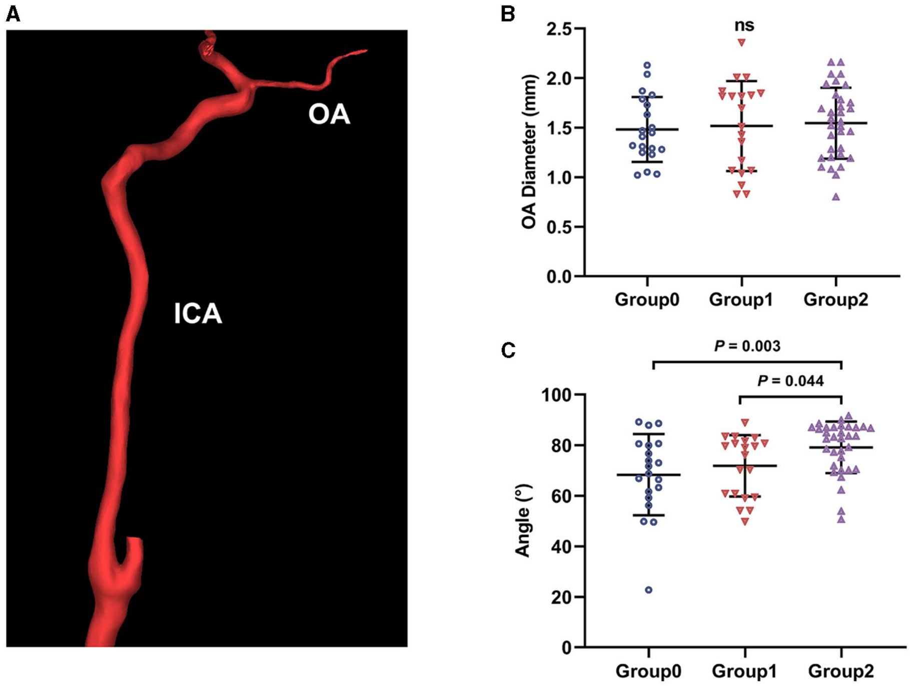

FIGURE 1
Ophthalmic artery (OA) three-dimensional reconstruction and morphological measurement. **(A)** The reconstructed OA model; ICA, internal carotid artery. **(B)** The initial OA diameter comparison between groups; ns, not significant. **(C)** Angle between OA and ICA comparison between groups.

tests, as appropriate. Pearson's correlation coefficient and linear regression were used to determine correlations between continuous variables. Non-normally distributed variables were converted into natural logarithms.

Results

Clinical characteristics

In total, 73 OA models were reconstructed (Figure 1A). Table 1 shows the clinical characteristics of the 73 participants. The groups were matched for age ($P = 0.084$), sex ($P = 0.173$) and type of ACS ($P = 0.721$, $P = 0.801$, $P = 0.591$, respectively). A higher proportion of patients with ACS had diabetes, and dyslipidemia ($P = 0.001$ and $P = 0.011$, respectively). There were no differences in peripheral arterial disease ($P = 0.577$), history of ischemic stroke ($P = 0.092$), family history of coronary atherosclerotic heart disease ($P = 0.679$), a current smoking status or hypertension ($P = 0.027$, $P = 0.021$ not significant after Bonferroni correction). The clinical, laboratory, echocardiographic, and medication details of the patients after PCI are shown in Table 2.

Coronary artery lesions of patients were assessed through angiography: two patients in the Group1 had a single vessel lesion (left anterior descending artery [LAD] involved), two patients had the left main stem and three vessel lesions (left main coronary artery, LAD, left circumflex artery [LCX], and right coronary artery [RCA] involved); three patients in the Group2 had single-vessel lesions (LAD or RCA involved). In addition, all the other patients had multiple vessel lesions (involving the LAD, LCX, and RCA). The mean time after PCI of Group1 was 10.30 ± 9.46 days, and that of Group 2 was 777.10 ± 525.21 days.

Morphological and hemodynamic changes

We obtained the initial OA morphological data of all participants by measuring the model. The mean diameters of the initial OA were 1.48±0.33 mm, 1.52±0.45 mm, and 1.54±0.36 mm for Group0, Group1, and Group2, respectively. No significant difference was found in the diameter ($P = 0.838$, Figure 1B). The angles between the OA and ICA were 68.34 ± 16.04°, 71.86 ± 12.16°, and 79.16 ± 10.23° in these groups, respectively. The angles of Group2 were greater than that of Group0 and Group1 ($P = 0.003$ and $P = 0.044$, Figure 1C).

The streamline charts of each OA model were drawn according to the CFD numerical simulation results (Figure 2A). The colors in the streamlined chart indicate blood flow velocity. The closer the streamline is to red, the higher the speed. Through quantitative measurement, the initial OA blood flow velocity was 0.20 m/s (0.16–0.27 m/s), 0.05 m/s (0.03–0.07 m/s) and 0.07 m/s (0.04–0.12 m/s) in Group0, Group1 and Group2, respectively. The blood flow velocities of the OA in all disease groups were lower than those of the control group ($P < 0.001$, Figure 2B). Moreover, the Group1 had slower OA blood velocities than Group2 ($P = 0.033$).

Figure 2C shows the contour charts of the WSS. The OA WSS of the three groups were 5.44 Pa (1.93–7.72 Pa), 2.57 Pa (0.85–5.31 Pa), and 3.55 Pa (1.21–6.96 Pa), respectively. The WSS of the initial OA in Group1 was significantly lower than that in Group0 ($P = 0.040$, Figure 2D). The pressure of the initial OA (Figure 2E)

TABLE 1 Baseline characteristics of the participants.

Variables	Group0 ($n = 20$)	Group1 ($n = 20$)	Group2 ($n = 33$)	P value
Age (y), mean ± SD	61.80 ± 4.35	62.70 ± 4.08	64.94 ± 6.18	0.084
Female sex, n (%)	8 (40)	4 (20)	6 (18)	0.173
STEMI, n (%)	-	4 (20)	8 (24)	0.721
NSTEMI, n (%)	-	6 (30)	11 (33)	0.801
UA, n (%)	-	10 (50)	14 (42)	0.591
Current smoking, n (%)	8 (40)	16 (80)	22 (67)	0.027
Hypertension, n (%)	12 (60)	18 (90)	29 (88)	0.021
Diabetes mellitus, n (%)	4 (20)	14 (70)	22 (67)	**0.001**
Dyslipidaemia, n (%)	10 (50)	18 (90)	26 (79)	**0.011**
PAD, n (%)	4 (20)	6 (30)	11 (33)	0.577
History of ischemic stroke, n (%)	2 (10)	8 (40)	10 (30)	0.092
Family history of CAD, n (%)	5 (25)	6 (30)	12 (36)	0.679

STEMI, ST-segment elevation myocardial infarction; NSTEMI, non-STEMI; UA, unstable angina; PAD, peripheral arterial disease; CAD, coronary atherosclerotic heart disease. Bonferroni correction was used for multiple comparisons. Bold values are significant.

was 313.20 Pa (204.25–441.47 Pa), 424.53 Pa (298.78–910.08 Pa), and 510.32 Pa (301.26–700.60 Pa) in Group0, Group1, and Group2, respectively. The Group1 and Group2 had a higher OA pressure than the control group ($P = 0.012$ and $P = 0.004$, Figure 2F).

Through calculation, we obtained mass flow data for each OA model (Figure 2G). The mass flow ratios of the OA to the ipsilateral ICA were 3.72% (2.47–5.32%), 1.91% (1.12–3.93%), and 1.74% (1.13–3.41%), respectively. The mass flow ratios in Group1 and Group2 were lower than those in Group0 ($P = 0.021$ and $P = 0.002$, Figure 2H).

Correlation between OA characteristics and clinical parameters

Table 3 shows the correlations between OA characteristics and clinical parameters. The pressure of the initial OA was positively correlated with the ratio of early to late transmitral flow velocity ($r = 0.306$, $P = 0.029$), troponin I (TnI, $r = 0.369$, $P = 0.006$), troponin T (TnT, $r = 0.318$, $P = 0.020$), and N-terminal pro-B-type natriuretic peptide (NT-proBNP , $r = 0.550$, $P < 0.001$). The pressure of the initial OA was negatively correlated with high-density protein ($r = -0.317$, $P = 0.021$). The mass flow ratios of the OA to the ipsilateral ICA were positively correlated with TnT ($r = 0.451$, $P = 0.001$), hemoglobin A1c levels ($r = 0.297$, $P = 0.043$), potassium ($r = 0.372$, $P = 0.006$). In contrast, it was negatively correlated with sodium ($r = -0.290$, $P = 0.035$).

Discussion

In this study, the morphological and hemodynamic changes of the OA in patients with ACS after PCI were observed using CFD. As reported in the literature, ocular complications after PCI include retinal complications and neuro-ophthalmic complications (8, 12). Retinal complications range from asymptomatic cotton wool spots and superficial hemorrhages to severe retinal thromboembolic events with vision loss. Atherosclerotic plaque, clots at the tip of the catheter, and foreign objects on the catheter or guide wire can all lead to a serious thromboembolic event from the heart to the eye (8). Neuro-ophthalmic complications of PCI may be caused by thromboembolic events in several important nuclei of ocular motility (13, 14).

Although reperfusion of ischemic myocardium is beneficial for improving cardiac function, delayed reperfusion is known to cause impaired recovery of contractile activity, induce arrhythmia, enhance metabolic defects, and produce structural damage to cardiomyocytes in the heart (3, 15). These abnormalities due to reperfusion of the ischemic heart are termed as IRI. The mechanism of myocardial IRI is related to a variety of factors. So far, studies have mainly focused on oxidative stress, inflammation, calcium overload, energy metabolism disorders, pyroptosis and ferroptosis (16–21). In addition to the local adverse effects on myocardium, myocardial IRI induces distant organ injury. It has been reported that myocardial IRI produces proinflammatory cytokines such as tumor necrosis factor-α (TNF-α), interleukin-1 (IL-1), and interleukin-6 (IL-6) (22). TNF-α can induce apoptosis by activating extrinsic apoptotic pathway (23). Apoptosis has been reported to play an important role in the development of the acute kidney injury (24). It was found that myocardial preconditioning could significantly reduce renal injury and apoptosis induced by myocardial IRI. The mechanism may be related to the inhibition of endogenous and extrinsic apoptotic pathways (25). Moreover, IRI damage underlies many ocular diseases, such as glaucoma, diabetic retinopathy, and RAO (26). IRI could lead to retinal ganglion cells death, retinal morphological degeneration, loss of retinal function and eventual loss of vision (27). We speculated that the ocular arteries after PCI might also be affected by IRI, which would further cause ocular lesions.

From a hemodynamic perspective, systemic changes in blood flow status may occur after PCI. For the most part, in the cardiovascular system, blood flow is considered laminar. When blood thinning drugs are taken, the whole blood viscosity decreases, as the Reynolds number rises and the laminar flow could be disordered and converted to turbulent. Flow turbulence enhances the energy deficit in the friction type, which increases the boundary layer blockage in the vessels and generates heat and increases the internal energy that affects the reduction of the biofluid/blood-heat-capacity-ratio. In addition, turbulence enhances the perfusion pressure necessary to push blood flow (28). Routine administration of blood thinning medications after PCI increases the risk of obstruction of internal flow due to enhanced boundary layer blockage caused by turbulence. In this

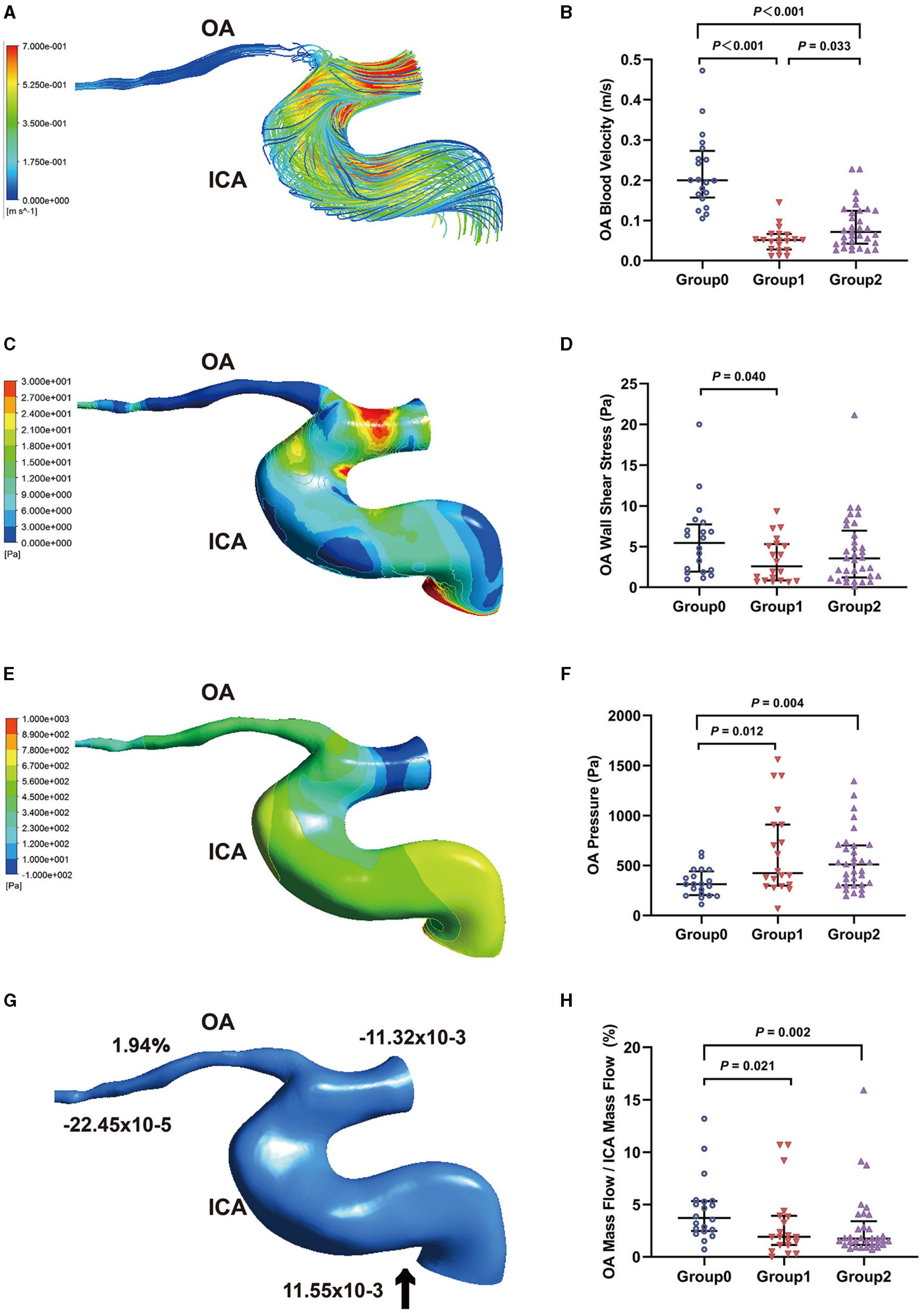

FIGURE 2

Hemodynamics characteristics of the ophthalmic artery (OA). **(A)** The streamline based on OA blood velocity. **(B)** Comparison of OA blood velocity. **(C)** The wall shear stress contour of OA. **(D)** Comparison of OA wall shear stress. **(E)** The pressure contour of OA **(F)** Comparison of OA pressure. **(G)** Mass flow (kg/s) and mass flow ratio of OA to ipsilateral internal carotid artery (ICA) (%). **(H)** Comparison of mass flow ratio of OA to ICA (%); Inlet (+), outlet (−), Blood flow direction (black arrow).

TABLE 2 Baseline characteristics of patients after PCI.

Variables	Group1 ($n = 20$)	Group2 ($n = 33$)	P value
Clinical characteristics			
BMI (kg/m^2), mean ± SD	24.76 ± 2.07	26.53 ± 2.50	**0.010**
DAC (cm), mean ± SD	92.20 ± 8.57	91.64 ± 9.97	0.834
Heart rate (bpm), mean ± SD	74.10 ± 10.86	68.58 ± 13.28	0.123
Systolic BP (mmHg), mean ± SD	140.90 ± 23.19	136.97 ± 23.39	0.555
Diastolic BP (mmHg), mean ± SD	80.40 ± 14.84	79.12 ± 19.10	0.799
Laboratory parameters			
TnI (ng/mL), median (IQR 25%−75%)	0.59 (0.06–3.77)	0.02 (0.003–0.54)	0.061
TnT (ng/mL), median (IQR 25%−75%)	0.07 (0.03–0.78)	0.18 (0.01–0.12)	0.133
CK (U/L), median (IQR 25%−75%)	61.50 (56.00–122.50)	95.00 (59.00–250.50)	0.368
CK–MB (ng/mL), median (IQR 25%−75%)	1.80 (1.45–4.63)	1.2 (0.83–4.60)	0.349
LDH (U/L), median (IQR 25%−75%)	175.00 (154.00–186.75)	194.00 (150.00–222.00)	0.826
NT–proBNP (pg/mL), median (IQR 25%−75%)	855.00 (137.00–1438.25)	229.50 (106.00–848.75)	0.106
Scr (μmol/L), mean ± SD	72.67 ± 10.65	67.11 ± 10.07	0.062
FBG (mmol/L), median (IQR 25%−75%)	6.50 (5.90–9.58)	6.35 (6.03–9.18)	0.732
HBA1c (%), median (IQR 25%−75%)	7.96 (6.03–8.65)	6.60 (6.10–7.65)	0.293
TC (mmol/L), mean ± SD	3.84 ± 0.97	3.75 ± 1.01	0.747
TG (mmol/L), mean ± SD	1.51 ± 0.60	1.32 ± 0.60	0.274
HDL (mmol/L), mean ± SD	1.15 ± 0.59	1.11 ± 0.27	0.723
LDL (mmol/L), mean ± SD	2.01 ± 0.81	2.06 ± 0.77	0.831
Sodium (mmol/L), mean ± SD	140.77 ± 2.36	139.61 ± 2.00	0.075
Potassium (mmol/L), mean ± SD	4.01 ± 0.43	3.98 ± 0.32	0.729
TyG index, mean ± SD	7.43 ± 0.62	7.29 ± 0.58	0.447
Echocardiography, mean ± SD			
LVEF (%)	60.90 ± 9.78	63.22 ± 7.16	0.324
E/A	0.77 ± 0.22	0.83 ± 0.23	0.388
Cardiac index (L/min/m^2)	2.65 ± 0.51	2.86 ± 0.60	0.206
Concomitant medication, n (%)			
Statin	16 (80)	31 (94)	0.184
Aspirin	16 (80)	27 (82)	0.870
Clopidogrel/Ticagrelor	18 (90)	21 (64)	**0.035**
ACE inhibitor/ARB	2 (10)	25 (76)	**<0.001**
Beta blocker	12 (60)	21 (64)	0.791
Calcium channel blocker	6 (30)	13 (39)	0.489
Insulin	2 (10)	4 (12)	0.813

BMI, body mass index; BP, blood pressure; TnI, troponin I; IQR, interquartile range; TnT, troponin T; CK, creatine kinase; CK-MB, creatine kinase isoenzyme-MB; LDH, lactate dehydrogenase; NT-proBNP, N-terminal pro-B-type natriuretic peptide; Scr, serum creatinine; FBG, fasting blood glucose; HBA1c, hemoglobin A1c; TC, total cholesterol; TG, triacylglycerol; HDL, high-density protein; LDL, low-density protein; TyG, triglyceride glucose index, calculated as the ln [fasting triglycerides (mg/dL) × fasting plasma glucose (mg/dL)/2]; LVEF, left-ventricular ejection fraction; E/A, ratio of early to late transmitral flow velocity; ACE, angiotensin-converting enzyme; ARB, angiotensin receptor blocker. $P < 0.05$ is significant (bold values).

study, we found that regardless of the length of time, the OA pressure of the disease groups was higher, and the mass flow ratio were lower than that of the control group. It further suggests that there are systemic changes in blood flow status after PCI. This provides a new perspective on the causes of ocular diseases after PCI.

TABLE 3 Association between OA characteristics and clinical parameters.

Variables	ln (pressure)		ln (mass flow ratio)	
	Correlation coefficient (r)	*P* value	Correlation coefficient (r)	*P* value
BMI (kg/m^2)	−0.256	0.065	−0.029	0.835
DAC (cm)	−0.014	0.921	0.043	0.761
Heart rate (bpm)	−0.163	0.245	0.239	0.084
Systolic BP (mmHg)	−0.112	0.425	0.052	0.711
Diastolic BP (mmHg)	−0.203	0.145	0.061	0.666
LVEF (%)	−0.299	0.099	−0.182	0.191
E/A	0.306	**0.029**	0.267	0.058
Cardiac index (L/min/m^2)	−0.071	0.629	0.191	0.189
ln (TnI) (ng/mL)	0.369	**0.006**	0.217	0.119
ln (TnT) (ng/mL)	0.318	**0.020**	0.451	**0.001**
ln (CK) (U/L)	0.237	0.087	0.184	0.186
ln (CK–MB) (ng/mL)	0.213	0.125	0.174	0.214
ln (LDH) (U/L)	−0.160	0.251	0.154	0.270
ln (NT–proBNP) (pg/mL)	0.550	**<0.001**	0.245	0.077
Scr (μmol/L)	−0.034	0.808	0.111	0.430
ln (HBA1c) (%)	−0.163	0.274	0.297	**0.043**
ln (FBG) (mmol/L)	−0.036	0.815	0.261	0.087
TC (mmol/L)	0.037	0.793	−0.035	0.804
TG (mmol/L)	0.000	0.998	0.039	0.784
HDL (mmol/L)	−0.317	**0.021**	−0.189	0.175
LDL (mmol/L)	0.167	0.233	0.072	0.609
Sodium (mmol/L)	−0.027	0.846	−0.290	**0.035**
Potassium (mmol/L)	−0.036	0.800	0.372	**0.006**
TyG index	0.036	0.819	0.165	0.284

Ln, natural log of the variable; BMI, body mass index; BP, blood pressure; LVEF, left-ventricular ejection fraction; E/A, ratio of early to late transmitral flow velocity; TnI, troponin I; TnT, troponin T; CK, creatine kinase; CK-MB, creatine kinase isoenzyme-MB; LDH, lactate dehydrogenase; NT-proBNP, N-terminal pro-B-type natriuretic peptide; Scr, serum creatinine; FBG, fasting blood glucose; HBA1c, hemoglobin A1c; TC, total cholesterol; TG, triacylglycerol; HDL, high-density protein; LDL, low-density protein; TyG, triglyceride glucose index, calculated as the ln [fasting triglycerides (mg/dL)×fasting plasma glucose (mg/dL)/2]. $P < 0.05$ is significant (bold values).

The effect of ACS on retrobulbar blood flow should not be ignored. Consistent with our previous study (10), the blood flow velocity of the initial OA in patients with ACS after PCI was lower than that in healthy controls. However, this study further found that OA blood flow velocity of patients with ACS after PCI within 3 months was slower than the blood flow velocity of patients with ACS more than 3 months after PCI. Unfortunately, retrobulbar blood flow data after PCI are lacking. Previous studies focused on the correlation between retinal blood vessel morphology and ischemic heart disease, and the flow velocity data were few and most of them were measured using color Doppler imaging. Moreover, there is a lack of long-term observational data on retrobulbar blood flow status in patients with ACS. The cardiac index is calculated by dividing the volume of blood pumped by the heart by the surface area of the body. The higher the cardiac index, the more blood ejection of the heart and the better the heart function. We also collected statistics on the cardiac index of all patients, and the cardiac index of all patients with ACS was lower than the normal value, and the Group1 had a lower cardiac index. As mentioned above, the OA originates from the ICA and receives blood from the ICA. The Group1 in this study was still in the acute stage of the disease course, and poor cardiac pumping function may be one of the reasons for the slow flow velocity of the OA. Similarly, the OA of patients with ACS after PCI <3 months had relatively low WSS. WSS is an important hydromechanical index related to many physiological and pathological phenomena in the cardiovascular system. There was growing evidence that atherosclerotic lesions preferentially originate in areas of flow disturbance associated with low WSS (29). In addition, low WSS accelerates endothelial turnover, leading to increased lipid uptake and promoting the formation of plaque necrotic cores (30). Moreover, the principal factor for plaque creation is time reaction between molecules and surface. Slow blood flow increases the retention time of blood through the artery, which increases the likelihood that blood particles will react with the vessel wall (31). In this study, we analyzed OA morphological data for all participants. There was no significant difference in the initial diameter of the OA, however, a larger angle was found in the OA of patients with ACS more than 3 months after PCI. This suggests that although the diameter of the OA has not changed significantly, the low flow velocity and low WSS may still affect the OA morphology (32). This suggests that more attention should be paid to the ocular condition of patients after PCI, because they may be more prone to arteriosclerosis or ocular vascular obstructive diseases.

In the correlation analysis, we found that the hemodynamic parameters of the OA correlated with some important markers of cardiac stress. Cardiac troponin T (cTnT) is considered as a marker of myocardial apoptosis and necrosis (33). The alternative mechanisms of cTnT release include increased myocardial stress due to stress and increased volumetric load. In addition, small increases in cTnT levels are associated with endothelial dysfunction and small vessel disease, not just myocardial damage (34). This suggests that cTnT may also be related to intracranial microvascular system lesions. NT-proBNP is a neurohormone mainly synthesized and secreted by ventricular myocardium, which is considered as a dynamic marker of cardiac stress (35). NT-proBNP is also associated with the regulation of retinal epithelial cells and glial cells and the function of retinal microvascular injury (36). Lower levels of NT-proBNP are associated with early microvascular changes, including loss of endothelial integrity (37), hemodynamic changes, and decreased coronary and cerebral microvascular density, which increase the risk of intracranial vascular disease (38).

This study has some limitations. ACS is an acute disease, and the first consideration the cardiologist in clinical practice is to save the life of patients. Therefore, our CTA examination was performed after the condition was stable. Moreover, the thickness of CTA scanning layer limits the accuracy of reconstruction. Finally, due to the lack of relevant research data, we set the same boundary conditions for all groups. Therefore, further research is needed to improve the integrity of these results.

Conclusions

This study provides evidence that the OA blood flow velocity of patients with ACS after PCI initially slowed down, which increased the risk of plaque formation, and then showed an increasing trend. Moreover, there was a correlation between OA hemodynamic parameters and clinical indexes related to cardiac stress. In addition to the improvement of systemic and ocular blood perfusion after PCI, ocular vessels may be affected by IRI and blood flow status changes, resulting in ocular lesions. More attention should be paid to the ocular condition of patients after PCI. This study provides a new perspective for the pathogenesis of ocular diseases after PCI, which needs to be further explored.

Data availability statement

The original contributions presented in the study are included in the article/supplementary material, further inquiries can be directed to the corresponding authors.

Ethics statement

The studies involving humans were approved by the Local Ethics Committee of the Beijing Friendship Hospital. The studies were conducted in accordance with the local legislation and institutional requirements. The participants provided their written informed consent to participate in this study.

Author contributions

W-lL: Data curation, Formal analysis, Investigation, Methodology, Writing – original draft. L-tW: Conceptualization, Data curation, Formal analysis, Investigation, Methodology, Writing – original draft, Writing – review & editing. J-lW: Conceptualization, Formal analysis, Funding acquisition, Investigation, Methodology, Resources, Supervision, Writing – review & editing. JS: Conceptualization, Formal analysis, Investigation, Methodology, Writing – original draft. X-rC: Data curation, Investigation, Methodology, Writing – original draft. Z-hZ: Investigation, Writing – original draft. J-xG: Investigation, Writing – original draft. Y-lW: Conceptualization, Funding acquisition, Methodology, Project administration, Resources, Supervision, Writing – review & editing. Z-yM: Conceptualization, Formal analysis, Project administration, Resources, Supervision, Writing – review & editing.

Funding

The author(s) declare that financial support was received for the research, authorship, and/or publication of this article. This work was supported by the National Natural Science Foundation of China (No. 82271124) and the Beijing Hospitals Authority Innovation Studio of Young Staff Funding Support (202103).

Acknowledgments

The authors thank Prof. Anqiang Sun and Dr. Shuqi Ren from Beihang University for their valuable contributions of methods to the study.

Conflict of interest

The authors declare that the research was conducted in the absence of any commercial or financial relationships that could be construed as a potential conflict of interest.

Publisher's note

References

1. Roth GA, Mensah GA, Johnson CO, Addolorato G, Ammirati E, Baddour LM, et al. Global burden of cardiovascular diseases and risk factors, 1990-2019: update from the GBD 2019 study. *J Am Coll Cardiol.* (2020) 76:2982–3021. doi: 10.1016/j.jacc.2020.11.010

2. Manda YR, Baradhi KM. *Cardiac Catheterization Risks and Complications.* Treasure Island (FL): StatPearls Publishing Copyright © 2023, StatPearls Publishing LLC. (2023).

3. Neri M, Riezzo I, Pascale N, Pomara C, Turillazzi E. Ischemia/reperfusion injury following acute myocardial infarction: a critical issue for clinicians and forensic pathologists. *Mediators Inflamm.* (2017) 2017:7018393. doi: 10.1155/2017/7018393

4. Tavakol M, Ashraf S, Brener SJ. Risks and complications of coronary angiography: a comprehensive review. *Glob J Health Sci.* (2012) 4:65–93. doi: 10.5539/gjhs.v4n1p65

5. La Macchia T, Albiero R, Invernizzi T, Ceravolo G, Ceravolo I. Branch retinal artery occlusion after percutaneous coronary intervention. *Case Rep Cardiol.* (2021) 2021:9985568. doi: 10.1155/2021/9985568

6. Hsien YM, Mustapha M, Hamzah JC, Maskon O, Ken CC, Hamdi CH. Why can't I see after my heart is fixed: a case series of ocular complications after cardiac intervention. *BMC Ophthalmol.* (2016) 16:32. doi: 10.1186/s12886-016-0209-1

7. Kinoshita N, Kakehashi A, Yasu T, Kuroki M, Tsurimaki Y, Ono R, et al. A new form of retinopathy associated with myocardial infarction treated with percutaneous coronary intervention. *Br J Ophthalmol.* (2004) 88:494–6. doi: 10.1136/bjo.2003.027136

8. Kojuri J, Mehdizadeh M, Rostami H, Shahidian D. Clinical significance of retinal emboli during diagnostic and therapeutic cardiac catheterization in patients with coronary artery disease. *BMC Cardiovasc Disord.* (2011) 11:5. doi: 10.1186/1471-2261-11-5

9. Cheng XR, Zhao L, Huang YX, Wang YL, Wang JL. Comparison of ophthalmic artery morphological characteristics and retinal vessel diameter for identifying ocular ischemic syndrome. *Invest Ophthalmol Vis Sci.* (2023) 64:20. doi: 10.1167/iovs.64.12.20

10. Wu LT, Wang JL, Wang YL. Ophthalmic artery morphological and hemodynamic features in acute coronary syndrome. *Invest Ophthalmol Vis Sci.* (2021) 62:7. doi: 10.1167/iovs.62.14.7

11. Kojima M, Irie K, Fukuda T, Arai F, Hirose Y, Negoro M. The study of flow diversion effects on aneurysm using multiple enterprise stents and two flow diverters. *Asian J Neurosurg.* (2012) 7:159–65. doi: 10.4103/1793-5482.106643

12. Braga J, Neves F, Costa J, Meira D. Diplopia after coronary revascularization. *Acta Med Port.* (2020) 33:685–8. doi: 10.20344/amp.11751

13. Kocabay G, Bayram T. Unilateral isolated partial oculomotor nerve paralysis after percutaneous intervention. *Angiology.* (2009) 60:385–6. doi: 10.1177/0003319708327647

14. Nicholson L, Jones R, Hughes DS. Lateral rectus palsy following coronary angiography and percutaneous coronary intervention. *BMJ Case Rep.* (2014) 2014:202307. doi: 10.1136/bcr-2013-202307

15. Neuzil J, Rayner BS, Lowe HC, Witting PK. Oxidative stress in myocardial ischaemia reperfusion injury: a renewed focus on a long-standing area of heart research. *Redox Rep.* (2005) 10:187–97. doi: 10.1179/135100005X57391

16. Xiang M, Lu Y, Xin L, Gao J, Shang C, Jiang Z, et al. Role of oxidative stress in reperfusion following myocardial ischemia and its treatments. *Oxid Med Cell Longev.* (2021) 2021:6614009. doi: 10.1155/2021/6614009

17. Yao Y, Li F, Zhang M, Jin L, Xie P, Liu D, et al. Targeting CaMKII-δ9 ameliorates cardiac ischemia/reperfusion injury by inhibiting myocardial inflammation. *Circ Res.* (2022) 130:887–903. doi: 10.1161/CIRCRESAHA.121.319478

18. Wang F, Gao Q, Yang J, Wang C, Cao J, Sun J, et al. Artemisinin suppresses myocardial ischemia-reperfusion injury via NLRP3 inflammasome mechanism. *Mol Cell Biochem.* (2020) 474:171–80. doi: 10.1007/s11010-020-03842-3

19. Tian L, Cao W, Yue R, Yuan Y, Guo X, Qin D, et al. Pretreatment with Tilianin improves mitochondrial energy metabolism and oxidative stress in rats with myocardial ischemia/reperfusion injury via AMPK/SIRT1/PGC-1 alpha signaling pathway. *J Pharmacol Sci.* (2019) 139:352–60. doi: 10.1016/j.jphs.2019.02.008

20. Shi H, Gao Y, Dong Z, Yang J, Gao R, Li X, et al. GSDMD-mediated cardiomyocyte pyroptosis promotes myocardial I/R injury. *Circ Res.* (2021) 129:383–96. doi: 10.1161/CIRCRESAHA.120.318629

21. Fang X, Wang H, Han D, Xie E, Yang X, Wei J, et al. Ferroptosis as a target for protection against cardiomyopathy. *Proc Natl Acad Sci U S A.* (2019) 116:2672–80. doi: 10.1073/pnas.1821022116

22. Aleshin A, Sawa Y, Ono M, Funatsu T, Miyagawa S, Matsuda H. Myocardial protective effect of FR167653; a novel cytokine inhibitor in ischemic-reperfused rat heart. *Eur J Cardiothorac Surg.* (2004) 26:974–80. doi: 10.1016/j.ejcts.2004.06.021

23. Baud V, Karin M. Signal transduction by tumor necrosis factor and its relatives. *Trends Cell Biol.* (2001) 11:372–7. doi: 10.1016/S0962-8924(01)02064-5

24. Lee HT, Kim JY, Kim M, Wang P, Tang L, Baroni S, et al. Renalase protects against ischemic AKI. *J Am Soc Nephrol.* (2013) 24:445–55. doi: 10.1681/ASN.2012090943

25. Huang CH, Lai CC, Yang AH, Chiang SC. Myocardial preconditioning reduces kidney injury and apoptosis induced by myocardial ischaemia and reperfusion. *Eur J Cardiothorac Surg.* (2015) 48:382–91. doi: 10.1093/ejcts/ezu453

26. Musayeva A, Unkrig JC, Zhutdieva MB, Manicam C, Ruan Y, Laspas P, et al. Betulinic acid protects from ischemia-reperfusion injury in the mouse retina. *Cells.* (2021) 10:2440. doi: 10.3390/cells10092440

27. Kim BJ, Braun TA, Wordinger RJ, Clark AF. Progressive morphological changes and impaired retinal function associated with temporal regulation of gene expression after retinal ischemia/reperfusion injury in mice. *Mol Neurodegener.* (2013) 8:21. doi: 10.1186/1750-1326-8-21

28. Kumar VRS, Choudhary SK, Radhakrishnan PK, Bharath RS, Chandrasekaran S, Sankar V, et al. Lopsided blood-thinning drug increases the risk of internal flow choking leading to shock wave generation causing asymptomatic cardiovascular disease. *Glob Chall.* (2021) 5:2000076. doi: 10.1002/gch2.202000076

29. Peiffer V, Sherwin SJ, Weinberg PD. Does low and oscillatory wall shear stress correlate spatially with early atherosclerosis? A systematic review. *Cardiovasc Res.* (2013) 99:242–50. doi: 10.1093/cvr/cvt044

30. Zuin M, Rigatelli G, Vassilev D, Ronco F, Rigatelli A, Roncon L. Computational fluid dynamic-derived wall shear stress of non-significant left main bifurcation disease may predict acute vessel thrombosis at 3-year follow-up. *Heart Vessels.* (2020) 35:297–306. doi: 10.1007/s00380-019-01494-y

31. Hashemi J, Patel B, Chatzizisis YS, Kassab GS. Study of coronary atherosclerosis using blood residence time. *Front Physiol.* (2021) 12:625420. doi: 10.3389/fphys.2021.625420

32. Chatzizisis YS, Coskun AU, Jonas M, Edelman ER, Feldman CL, Stone PH. Role of endothelial shear stress in the natural history of coronary atherosclerosis and vascular remodeling: molecular, cellular, and vascular behavior. *J Am Coll Cardiol.* (2007) 49:2379–93. doi: 10.1016/j.jacc.2007.02.059

33. Clerico A, Zaninotto M, Padoan A, Masotti S, Musetti V, Prontena C, et al. Evaluation of analytical performance of immunoassay methods for cTnI and cTnT: from theory to practice. *Adv Clin Chem.* (2019) 93:239–62. doi: 10.1016/bs.acc.2019.07.005

34. Schneider AL, Rawlings AM, Sharrett AR, Alonso A, Mosley TH, Hoogeveen R, et al. High-sensitivity cardiac troponin T and cognitive function and dementia risk: the atherosclerosis risk in communities study. *Eur Heart J.* (2014) 35:1817–24. doi: 10.1093/eurheartj/ehu124

35. Ravassa S, Kuznetsova T, Varo N, Thijs L, Delles C, Dominiczak A, et al. Biomarkers of cardiomyocyte injury and stress identify left atrial and left ventricular remodelling and dysfunction: a population-based study. *Int J Cardiol.* (2015) 185:177–85. doi: 10.1016/j.ijcard.2015.03.046

36. Aaltonen V, Kinnunen K, Jouhilahti EM, Peltonen J, Nikinmaa M, Kaarniranta K, et al. Hypoxic conditions stimulate the release of B-type natriuretic peptide from human retinal pigment epithelium cell culture. *Acta Ophthalmol.* (2014) 92:740–4. doi: 10.1111/aos.12415

37. Reinhard H, Wiinberg N, Hansen PR, Kjær A, Petersen CL, Winther K, et al. NT-proBNP levels, atherosclerosis and vascular function in asymptomatic type 2 diabetic patients with microalbuminuria: peripheral reactive hyperaemia index but not NT-proBNP is an independent predictor of coronary atherosclerosis. *Cardiovasc Diabetol.* (2011) 10:71. doi: 10.1186/1475-2840-10-71

38. Cushman M, Judd SE, Howard VJ, Kissela B, Gutiérrez OM, Jenny N, et al. N-terminal pro-B-type natriuretic peptide and stroke risk: the reasons for geographic and racial differences in stroke cohort. *Stroke.* (2014) 45:1646–50. doi: 10.1161/STROKEAHA.114.004712

frontiers | Frontiers in Medicine

TYPE Original Research
PUBLISHED 18 March 2024
DOI 10.3389/fmed.2024.1381758

EDITED BY
Kai Jin,
Zhejiang University, China

REVIEWED BY
Lichao Yang,
Cranfield University, United Kingdom
Lei Wang,
Wenzhou Medical University, China

*CORRESPONDENCE
Quanyong Yi
✉ quanyong_yi@163.com
Shaodong Ma
✉ mashaodong@nimte.ac.cn

[†]These authors have contributed equally to this work

RECEIVED 04 February 2024
ACCEPTED 04 March 2024
PUBLISHED 18 March 2024

CITATION
Zhu X, Huang W, Ma S and Yi Q (2024) Robust and accurate corneal interfaces segmentation in 2D and 3D OCT images.
Front. Med. 11:1381758.
doi: 10.3389/fmed.2024.1381758

Robust and accurate corneal interfaces segmentation in 2D and 3D OCT images

Xueli Zhu[1,2†], Wei Huang[2,3†], Shaodong Ma[2*] and Quanyong Yi[4*]

[1]Department of Ultrasound, The First Affiliated Hospital of Ningbo University, Ningbo, China, [2]Institute of Biomedical Engineering, Ningbo Institute of Materials Technology and Engineering, Chinese Academy of Sciences, Ningbo, China, [3]Department of Biomedical Engineering, Hainan University, Hainan, Haikou, China, [4]Ningbo Eye Hospital, Wenzhou Medical University, Ningbo, China

Segmentation of corneal layer interfaces in optical coherence tomography (OCT) images is important for diagnostic and surgical purposes, while manual segmentation is a time-consuming and tedious process. This paper presents a novel technique for the automatic segmentation of corneal layer interfaces using customized initial layer estimation and a gradient-based segmentation method. The proposed method was also extended to three-dimensional OCT images. Validation was performed on two corneal datasets, one with 37 B-scan images of healthy human eyes and the other with a 3D volume scan of a porcine eye. The approach showed robustness in extracting different layer boundaries in the low-SNR region with lower computational cost but higher accuracy compared to existing techniques. It achieved segmentation errors below 2.1 pixels for both the anterior and posterior layer boundaries in terms of mean unsigned surface positioning error for the first dataset and 2.6 pixels (5.2 μm) for segmenting all three layers that can be resolved in the second dataset. On average, it takes 0.7 and 0.4 seconds to process a cross-sectional B-scan image for datasets one and two, respectively. Our comparative study also showed that it outperforms state-of-the-art methods for quantifying layer interfaces in terms of accuracy and time efficiency.

KEYWORDS

segmentation, optical coherence tomography, cornea, layer, eye

1 Introduction

Optical coherence tomography (OCT) can produce detailed cross-sectional images of internal structures in biological tissues (1). Because of its non-invasive and non-contact characteristics, it has been widely used in clinical ophthalmology (1–3), particularly in the retina (1, 2) and cornea (3). Measurements derived from OCT images, such as corneal layer thickness and curvature, can provide important diagnostic information for the management of ectasia, angle assessment, corneal abnormalities and anterior segment tumors (4). Reliable and accurate segmentation methods are required for automatic processing of corneal OCT images to obtain corneal parameters (5, 6), while manual segmentation is not feasible due to the large volume of OCT data generated in clinics.

Several approaches to automated corneal segmentation have been proposed to address the aforementioned issue, with varying degrees of success. Li et al. (5, 7) proposed a fast active contour (FAC) algorithm with second-order polynomial fitting for automated corneal segmentation. Eichel et al. (8) presented a semi-automatic segmentation method using enhanced intelligent scissors and a global optimization method.

Shen et al. (9) used a novel method for the anterior segment without segmenting the posterior surface. However, none of the above methods can effectively deal with image regions with a low signal-to-noise ratio (SNR) or artifacts introduced during image acquisition, such as the central and horizontal artifacts described in Section 2. More robust methods have been proposed in recent years. LaRocca et al. (10) presented an approach based on graph theory and dynamic programming with better segmentation performance in terms of robustness against artifacts. A customized Hough transform and refinement using Kalman filtering by Zhang et al. (11) is proposed for low computational cost. However, these studies modeled the interface as a parabola, which is not suitable for uneven layer interfaces. Furthermore, extrapolation into the low SNR region is an inaccurate way to segment corneal boundaries. William et al. proposed a level set with shape constraint model (12) and a graph cut model (13), but both require customized optimal weighting. Deep learning based methods have emerged in recent years. dos Santos et al. (14) proposed a modified U-net model with fewer parameters and fast processing speed. Unfortunately, deep learning techniques require a large amount of labeled data and intensive computational effort for training.

To address the above-mentioned limitations, we propose a novel gradient-based segmentation technique for corneal layer boundaries in this paper. It not only works in two-dimensional (2D) B-scans, but also can be extended to three-dimensional (3D) corneal images segmentation. The proposed method is able to detect the corneal layer boundaries accurately with lower computational cost compared to other state-of-the-art methods, by equipping with novel initial estimation and refinement techniques. The proposed method has been evaluated on two newly-constructed AS-OCT datasets with expert manual annotation, and the results have demonstrated the superiority.

2 Materials and methods

The proposed method involves three key stages: pre-processing, estimation and refinement of the anterior corneal surface, and estimation and refinement of the other layers including the posterior surface and the epithelial-stromal interface (if visible). The whole process is illustrated by the flowchart in Figure 1. In this paper, the following notations are used to describe the proposed segmentation technique: Y and X denote the depth and width of an image, respectively. The width and height of an image range from 1 to X and from 1 to Y respectively. The intensity of a pixel at (x, y) of an image I is represented by $I(x, y)$.

2.1 Materials

This study was approved by the ethics committee of the Cixi Institute of Biomedical Engineering, Chinese Academy of Sciences, and adhered to the principles of the Declaration of Helsinki. Written informed consent was obtained from each subject before they participated in the study.

Two datasets were used in the experiments. Dataset1 consists of 37 anterior segment OCT (AS-OCT) B-scan images of healthy eyes acquired with a Visante AS-OCT system [see Williams et al. (13) for details]. Briefly, each image covers a 16 mm wide region sampled by 256 A-scans of 1024 points to a depth of 8 mm. The pixel resolution is therefore $60\mu m \times 18\mu m$. All images were manually delineated by two ophthalmologists, one of whom marked the images twice in a masked fashion. All 37 images were used as test data for validation.

Dataset 2 is a 3D volume scan of a porcine cornea acquired with an in-house spectral domain OCT device at a scan rate of 100 μs per A-scan using a light source with a central wavelength of 840 nm. It consists of 421 raster B-scan images of a 15.1 mm region. The images have an axial resolution of 1.9 μm and a transverse resolution of 15 μm with a gap of 20 μm between consecutive B-scans. Three visible layer interfaces (air-epithelium, epithelium-stroma and endothelium-aqueous) of randomly selected 6 B-scans were manually marked twice by an experienced grader for validation purposes.

All images in dataset 1 generated by AS-OCT were used to evaluate the performance of the algorithm. These images were acquired using the Visante AS-OCT system, which is a time-domain system that acquires images at 2,000 axial scans per second in 1,300 nm infrared light. Each B-scan, 37 B-scans in total, consists of 816 A-scans and 406 lateral pixels in each A-scan. The scan width and depth are 16 mm and 8 mm respectively. The pixel resolution is therefore 19.70 μm × 19.60 μm. The layer interfaces for all 37 test datasets were marked by three different graders simultaneously. Test data for the second dataset, obtained from a home-made OCT, was generated by randomly selecting 6 B-scans from a pool of 421 OCT images. The layer boundaries for the test data were then delineated by an experienced grader. The scan rate of the home-built spectral domain OCT system is 100 ms in each A-scan using a light source with a central wavelength of 840 nm. Each B-scan image contains 1000 A-scans of 15.11 mm with 1024 pixels of 1.9511 mm. The pixel resolution for the second dataset is therefore 1.905 μm × 15.113 μm.

2.2 Pre-processing

The first step is to remove unwanted structures and noise (e.g., the iris and high intensity artifacts at the apex position) from the image, as shown in Figure 2, to reduce their detrimental effect on segmentation performance. This is achieved by cropping the image, after which all the content remaining in the image becomes a region of interest (ROI). It is observed that the apex of the cornea in OCT images has a relatively higher intensity than the region above it, as the scattered light from other regions is much weaker than that in the center. Based on this observation, the top resizing location can be obtained by finding the first local maximum of intensity summation in each row by the equation $S(y) = \sum_{x=1}^{x=X} I(x, y)$ above a threshold (in this case, mean intensity summation is used) to reduce computational cost. Therefore, all rows 15 pixels above are empirically cropped. Similarly, the lower resizing position can be estimated from typical corneal thickness and the axial resolution of the image. The left and right parts are also cropped to remove unwanted structures and the low SNR region on both sides.

As shown in Figure 2, two main types of artifacts are present in OCT images: horizontal artifacts and central noise artifacts. The former appears as long horizontal stripes of high intensity, while the

FIGURE 1
Flowchart of the proposed method to segment the corneal layer interface.

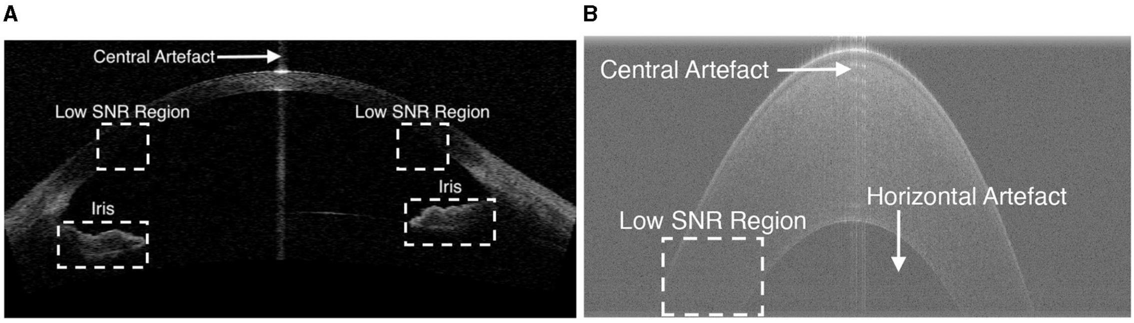

FIGURE 2
Example OCT images showing low SNR regions, horizontal artifacts, central artifacts and the iris. **(A)** An example image in Dataset1. **(B)** An zoomed-in cornea image in Dataset2.

latter is characterized as a vertical saturation region. It is essential to eliminate these artifacts as they have a significant negative impact on the segmentation algorithm.

The horizontal artifact is characterized as adjacent rows with higher mean intensity than others, an efficient way to mitigate it is to subtract the pixel value of each row from the mean intensity of that row.

The central noise artifact is detected by finding a sudden increase in the average intensity of the A-scans, as it is characterized by relatively higher intensity pixels vertically. The whole image is divided equally into three regions and the average intensity (μ) of the A-scans in the peripheral region is calculated. Assuming that the central artifact only occurs in the central region, we therefore consider the A-scan in the central region above a certain threshold [$\frac{4}{3}\mu$ (10)] as the region contaminated by the central artifact. Once the artifact is detected, the region within the artifact is not included in the subsequent processes.

It is necessary to suppress noise in OCT images as the additive thermal and electronic noise can degrade the performance of the algorithm. A 5×5 Wiener denoiser (15) is used to increase the image SNR. For simplicity, the image after artifact suppression and denoising is still denoted as $I(x, y)$.

2.3 Coarse segmentation of anterior surface

In this section we will focus on approximating the position of the anterior surface boundary, as the air-epithelium interface is generally the region with the best quality (high SNR) in OCT images. The main feature used in the search is the bright-to-dark or dark-to-bright transitions in the axial (vertical) direction. Instead of using a gradient with a directional filter to extract the corresponding boundary (10), a novel adapted estimation method is presented.

It is observed that relatively high pixel intensity occurs at adjacent corneal layer boundaries as a result of over-exposure of reflected and scattered light at the edge in the OCT system. Therefore, the position of the anterior interface can be easily estimated based on the prior assumption that the strongest response of an OCT system (the pixel with the highest intensity) in each A-scan mostly occurs near the corneal boundary instead of random noise. In addition, only pixels with local maxima in A-scans are considered as candidate pixels to reduce computational cost and improve accuracy by excluding other pixels.

To estimate the anterior corneal boundary, we defined a "boundary function" to characterize the corneal interface. In essence, the "boundary function" is a mathematical optimisation objective function that aims to determine the position of the boundary in each A-scan. Therefore, the anterior boundary can be obtained by maximizing the "boundary function" in a predefined region according to pixel resolution and layer thickness to find the optimal input argument. The function is defined in each A-scan in the Equation 1.

$$G(x) = T^{+}(x) - T^{-}(x) \tag{1}$$

Two constraints are used in this function to characterize the corneal boundaries (Equation 2). $T^{+}(x)$ is used to account for the difference in pixel intensity between two boundary pixels as a result of over-exposure of scattered and reflected light. The second constraint, $T^{-}(x)$, aims to test the lowest intensity of all candidate pixels between two boundary pixels, as there is less scattered light within the corneal layer with similar tissue. The anterior surface is

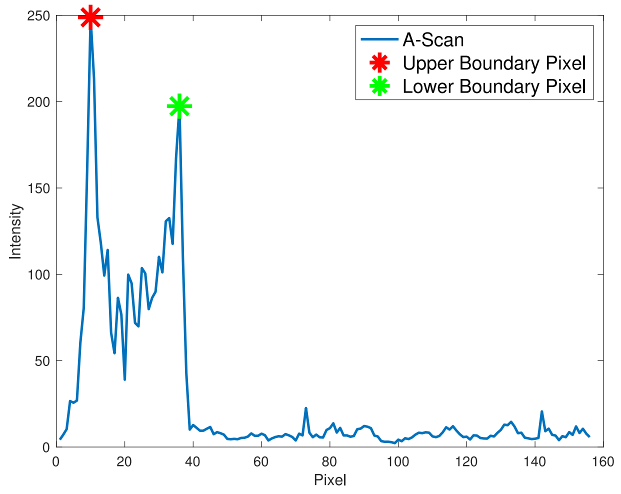

FIGURE 3
Corneal boundaries in an A-scan.

coarsely segmented by finding the top pixel in the axial direction, as shown in Figure 3.

$$\begin{aligned} T^{+}(x) &= |I(x,y_1) - I(x,y_2)| \qquad y_1, y_2 \in [1, Y] \\ T^{-}(x) &= \min\nolimits_{\mu\in[y1,y2]} I(x,\mu) \end{aligned} \tag{2}$$

Due to noise in low-SNR regions, the stability problem that some candidate pixels are in random noise should be addressed. To deal with random noise in low-SNR regions (usually in the outer parts), a second-order polynomial approximation (5, 7, 10) is used to fit the profile to eliminate the effect of random noise and form a smooth boundary (other layer boundaries without a predefined approximation model can simply use a median filter to address this problem).

2.4 Refinement of segmentation

In this section, a novel method is proposed to refine the boundary estimated above. In order to precisely refine the layer boundary, the tactic used is that the latter boundary pixels are determined based on the previously determined boundary pixels with a constant decay weight.

The actual boundary is defined as the maximum intensity change (dark to light or light to dark) in the axial direction. Therefore, the actual layer boundary is found by the maximum absolute vertical gradient. Assuming that the SNR in the center of the corneal image is relatively high compared to the outer part, a non-linear adjustment is considered here, which means that actual boundary pixels at the periphery need more actual central boundary pixels to be confirmed, while central boundary pixels need only a small amount of actual interface pixels to be decided. Therefore, the whole image in the center is divided into two parts to find the actual boundary.

First, the magnitude of the image gradient in the axial direction, symbolized as $g(x,y)$, is calculated using the forward difference gradient operator $\frac{\partial I}{\partial y} = \frac{I(x,y+1)-I(x,y)}{2}$, and then for each of the latter refined boundary pixels from the center to the periphery is determined based on the maximum summation of the absolute gradient of all previously determined boundary pixels with a geometric distribution decay (constant p) according to Equation 3 by iteratively shifting previous refined pixels up and down in a limited search region (in this case with 5 pixels up and down from the approximated air-epithelium layer interface). The pseudocode for the detailed refinement procedure is shown in Algorithm 1.

```
procedure MaxGrad($g(x,y), f_e(x)$)                    ▷ image gradient: $g(x,y)$, estimated pixels: $f_e(x)$
    limited search region: $a \in$ predefined region
    geometric distribution factor: $p$                  ▷ normalized linear distribution
    $f_{new}(x) \leftarrow f_e$
    for each pixel $(I, f_{new}(I)), I \in X$, from center $C$ to periphery do
        $T_a \leftarrow \sum_{i=C}^{I}[g(f_{new}(i)+a) \times p(1-p)^{i-C+1}]$   ▷ right portion as example
        $f_{new}(I) \leftarrow \arg\max(T_a)$
    end for
    return $f_{new}(x)$
end procedure
```

Algorithm 1. Boundary refinement.

$$y = f(x|p) = p(1-p)^x;\ x = 0, 1, 2, \ldots \tag{3}$$

After the actual air-epithelium is detected with the proposed method, to smooth the curve of the layer interface, the Savitzky-Golay filter (16–18), with the first-order polynomial and 21-frame length (11), is implemented. Figure 4 shows the refined anterior surface.

2.5 Estimation of other layer interfaces

Our proposed method for approximating other layers is based on the refined air-epithelium layer interface, as they will have similar boundary profiles. Other layer interfaces can be estimated by maximizing the summation of the absolute gradient, according to the Equation 4, in a region S vertically below the air-epithelium profile (based on typical thickness and pixel resolution). Approximations of other layers in different datasets are shown in Figure 4.

$$\arg\max\nolimits_{\mu\in S} \sum g(x, f(x)+\mu) \tag{4}$$

2.6 Refinement of other layer interfaces

Refinement of other layer interfaces based on the initial estimation in Section 2.5 is performed using a similar technique to that used to adjust the air-epithelium interface in Section 2.4. According to Liu et al. and González-Méijome et al.

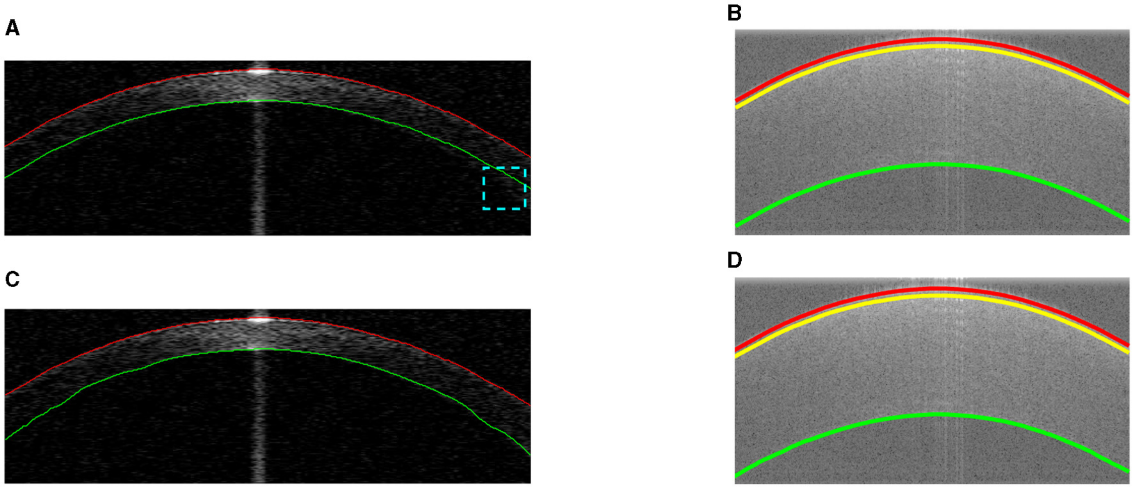

FIGURE 4
Example segmentations on different datasets. Red and green lines represent the segmented anterior and posterior layer boundaries (misalignment highlighted in cyan). The yellow line shows the epithelium-stroma interface. **(A)** Coarse segmentation in Dataset1. **(B)** Coarse segmentation in Dataset2. **(C)** Final segmentation in Dataset1. **(D)** Final segmentation in Dataset2.

(19, 20), the cornea is relatively thinner at the center than at the periphery, as shown in Figure 4. Therefore, a normalized linear growth geometric distribution factor p ($p \in [0,1]$) from the center to the periphery is used based on the locality of the data points, which means that the approximated data points at the periphery have more ability to explore the layer interface instead of considering the predetermined candidate pixels more than those at the center. However, due to the low SNR at the periphery near the layer boundary, the issue of segmentation stability is raised. To address this issue of refinement flexibility, the refinement technique in the Section 2.4 is again used with a low geometric distribution factor for curve smoothing. Figure 4 shows the final segmentation of all visual corneal layers.

2.7 Three-dimensional segmentation

Reconstruction of 3D surface maps of the cornea follows the method for segmentation of 2D B-scans described in the previous sections. There are three main steps: preprocessing, estimation and refinement.

Similar processing steps are implemented to crop the 3D volume image to ensure that only the ROI remains and that various artifacts are removed.

To estimate the air-epithelial interface, the "boundary function" approximation described in Section 2.3 is used with a quadratic surface fit to eliminate the effect of random noise. A similar refinement technique is used in Section 2.4. In 3D segmentation, the starting pixel is in the center of the cornea as we assume that high resolution is presented in the center of the image while low SNR appears in the periphery. For non-linear adaptation, additional information from neighboring pixels was introduced. Candidate pixels are considered using geodesic distance transform (here the city block method is used) (21). Each candidate pixel from the center to the periphery (the distance after transformation) is determined based on the maximum summation of the absolute gradient of all previously refined pixels with geometric distribution decay in a limited region, which means that the algorithm considers more the neighboring candidate pixels and less the distant candidate pixels. A 3×3×3 median filter is used for curve smoothing.

Other layer interfaces can be approximated by maximizing the sum of the absolute gradient of all estimated pixels in a limited region by shifting the refined air-epithelium profile, following Equation 5.

$$\arg\max_{\mu \in S} \sum g(x, y, f(x, y) + \mu) \tag{5}$$

Then the same refinement method mentioned above is used to find the actual boundary pixels. The final segmentation result is shown in Figure 5.

2.8 Experiments

The algorithm is implemented in Matlab and runs without parallel processing on a Win10 64-bit OS PC with Intel Core i5-7500 CPU @ 3.40 GHz and 8.00 GB RAM.

To evaluate the performance of our method and the other (13), the segmentation results of different layer surfaces were compared with the ground truth described in Section 2.1. The mean unsigned surface position error (MSPE) (13) is used as a metric to evaluate performance. In order to examine the intra- and inter-observer agreement, for Dataset1 the annotations of the same observers and between observers were also compared. For Dataset2, due to data availability, only intra-observer variation was assessed.

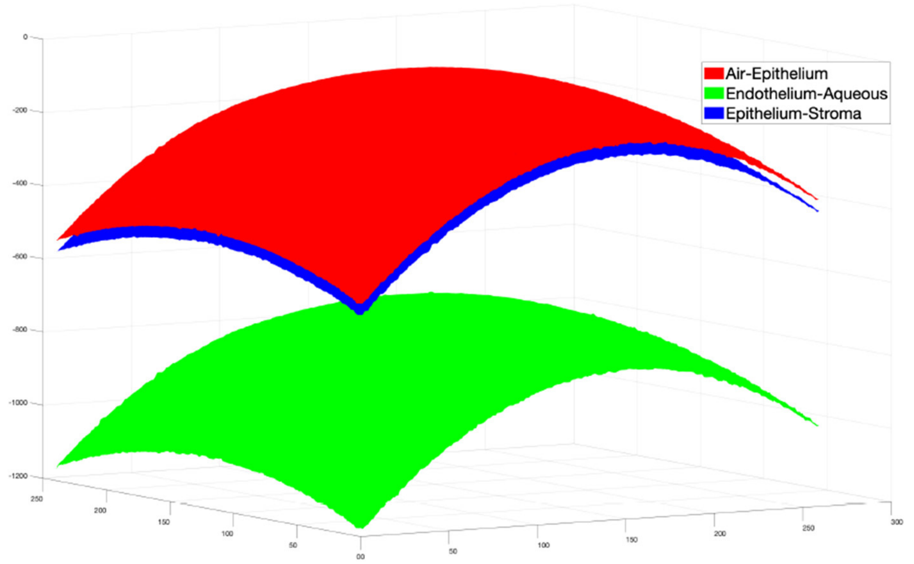

FIGURE 5
Surfaces reconstructed from 3D segmentation.

TABLE 1 Results on Dataset1 in mean unsigned surface positioning error.

Corneal layer boundary	Proposed method	Williams' method	Inter-observer variation	Intra-observer variation
Anterior	0.62 ± 0.61	1.21 ± 1.64	0.80 ± 0.90	0.92 ± 1.46
Posterior	2.15 ± 2.26	2.82 ± 1.26	1.25 ± 1.46	1.62 ± 2.33

3 Results and discussion

The proposed method was first compared with Williams et al. (13), which used dataset1. The comparison results between the proposed method and that of Williams et al. are summarized in Table 1. A significant improvement in accuracy can be observed: our mean ± standard deviation MSPEs on the anterior and posterior interfaces are 0.62 ± 0.61 and 2.15 ± 2.26 pixels, while theirs are 1.21 ± 1.64 and 2.82 ± 1.26 pixels. In addition, the processing time of our proposed algorithm (0.74 s) is much lower than theirs (2.53 s). Furthermore, an observer variation test was also performed, as shown in Table 1. The mean pixel error of our method for the anterior boundary (0.62 ± 0.61) is lower than the interobserver variation (0.80 ± 0.90) and the intraobserver variation (0.92 ± 1. 46), and the mean pixel error of our method for the posterior boundary (2.15 ± 2.26) is slightly higher than the inter-observer variation (1.25 ± 1.46) and the intra-observer variation (1.62 ± 2.33). These results demonstrate the good performance of our proposed method.

The proposed method was also tested on Dataset2 and the results are summarized in Table 2. The MSPE in pixels for all three layers (2.67 ± 0.40 pixels for epithelium-air, 2.30 ± 0.40 pixels for epithelium-stroma and 2.62 ± 0. 44 pixels for endothelium-aqueous) are lower than those of the intra-observer variation (4.47 ± 5.76 pixels for epithelium-air, 5.90 ± 4.25 pixels for epithelium-stroma, and 5.14 ± 3.13 pixels for endothelium-aqueous). Considering the high resolution of the images, the actual error is comparatively small, e.g. the MSPE is 5.2 μm for the endothelium-aqueous layer interface, which is comparable to those of other methods (10, 11, 13). The technique has demonstrated high speed segmentation with an average segmentation time of 0.42 seconds per image for three visible interfaces.

TABLE 2 Results on Dataset2 in mean unsigned surface positioning error.

Corneal layer boundary	Mean ± standard deviation	Intra-observer variation
Epithelium-air	2.67 ± 0.40	4.47 ± 5.76
Epithelium-stroma	2.30 ± 0.39	5.90 ± 4.25
Endothelium-aqueous	2.62 ± 0.44	5.14 ± 3.13

TABLE 3 3D segmentation results in Dataset2.

Mean unsigned surface positioning error (MSPE)	
Corneal layer boundary	Mean ± standard deviation
Epithelium-air	7.06 ± 9.03
Epithelium-stroma	7.03 ± 10.31
Endothelium-aqueous	12.47 ± 13.10

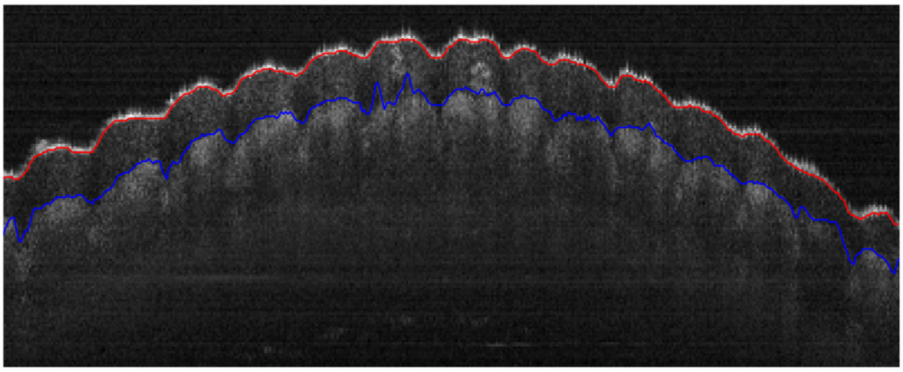

FIGURE 6
Segmentation of the epidermal layer of a fingerprint with uneven surfaces, where the red and blue curves represent the anterior and posterior layer interfaces, respectively.

To test the performance of our extended 3D segmentation method, the surfaces of the layer interfaces were constructed using our proposed 2D segmentation method on each B-scan image in Dataset2. In our experiment, B-scans from 51 to 310 were segmented to construct the surfaces. The surfaces from the direct 3D segmentation method were compared with those from the 2D constructed surfaces, and the results are shown in Table 3.

To further demonstrate the robustness of the proposed algorithm, an OCT image of a fingerprint image was segmented and the results are shown in Figure 6. Although the layer interfaces are more irregular compared to those of the cornea, the results are appealing and demonstrate the robustness of our method in dealing with complex surfaces such as the diseased cornea in the future.

4 Conclusion

A novel technique for automatic segmentation of corneal layer interfaces in OCT images has been proposed and validated. The proposed method outperforms state-of-the-art methods in terms of accuracy and time efficiency. The method is extended to 3D segmentation with relatively high accuracy. The method could be used to segment more layer boundaries resolved by OCT imaging techniques. Thus, the method has significant potential for clinical care.

Data availability statement

The raw data supporting the conclusions of this article will be made available by the authors, without undue reservation.

Ethics statement

The studies involving humans were approved by the Ethics Committee of Cixi Institute of Biomedical Engineering, Chinese Academy of Sciences. The studies were conducted in accordance with the local legislation and institutional requirements. The participants provided their written informed consent to participate in this study.

Author contributions

XZ: Data curation, Formal analysis, Investigation, Methodology, Validation, Visualization, Writing – original draft, Writing – review & editing. WH: Methodology, Project administration, Resources, Writing – original draft, Writing – review & editing. SM: Conceptualization, Funding acquisition, Investigation, Project administration, Software, Visualization, Writing – review & editing. QY: Data curation, Formal analysis, Funding acquisition, Investigation, Methodology, Supervision, Validation, Writing – review & editing.

Funding

The author(s) declare financial support was received for the research, authorship, and/or publication of this article. This work was supported by Ningbo Public Welfare Fund (Grant Number: 2023S116) and Ningbo "'2025 S & T Megaprojects" (Grant Number: 2022Z127).

Conflict of interest

The authors declare that the research was conducted in the absence of any commercial or financial relationships that could be construed as a potential conflict of interest.

Publisher's note

References

1. Huang D, Swanson E, Lin C, Schuman J, Stinson W, Chang W, et al. Optical coherence tomography. *Science*. (1991) 254:1178–81. doi: 10.1126/science.1957169

2. Fujimoto JG, Drexler W, Schuman JS, Hitzenberger CK. Optical coherence tomography (OCT) in ophthalmology: introduction. *Opt Express*. (2009) 17:3978. doi: 10.1364/OE.17.003978

3. Radhakrishnan S. Real-time optical coherence tomography of the anterior segment at 1310 nm. *Arch Ophthalmol*. (2001) 119:1179. doi: 10.1001/archopht.119.8.1179

4. Ramos JLB Li Y, Huang D. Clinical and research applications of anterior segment optical coherence tomography - a review. *Clini Experim Ophthalmol*. (2009) 37:81–9. doi: 10.1111/j.1442-9071.2008.01823.x

5. Li Y, Shekhar R, Huang D. Segmentation of 830- and 1310-nm LASIK corneal optical coherence tomography images. In: Sonka M, Fitzpatrick JM, editors. *Medical Imaging 2002: Image Processing*. Washington: SPIE (2002).

6. Zhao M, Kuo AN, Izatt JA. 3D refraction correction and extraction of clinical parameters from spectral domain optical coherence tomography of the cornea. *Opt Express*. (2010) 18:8923. doi: 10.1364/OE.18.024595

7. Li Y, Shekhar R, Huang D. Corneal pachymetry mapping with high-speed optical coherence tomography. Ophthalmology. (2006) 113:792–799.e2. doi: 10.1016/j.ophtha.2006.01.048

8. Eichel J, Mishra A, Fieguth P, Clausi D, Bizheva K. A novel algorithm for extraction of the layers of the Cornea. In: *2009 Canadian Conference on Computer and Robot Vision*. Washington DC: IEEE (2009).

9. Shen M, Cui L, Li M, Zhu D, Wang MR, Wang J. Extended scan depth optical coherence tomography for evaluating ocular surface shape. *J Biomed Opt*. (2011) 16:056007. doi: 10.1117/1.3578461

10. LaRocca F, Chiu SJ, McNabb RP, Kuo AN, Izatt JA, Farsiu S. Robust automatic segmentation of corneal layer boundaries in SDOCT images using graph theory and dynamic programming. *Biomed Opt Express*. (2011) 2:1524. doi: 10.1364/BOE.2.001524

11. Zhang T, Elazab A, Wang X, Jia F, Wu J, Li G, et al. A novel technique for robust and fast segmentation of corneal layer interfaces based on spectral-domain optical coherence tomography imaging. *IEEE Access*. (2017) 5:10352–63. doi: 10.1109/ACCESS.2017.2712767

12. Williams D, Zheng Y, Bao F, Elsheikh A. Automatic segmentation of anterior segment optical coherence tomography images. *J Biomed Opt*. (2013) 18:056003. doi: 10.1117/1.JBO.18.5.056003

13. Williams D, Zheng Y, Bao F, Elsheikh A. Fast segmentation of anterior segment optical coherence tomography images using graph cut. *Eye Vision*. (2015) 2:1. doi: 10.1186/s40662-015-0011-9

14. dos Santos VA, Schmetterer L, Stegmann H, Pfister M, Messner A, Schmidinger G, et al. CorneaNet: fast segmentation of cornea OCT scans of healthy and keratoconic eyes using deep learning. *Biomed Opt Express*. (2019) 10:622. doi: 10.1364/BOE.10.000622

15. Shah AA, Malik MM, Akram MU, Bazaz SA. Comparison of noise removal algorithms on Optical Coherence Tomography (OCT) image. In: *2016 IEEE International Conference on Imaging Systems and Techniques (IST)*. Chania: IEEE (2016).

16. Gorry PA. General least-squares smoothing and differentiation by the convolution (Savitzky-Golay) method. *Anal Chem*. (1990) 62:570–3. doi: 10.1021/ac00205a007

17. Savitzky A, Golay MJE. Smoothing and differentiation of data by simplified least squares procedures. *Anal Chem*. (1964) 36:1627–39. doi: 10.1021/ac60214a047

18. Orfanidis SJ. *Introduction to Signal Processing*. Upper Saddle River: Prentice-Hall, Inc. (1995).

19. Liu Z, Huang AJ, Pflugfelder SC. Evaluation of corneal thickness and topography in normal eyes using the Orbscan corneal topography system. *Br. J. Ophthalmol*. (1999) 83:774–8. doi: 10.1136/bjo.83.7.774

20. González-Méijome JM, Cerviño A, Yebra-Pimentel E, Parafita MA. Central and peripheral corneal thickness measurement with Orbscan II and topographical ultrasound pachymetry. *J Cataract Refract Surg*. (2003) 29:125–32. doi: 10.1016/S0886-3350(02)01815-1

21. Soille P. *Morphological Image Analysis*. Berlin: Springer Berlin Heidelberg. (2004). doi: 10.1007/978-3-662-05088-0

frontiers | Frontiers in Immunology

TYPE Original Research
PUBLISHED 22 March 2024
DOI 10.3389/fimmu.2024.1325868

EDITED BY
Kai Jin,
Zhejiang University, China

REVIEWED BY
Xin Ye,
Zhejiang Provincial People's Hospital, China
Yao Tan,
Jinan University, China

*CORRESPONDENCE
Fangkun Zhao
✉ fkzhao@cmu.edu.cn
Bo Qu
✉ qubo@cmu.edu.cn

RECEIVED 22 October 2023
ACCEPTED 19 February 2024
PUBLISHED 22 March 2024

CITATION
Yuan W, Li X, Wang G, Qu B and Zhao F (2024) Association of autoimmune and allergic diseases with senile cataract: a bidirectional two-sample Mendelian randomization study.
Front. Immunol. 15:1325868.
doi: 10.3389/fimmu.2024.1325868

Association of autoimmune and allergic diseases with senile cataract: a bidirectional two-sample Mendelian randomization study

Weichen Yuan[1,2], Xiangrui Li[1,2], Guan Wang[1,2], Bo Qu[1,2]* and Fangkun Zhao[1,2]*

[1]Department of Ophthalmology, The Fourth Affiliated Hospital of China Medical University, Shenyang, China, [2]Key Lens Research Laboratory of Liaoning Province, Shenyang, China

Background: Many observational studies have been reported that patients with autoimmune or allergic diseases seem to have a higher risk of developing senile cataract, but the views are not consistent. In order to minimize the influence of reverse causality and potential confounding factors, we performed Mendelian Randomization (MR) analysis to investigate the genetic causal associations between autoimmune, allergic diseases and senile cataract.

Methods: Single nucleotide polymorphisms associated with ten common autoimmune and allergic diseases were obtained from the IEU Open genome-wide association studies (GWAS) database. Summary-level GWAS statistics for clinically diagnosed senile cataract were obtained from the FinnGen research project GWAS, which consisted of 59,522 individuals with senile cataracts and 312,864 control individuals. MR analysis was conducted using mainly inverse variance weighted (IVW) method and further sensitivity analysis was performed to test robustness.

Results: As for ten diseases, IVW results confirmed that type 1 diabetes (OR = 1.06; 95% CI = 1.05-1.08; $p = 2.24\times10^{-12}$), rheumatoid arthritis (OR = 1.05; 95% CI = 1.02-1.08; $p = 1.83\times10^{-4}$), hypothyroidism (OR = 2.4; 95% CI = 1.42-4.06; $p = 1.12\times10^{-3}$), systemic lupus erythematosus (OR = 1.02; 95% CI = 1.01-1.03; $p = 2.27\times10^{-3}$), asthma (OR = 1.02; 95% CI = 1.01-1.03; $p = 1.2\times10^{-3}$) and allergic rhinitis (OR = 1.07; 95% CI = 1.02-1.11; $p = 2.15\times10^{-3}$) were correlated with the risk of senile cataract. Celiac disease (OR = 1.04; 95% CI = 1.01-1.08; $P = 0.0437$) and atopic dermatitis (OR = 1.05; 95% CI = 1.01-1.10; $P = 0.0426$) exhibited a suggestive connection with senile cataract after Bonferroni correction. These associations are consistent across weighted median and MR Egger methods, with similar causal estimates in direction and magnitude. Sensitivity analysis further proved that these associations were reliable.

Conclusions: The results of the MR analysis showed that there were causal relationships between type 1 diabetes, rheumatoid arthritis, hypothyroidism, systemic lupus erythematosus, asthma, allergic rhinitis and senile cataract. To clarify the possible role of autoimmune and allergy in the pathophysiology of senile cataract, further studies are needed.

KEYWORDS

autoimmune diseases, allergy, Mendelian randomization, senile cataract, GWAS - genome-wide association study

Introduction

Senile cataract, also known as age-related cataract, is one of the leading causes of treatable blindness in the world, affecting 17% of the global population (1). Senile cataract is the most common type of cataract among adults, with onset between ages of 45 and 50. Even with the rapid development of cataract surgery, senile cataract still causes a huge disease and economic burden, especially in developing countries (2). Identifying potential risk factors to determine the mechanism of cataract formation and preventive methods is therefore of paramount importance. Currently, risk factors such as ageing, smoking, alcohol consumption, hypertension, and diabetes have been proved to contribute to the occurrence of cataract (3–7). However, the influence of immune related diseases as risk factors on cataract is not well studied.

Protecting the host from infection is the primary function of the immune system. The inability to distinguish self from non-self is often referred to as a breach of tolerance and is the underlying mechanism for autoimmune disease. The overall prevalence of autoimmune diseases in the general population is in the range of 3-5% (8). There are almost 100 different types of autoimmune diseases, the most common of which are autoimmune thyroid disease and type 1 diabetes (T1D) (9). The incidence of allergic diseases, represented by asthma, atopic dermatitis (AD) and allergic rhinitis (AR) , has increased dramatically in the past three decades, and now affects approximately 20% of the population, becoming a public health problem that imposes a heavy burden on society (10). Evidence from previous observational studies suggests that some autoimmune and allergic diseases, such as celiac disease (CeD) (11), systemic lupus erythematosus (SLE) (12), T1D (13), multiple sclerosis (MS) (14), psoriasis (15), asthma (16) and AR (17) may increase the risk of cataracts. These observational studies tend to be susceptible to selection bias, residual confounders and reverse causation. Thus, assessing the causal relationship between autoimmune and allergic diseases and the development of senile cataract can provide clues for the etiology of senile cataract.

Mendelian randomization (MR), as an epidemiological approach, has been widely used to evaluate the potential causal association between exposures and disease results (18). This approach minimizes residual confounding because genetic variants are randomly assembled at the time of conception and are therefore independent of personal lifestyle and environmental factors (19). At the same time, the interference of reverse causality can also be avoided (20). Compared with the gold standard randomized controlled trial (RCT) that established causality, MR used data from large-scale GWAS which is timelier and the sample size is larger. In addition, sometimes randomized controlled trials cannot be conducted because they are costly, unfair, and even unethical. MR studies can overcome these shortcomings while results are broadly consistent with RCTs (21).

Lens epithelial cells are the most active metabolic cells in the lens, which undergo oxidation, insolubility and cross-linking during cataract formation. These cells then migrate to the lens equator to form lens fibers, which are gradually compressed in the center, resulting in hardening and opacity of the lens nucleus (22). The pathophysiological mechanism of lens opacity in cataract is usually attributed to oxidative stress (23). Studies on the mechanisms of autoimmunity or allergy in patients with cataract are not common and have only been reported in a few publications (24–26). It is still unclear whether autoimmune, allergic diseases and senile cataract are linked through a shared genetic etiology. To our knowledge, there are currently no MR study evaluating the association between autoimmunity, allergic disease and senile cataract. Through this study, it is possible for us to reveal the genetic characteristics and immune related biological processes associated with senile cataract, bridging the significant knowledge gap about the complex causes of this disease.

Methods

MR assumptions and study design

T1D, rheumatoid arthritis (RA), hypothyroidism, SLE, CeD, MS, psoriasis, asthma, AR and atopic dermatitis (AD) included in our study were determined according to previously published observational studies. In order to assess the causal connections between senile cataract and these diseases, we conducted a two-sample MR analysis. Summary-level data from the GWASs were obtained for autoimmune, allergic diseases and senile cataract. In order to obtain reliable results, the MR analysis meets the following three assumptions (1) instrumental variables (IVs) finally included in the use must be closely related to autoimmune or allergic diseases; (2) IVs and confounding factors (affecting autoimmune, allergic diseases and senile cataract) were independent of each other; (3) IVs only affect senile cataract only through autoimmune or allergic disease. Figure 1 shows the flow chart of MR research between autoimmune, allergic diseases and senile cataract and three MR assumptions. To minimize bias due to ethnic stratification, we restricted included individuals to European population.

Exposure sources of autoimmune and allergic diseases

Summary level data for all 10 exposures were obtained from Integrative Epidemiology Unit (IEU) Open GWAS database (https://gwas.mrcieu.ac.uk/). We prioritized using the GWAS dataset with the largest samples size as exposures. If any of the following three situations occur, we will select other relatively large GWAS data: 1) insufficient instrumental variables; 2) racial differences or sample overlap; 3) significant pleiotropy in preliminary analysis. Ultimately, summary GWAS data for hypothyroidism and psoriasis were from UK Biobank. The GWAS summary data for T1D (27), RA (28), CeD (29), SLE (30), MS (31), asthma (32), AR (33) and AD (34) were abstracted from different publicly available GWASs. Detailed information for the data sources was presented in Table 1.

A quality check of the single nucleotide polymorphisms (SNPs) is performed to meet the basic assumptions of MR: (1) SNPs associated with autoimmune diseases reached the genome-wide significance threshold ($P<5\times10^{-8}$). (2) We further clumped the SNPs in linkage disequilibrium (LD) analysis ($R^2 < 0.001$, clumping distance = 10,000kb). (3) The palindromic SNPs with intermediate allele frequencies were eliminated. (4) When the original SNP was not available, proxy SNPs with $r^2 > 0.9$ according to LD link (https://ldlink.nci.nih.gov/) were used. To ensure robust associations between instrumental and endogenous variables and to prevent weak instrumental variable bias, we calculated R^2 [$R^2 = 2 \times \mathrm{EAF} \times (1 - \mathrm{EAF}) \times b^2$], representing the proportion of variation explained by instrumental variable SNPs. Simultaneously, we performed calculations of the F-statistic [$F = R^2 \times (N-2) \;/\; (1-R^2)$] to assess the potency of IVs, whereby IVs with an F-statistic exceeding 10 are deemed to be valid (35).

Outcome sources of senile cataract

To reduce bias due to sample overlap, the summary statistics for the senile cataract GWAS were selected from the FinnGen research project (https://r9.finngen.fi/), including 59,522 cases of senile cataracts and 312,864 cases of population controls. This study defines senile cataract by H25 of the International Classification of Disease-10 (36).

All analyses were based on publicly shared databases and no additional ethical approvals were required.

Statistical analysis

MR analysis

The "TwoSampleMR" R package (version 0.5.7) was used for bidirectional univariable two-sample MR analysis between autoimmune, allergic diseases and senile cataract. Inverse variance weighted (IVW) methods were applied to evaluate

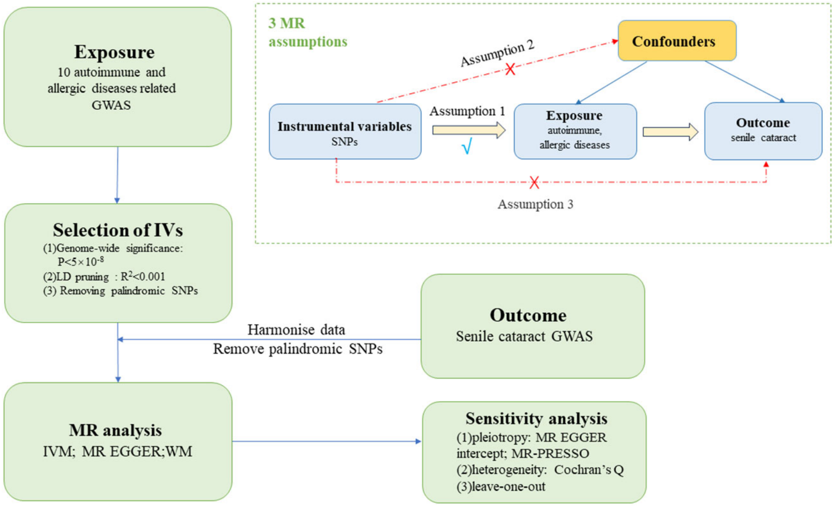

FIGURE 1
The flow chart of MR research and three MR assumptions.

TABLE 1 Sources and characteristics of exposure.

Exposure	GWAS-ID	Author, Journal/Consortium	Sample size	PMID
Type 1 diabetes	ebi-a-GCST90018925	Sakaue et al., Nat. Genet.	457,695	34594039
Rheumatoid arthritis	ebi-a-GCST005569	Eyre et al., Nat. Genet.	47,580	23143596
Hypothyroidism	ukb-a-77	UK Biobank	337,159	NA
Systemic lupus erythematosus	ebi-a-GCST003156	Bentham et al., Nat. Genet.	14,267	26502338
Celiac disease	ieu-a-1060	Dubios et al., Nat. Genet.	11,950	20190752
Multiple sclerosis	ebi-a-GCST001198	Sawcer et al., Nature	26,621	21833088
Psoriasis	ukb-a-100	UK Biobank	337,159	NA
Asthma	ebi-a-GCST90014325	Valette et al., Commun Biol.	408,442	34103634
Allergic rhinitis	ebi-a-GCST90013920	Mbatchou et al., Nat. Genet.	407,746	34017140
Atopic dermatitis	ebi-a-GCST90027161	Sliz et al., J Allery Clin Immunol.	796,661	34454985

thecausality between autoimmune, allergic disease-related IVs and senile cataract risk, as the IVW approach is most effective in terms of statistical power when all IVs were valid and there is no horizontal pleiotropy (37). Cochrane's Q test was applied to test whether heterogeneity existed, and if so, an IVW random-effects model was used, otherwise an IVW fixed-effects model was used. The effect size is indicated by the odds ratio (OR) along with its 95% confidence interval (CI). However, even if only one genetic variation is invalid, the IVW method may provide biased estimates. In order to solve the robustness, two other methods are carried out, including weighted median (WM) method and MR-Egger test. WM gives a reliable estimate assuming that no less than 50% of the IVs are valid (35). The results of MR Egger remain valid when SNPs with pleiotropy were more than 50% (38).

Sensitivity analysis

If genetic variants have horizontal pleiotropy, our IVW results will be invalidated. Intercept terms obtained from the MR-Egger regression were used to evaluate imbalanced pleiotropic effects (39). The MR-Egger estimate would be equal to the IVW estimate if the intercept term was zero and the test *p*-value is greater than 0.05. The MR pleiotropy residual sum and outlier (MR-PRESSO) method (R package “MR-PRESSO” v1.0) can also detect the outliers that may possess the characteristic of horizontal pleiotropy and provide corrected estimates after removing outliers (40). Cochrane's Q test was used to test heterogeneity (41). If heterogeneity exists, we will use IVW random-effects model to calculate the main results. Leave-one-out analysis is conducted to assess the sensitivity of results to individual variants by sequentially excluding one SNP at a time to estimate whether results are biased or driven by individual SNPs (42). In order to reduce false positive rate in batch analysis, we use Bonferroni method for multiple testing. The threshold for statistical significance was defined as a *p*-value $<5\times10^{-3}$ (p =0.05 / (ten exposures × one outcome) adjusted for ten exposures and one outcome using the Bonferroni method. A p-value ranging from 0.005 to 0.05 was deemed to indicate suggestive significance.

Results

Selection of IVs associated with autoimmune diseases

In this study, we reported our MR analysis according to STROBE-MR (Strengthening the Reporting of Mendelian Randomization Studies) guidelines to improve the clarity, transparency and reproducibility of the study (Supplementary Table S1).

The number of SNPs ranged from 7 to 117, after quality control steps by LD effects and palindromic. The F-statistic of SNPs ranges from 29.4 to 2815.2, indicating that each SNP revealed adequate validity. The detailed information for each SNP and its R^2 and F-statistic value were shown in Supplementary Table S2.

MR analysis

IVW analysis showed that T1D (OR = 1.06; 95% CI = 1.05-1.08; $p = 2.24\times10^{-12}$), RA (OR = 1.05; 95% CI = 1.02-1.08; $p = 1.83\times10^{-4}$), hypothyroidism (OR = 2.4; 95% CI = 1.42-4.06; $p = 1.12\times10^{-3}$), SLE (OR = 1.02; 95% CI = 1.01-1.03; $p = 2.27\times10^{-3}$), asthma (OR=1.07; 95% CI = 1.03-1.12; $p = 1.2\times10^{-3}$) and AR (OR = 1.07; 95% CI = 1.02-1.11; $p = 2.15\times10^{-3}$) were causally associated with a significantly increased risk of senile cataract in European populations. CeD (OR = 1.04; 95% CI = 1.01-1.08; $P = 0.0437$) and AD (OR = 1.05; 95% CI = 1.01-1.10; $P = 0.0426$) exhibits a suggestive connection with senile cataract after Bonferroni correction. There was insufficient evidence to suggest that genetically predicted MS (OR = 1.01, 95% CI = 0.98-1.04; $P = 0.45$) and psoriasis (OR = 0.18; 95% CI =0.03-1.1; P =0.443) were associated with senile cataracts. These associations are consistent across WM and MR Egger methods, with similar causal estimates in direction and magnitude (Figure 2).

No genetic predisposition to any of the 10 diseases was associated with senile cataract in the inverse analysis with IVs to senile cataract as exposure and the 10 diseases as outcomes (Figure 3).

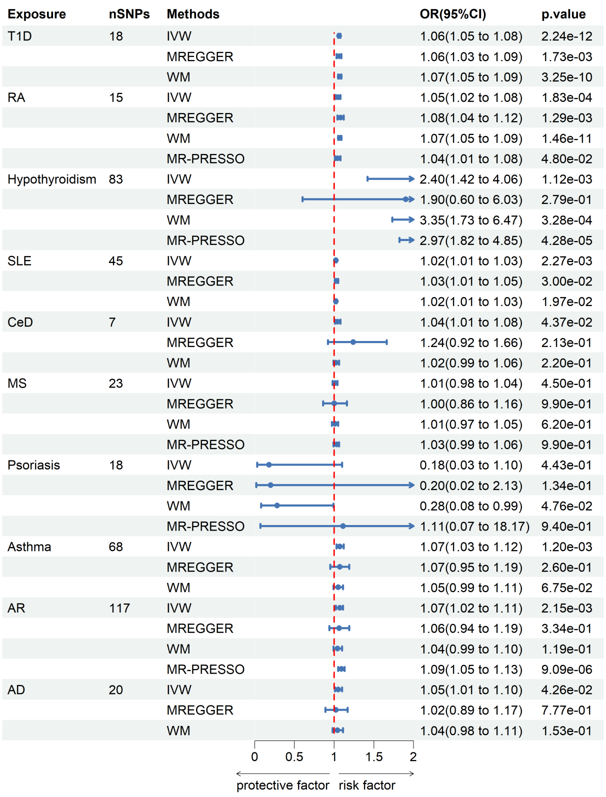

Exposure	nSNPs	Methods	OR(95%CI)	p.value
T1D	18	IVW	1.06(1.05 to 1.08)	2.24e-12
		MREGGER	1.06(1.03 to 1.09)	1.73e-03
		WM	1.07(1.05 to 1.09)	3.25e-10
RA	15	IVW	1.05(1.02 to 1.08)	1.83e-04
		MREGGER	1.08(1.04 to 1.12)	1.29e-03
		WM	1.07(1.05 to 1.09)	1.46e-11
		MR-PRESSO	1.04(1.01 to 1.08)	4.80e-02
Hypothyroidism	83	IVW	2.40(1.42 to 4.06)	1.12e-03
		MREGGER	1.90(0.60 to 6.03)	2.79e-01
		WM	3.35(1.73 to 6.47)	3.28e-04
		MR-PRESSO	2.97(1.82 to 4.85)	4.28e-05
SLE	45	IVW	1.02(1.01 to 1.03)	2.27e-03
		MREGGER	1.03(1.01 to 1.05)	3.00e-02
		WM	1.02(1.01 to 1.03)	1.97e-02
CeD	7	IVW	1.04(1.01 to 1.08)	4.37e-02
		MREGGER	1.24(0.92 to 1.66)	2.13e-01
		WM	1.02(0.99 to 1.06)	2.20e-01
MS	23	IVW	1.01(0.98 to 1.04)	4.50e-01
		MREGGER	1.00(0.86 to 1.16)	9.90e-01
		WM	1.01(0.97 to 1.05)	6.20e-01
		MR-PRESSO	1.03(0.99 to 1.06)	9.90e-01
Psoriasis	18	IVW	0.18(0.03 to 1.10)	4.43e-01
		MREGGER	0.20(0.02 to 2.13)	1.34e-01
		WM	0.28(0.08 to 0.99)	4.76e-02
		MR-PRESSO	1.11(0.07 to 18.17)	9.40e-01
Asthma	68	IVW	1.07(1.03 to 1.12)	1.20e-03
		MREGGER	1.07(0.95 to 1.19)	2.60e-01
		WM	1.05(0.99 to 1.11)	6.75e-02
AR	117	IVW	1.07(1.02 to 1.11)	2.15e-03
		MREGGER	1.06(0.94 to 1.19)	3.34e-01
		WM	1.04(0.99 to 1.10)	1.19e-01
		MR-PRESSO	1.09(1.05 to 1.13)	9.09e-06
AD	20	IVW	1.05(1.01 to 1.10)	4.26e-02
		MREGGER	1.02(0.89 to 1.17)	7.77e-01
		WM	1.04(0.98 to 1.11)	1.53e-01

FIGURE 2
Mendelian randomization estimates from instrument variants for autoimmune and allergic diseases on risk of senile cataract.

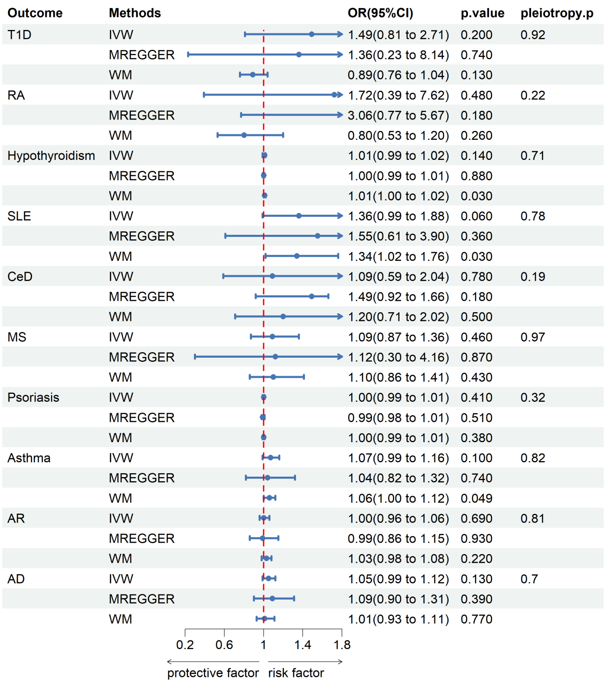

Outcome	Methods	OR(95%CI)	p.value	pleiotropy.p
T1D	IVW	1.49(0.81 to 2.71)	0.200	0.92
	MREGGER	1.36(0.23 to 8.14)	0.740	
	WM	0.89(0.76 to 1.04)	0.130	
RA	IVW	1.72(0.39 to 7.62)	0.480	0.22
	MREGGER	3.06(0.77 to 5.67)	0.180	
	WM	0.80(0.53 to 1.20)	0.260	
Hypothyroidism	IVW	1.01(0.99 to 1.02)	0.140	0.71
	MREGGER	1.00(0.99 to 1.01)	0.880	
	WM	1.01(1.00 to 1.02)	0.030	
SLE	IVW	1.36(0.99 to 1.88)	0.060	0.78
	MREGGER	1.55(0.61 to 3.90)	0.360	
	WM	1.34(1.02 to 1.76)	0.030	
CeD	IVW	1.09(0.59 to 2.04)	0.780	0.19
	MREGGER	1.49(0.92 to 1.66)	0.180	
	WM	1.20(0.71 to 2.02)	0.500	
MS	IVW	1.09(0.87 to 1.36)	0.460	0.97
	MREGGER	1.12(0.30 to 4.16)	0.870	
	WM	1.10(0.86 to 1.41)	0.430	
Psoriasis	IVW	1.00(0.99 to 1.01)	0.410	0.32
	MREGGER	0.99(0.98 to 1.01)	0.510	
	WM	1.00(0.99 to 1.01)	0.380	
Asthma	IVW	1.07(0.99 to 1.16)	0.100	0.82
	MREGGER	1.04(0.82 to 1.32)	0.740	
	WM	1.06(1.00 to 1.12)	0.049	
AR	IVW	1.00(0.96 to 1.06)	0.690	0.81
	MREGGER	0.99(0.86 to 1.15)	0.930	
	WM	1.03(0.98 to 1.08)	0.220	
AD	IVW	1.05(0.99 to 1.12)	0.130	0.7
	MREGGER	1.09(0.90 to 1.31)	0.390	
	WM	1.01(0.93 to 1.11)	0.770	

FIGURE 3
Mendelian randomization estimates from instrument variants for senile cataract on risk of autoimmune and allergic diseases.

Sensitivity analysis

Sensitivity analyses were performed to check the reliability of the IVW results. The effect of pleiotropy of exposures may be negligible given the intercept value, as no evidence of directional pleiotropy was found in the MR-Egger regression analysis ($p>0.05$) (Table 2). Cochrane's Q test showed that there was heterogeneity in MR analysis results between RA, hypothyroidism, SLE, psoriasis, asthma, AR with senile cataract ($p<0.05$) (Table 2). When the number of IVs is large, the existence of heterogeneity is unavoidable. Since we used random effects IVW as the primary analysis method, heterogeneity is acceptable and does not affect the estimation of causality (43). The MR-PRESSO test suggested that there were horizontal pleiotropic outliers for RA, hypothyroidism, MS, psoriasis and AR. The outliers-corrected results were shown in Figure 2. The results show that removing outliers did not affect the causal relationships implied by the main IVW results. Leave-one-out analysis results show that all SNPs are evenly distributed on the side of 0. It seems that no SNPs can strongly promote the overall effect of each exposure on senile cataract. The visualized scatter plots and Leave-one-out plots are shown in Figures 4, 5.

Discussion

In our study, a comprehensive bidirectional two-sample MR study was performed to investigate the causal associations between liabilities to ten diseases and the risk of senile cataract. MR analysis suggested a significant causal relationship between T1D, RA, hypothyroidism, SLE, asthma, AR and senile cataract. To the best of our knowledge, this is the first study to investigate the genetic causal links between autoimmune, allergic disease and senile cataract, making a significant contribution to understanding of the mechanism underlying senile cataract.

As a relatively common autoimmune disease, T1D is charactered by a complete lack of insulin due to the destruction of pancreatic beta cells, and insulin therapy must be given (44). Wen-Li Lu et al. reported that T1D patients had a higher risk of cataract compared to age- and sex-matched general population using cohort methodology in Taiwan (n=3,622) (13). Potential pathophysiological mechanisms may involve the aldose reductase pathway, oxidative stress, osmotic damage and autoimmunity (45). Papadimitriou et al. proposed an autoimmune hypothesis for acute bilateral cataract in T1D (24). Cataract formation typically occurs within weeks or months of the initiation of insulin therapy, coinciding with the time when insulin autoantibody became positive and the immunoreactivity of insulin receptors in the lens decreases. Further studies are necessary for clarification of these points and possibly for histological evidence of autoimmune processes (24). RA is a common autoimmune disease associated with hyperplasia of the joint tissues and the inflammation of the synovium, which can eventually lead to several serious systemic diseases, including pulmonary, cardiovascular, skeletal and psychological diseases (46). Eye diseases such as dry eye, glaucoma are common complications of RA, with a prevalence

TABLE 2 The results of sensitivity analysis.

Exposure	MRPRESSO *p*	Heterogeneity *p*	MR-Egger intercept	Pleiotropy *p*
Type 1 diabetes	0.107	0.09	0.00264	0.58
Rheumatoid arthritis	0.004*	1.18×10^{-4}*	-0.0104	0.09
Hypothyroidism	<0.001*	5.27×10^{-6}*	0.00135	0.66
Systemic lupus erythematosus	0.053	0.04*	-0.00398	0.35
Celiac disease	0.219	0.174	-0.0395	0.29
Multiple sclerosis	0.048*	0.06	0.00186	0.86
Psoriasis	0.021*	4.17×10^{-4}*	-0.000765	0.14
Asthma	0.71	1.17×10^{-3}*	0.000269	0.94
Allergic rhinitis	<0.001*	2.76×10^{-5}*	0.000518	0.85
Atopic dermatitis	0.915	0.906	0.00609	0.69

MRPRESSO, MR pleiotropy residual sum and outlier; IVW, inverse variance weighted.
*p<0.05 was considered statistically significant.

rate of about 18% (47). No related reports about RA increasing susceptibility to senile cataract directly were retrieved in PubMed database. However, in the treatment of RA, glucocorticoids (GCs) are commonly used. Posterior subcapsular cataract are known as side effects of long-term use of GCs (48), but it is still inconclusive whether the risk of cataract will increase during the treatment of RA with GCs (49). Our MR analysis provided genetic evidence that the onset of RA may increase the genetic susceptibility to cataract (OR=1.05). Primary hypothyroidism is defined by a high thyrotropin concentration along with low thyroid hormone concentrations or concentrations within the reference range. Hypothyroidism is usually an autoimmune disease in adults, which primarily affects middle-aged and elderly females (50). Limin Wei et al. published a case report that an East Asian 19-year-old male with Klinefelter Syndrome presenting cleft palate, hypothyroidism, cataract, and diabetes (51). This patient did not have congenital cataract because they were not diagnosed in infancy. Therefore, it is inferred that the formation of cataract in this patient may be related to hypothyroidism or diabetes, and there may be a potential genetic relationship between these diseases (51). Our results of MR analysis further verified this conjecture. SLE is a long-lasting autoimmune disease affecting multiple organs. It occurs when there is a failure in the regulation and tolerance of the immune system, affecting both the innate and adaptive immune responses (52). Cataract is the most prevalent ocular impairment in SLE. According to Alderaan et al., cataract development among patients with SLE is multifactorial and associated with the cumulative prednisone dose equivalent, systolic blood pressure and disease activity (12). Celiac disease, also known as gluten intolerance, is a condition that affects the small intestine and is characterized by an immune-mediated enteropathy. Ocular disease associated with celiac disease can sometimes be the first sign of the condition (53). Mollazadegan et al. conducted an European population-based cohort study (n=28756) and identified a moderate increase in the risk of cataract development among individuals diagnosed with biopsy-verified CeD (11). The cause of the condition has not been fully established, but research suggests that it may be related to a lack of absorption of vitamins and trace elements, dehydration, autoimmune factors and oxidative stress (11). Above findings supported the results obtained from our MR analyses, indicating that there is a positive association between genetically proxied autoimmune diseases and the risk of senile cataract.

Oxidative stress is the result of the imbalance between oxidant production and antioxidant defense mechanism. Reaction intermediates (free radicals and peroxides) that cannot be eliminated in time can have toxic effects on cellular components such as DNA, proteins, and lipids (54). The inflammatory response is associated with increased production of reactive oxygen species (ROS) and reactive nitrogen species (RNS), which is a shared characteristic among different autoimmune diseases, including RA, hypothyroidism, T1D, SLE, and others (55, 56). Lipid peroxidation caused by increased free radicals due to increased oxidative pressure of the lens or decreased ability to remove ROS is also an important pathological mechanism for cataract formation. Oxidative stress and autoimmunity-induced DNA damage, telomerase inhibition, and significant telomere shortening also accelerate aging (57, 58). Therefore, it can be inferred that the oxidative stress state of patients with autoimmune diseases may increase their susceptibility to senile cataract. A large amount of evidence suggests that autophagy deficiency is related to the development of autoimmunity. Meanwhile, the destruction of autophagy of lens cells can also lead to the loss of anti-stress ability and inhibit differentiation, and eventually lead to the formation of cataract (59, 60). Ferroptosis is a newly discovered type of iron-dependent programmed cell death characterized by excessive iron accumulation, elevated lipid peroxides, reactive oxygen species, reduced glutathione and glutathione peroxidase levels. A large and emerging literature on ferroptosis demonstrates the critical role of these pathological processes in autoimmune and

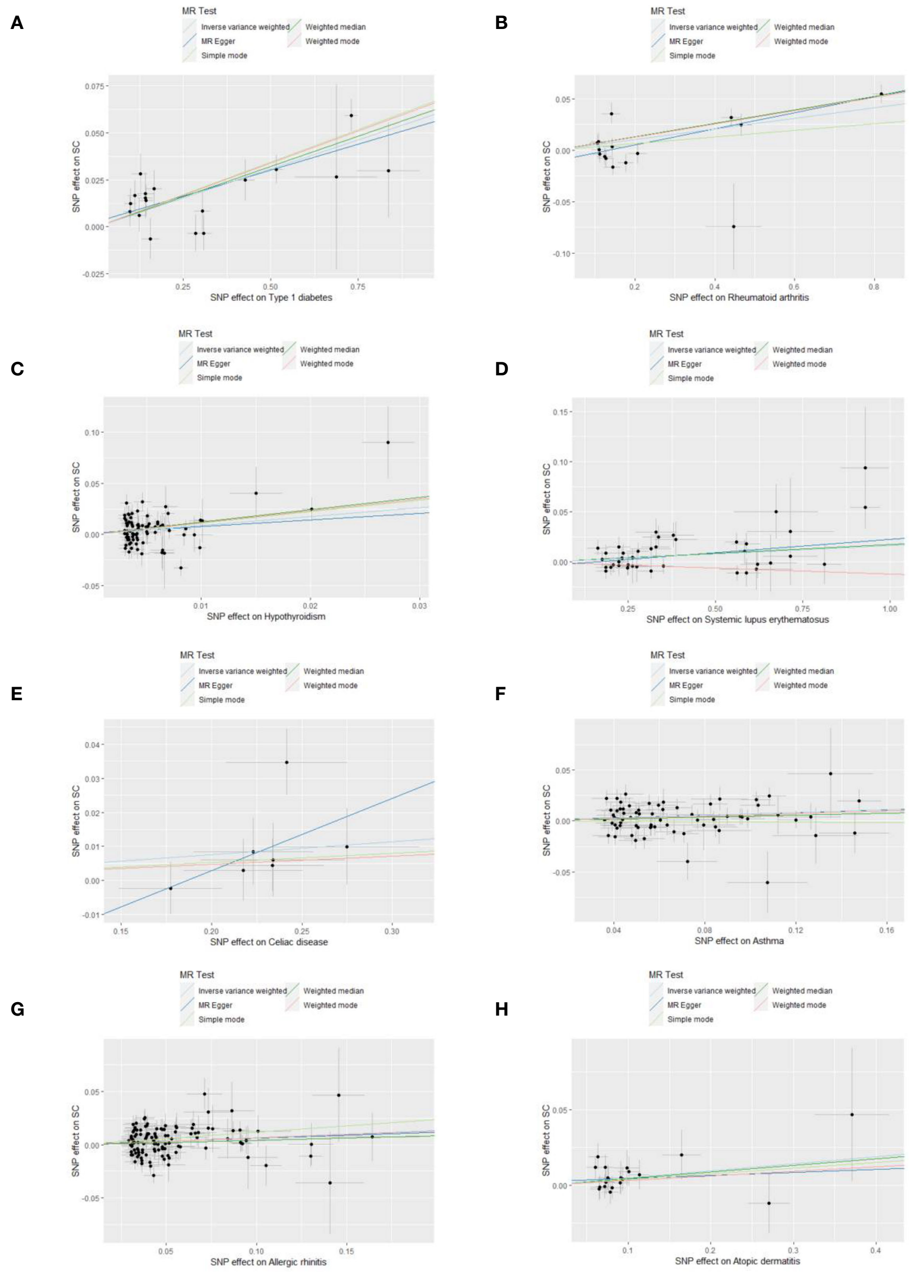

FIGURE 4
Scatter plots show the MR effect of each exposure on senile cataract in different MR methods. **(A)** Type 1 diabetes on senile cataract. **(B)** Rheumatoid arthritis on senile cataract. **(C)** Hypothyroidism on senile cataract. **(D)** Systemic lupus erythematosus on senile cataract. **(E)** Celiac disease on senile cataract. **(F)** Asthma on senile cataract. **(G)** Allergic rhinitis on senile cataract. **(H)** Allergic dermatitis on senile cataract.

ocular diseases (61). In addition, improper degradation of DNA during programmed death may also lead to autoimmune diseases and cataract (62).

Asthma is a chronic inflammatory disorder involving a large number of cells and cellular elements in the respiratory system (63). Li et al. found that cataracts had a positive correlation with asthma after adjusting for confounding factors by analyzing nationally representative samples from the National Health Interview Survey (NHIS) (16). Asthma may be closely related to cataracts through the PI3K-AKT-mTOR signaling pathway. In addition, allergy-induced inflammation or immune dysregulation is also one of the potential mechanisms leading to cataract formation (26). AR is a chronic inflammatory disease of the upper respiratory tract characterized by sneezing, itching, nasal congestion, and rhinorrhea (64). A Korean population-based survey reported that people with asthma and AR were more likely to develop senile cataracts but not with AD (17). Intranasal corticosteroids, a well-established and effective treatment for AR, does not appear to increase the risk of cataract in patients (65). The association between allergic diseases and cataracts may be attributed to multiple mechanisms, such as having similar risk

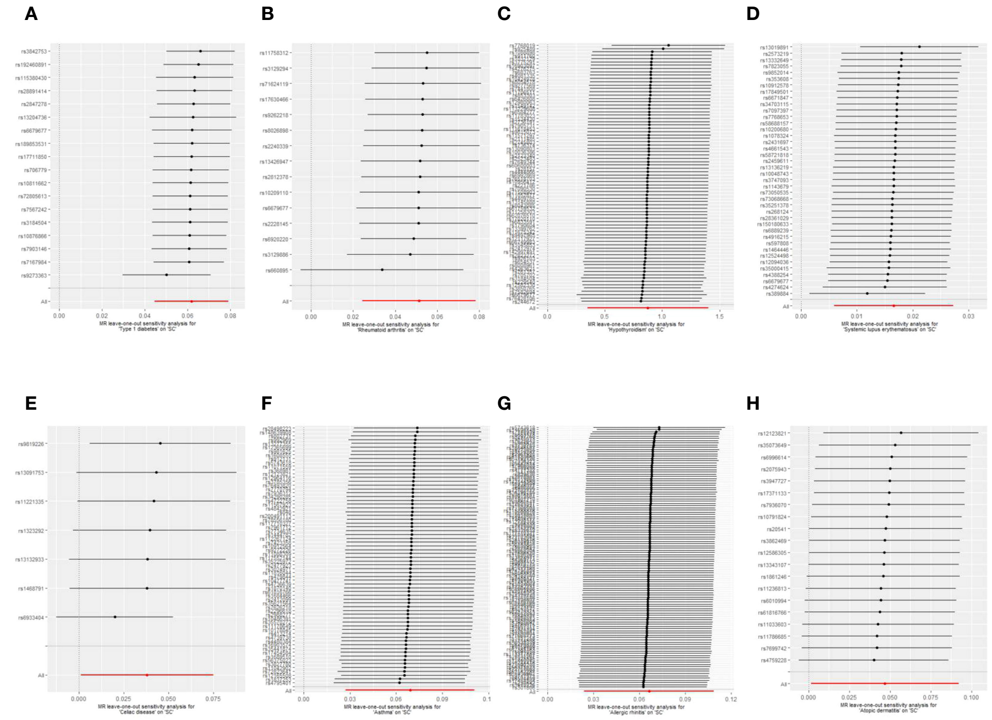

FIGURE 5
Leave-one-out plots of the causal relationships between autoimmune, allergic diseases and senile cataract. **(A)** Type 1 diabetes on senile cataract. **(B)** Rheumatoid arthritis on senile cataract. **(C)** Hypothyroidism on senile cataract. **(D)** Systemic lupus erythematosus on senile cataract. **(E)** Celiac disease on senile cataract. **(F)** Asthma on senile cataract. **(G)** Allergic rhinitis on senile cataract. **(H)** Allergic dermatitis on senile cataract.

factors, hypertension, hyperglycemia, etc. Other factors including inflammation and oxidative stress may also increase susceptibility to cataract (66). Our results showed that there is a suggestive genetic association between AD and senile cataract (p=0.0426). Therefore, as for whether AD increases the risk of senile cataract, based on our MR analysis and previous research results, we cannot determine the causal relationship between them, and further RCT is needed (17, 67).

A cause-and-effect relationship between the risk of senile cataract and MS, psoriasis could not be established in our study. Classified as an organ-specific, T-cell-mediated autoimmune disease, MS is the most common disabling disease in young adults that is not caused by physical trauma (68). A European population-based cohort study (n = 39,444) showing MS patients under the age of 50, especially young men, are at higher risk of developing cataract, compared with healthy controls (14). This result is contrary to the results of our MR analysis that there is no causal relationship between MS and the onset of cataract. Compared to observational studies, our MR study results are more compelling due to its ability to reduce confounding factors and reverse-causal association bias to some extent. Nonetheless, more advanced RCTs should be designed to confirm the causal association between the two diseases. Psoriasis, a polygenic disease characterized by erythematous plaques with silvery scales, is a chronic inflammatory autoimmune skin disorder affecting 1-3% of the world's population (69). Fuying Chen and colleagues have identified a new condition called the CAOP syndrome, which involves cataracts, alopecia, oral mucosal disorders and psoriasis-like symptoms (70). Contrary to our results, a population-based cohort by Chun-Yu Cheng has been observed a positive correlation between psoriasis and cataract. The common pathogenesis of cataract and psoriasis may be related to interleukin-6, C-reactive protein, intracellular adhesion molecule- 1, oxidative stress and so on (15). These differences in causality may be due to potential confounding factors, such as steroid hormone use and ultraviolet radiation, because observational studies are difficult to escape the influence of confounding factors. Therefore, there is likely no causal relationship between psoriasis and senile cataract based on MR analysis.

Senile cataract, as a reversible blinding eye disease with a high incidence rate, has caused great damage to labor productivity and brought a heavy economic burden around the world, especially in developing countries with in adequate surgical facilities. Understanding which factors increase the risk of cataracts can help identify high-risk individuals. Through the findings of this paper, people with autoimmune diseases should have regular anterior segment examinations through slit lamp microscopy while actively treating the primary disease, which will help ophthalmologists formulate preventive strategies in real time or select the most appropriate time for surgical treatment.

The main strength of our study is that we conducted an MR analysis and explored the genetic causal relationship between autoimmune, allergic diseases and the risk of senile cataract for the first time. Furthermore, various techniques were employed to perform sensitivity analysis, identifying outliers and correcting any potential pleiotropy and heterogeneity. With the increasing availability of a large amount of genetic data, the extension of GWAS may achieve early prediction of senile cataract and make it possible to achieve genetic-based treatment. The current study also has several limitations. Firstly, we used conventional methods that outcomes data were obtained from the FinnGen database and exposures data were obtained from other GWASs study on European ancestry in IEU Open GWAS database to reduce sample overlap. However, it is difficult to determine whether overlapping subjects were included in our MR analysis. Secondly, there is a possibility that a complete identification of all SNPs linked to these diseases was not achieved. By utilizing a restricted number of SNPs to establish the causal associations, it is possible that the statistical power of certain analyses may have been diminished. Thirdly, there may be potential confounding factors, such as the use of steroid hormone mediating the causality of autoimmune diseases on cataract, but due to the limitations of GWAS, we are not yet able to perform multivariate MR and mediation analysis. Last but not least, the data related to autoimmune, allergic diseases and senile cataracts were mostly from European ancestry. The results of our study should not be directly generalized to other ethnic groups.

Conclusion

In summary, our current findings provide strong genetic evidence in support of the causal relationship among type 1 diabetes, rheumatoid arthritis, hypothyroidism, systemic lupus erythematosus, asthma, allergic rhinitis and senile cataract in a European population. Our study confirms previous observational studies, suggesting that autoimmune and allergy processes may be risk factors of senile cataract. The results of this study suggest that patients with autoimmune or allergy diseases should pay attention to the prevention and treatment of senile cataract and further studies are needed to clarify the potential role of autoimmune and allergy in the pathophysiology of senile cataract.

Data availability statement

The original contributions presented in the study are included in the article/Supplementary Material. Further inquiries can be directed to the corresponding authors.

Ethics statement

All analyses were based on publicly shared databases and no additional ethical approvals were required.

Author contributions

WY: Writing – original draft, Software, Formal analysis, Conceptualization. XL: Writing – original draft, Visualization. GW: Writing – original draft, Resources. BQ: Writing – review & editing, Supervision. FZ: Writing – review & editing, Funding acquisition, Investigation, Supervision.

Funding

The author(s) declare financial support was received for the research, authorship, and/or publication of this article. This work was supported by grants from Scientific Research Project of Liaoning Provincial Department of Education in 2021 (No. LJKZ0773).

Conflict of interest

The authors declare that the research was conducted in the absence of any commercial or financial relationships that could be construed as a potential conflict of interest.

Publisher’s note

Supplementary material

The Supplementary Material for this article can be found online at: https://www.frontiersin.org/articles/10.3389/fimmu.2024.1325868/full#supplementary-material

References

1. Hashemi H, Pakzad R, Yekta A, Aghamirsalim M, Pakbin M, Ramin S, et al. Global and regional prevalence of age-related cataract: a comprehensive systematic review and meta-analysis. *Eye (Lond)*. (2020) 34:1357–70. doi: 10.1038/s41433-020-0806-3

2. He M, Wang W and Huang W. Variations and trends in health burden of visual impairment due to cataract: A global analysis. *Invest Ophthalmol Vis Sci*. (2017) 58:4299–306. doi: 10.1167/iovs.17-21459

3. Mitchell P, Cumming RG, Attebo K, Panchapakesan J. Prevalence of cataract in Australia: the Blue Mountains eye study. *Ophthalmology*. (1997) 104:581–8. doi: 10.1016/S0161-6420(97)30266-8

4. Yu X, Lyu D, Dong X, He J and Yao K. Hypertension and risk of cataract: a meta-analysis. *PloS One*. (2014) 9:e114012. doi: 10.1371/journal.pone.0114012

5. Ye J, He J, Wang C, Wu H, Shi X, Zhang H, et al. Smoking and risk of age-related cataract: a meta-analysis. *Invest Ophthalmol Vis Sci*. (2012) 53:3885–95. doi: 10.1167/iovs.12-9820

6. Chua SYL, Luben RN, Hayat S, Broadway DC, Khaw KT, Warwick A, et al. Alcohol consumption and incident cataract surgery in two large UK cohorts. *Ophthalmology*. (2021) 128:837–47. doi: 10.1016/j.ophtha.2021.02.007

7. Pek A, Szabo D, Sandor GL, Toth G, Papp A, Nagy ZZ, et al. Relationship between diabetes mellitus and cataract in Hungary. *Int J Ophthalmol*. (2020) 13:788–93. doi: 10.18240/ijo

8. Jacobson DL, Gange SJ, Rose NR and Graham NM. Epidemiology and estimated population burden of selected autoimmune diseases in the United States. *Clin Immunol Immunopathol*. (1997) 84:223–43. doi: 10.1006/clin.1997.4412

9. Wang L, Wang FS and Gershwin ME. Human autoimmune diseases: a comprehensive update. *J Intern Med*. (2015) 278:369–95. doi: 10.1111/joim.12395

10. Nwaru BI, Virtanen SM. Allergenic food introduction and childhood risk of allergic or autoimmune disease. *JAMA*. (2017) 317:86. doi: 10.1001/jama.2016.18329

11. Mollazadegan K, Kugelberg M, Lindblad BE, Ludvigsson JF. Increased risk of cataract among 28,000 patients with celiac disease. *Am J Epidemiol*. (2011) 174:195–202. doi: 10.1093/aje/kwr069

12. Alderaan K, Sekicki V, Magder LS and Petri M. Risk factors for cataracts in systemic lupus erythematosus (SLE). *Rheumatol Int*. (2015) 35:701–8. doi: 10.1007/s00296-014-3129-5

13. Lu WL, Shen PC, Lee CH, Su YT and Chen LM. High risk of early cataracts in young type 1 diabetes group: A nationwide cohort study. *Int J Endocrinol*. (2020) 2020:8160256. doi: 10.1155/2020/8160256

14. Bazelier MT, Mueller-Schotte S, Leufkens HG, Uitdehaag BM, van Staa T, de Vries F. Risk of cataract and glaucoma in patients with multiple sclerosis. *Mult Scler*. (2012) 18:628–38. doi: 10.1177/1352458511426737

15. Cheng CY. Risk of incident cataract in patients with psoriasis: A population-based cohort study. *J Dermatol*. (2022) 49:359–67. doi: 10.1111/1346-8138.16261

16. Li W, Wang B. Cross-sectional study of the association between asthma and cataract among 40 years and older in the USA. *BMC Ophthalmol*. (2022) 22:340. doi: 10.1186/s12886-022-02564-y

17. Lee YB, Lee JH, Kang MJ, Choi JY, Kim JW, Yu DS, et al. Association between allergic diseases and ophthalmologic diseases, including cataracts and glaucoma, using the Korean National Health and Nutrition Examination Survey 2010-2012: A STROBE-compliant article. *J Dermatol*. (2018) 45:463–7. doi: 10.1111/1346-8138.14193

18. Skrivankova VW, Richmond RC, Woolf BAR, Yarmolinsky J, Davies NM, Swanson SA, et al. Strengthening the reporting of observational studies in epidemiology using mendelian randomization: the STROBE-MR statement. *JAMA*. (2021) 326:1614–21. doi: 10.1001/jama.2021.18236

19. Smith GD, Ebrahim S. 'Mendelian randomization': can genetic epidemiology contribute to understanding environmental determinants of disease? *Int J Epidemiol*. (2003) 32:1–22. doi: 10.1093/ije/dyg070

20. Zheng J, Baird D, Borges MC, Bowden J, Hemani G, Haycock P, et al. Recent developments in mendelian randomization studies. *Curr Epidemiol Rep*. (2017) 4:330–45. doi: 10.1007/s40471-017-0128-6

21. Mokry LE, Ahmad O, Forgetta V, Thanassoulis G, Richards JB. Mendelian randomisation applied to drug development in cardiovascular disease: a review. *J Med Genet*. (2015) 52:71–9. doi: 10.1136/jmedgenet-2014-102438

22. Liu YC, Wilkins M, Kim T, Malyugin B and Mehta JS. Cataracts. *Lancet*. (2017) 390:600–12. doi: 10.1016/S0140-6736(17)30544-5

23. Vinson JA. Oxidative stress in cataracts. *Pathophysiology*. (2006) 13:151–62. doi: 10.1016/j.pathophys.2006.05.006

24. Papadimitriou DT, Bothou C, Skarmoutsos F, Alexandrides TK, Papaevangelou V, Papadimitriou A. The autoimmune hypothesis for acute bilateral cataract in type 1 diabetes. *Diabetes Metab*. (2016) 42:386–7. doi: 10.1016/j.diabet.2016.04.006

25. Ranjan M, Nayak S, Kosuri T and Rao BS. Immunochemical detection of glycated lens crystallins and their circulating autoantibodies in human serum during aging. *Mol Vis*. (2008) 14:2056–66.

26. Zhao Y, Li X, Xu Z, Hao L, Zhang Y and Liu Z. PI3K-AKT-mTOR signaling pathway: the intersection of allergic asthma and cataract. *Pharmazie*. (2019) 74:598–600. doi: 10.1691/ph.2019.9080

27. Sakaue S, Kanai M, Tanigawa Y, Karjalainen J, Kurki M, Koshiba S, et al. A cross-population atlas of genetic associations for 220 human phenotypes. *Nat Genet*. (2021) 53:1415–24. doi: 10.1038/s41588-021-00931-x

28. Eyre S, Bowes J, Diogo D, Lee A, Barton A, Martin P, et al. High-density genetic mapping identifies new susceptibility loci for rheumatoid arthritis. *Nat Genet*. (2012) 44:1336–40. doi: 10.1038/ng.2462

29. Dubois PC, Trynka G, Franke L, Hunt KA, Romanos J, Curtotti A, et al. Multiple common variants for celiac disease influencing immune gene expression. *Nat Genet*. (2010) 42:295–302. doi: 10.1038/ng.543

30. Bentham J, Morris DL, Graham DSC, Pinder CL, Tombleson P, Behrens TW, et al. Genetic association analyses implicate aberrant regulation of innate and adaptive immunity genes in the pathogenesis of systemic lupus erythematosus. *Nat Genet*. (2015) 47:1457–64. doi: 10.1038/ng.3434

31. The International Multiple Sclerosis Genetics Consortium & The Wellcome Trust Case Control Consortium 2. Genetic risk and a primary role for cell-mediated immune mechanisms in multiple sclerosis. *Nature*. (2011) 476:214–9. doi: 10.1038/nature10251

32. Valette K, Li Z, Bon-Baret V, Chignon A, Berube JC, Eslami A, et al. Prioritization of candidate causal genes for asthma in susceptibility loci derived from UK Biobank. *Commun Biol*. (2021) 4:700. doi: 10.1038/s42003-021-02227-6

33. Mbatchou J, Barnard L, Backman J, Marcketta A, Kosmicki JA, Ziyatdinov A, et al. Computationally efficient whole-genome regression for quantitative and binary traits. *Nat Genet*. (2021) 53:1097–103. doi: 10.1038/s41588-021-00870-7

34. Sliz E, Huilaja L, Pasanen A, Laisk T, Reimann E, Magi R, et al. Uniting biobank resources reveals novel genetic pathways modulating susceptibility for atopic dermatitis. *J Allergy Clin Immunol*. (2022) 149:1105–12 e9. doi: 10.1016/j.jaci.2021.07.043

35. Bowden J, Davey Smith G, Haycock PC and Burgess S. Consistent estimation in mendelian randomization with some invalid instruments using a weighted median estimator. *Genet Epidemiol*. (2016) 40:304–14. doi: 10.1002/gepi.21965

36. Kurki MI, Karjalainen J, Palta P, Sipila TP, Kristiansson K, Donner KM, et al. FinnGen provides genetic insights from a well-phenotyped isolated population. *Nature*. (2023) 613:508–18. doi: 10.1038/s41586-022-05473-8

37. Burgess S, Butterworth A, Thompson SG. Mendelian randomization analysis with multiple genetic variants using summarized data. *Genet Epidemiol*. (2013) 37:658–65. doi: 10.1002/gepi.21758

38. Bowden J, Davey Smith G, Burgess S. Mendelian randomization with invalid instruments: effect estimation and bias detection through Egger regression. *Int J Epidemiol*. (2015) 44:512–25. doi: 10.1093/ije/dyv080

39. Zhu Z, Zhang F, Hu H, Bakshi A, Robinson MR, Powell JE, et al. Integration of summary data from GWAS and eQTL studies predicts complex trait gene targets. *Nat Genet*. (2016) 48:481–7. doi: 10.1038/ng.3538

40. Verbanck M, Chen CY, Neale B and Do R. Detection of widespread horizontal pleiotropy in causal relationships inferred from Mendelian randomization between complex traits and diseases. *Nat Genet*. (2018) 50:693–8. doi: 10.1038/s41588-018-0099-7

41. Bowden J, Del Greco MF, Minelli C, Davey Smith G, Sheehan N and Thompson J. A framework for the investigation of pleiotropy in two-sample summary data Mendelian randomization. *Stat Med*. (2017) 36:1783–802. doi: 10.1002/sim.7221

42. Emdin CA, Khera AV and Kathiresan S. Mendelian randomization. *JAMA*. (2017) 318:1925–6. doi: 10.1001/jama.2017.17219

43. Burgess S, Davey Smith G, Davies NM, Dudbridge F, Gill D, Glymour MM, et al. Guidelines for performing Mendelian randomization investigations: update for summer 2023. *Wellcome Open Res*. (2019) 4:186. doi: 10.12688/wellcomeopenres

44. Katsarou A, Gudbjornsdottir S, Rawshani A, Dabelea D, Bonifacio E, Anderson BJ, et al. Type 1 diabetes mellitus. *Nat Rev Dis Primers*. (2017) 3:17016. doi: 10.1038/nrdp.2017.16

45. Obrosova IG, Chung SS and Kador PF. Diabetic cataracts: mechanisms and management. *Diabetes Metab Res Rev*. (2010) 26:172–80. doi: 10.1002/dmrr.1075

46. McInnes IB, Schett G. The pathogenesis of rheumatoid arthritis. *N Engl J Med*. (2011) 365:2205–19. doi: 10.1056/NEJMra1004965

47. Turk MA, Hayworth JL, Nevskaya T and Pope JE. Ocular manifestations in rheumatoid arthritis, connective tissue disease, and vasculitis: A systematic review and metaanalysis. *J Rheumatol*. (2021) 48:25–34. doi: 10.3899/jrheum.190768

48. Black RL, Oglesby RB, Von Sallmann L and Bunim JJ. Posterior subcapsular cataracts induced by corticosteroids in patients with rheumatoid arthritis. *JAMA*. (1960) 174:166–71. doi: 10.1001/jama.1960.63030020005014

49. Black RJ, Hill CL, Lester S and Dixon WG. The association between systemic glucocorticoid use and the risk of cataract and glaucoma in patients with rheumatoid arthritis: A systematic review and meta-analysis. *PloS One*. (2016) 11:e0166468. doi: 10.1371/journal.pone.0166468

50. Iglesias P, Bajo MA, Selgas R and Diez JJ. Thyroid dysfunction and kidney disease: An update. *Rev Endocr Metab Disord*. (2017) 18:131–44. doi: 10.1007/s11154-016-9395-7

51. Wei L, Liu Y, Sun S, Tang Y, Chen S and Song G. Case report of 49,XXXXY syndrome with cleft palate, diabetes, hypothyroidism, and cataracts. *Med (Baltimore)*. (2019) 98:e17342. doi: 10.1097/MD.0000000000017342

52. Tsokos GC, Lo MS, Costa Reis P, Sullivan KE. New insights into the immunopathogenesis of systemic lupus erythematosus. *Nat Rev Rheumatol*. (2016) 12:716–30. doi: 10.1038/nrrheum.2016.186

53. Fousekis FS, Katsanos A, Katsanos KH, Christodoulou DK. Ocular manifestations in celiac disease: an overview. *Int Ophthalmol*. (2020) 40:1049–54. doi: 10.1007/s10792-019-01254-x

54. Ramani S, Pathak A, Dalal V, Paul A and Biswas S. Oxidative stress in autoimmune diseases: an under dealt Malice. *Curr Protein Pept Sci*. (2020) 21:611–21. doi: 10.2174/1389203721666200214111816

55. Ruggeri RM, Campenn IA, Giuffrida G, Casciaro M, Barbalace MC, Hrelia S, et al. Oxidative stress as a key feature of autoimmune thyroiditis: an update. *Minerva Endocrinol*. (2020) 45:326–44. doi: 10.23736/S0391-1977.20.03268-X

56. Smallwood MJ, Nissim A, Knight AR, Whiteman M, Haigh R and Winyard PG. Oxidative stress in autoimmune rheumatic diseases. *Free Radic Biol Med*. (2018) 125:3–14. doi: 10.1016/j.freeradbiomed.2018.05.086

57. Babizhayev MA, Yegorov YE. Telomere attrition in lens epithelial cells - a target for N-acetylcarnosine therapy. *Front Biosci (Landmark Ed)*. (2010) 15:934–56. doi: 10.2741/3655

58. Weyand CM, Goronzy JJ. The immunology of rheumatoid arthritis. *Nat Immunol*. (2021) 22:10–8. doi: 10.1038/s41590-020-00816-x

59. Keller CW, Adamopoulos IE, Lunemann JD. Autophagy pathways in autoimmune diseases. *J Autoimmun*. (2023) 136:103030. doi: 10.1016/j.jaut.2023.103030

60. Chai P, Ni H, Zhang H and Fan X. The evolving functions of autophagy in ocular health: A double-edged sword. *Int J Biol Sci*. (2016) 12:1332–40. doi: 10.7150/ijbs.16245

61. Liu K, Li H, Wang F and Su Y. Ferroptosis: mechanisms and advances in ocular diseases. *Mol Cell Biochem*. (2023) 478:2081–95. doi: 10.1007/s11010-022-04644-5

62. Nagata S. DNA degradation in development and programmed cell death. *Annu Rev Immunol*. (2005) 23:853–75. doi: 10.1146/annurev.immunol.23.021704.115811

63. Asher MI, Montefort S, Bjorksten B, Lai CK, Strachan DP, Weiland SK, et al. Worldwide time trends in the prevalence of symptoms of asthma, allergic rhinoconjunctivitis, and eczema in childhood: ISAAC Phases One and Three repeat multicountry cross-sectional surveys. *Lancet*. (2006) 368:733–43. doi: 10.1016/S0140-6736(06)69283-0

64. Skoner DP. Allergic rhinitis: definition, epidemiology, pathophysiology, detection, and diagnosis. *J Allergy Clin Immunol*. (2001) 108:S2–8. doi: 10.1067/mai.2001.115569

65. Valenzuela CV, Liu JC, Vila PM, Simon L, Doering M and Lieu JEC. Intranasal corticosteroids do not lead to ocular changes: A systematic review and meta-analysis. *Laryngoscope*. (2019) 129:6–12. doi: 10.1002/lary.27209

66. Paik JS, Han K, Nam G, Park SK, Hwang HS, Chun YH, et al. Increased risk of cataract surgery in patients with allergic disease: a population based cohort study. *Sci Rep*. (2022) 12:21258. doi: 10.1038/s41598-022-25589-1

67. Rim TH, Kim DW, Kim SE and Kim SS. Factors associated with cataract in korea: A community health survey 2008-2012. *Yonsei Med J*. (2015) 56:1663–70. doi: 10.3349/ymj.2015.56.6.1663

68. Dobson R, Giovannoni G. Multiple sclerosis - a review. *Eur J Neurol*. (2019) 26:27–40. doi: 10.1111/ene.13819

69. Chandran NS, Greaves M, Gao F, Lim L and Cheng BC. Psoriasis and the eye: prevalence of eye disease in Singaporean Asian patients with psoriasis. *J Dermatol*. (2007) 34:805–10. doi: 10.1111/j.1346-8138.2007.00390.x

70. Chen F, Ni C, Wang X, Cheng R, Pan C, Wang Y, et al. S1P defects cause a new entity of cataract, alopecia, oral mucosal disorder, and psoriasis-like syndrome. *EMBO Mol Med*. (2022) 14:e14904. doi: 10.15252/emmm.202114904

frontiers | Frontiers in Medicine

TYPE Original Research
PUBLISHED 14 May 2024
DOI 10.3389/fmed.2024.1400137

Cross-modality transfer learning with knowledge infusion for diabetic retinopathy grading

Tao Chen[1,2†], Yanmiao Bai[2†], Haiting Mao[1,2], Shouyue Liu[1,2], Keyi Xu[1,2], Zhouwei Xiong[1,2], Shaodong Ma[2], Fang Yang[1,2]* and Yitian Zhao[1,2]*

[1]Cixi Biomedical Research Institute, Wenzhou Medical University, Ningbo, China, [2]Institute of Biomedical Engineering, Ningbo Institute of Materials Technology and Engineering, Chinese Academy of Sciences, Ningbo, China

Background: Ultra-wide-field (UWF) fundus photography represents an emerging retinal imaging technique offering a broader field of view, thus enhancing its utility in screening and diagnosing various eye diseases, notably diabetic retinopathy (DR). However, the application of computer-aided diagnosis for DR using UWF images confronts two major challenges. The first challenge arises from the limited availability of labeled UWF data, making it daunting to train diagnostic models due to the high cost associated with manual annotation of medical images. Secondly, existing models' performance requires enhancement due to the absence of prior knowledge to guide the learning process.

Purpose: By leveraging extensively annotated datasets within the field, which encompass large-scale, high-quality color fundus image datasets annotated at either image-level or pixel-level, our objective is to transfer knowledge from these datasets to our target domain through unsupervised domain adaptation.

Methods: Our approach presents a robust model for assessing the severity of diabetic retinopathy (DR) by leveraging unsupervised lesion-aware domain adaptation in ultra-wide-field (UWF) images. Furthermore, to harness the wealth of detailed annotations in publicly available color fundus image datasets, we integrate an adversarial lesion map generator. This generator supplements the grading model by incorporating auxiliary lesion information, drawing inspiration from the clinical methodology of evaluating DR severity by identifying and quantifying associated lesions.

Results: We conducted both quantitative and qualitative evaluations of our proposed method. In particular, among the six representative DR grading methods, our approach achieved an accuracy (ACC) of 68.18% and a precision (pre) of 67.43%. Additionally, we conducted extensive experiments in ablation studies to validate the effectiveness of each component of our proposed method.

Conclusion: In conclusion, our method not only improves the accuracy of DR grading, but also enhances the interpretability of the results, providing clinicians with a reliable DR grading scheme.

KEYWORDS

ultra-wide-field image, domain adaptation, diabetic retinopathy, lesion segmentation, disease diagnosis

EDITED BY
Kai Jin,
Zhejiang University, China

REVIEWED BY
Meng Wang,
Agency for Science, Technology and Research (A*STAR), Singapore
Xiayu Xu,
Xi'an Jiaotong University, China

*CORRESPONDENCE
Fang Yang
✉ yangf@nimte.ac.cn
Yitian Zhao
✉ yitian.zhao@nimte.ac.cn

[†] These authors have contributed equally to this work and share first authorship

RECEIVED 13 March 2024
ACCEPTED 15 April 2024
PUBLISHED 14 May 2024

CITATION
Chen T, Bai Y, Mao H, Liu S, Xu K, Xiong Z, Ma S, Yang F and Zhao Y (2024) Cross-modality transfer learning with knowledge infusion for diabetic retinopathy grading. *Front. Med.* 11:1400137. doi: 10.3389/fmed.2024.1400137

1 Introduction

Diabetic Retinopathy (DR), a typical fundus disease caused by the high level of blood glucose and high blood pressure, is one of the leading causes of visual impairment and blindness (1). The severity of DR can be classified into five stages based on the presence and quantity of retinal lesions, including microaneurysms (MAs), hemorrhages (HEs), soft exudates (SEs), and hard exudates (EXs). These stages encompass normal, mild non-proliferative DR (NPDRI), moderate non-proliferative DR (NPDRII), severe non-proliferative DR (NPDRIII), and proliferative DR (PDR). Accurate grading of DR severity assumes pivotal importance as it guides clinicians in devising personalized treatment strategies. However, the precise determination of DR severity levels can be a time-consuming task for ophthalmologists and presents a formidable challenge for novice ophthalmology residents. Therefore, the development of an automated system for early detection and severity grading of DR holds immense potential, offering substantial benefits to both patients and ophthalmologists alike.

Over the past half-century, the diagnosis of DR has predominantly relied on the utilization of Color Fundus Photography (CFP), as illustrated in Figure 1A, wherein critical retinal lesion anomalies are depicted. CFP serves as a reasonably effective screening tool for early-stage DR. Nevertheless, CFP exhibits a limited imaging range, typically spanning from 30° to 60°, thereby posing challenges in the identification of anomalies beyond this range. This limitation results in less ideal automated DR grading results.

Optos Ultra-Wide-Field (UWF) imaging technology is a novel non-invasive imaging method with a high resolution and short acquisition durations of 0.25 s. Compared to CFP images, UWF images exhibit a wide imaging range of up to 180°−200°, covering approximately 80.0% of the retina in a single frame (2, 3). This enables UWF images to more effectively detect peripheral retinal lesions (4, 5), as shown in Figure 1B. This enables UWF imagesto hold more advantage in diagnosing DR in comparison to CFP images (6–10). Thus, developing an automated DR grading algorithm based on UWF images is more meaningful.

Over the last decade, methods for automatic screening or grading of DR severity using CFP images have been rapidly developed with remarkable accuracy of $\geq$ 90.0% (11–17). This is largely due to the large scale, high quality CFP dataset that is publicly available, which provide pixel-level annotations and image-level annotations, such as EyePACS (18), DDR (18), IDRiD (19) etc. Despite several studies (20, 21) have conducted DR grading using UWF images, the performance of these methods has been found to be less satisfactory compared to those using the CFP iamges. The reasons may be attributed to the following factors: (1) The scarcity of large-scale annotated data for deep learning training in UWF imaging poses a significant challenge in training high-performing grading models using fully supervised methods. The only public available dataset of UWF contains 256 UWF images with DR (22). (2) The lesion information is crucial for enhancing the precision of DR grading. However, the contrast divergence between lesions and ordinary tissue in UWF images is slight, which hampers precise grading of DR.

To address these challenges, we aim to utilize a substantial dataset of well-annotated CFP images along with knowledge infusion to enhance the performance of DR grading. Recent studies have explored unsupervised domain adaptation learning methods to mitigate the domain-shift issue between the source and target domains (23–25). These methods leverage external labeled datasets to acquire general knowledge of diseases and transfer this knowledge to object categories without labels. In this study, we design a transfer learning model utilizing the rich pixel-level and image-level annotations available in CFP images to facilitate the DR grading in UWF images. A preliminary version of this work has been previously published in conference proceedings (26). In this paper, we present the following extensions:

1) To enhance the recognition of complex lesions for the lesion segmentation task, we introduce a novel roll-machine modulated feature fusion block. To enable comprehensive evaluation, we construct a new dataset called UWF-seg, which includes 27 images with annotations of different lesions. We provide evaluations on UWF-seg and additional result analyses to further validate the effectiveness of our proposed method.

2) To gain deeper insights into proposed method, we conduct extensive additional experiments, including evaluations with a larger set of unlabeled images, exploration of different loss weights, and analysis of different exemplar images. Moreover, we carefully examine failure cases to identify potential limitations for improvement.

3) We enrich the discussion in this study by providing a more comprehensive analysis of the relationship and comparison between our work and related studies. Additionally, we offer a detailed technical description of our proposed method and engage in an in-depth discussion of its limitations. Finally, we outline future research directions to address these limitations and extend the scope of our work.

2 Related works

2.1 Computer-aided diagnosis in UWF

In this section, we survey the current studies that utilizes UWF imaging to identify a range of retinal diseases, with a particular emphasis on the computer-aided diagnosis of diabetic retinopathy. Recently, deep learning models have been applied to UWF images with the goal of detecting various retinal diseases. For instance, central retinal vein occlusion (27, 28), Sickle cell retinopathy (29, 30) and retinal detachments (31, 32), respectively. These studies have underscored the clinical advantages of employing UWF imaging in diagnosing various peripheral retinal pathologies. Nagasawa et al. (33) conducted a study to assess the accuracy of utilizing UWF fundus images alongside the VGG16 model for detecting PDR. In a subsequent investigation (34), they extended their research by comparing the accuracy of VGG16 using two distinct types of retinal images for DR grading. These methodologies primarily concentrate on the binary classification of DR, placing a premium on practical clinical relevance over architectural enhancements in network design. In efforts to refine the precision of DR grading, Liu et al. (35) curated

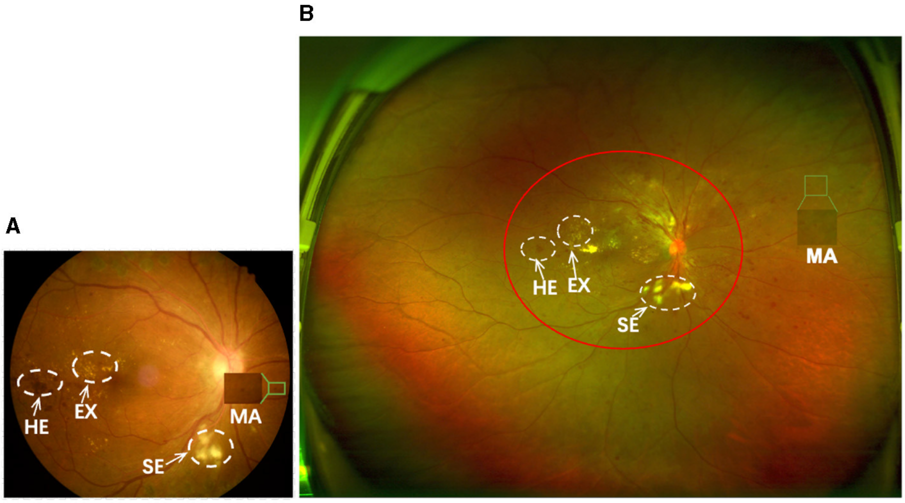

FIGURE 1
(A, B) are samples of CFP and UWF with DR, respectively. The imaging area of **(A)** is approximately that of the red circle in **(B)**. Both can show important lesions associated with DR, but **(B)** gives a more complete picture of the retinopathy.

a proprietary UWF dataset comprising 101 DR fundus images. They devised a deep learning-based automatic classification model integrating a novel preprocessing technique, achieving an average accuracy of 0.72. However, the utilization of UWF imaging in detecting DR-related lesions remains relatively underexplored, with only a few researchers delving into this domain. For example, Levenkova et al. (36) utilized support vector machine (SVM) algorithms to identify features of DR lesions, categorizing them into bright lesions (such as cotton wool spots and exudates) and dark lesions (including microaneurysms, spots, and flame-shaped hemorrhages). However, their study exclusively focused on segmenting bright and dark signs, neglecting the comprehensive diagnosis of DR grade. The efficacy of these methodologies in addressing DR challenges largely hinges on the availability of meticulously annotated data. Nevertheless, the scarcity of UWF data and the prohibitive costs associated with labeling pose significant barriers, thus constraining access to this valuable resource and hindering the broader implementation of deep learning techniques in this domain.

Furthermore, many current learning-based methods for grading DR lack interpretability and fail to integrate prior knowledge to inform the classification process. Thus, there is a critical need to develop an interpretable approach for DR grading using UWF images in an unsupervised manner, capitalizing on inherent lesion features. In particular, Ju et al. (7) introduced a methodology that incorporates CFP images to aid in training diagnostic models based on UWF images. They utilized an enhanced CycleGAN framework to bridge the domain disparity between CFP and UWF images, thereby generating new data with UWF image characteristics. Subsequently, these generated images underwent labeling via pseudo-labeling techniques. While the model exhibited promising performance across various retinal disease diagnosis tasks, including DR grading, its reliance primarily on a GAN-based model for transforming CFP images into UWF fundus images is notable. This strategy aimed to augment the limited UWF imaging dataset with additional data. However, the approach encountered challenges in effectively transferring knowledge from CFP images to UWF images. Consequently, the model's performance remains susceptible to the potential impact of synthesized UWF images.

2.2 Domain adaptation

Domain adaptation (DA) serves as a crucial paradigm within the realm of transfer learning in machine learning, aimed at mitigating the distribution disparity between domains. Fundamentally, it involves identifying similarities between different data distributions in related tasks and harnessing these similarities to facilitate cross-domain recognition problems (37–39). Several systematic reviews (40–42) offer comprehensive insights into this method from various perspectives. For instance, domain adaptation from general to complex situations, including methods based on domain distribution difference (43, 44), adversarial learning (45, 46), reconstruction-based methods (47, 48), and sample generation-based methods (49, 50). Recently, the efficacy of DA leveraging deep architecture has garnered empirical support across numerous vision tasks, including textual emotion (51), object detection (52), and pose estimation (53). Unsupervised domain adaptation (UDA) represents a notable advancement, facilitating the prediction of target domain data without necessitating manual annotation (43). This approach offers a potential and viable avenue for mitigating the challenges associated with limited labeled data.

In the realm of medical image analysis, Unsupervised Domain Adaptation (UDA) stands as a widely explored area aimed at mitigating disparities between cross-domain datasets derived from various imaging equipment types, thereby enhancing image segmentation or classification. Kamnitsas et al. (54)

introduced UDA techniques to biomedical imaging, presenting an unsupervised domain-adaptive network tailored for brain lesion segmentation. Furthermore, Chai et al. (55) delved into the potential of reducing disparities between Optical Coherence Tomography (OCT) images captured using Topcon and Nidek devices, with the aim of achieving more effective segmentation of the choroid region. Due to the substantial scarcity of data in certain intricate medical image tasks, there has been widespread interest in employing unsupervised transfer learning to alleviate data constraints, leading to notable advancements as evidenced by works (24, 56, 57). Zhang et al. (58) introduced a cooperative UDA algorithm tailored for microscopy image disease diagnosis, demonstrating that the integration of rich labeled data from relevant domains can effectively enhance learning in cross-domain detection tasks. In the domain of DR grading, the predominant focus has been on the transition between DR lesion detection and grading tasks (59–61). However, these approaches have primarily been developed based on conventional color fundus images. In our prior investigation (26), we explored the application of UDA to train a diagnostic model for UWF images, leveraging the assistance of CFP images. Our experimental findings demonstrated that the proposed method effectively transfers knowledge from CFP images pertaining to DR to UWF images, consequently leading to enhanced performance in DR disease recognition tasks.

3 Proposed method

3.1 Problem formulation

Given annotated color fundus photography (CFP) images X^S as the source domain and ultra-widefield (UWF) images without any annotations X^T as the target domain, our objective is to leverage the high-quality annotated CFP images to train a robust diabetic retinopathy (DR) grading model for UWF images in an unsupervised manner. Additionally, we incorporate a lesion segmentation model $G(\cdot)$ to augment the grading model $C(\cdot)$ with extra knowledge, mirroring the clinical process of assessing DR severity and enhancing grading accuracy. To train the segmentation model, our aim is to minimize the disparity between the predicted lesion maps from UWF images and the ground truth lesion maps from CFP images, as formulated by the following objective function (Equation 1):

$$\min_{G} \sum_{l=1}^{L} \mathcal{L}_{Seg}(G(X^S), G(X^T), s_l^S, s_l^T) \tag{1}$$

where s_l^S denotes the the CFP lesion maps of pixel-level annotated CFP images and s_l^T is the UWF predicted lesion maps. L is the total number of lesion varieties related to a particular disease. The optimization function for the disease grading model is defined as Equation 2:

$$\min_{C} \mathcal{L}_{Cls}\left(C\left(\mathbf{X}^T + G(X^T)\right) \cdot \mathrm{LEAM}\left(G\left(\mathbf{X}^T\right)\right), \mathbf{y_c}^I\right) \tag{2}$$

where y_c^I denotes the disease severity classification prediction for image-level annotated CFP data. Thus, the pivotal aspect in achieving collaborative learning across different modules lies in the design and optimization of $G(\cdot)$, $C(\cdot)$, and $LEAM(\cdot)$. The overall architecture of the proposed framework is illustrated in Figure 2.

3.2 Unsupervised DR grading module

The DR grading module comprises a deep feature extractor $F_E(\cdot)$, a label predictor C, and a domain predictor D, facilitating unsupervised domain adaptation for knowledge transfer. Meanwhile, to enhance the extraction of discriminative features tailored for diabetic retinopathy (DR) classification, we employ two classifiers, C_1 and C_2. These classifiers aid the feature extractor in disregarding domain differences. Given the complexity of domain adaptation evaluation, we employ the pretrained ResNet50 encoder (62) in the hierarchical module. Compared to ResNet128 and ResNet32, ResNet50 has moderate depth and parameter count, making it easier to train and fine-tune for feature extraction. Thus, it can extract n-dimensional feature vectors, denoted as f^S and f^T, corresponding to the source and target domains, respectively.

Subsequently, a class label predictor C and a domain predictor D follow. The label predictor estimates the probability of DR severity grading, while the domain predictor ensures learned feature invariance across domains. The feature vector f is mapped to $d = 0$ (for input from the source domain S) or $d = 1$ (for input from the target domain T) by the domain predictor, ensuring similar feature distributions across domains. The domain predictor D comprises two fully connected (FC) layers. The first FC layer is accompanied by batch normalization (BN) and a ReLU activation function, while the second layer is followed by BN and a softmax activation function. The feature vector f is transformed by D into either d=0 (when the input is X^S or d=1 (when the input is X^T), ensuring that the feature distributions from both domains remain as similar as possible. While the domain predictor effectively achieves domain alignment, it may not guarantee class discriminability. To ensure discriminative feature representations, we maximize the discrepancy between the two classifiers, C_1 and C_2, to obtain highly discriminative features. The details of the loss function are as follows in Equation 3:

$$\begin{aligned}\mathcal{L}_{cd} = \mathbb{E}_{x_j^t \sim \mathcal{D}_t} &\left\| C_1\left(G\left(\hat{x}_j^t\right)\right) - C_2\left(G\left(\hat{x}_j^t\right)\right)\right\|_1 \\ &+ \left\| C\left(G\left(\hat{x}_j^t\right)\right) - C_1\left(G\left(\hat{x}_j^t\right)\right)\right\|_1 \\ &+ \left\| C\left(G\left(\hat{x}_j^t\right)\right) - C_2\left(G\left(\hat{x}_j^t\right)\right)\right\|_1\end{aligned} \tag{3}$$

C, C_1, and C_2 denote three pre-trained classifiers trained via supervised learning on the source domain. When G and C are fixed, maximizing the discrepancy between C_1 and C_2 in the target domain enables them to identify target samples not captured by the support vectors of the source. By training G to minimize this discrepancy, while C_1 and C_2 remain fixed, the resulting target features become highly discriminative. The primary classifier C defines a decision hyperplane between C_1 and C_2, optimizing the distance between the support vectors and the decision boundary. It's important to note that the class predictor C is utilized during both training and testing procedures to obtain grading labels, while the domain predictor D, C_1, and C_2 are only employed during training.

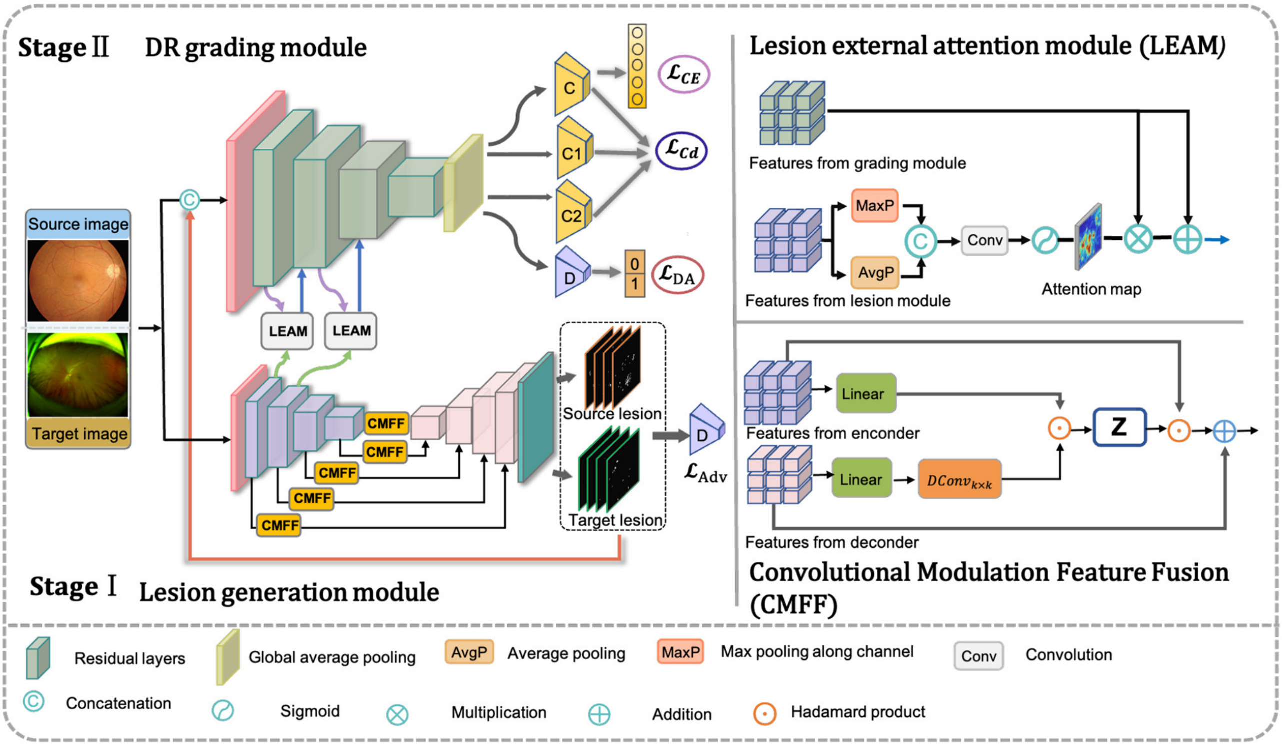

FIGURE 2
Framework of the proposed method. Our net includes three components: the DR grading module based on transfer learning, adversarial multi-lesion masks generate network, and lesion external attention module. The input data consists of a very small set of unlabeled target images and a large set of annotated source images. The adversarial multi-lesion masks generate network is used to learn multi-lesion masks, where target lesion predicted will with the original images as inputs for training DR grading module based on transfer learning. At the same time, the lesion external attention module aims to force classification network to pay those lesions for improving the final disease grading performance.

3.3 Adversarial lesion segmentation module

To mimic the clinical process of assessing DR severity, we introduce an adversarial domain adaptation (DA)-based UWF segmentation model. This model serves as an ancillary tool for UWF lesion segmentation. A schematic diagram of the lesion segmentation subnet is depicted in the orange section of Figure 2. As illustrated, the framework comprises two primary components: the convolutional modulation-based lesion generator $G(\cdot)$ and the adversarial domain discriminator $D(\cdot)$. We denote pixel-level lesion annotations as X^S, and the target domain data without such annotations as X^T. Here, X^S and X^T belong to $R^{C\times W\times H}$, where H, W, and C represent the height, width, and number of channels of the input, respectively. Additionally, M^S and M^T represent the lesion prediction results for the source and target domain data, respectively. The proposed UWF lesion segmentation subnet is elaborated as follows.

3.3.1 The convolutional modulation-based lesion generator

Our proposed model is implemented based on a U-shaped structure, also known as a Res-Unet proposed by Xiao et al. (63). We extended the Res-UNet with the deeper multi-scale residual module and modified it to be a lesion generator. Specifically, the encoder and decoder components for the mask generator comprise nine feature mapping tuples. Additionally, two convolutional layers with Sigmoid activation are appended to generate a lesion mask for the input image. This architecture serves as the segmentation backbone network (**Base**) for the lesion segmentation task.

In addition, we introduce a Convolutional Modulation Feature Fusion block (CMFF) to enhance the model's ability to learn complex lesions and achieve accurate segmentation in a larger receptive field of UWF images. The convolutional modulation operation (64) encodes spatial features to simplify self-attention and can better leverage large kernels ($\geq 7\times 7$) nested in convolutional layers. Inspired by U-Transformer (65), we employ multiple CMFF blocks instead of traditional skip connections, aiming to fully integrate multi-scale high-level feature maps with relevant encoding features, as illustrated in Figure 2. A second CMFF block is positioned at the end of the encoder to assimilate distant knowledge from the input image and associate each pixel in the high-level semantic features learned by the encoder. This approach enables the model to capture the receptive field of the entire image and achieve accurate lesion segmentation in UWF images, as depicted in Figure 2. Taking the first CMFF block as an example, for the feature maps X_i and $Y_i \in R^{C\times W\times H}$ from the encoder and decoder, respectively, the CMFF operation can be expressed as follows in Equations 4–7:

$$Z_i = A_i \odot V_i \tag{4}$$

$$A_i = DConv_{k\times k}(W_1 Y_i) \tag{5}$$

$$V_i = W_2 X_i \tag{6}$$

$$F_i = Z_i \odot X_i \oplus Y_i \tag{7}$$

where $\odot$ denotes Hadamard product, W_1 and W_2 are weight matrices of two linear layers, $DConv_{k\times k}$ denotes denotes a depthwise convolution with kernel size k × k.

3.3.2 Adversarial domain discriminator

The lesion generator $G(\cdot)$ is trained on images with pixel-level lesion annotations from the source domain (CFP images) and unlabeled UWF images from the target domain as input, enabling automatic lesion segmentation. With pixel-level annotated lesion masks Y^S of the source domain, a combination of Dice loss $\mathcal{L}_{Dice}$ and cross-entropy loss $\mathcal{L}_{CE}$ is employed to minimize the difference between the predicted lesion map M^S and the ground-truths Y^S. The trained $G(\cdot)$ is capable of outputting a segmentation result, which represents a structured output containing feature similarity between the source and target domains.

To further transfer knowledge from the source domain to the target domain in the output space, an adversarial domain discriminator $D(\cdot)$ needs to be introduced. The primary objective of $D(\cdot)$ is to ensure that the generated sample closely resembles real data. In our implementation, we consider the source lesion maps M^S predicted by $G(\cdot)$ as the real data branch and the target lesion maps M^T predicted from the UWF data as the fake data branch. By using M^S and M^T as inputs for $D(\cdot)$, with an adversarial loss, we aim to reduce the domain gap between the source and target domains, thereby enhancing the accuracy of lesion prediction in the target domain images. The total loss for optimizing the lesion segmentation task can be defined as in Equations 8–10:

$$\mathcal{L}_{Total} = \mathcal{L}_{Adv} + \lambda \mathcal{L}_{Seg}. \tag{8}$$

$$\mathcal{L}_{Adv} = \min_{G}\max_{D} \mathbb{E}[log(D(M^S)] + \mathbb{E}[log(1 - D(M^T)]. \tag{9}$$

$$\begin{aligned} \mathcal{L}_{Seg} = \mathcal{L}_{Dice}\left(M^s, Y^s\right) + \mathcal{L}_{CE}\left(M^s, Y^s\right) = \\ \sigma \frac{2 \times \left|M^s \cap Y^s\right|}{\left(|M^s| + |Y^s|\right)} + \\ \mathbb{E}\left[-Y^s \cdot \log M^s - \left(1 - Y^s\right) \cdot \log\left(1 - M^s\right)\right]. \end{aligned} \tag{10}$$

where λ the balance weight of two objective functions, σ the balance weight of Dice loss and cross-entropy loss.

The domain discriminator consists of four convolutional tuple maps, as illustrated in the Figure 2. Each tuple comprises convolutional operations with varying kernel sizes aimed at progressively encoding contextual information to expand the receptive field. Specifically, the first tuple conducts convolutional operations with a kernel size of 7×7 and padding of 3. Subsequently, the second and third tuples perform convolutional operations with a kernel size of 5×5 and padding of 2. The final convolutional operation employs a kernel size of 3×3 and padding of 1. A stride of 2 is applied for each tuple, with linear ReLU activation and batch normalization also incorporated. The output of the last convolutional layer undergoes spatial dimensionality reduction via an adaptive average pooling layer. Subsequently, a binary output is generated through a fully connected layer and Sigmoid activation function, facilitating the distinction of whether the predicted lesion map output originates from the source domain or the target domain.

3.3.3 Lesion external attention module

Despite the integration of the generated lesion maps with the grading module, the independent nature of the lesion generation module and the grading module hinders the effective utilization of lesion information to guide the learning process of the grading module. Furthermore, the disease grading task is confronted with challenges beyond the diverse lesion types of varying clinical significance. The disease grading task also encounters challenges stemming from complex background artifacts (such as eyelash and eyelid interference) and noise present in ultra-widefield (UWF) images, particularly when employing unsupervised approaches. To improve the integration of filtered lesion knowledge into the grading module, we introduce a Lesion External Attention Module (LEAM). Unlike previous self-attention mechanisms (66), we utilize an external module, specifically the lesion generation module, to generate the lesion attention map. This attention map is subsequently used to re-calibrate the features within the grading module. The LEAM acts as a bridge, facilitating the effective utilization of lesion information obtained from the lesion generation module to guide the learning process of the grading module. This mechanism assists the grading module in a human-like manner for classification, automatically extracting task-specific lesion regions while ignoring irrelevant information to enhance grading accuracy.

The details of LEAM are illustrated in Figure 2. We begin by extracting the feature maps f_i^L from the lesion generation module, where i represents the i-th intermediate layer of the generator $G_L(\cdot)$. Max pooling and average pooling are performed across channels to obtain two spatial lesion descriptors. Max pooling helps capture locally important features in the image, while average pooling aids in extracting global features and reducing noise. Combining both enhances feature representation, enabling the model to better understand the image. Subsequently, these concatenated descriptors are fed into a convolutional layer followed by a sigmoid activation layer to generate the lesion attention map.

In our approach, the disease grading module and LEAM are intricately integrated. Initially, we utilize $G_L(\cdot)$ to extract the lesion feature maps. Once pre-trained, $f_{l=i}^L$ (where i denotes the i-th different intermediate base layer of the U-shaped network encoder) serves as input to the LEAM. Following maximum pooling, average pooling, and convolution operations, a lesion attention map $m_{l=i}^L$ is produced. Subsequently, we multiply the feature maps f_i^G from the grading module (with i denoting the i-th intermediate layer of the grading module) by m_i^L. This is followed by an element-wise summation operation with f_i^G to derive the new feature maps $\widetilde{f_i^G}$. The overall attention process can be summarized as follows in Equation 11:

$$\begin{aligned} m_i^L &= \sigma\left(\mathbf{Conv}\left(\mathbf{Avg\,Pool}\left(f_i^L\right) \parallel \mathbf{MaxPool}\left(f_i^L\right)\right)\right), \\ \widetilde{f_i^G} &= (f_i^G \otimes m_i^L) \oplus f_i^G, \end{aligned} \tag{11}$$

TABLE 1 The summary and distribution statistics in our project image datasets.

Dataset	Annotation modes	Images	Nomal	NPDRI	NPDRII	NPDRIII	PDR	Tasks
IDRID	Pixel-level	81	-	-	-	-	-	Seg-Source
EYEPACS	Image-level	8,000	1,715	1,715	1,714	1,514	1,342	Grad-Source
DeepDRiD	Image-level	206	60	57	56	23	4	Grad-Target
Local-UWF	Pixel-level	27	0	6	9	7	5	Seg-Target
	Image-level	1212	412	202	193	218	187	Grad-Target

where ∥ denotes the concatenation operation, σ denotes the sigmoid activation function. $\otimes$ and $\oplus$ demote the element-wise multiplication and element-wise sum, respectively. This design allows more multi-scale pathological information to be extracted from UWF images, which helps our unsupervised transfer learning framework to be more accurate and robust.

4 Experiments

4.1 Data description

In our experiment, two types of datasets were involved: source domain and target domain. A summary of used datasets related to this experiment is provided in Table 1.

For the source domain data, publicly accessible datasets with annotations, such as IDRID and EYEPACS, are available. However, for the target domain data, there is currently no publicly available dataset with high-quality lesion segmentation labels. Therefore, one of the primary objectives of our benchmark is to introduce a fine-grained lesion annotated dataset to facilitate a more comprehensive evaluation of the proposed lesion segmentation subnetwork and enable a more interpretable diagnosis of DR. Additionally, we assess the grading performance of our DeepMT-DR method on the public UWF dataset, namely DeepDRiD. Detailed information about existing datasets and our proposed dataset is provided below.

4.1.1 IDRID

IDRID is the DR dataset providing pixel-level multi-lesion annotations, is one of the most commonly used public datasets for DR segmentation tasks. It comprises 81 CFP images depicting DR symptoms, with 54 allocated for training and 27 for testing. Medical experts meticulously annotated four types of lesions–MA (80), HE (80), EX (81), and SE (40)–using binary masks. This dataset serves as the source domain data to train the lesion generator.

4.1.2 EyePACS

EyePACS sourced from the DR Challenge - Kaggle Diabetic Retinopathy Detection Competition,[1] comprises 88,702 CFP images and offers image-level grading annotations across five categories. To maximize the inclusion of diseased samples, we randomly sampled 8,000 images (approximately 1,600 images per category) from EyePACS, creating a new subset to serve as the source domain for training the grading subnetwork.

4.1.3 DeepDRiD

DeepDRiD is the only DR dataset providing multi-grading annotations, to the best of our knowledge. It contains 256 UWF images with symptoms of DR and is into UWF Set-A (77 patients, 154 images) for training, UWF Set-B (25 patients, 50 images) for testing and UWF Set-C (26 patients, 52 images) for validating. We use the UWF Set-C to evaluate the grading performance of our DeepMT-DR method.

4.1.4 Local UWF

We have compiled a finely annotated Diabetic Retinopathy (DR) Ultra-Widefield (UWF) dataset, comprising two distinct subsets. The first subset, named UWF segmentation subset (UWF-Seg), consists of 27 images annotated with pixel-level lesion labels and image-level grading annotations. Lesion annotations encompass Microaneurysms (MA), Hemorrhages (HE), Exudates (EX), and Soft Exudates (SE), making this subset specifically tailored for evaluating segmentation performance. The second subset, named UWF grading subset (UWF-Grad), comprises 877 images annotated with grading labels by three ophthalmologists, ranging from 0 to 4. During the segmentation sub-network training, UWF-Grad served as the target domain, while UWF-Seg was utilized for testing. For training the grading model, the person-UWF dataset was partitioned into 60% for training and 40% for testing. It is noteworthy that our proposed method underwent training without leveraging any labels.

Dataset construction: The UWF image data were mainly collected from local partner hospitals. To fully protect patient privacy, data security regulations was strictly adhered in our dataset construction. All the images were captured by Optos Daytona (P200T) UWF canning laser ophthalmoscope with an imaging resolution of 3900×3072 pixels. To ensure data quality and task accuracy, three selection principles were adopted: 1. Removal of images with quality issues and non-standard imaging; 2. Deletion of images with severe blurriness; 3. Prioritization of images without laser treatment. For the UWF-seg dataset, images with higher severity of diabetic retinopathy and a greater diversity of lesion types were selected.

Dataset annotation: Lesion annotation in the UWF-seg dataset was conducted using the ITK-SNAP (67) annotation software. The annotations were based on detailed clinical features. Specifically: Microaneurysms (MA) were annotated based on obvious borders

---

[1] https://www.kaggle.com/c/diabetic-retinopathy-detection/

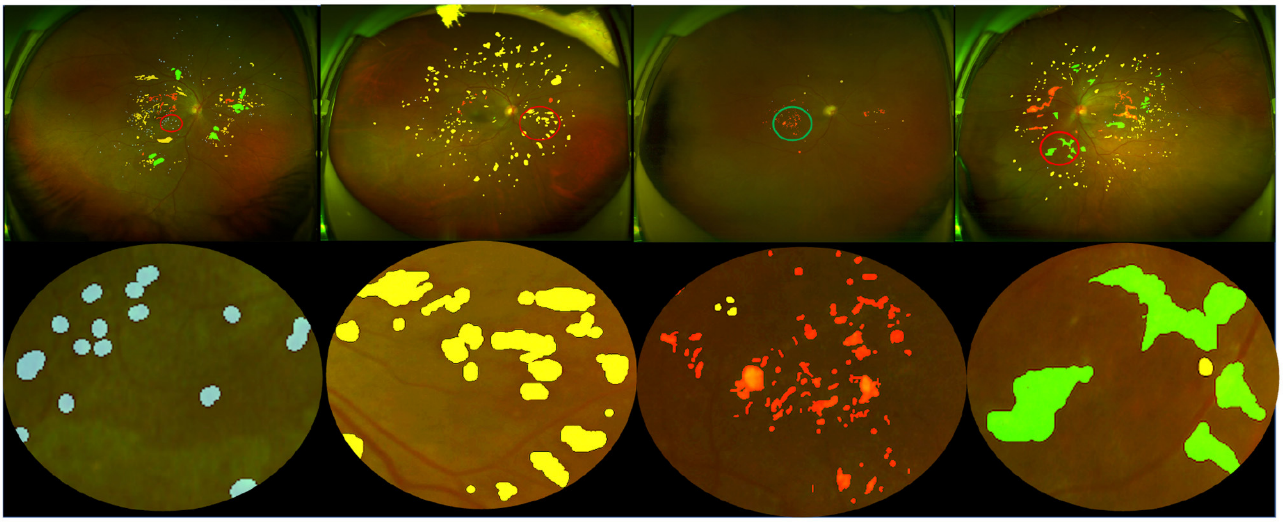

FIGURE 3
Pixel-level annotation examples from UWF-seg, including four different lesions. The blue, yellow, red, and green denote microaneurysm, hemorrhage, hard exudate, and soft exudate, respectively.

TABLE 2 Values of some key hyper-parameters in the three training stages.

	Initial learning rate	Weight	Batch
StageI	0.0001	0.0005	8
StageII	0.0005	0.0005	32
StageIII	Same as Stage II		

and red spots of various sizes distributed at the ends of blood vessels; Hemorrhages (HE) typically manifested as circular or patchy red spots distributed throughout the entire fundus image, often with a relatively large volume; Exudates (EX) were annotated based on their obvious borders and sediment-like appearance, which was relatively small and bright white or yellow-white in color; Soft exudates (SE) usually presented as areas with unclear borders and a fluffy texture, exhibiting a pale white or pale yellow-white color, often growing along the direction of the nerve fiber layer. Partial annotation examples and their corresponding lesion annotations are illustrated in Figure 3. Additionally, DR grading annotations strictly adhered to international DR severity scales.

Data pre-processing: The IDRID, EyePACS, DeepDRiD, and Local-UWF datasets exhibit variations in lighting conditions and resolutions. Consequently, a preprocessing method based on Van Grinsven et al. (68) was employed to standardize image quality and enhance texture details. Moreover, to address class imbalance and improve model robustness, horizontal and vertical flipping, along with rotation at consistent angles, were applied to both images and labels. Notably, UWF images often contain structural artifacts like eyelids and eyelashes, which can negatively impact tasks such as lesion segmentation by causing model overfitting. To mitigate this issue, a preprocessing approach similar to that of Ju et al. (7) was adopted. Specifically, U-Net segmentation networks were trained to remove artifacts while preserving essential semantic information. Subsequently, all images underwent the center-cut method to trim the edges of the UWF fundus images.

4.2 Evaluation metrics

To quantitatively evaluate the performance of the lesion segmentation task, we compute several metrics including the Dice Similarity Coefficient (Dice), Area Under the Curve of the Receiver Operating Characteristic (AUC-ROC), Area Under the Curve of the Precision-Recall (AUC-PR), and Mean Absolute Error (MAE). The MAE is defined as:

$$MAE = \frac{1}{w \times h} \sum_{x}^{w} \sum_{y}^{h} \left| M_i(x, y) - Y(x, y) \right|$$

where M_i indicates the final prediction of the DR lesion. To evaluate the performance of DR grading, we utilize several widely-used metrics for multi-class classification, including Accuracy (ACC), Weighted Sensitivity (Sen), Specificity (Spe), and the quadratic weighted kappa metric. The kappa metric is defined as follows:

$$kappa = \frac{p_o - p_e}{1 - p_e}$$

where p_o and p_e represent the extent to which raters agree and the expected probability of chance agreement, respectively.

4.3 Implementation details

The training methodology for the DeepMT-DR model comprises three stages. In the first stage, we train the auxiliary task subnet, which focuses on UWF lesion segmentation. The primary objective of this stage is to extract adequate pathological features to support the main DR grading task. In the second stage, we pre-train

TABLE 3 Comparison of unsupervised segmentation of bright lesion based on convolutional modulation adversarial lesion generators.

Lesion	Bright lesion (EX+SE)			
Methods	Dice	AUC-ROC	AUC-PR	MAE
Base1	0.647 + 0.121	0.989 + 0.008	0.712 + 0.143	0.011 + 0.010
Base2	0.318 + 0.165	0.976 + 0.024	0.289 + 0.214	0.010 + 0.003
Base2+Adv	0.416 + 0.166	0.950 + 0.056	0.381 + 0.209	0.004 + 0.002
Base2+Adv+CMFF	0.417 + 0.161	0.970 + 0.032	0.443 + 0.203	0.006 + 0.003

TABLE 4 Comparison of unsupervised segmentation of dark lesion based on convolutional modulation adversarial lesion generators.

Lesion	Dark lesion (MA+HE)			
Methods	Dice	AUC-ROC	AUC-PR	MAE
Base1	0.522 + 0.127	0.963 + 0.037	0.544 + 0.175	0.013 + 0.018
Base2	0.295 + 0.181	0.890 + 0.060	0.289 + 0.203	0.029 + 0.021
Base2+Adv	0.429 + 0.150	0.906 + 0.055	0.435 + 0.199	0.015 + 0.014
Base2+Adv+CMFF	0.451 + 0.154	0.903 + 0.053	0.446 + 0.192	0.017 + 0.017

the DR grading subnet using the CFP DR severity classification task to enhance UWF performance. In the third stage, we utilize prior knowledge and the proposed LEAM to fine-tune the DR grading module, leveraging the models pretrained in the first two stages. Furthermore, in all training stages, we optimize the model parameters using the Adam optimizer, augmented with weight decay. Table 2 presents the values assigned to the critical hyper-parameters during the training stages. In our implementation, all images were resized to 512×512 pixels. We implemented the proposed networks using Python based on the PyTorch package, and the PC we used contained two GPUs (NVIDIA GeForce GTX 3090 Ti 24GB each).

4.4 Lesion segmentation performances

Before quantifying the impact of lesion information on grading performance, we first demonstrate the effectiveness of the adversarial lesion generator based on convolutional modulation for unsupervised segmentation on the UWF-seg dataset. We evaluate two different types of lesions: dark lesions and bright lesions, which are key indicators of diabetic retinopathy (DR), using metrics including Dice similarity coefficient, AUC-ROC, AUC-PR, and mean absolute error (MAE). Dark lesions such as microaneurysms (MA), blot hemorrhages, dot hemorrhages, and flame hemorrhages are clinical signs observed in the early stages of DR. On the other hand, bright lesions such as hard exudates (EX) and soft exudates (SE) are characteristic of more severe stages of the disease. Therefore, detecting both bright and dark lesions without further subdividing them into specific types is sufficient for initial DR grading. We investigate each proposed component of the final model alongside two baselines. **Base1:** The pre-trained base segmentation model is trained in a fully supervised manner using 54 CFP images from IDRID and evaluated using the 27 IDRID test images, aiming to enhance the quality of knowledge learned from the source domain. **Base2:** The pre-trained base segmentation model uses 81 CFP images without an adversarial transfer strategy, and is directly tested on the UWF-seg dataset.

The detailed segmentation performances of these methods are reported in Tables 3, 4. For **Base1**, several metrics such as Dice and AUC-ROC are already comparable to most segmentation models trained on the same data, fully demonstrating that the improved Base possesses good lesion extraction capabilities. For **Base2**, applying the model trained on the source domain directly to the target domain, the Dice value for bright and dark lesions were only 31.8%, 29.5%, respectively, demonstrating a significant domain bias problem between the source and target domain data. On the UWF-seg dataset, a adversarial domain adaptation based UWF lesion segmentation model consistently outperforms Base2. the Dice value for bright and dark lesions increases by 9.8%, 13.4%, respectively, proving that adversarial domain adaptation can indeed benefit the UWF segmentation results. It is worth noting that, for bright lesions, the value of AUC-ROC actually decreased. This may be because AUC-ROC is more sensitive to the classification boundary between positive and negative classes, leading to more mis-classifications on the decision boundary of the classifier. Furthermore, after improving AUC-ROC, the AUC-PR values tend to be generally lower. This is because pathological regions related to DR typically represent only a small portion of the image, while normal regions constitute the vast majority. Consequently, models often predict normal regions more easily while neglecting pathological ones. To address this issue, we can adjust the threshold to strike a balance between the two. With the CMFF design, which exploits more contextual information to improve the identification of complex lesions, a clear improvement is observed. Specifically, significant improvements were observed for dark lesions, with an average gain of 2.2% for the Dice value.

Figure 4 compares the subjective segmentation results of two different lesions for the pre-trained lesion segmentation model adopting the limited UWF data. As seen, the lesion segmented masks by our method are more close to the ground-truth.

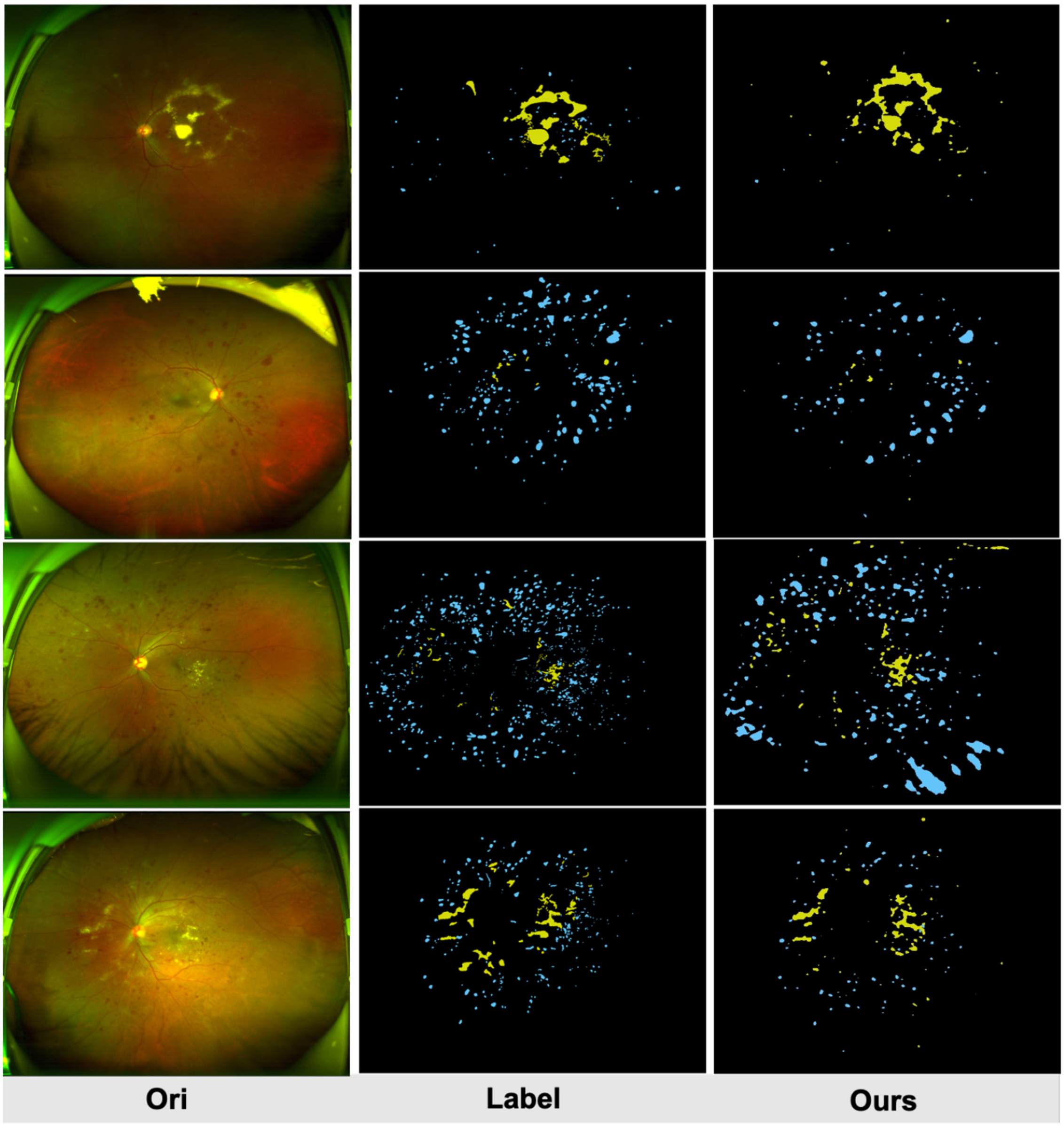

FIGURE 4
Qualitative multi-lesion segmentation results. Yellow and blue represent light and dark lesions, respectively.

4.5 DR grading performances

The proposed method was first compared the following four representative types of UDA methods which were designed for classification. These methods include: Domain Separation Networks (**DSN**) (69), Adversarial Discriminative Domain Adaptation (**ADDA**) (70), Maximum Classifier Discrepancy (**MCD**) (71), Dynamic Weighted Learning (**DWL**) (72), and the (**ULTRA**) (26), As in the top half of Table 5. Note, ULTRA is a model specifically proposed for DR grading in UWF image. Furthermore, although our approach is unsupervised, fully supervised training can also be performed when the labels of the UWF images are available, which we define as Ours*. So, we also compared the proposed method to the state-of-the-art deep-learning-based methods for UWF image DR classification, for example, **VGG-16** (73), **ResNet50** (62), and **CycleGAN** (7). Notably, **CycleGAN** method is the only method that uses CFP images to aid the training of UWF images. As in the lower part of Table 5.

4.5.1 Classification performance of local-UWF

In general, deep learning methods trained in a fully supervised manner tend to yield superior classification results compared to unsupervised DA methods, and the difference in performance is relatively significant. This fact further underscores the significant challenges associated with leveraging CFP images to aid in

TABLE 5 The DR grading results over the Local-UWF dataset.

Methods	Acc	PRE	F1	Kappa
DSN (69)	0.5027	0.3582	0.6097	0.3287
ADDA (70)	0.5396	0.5513	0.5447	0.4142
MCD (71)	0.5523	0.4816	0.5377	0.4874
DWL (72)	0.5646	0.5160	0.6049	0.4282
ULTRA (26)	0.5832	0.5210	0.5518	0.4903
VGG-16 (73)	0.6417	0.6496	0.6411	0.5370
Resnet50 (62)	0.6563	0.6423	0.6734	0.5478
CycleGAN* (7)	0.6292	0.6278	0.6389	0.5159
Ours	0.5912	0.5240	0.6423	0.4648
Ours*	0.6813	0.6743	0.6889	0.5861

*Indicates the method is fully supervised, i.e., the grading labels of UWF images are used in the training phase.

the diagnosis of UWF images. However, the proposed method outperforms these UDA methods in most metrics.

For example, our method demonstrates a significant advantage over the **DWL** method, with an increase in accuracy and *Kappa* of approximately 2.66% and 3.66%, respectively. Furthermore, despite incorporating a reconstruction loss in the DSN method to capture more generalized features, this also introduces a tendency for the model to disregard image-specific details, such as lesions present in CFP and UWF images, resulting in suboptimal performance of the DSN approach for this particular task. When trained in a supervised manner, most of the models perform well, demonstrating the feasibility of grading UWF images with DL methods. Compared with the state-of-the-art deep learning method, Ours* demonstrated competitive performance across all metrics. For example, our method exhibits a significant advantage over the **CycleGAN** method, with increases in accuracy, precision, F1 score, and Kappa of approximately 5.21%, 4.65%, 4.99%, and 7.02%, respectively. The main reason for this is that the **CycleGAN** method generates UWF images from CFP images by style transfer, and the performance of the grading model depends on the quality of the synthesized images.

To analyze the performance of the proposed model for UWF DR grading, we have provided the confusion matrix in Figure 5. This matrix displays the recognition results of the model across different categories. Overall, the proposed model performs well in all classes except for class 1.

4.6 Ablation study

In this section, we perform an ablation study to analyze the effectiveness of each key component. Our Net employs three main components to form its classification framework: unsupervised DR grading module, adversarial lesion segmentation module and Lesion external attention module, so we analyze and discuss the network under different scenarios to validate the performance of each key component of our model. The results of different combinations of these modules are reported in Table 6.

4.6.1 The effectiveness of unsupervised DR grading module

To explore the impact of the UDA DR grading sub-network, we employed a ResNet-50 grading model as the backbone, denoted as M_{CFP}, which was trained solely on the EyePACS subset and tested on the UWF dataset. It's important to note that the backbone model achieves an accuracy of 26.47% (as shown in Table 6), indicating the significant domain gap between CFP images and UWF images.

Furthermore, we explored the C1+C2+D method, which involves joint training using both CFP and UWF images with UDA techniques. Encouragingly, this method outperformed the M_{CFP} backbone model, demonstrating significant improvements across several indicators. This result underscores the effectiveness of leveraging UDA to jointly train CFP and UWF images, thereby reducing domain discrepancies and enhancing the accuracy of DR grading. By leveraging the complementary information from both CFP and UWF domains, our approach showcases its efficacy in achieving superior performance in DR grading tasks. These findings underscore the potential of UDA techniques and the integration of diverse image sources for enhancing the accuracy and reliability of DR grading models.

4.6.2 The effectiveness of adversarial lesion segmentation module

As described in Section 3.3, a pivotal component of our proposed method is the adversarial lesion segmentation module, aimed at capturing multi-lesion features from annotated UWF images. This addresses the challenge of lacking prior guidance during the decision-making stage of DR. Detailed ablation results for the adversarial lesion segmentation module are presented in Section 4.4. Specifically, we observe an increase of approximately 1.05% in accuracy (ACC) for M_{Lesion} compared to M_{Transfer}. This suggests that the lesion generation module provides additional lesion information, and the specific lesion features are beneficial for distinguishing DR subtypes, aligning with the findings of epidemiological studies.

4.6.3 The effectiveness of the LEAM

In Section 3.3.3, we introduced the incorporation of fully integrated lesion features into our approach. To ascertain the effectiveness of the Lesion External Attention Module (LEAM), we compared the performance of the model with and without LEAM, denoted as M_{Lesion} and M_{Ours} respectively. The results demonstrated that the feature fusion strategy facilitated by LEAM significantly enhances the classification performance, with a 3.49% increase in accuracy (ACC) and a 6.48% increase in kappa. This observation suggests that the proposed LEAM effectively embeds lesion-specific knowledge into the grading module. By focusing attention on salient lesion features, LEAM facilitates the extraction and integration of crucial information, thereby improving the overall capability of the grading model to accurately classify retinal images.

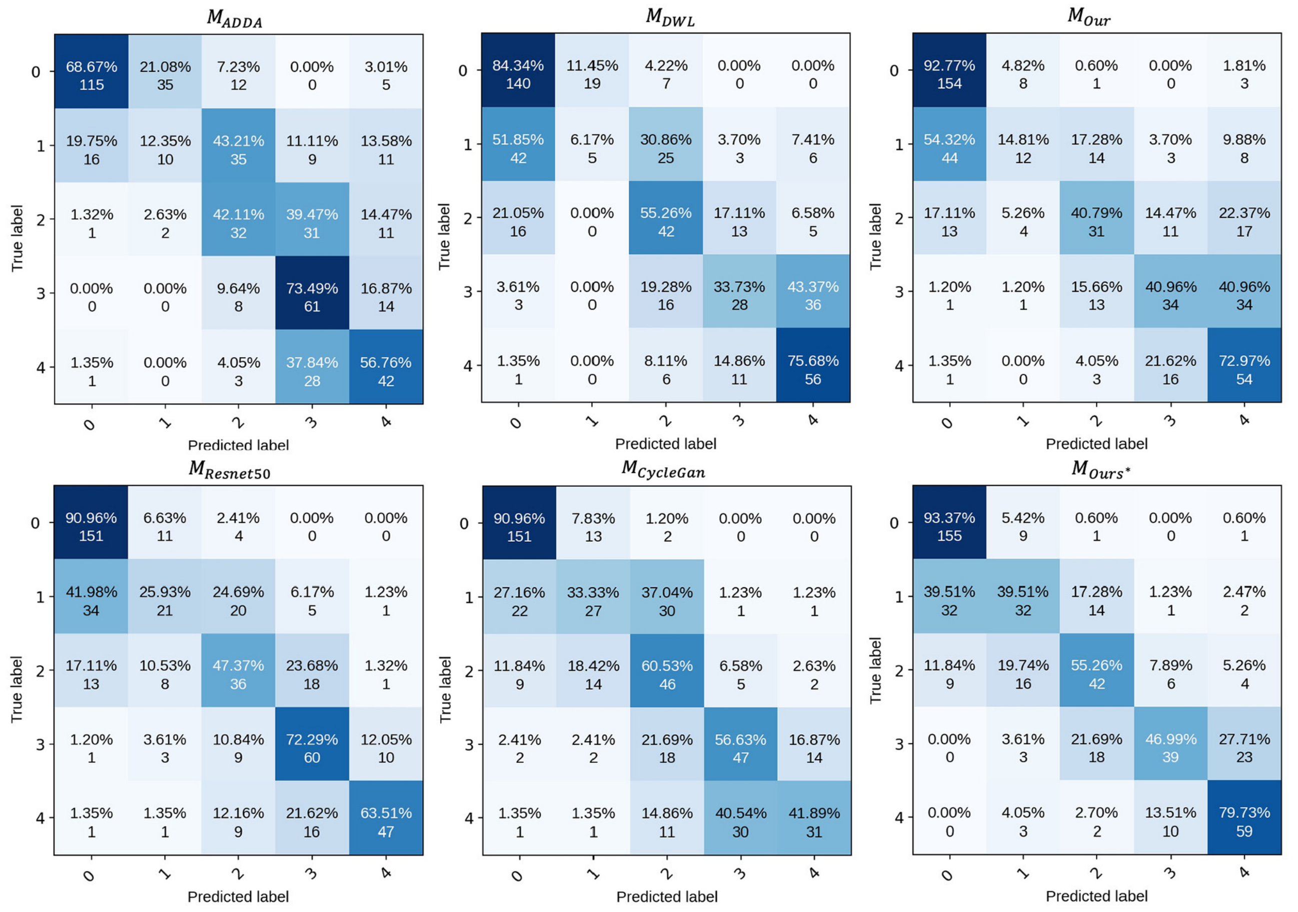

FIGURE 5
Confusion matrix of proposed model.

TABLE 6 Performance comparisons of ablation studies.

Method	Training	Resnet-50	C1+C2+D	Lesion	LEAM	ACC	PRE	F1	Kappa
M_{CFP}	C_{label}	✓				0.2647	0.4397	0.2786	0.1057
M_{Transfer}	$C_{label}/U_{unlabel}$	✓	✓			0.5458	0.5340	0.5955	0.4069
M_{Lesion}	$C_{label}/U_{unlabel}$	✓	✓	✓		0.5563	0.4493	0.6262	0.4001
M_{Ours}	$C_{label}/U_{unlabel}$	✓	✓	✓	✓	0.5912	0.5240	0.6423	0.4648

C and *U* denotes the CFP and UWF datasets, respectively.

5 Discussions and conclusion

Several existing studies have highlighted the significant advantages of ultra-widefield (UWF) imaging over color fundus photography (CFP) in monitoring diabetic retinopathy (DR) progression. However, due to limited datasets and annotations, the field of UWF-based DR-assisted diagnosis remains relatively unexplored. Moreover, most existing studies utilizing UWF images and deep learning methods for DR diagnosis employ end-to-end models lacking guidance from prior knowledge and interpretability in decision-making.

In this study, we introduce a deep learning-based method aimed at robust predictions for DR in UWF photography, focusing on unsupervised lesion-aware domain adaptation. However, achieving robust predictions for DR in an unsupervised manner presents two significant challenges: Firstly, overall metrics for segmenting UWF lesions need improvement, and there is a lack of detailed class information; secondly, lesion segmentation and disease grading are separate tasks requiring individual attention and improvement.

The main contribution of our work lies in accomplishing the tasks of lesion segmentation and automatic grading of DR using CFP images to assist UWF image analysis through the innovative application of unsupervised domain adaptation (UDA) methods. We aim to incorporate clinical priors into the deep learning algorithm through lesion segmentation of UWF images and the explicit utilization of light-dark lesion data to enhance

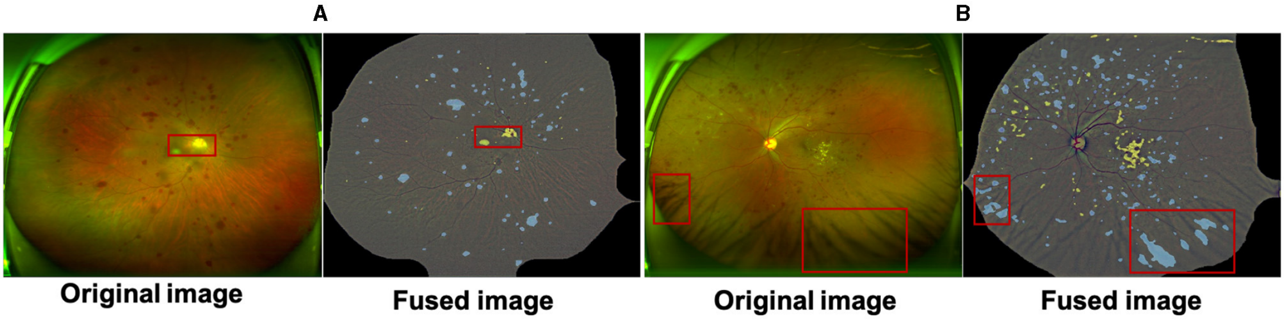

FIGURE 6
The macula and optic cup in **(A)** are incorrectly identified as bright lesions; the intersection of the eyelashes and fundus in **(B)** is also incorrectly detected as a dark lesion. All samples are a fusion of the pre-processed maps with the results of the lesion features.

DR classification accuracy. Our ablation study demonstrates the effectiveness of our specifically designed components.

5.1 Limitations

5.1.1 The performance of UWF segmentation network needs to be improved

In this work we proposes a UWF lesion segmentation network based on adversarial domain transfer, which simulates the process of clinical doctors diagnosing DR based on detailed lesion features. Although this method achieved certain segmentation results on the UWF-seg dataset, the overall performance still needs to be improved. UWF images are often obstructed by eyelids and eyelashes, and these artifacts may affect the screening performance of models trained on clean images. Although pre-processing can remove some artifacts, it also masks useful information in the surrounding area and there are still some false positives cases. As Figure 6A shows, the macula and the optic disc will be wrongly detected as bright lesions, where Figure 6B shows that the intersection of eyelashes and fundus will also be wrongly segmented as a lesion area. Therefore, an effective method for removing UWF image artifacts while preserving key structures is urgently needed. In addition, the irregular shape of lesions, their similarity to surrounding normal tissues, and mutual occlusion make them difficult to segment correctly using unsupervised methods. To overcome these challenges, future research can adopt deep reinforcement learning or semi-supervised training to improve the model's segmentation ability for complex lesions.

5.1.2 Collaborative training framework needs to be developed

In this work, we propose an ULTRA (Unsupervised Lesion Transfer Learning for Disease Recognition and Assessment) network based on UWF images for automatic grading of diabetic retinopathy (DR), and its effectiveness has been demonstrated through extensive experiments. However, our approach treats lesion segmentation and disease diagnosis as separate tasks and combines their features using a specific fusion strategy. This requires manual selection of fusion strategies and hyperparameter tuning, potentially resulting in information loss in the fusion process.

To address this limitation, future research could explore the development of a collaborative training framework and optimize joint training strategies to ensure the accuracy of both lesion segmentation and disease diagnosis. By enhancing the effectiveness of joint learning, such efforts can lead to improved performance and reliability in automated DR grading systems based on UWF images.

5.2 Analysis on failure cases

We further analyze the failed classification cases by GradCAM. Specifically, Figure 7A demonstrates successful predictions of DR severity grading by the model, while Figure 7B displays examples of misclassifications. All images are preprocessed and overlaid with heatmaps. it is observed that in Figures 4–6A, despite the presence of interfering factors such as eyelash artifacts, ULTRA consistently disregards these artifacts and focuses primarily on lesion information, resulting in accurate predictions of DR severity with high confidence. Based on our observation on cases shown in Figure 7A, we found that proposed model pays more attention to lesion information, despite the presence of interfering factors such as eyelash artifacts, resulting in accurate predictions of DR severity with high confidence. However, at times, these interfering factors can cause confusion, as evident in Figure 7B. These misclassifications typically occur in the No DR or NPDRI stages, where the model lacks sufficient reliable attention and tends to prioritize peripheral artifacts, mistakenly identifying them as lesions, particularly in the vicinity of eyelashes. Notably, in the first example, the optic disc may be misinterpreted as exudates or a large hemorrhage, and the intersection between the eyelashes and eyelid is incorrectly identified, leading to the erroneous classification of the case as NPDRIII instead of No DR. In the third example, a PDR image is incorrectly diagnosed as NPDRIII primarily due to the failure in accurately identifying the patchy hemorrhage in the image. It also shows that our proposed use of a lesion prior as one of the classification features is feasible, and there is reason to believe that as lesion performance improves in future work, our model will be able to more accurately identify the degree of DR severity.

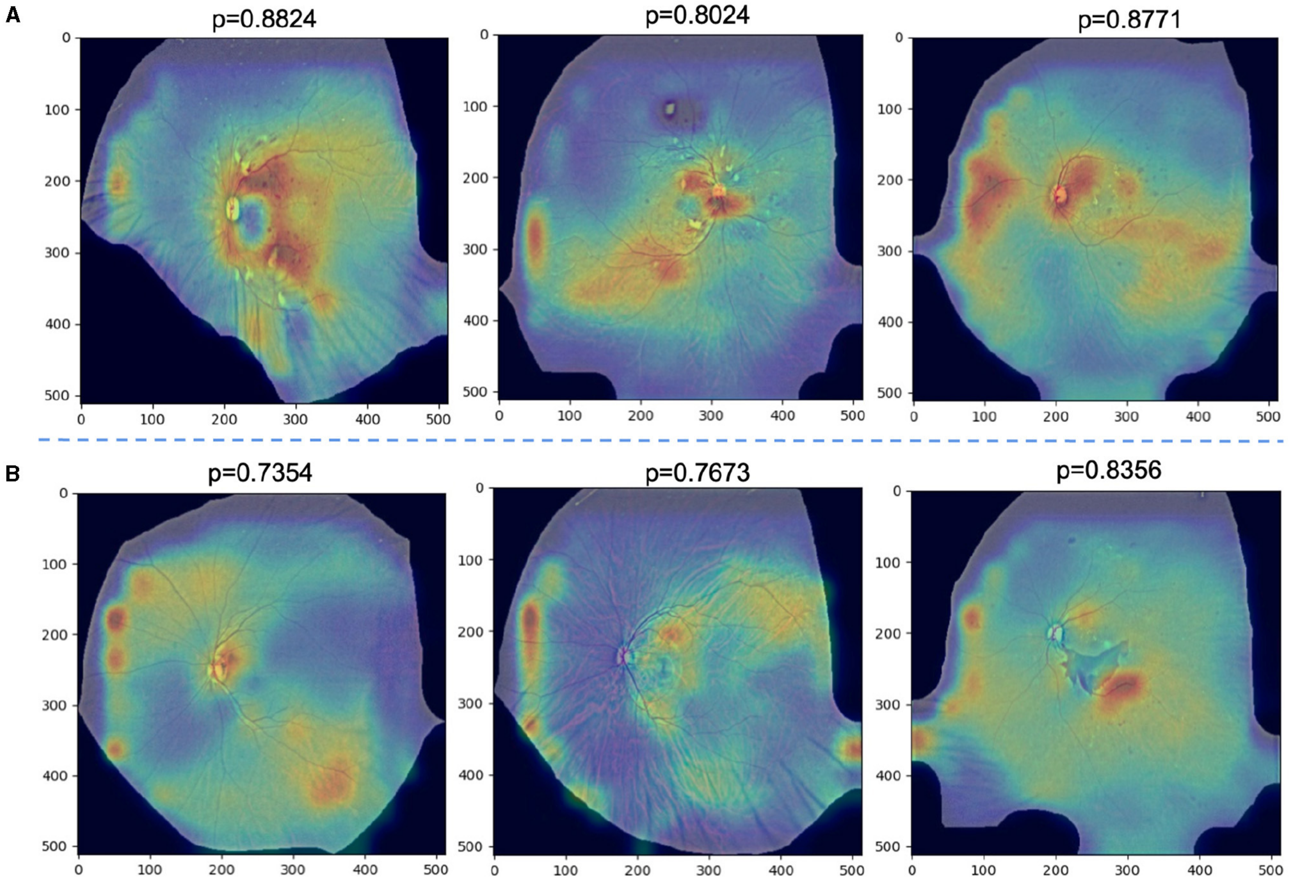

FIGURE 7
(A) Examples of successfully ignored the artifact model and instead focused on specific lesions and correctly identified the degree of DR severity with a high confidence rate. **(B)** Examples of misclassifications.

5.3 Conclusion

In this work, we designed a specific approach and strategies to solve the above mentioned issues. Specifically, we proposed a novel DR grading network for unsupervised lesion-aware domain adaptation in UWF images. Our approach tackles the task of grading DR by leveraging unsupervised domain adaptation techniques while explicitly considering the presence of lesions. By incorporating lesion-specific knowledge into the model, we aimed to improve its ability to generalize across different domains and accurately grade UWF images. To achieve this, we developed a comprehensive framework that combines DA strategies with lesion-aware mechanisms. By leveraging unsupervised learning techniques, our approach can effectively adapt the grading model from a source domain (e.g., CFP images) to a target domain (e.g., UWF images) without the need for labeled data in the target domain. Moreover, our framework incorporates lesion-aware mechanisms, such as the Lesion Embedding Attention Module (LEAM), to ensure that the model can effectively capture and exploit the discriminative information present in lesion regions. By integrating these novel components and adopting a holistic approach, our proposed method aims to address the challenges associated with domain shift and the unique characteristics of UWF images in DR grading. Through experimental evaluations and comparisons, we demonstrate the effectiveness and superiority of our approach in accurately grading UWF images, thus contributing to improved diagnosis and management of diabetic retinopathy.

Data availability statement

Publicly available datasets were analyzed in this study. This data can be found here: https://www.kaggle.com/c/diabetic-retinopathy-detection/overview.

Ethics statement

The studies involving humans were approved by Eye Pricture Archive Communication System. The studies were conducted in accordance with the local legislation and institutional requirements. The participants provided their written informed consent to participate in this study.

Author contributions

TC: Writing – original draft, Writing – review & editing, Supervision, Validation. YB: Writing – original draft, Writing – review & editing, Data curation, Software. HM: Writing – original draft, Writing – review & editing, Project administration. SL: Writing – original draft, Writing – review & editing, Formal analysis. KX: Writing – original draft, Writing – review & editing, Visualization. ZX: Writing – original draft, Writing – review & editing, Funding acquisition. SM: Writing – original draft, Writing – review & editing, Formal analysis. FY: Writing – original draft, Writing – review & editing. YZ: Writing – original draft, Writing – review & editing.

Funding

The author(s) declare that no financial support was received for the research, authorship, and/or publication of this article.

Conflict of interest

The authors declare that the research was conducted in the absence of any commercial or financial relationships that could be construed as a potential conflict of interest.

Publisher's note

References

1. Yong JK, Kim BH, Bo MC, Sun HJ, Choi KS. Bariatric surgery is associated with less progression of diabetic retinopathy: a systematic review and meta-analysis. *Surg Obes Relat Dis*. (2017) 13:352. doi: 10.1016/j.soard.2016.10.002

2. Torres-Villaros H, Fajnkuchen F, Amari F, Janicot L. Giocanti-Aurégan A. Comparison of Ultra-Wide Field Photography to Ultra-Wide Field Angiography for the Staging of Sickle Cell Retinopathy. *J Clini Med*. (2022) 11:936. doi: 10.3390/jcm11040936

3. Kiss S, Berenberg TL. Ultra widefield fundus imaging for diabetic retinopathy. *Curr Diab Rep*. (2014) 14:1–7. doi: 10.1007/s11892-014-0514-0

4. Ju L, Wang X, Zhou Q, Zhu H, Harandi M, Bonnington P, et al. Bridge the domain gap between ultra-wide-field and traditional fundus images via adversarial domain adaptation. *arXiv*. (2020) [Preprint]. arXiv:2003.10042. doi: 10.48550/arXiv.2003.10042

5. Nagiel A, Lalane RA, Sadda SR, Schwartz SD. Ultra-widefield fundus imaging: a review of clinical applications and future trends. *Retina*. (2016) 36:660–78. doi: 10.1097/IAE.0000000000000937

6. Singh RP, Hsueh J, Han MM, Kuriyan AE, Conti FF, Steinle N, et al. Protecting vision in patients with diabetes with ultra-widefield imaging: a review of current literature. *Ophthal Surg Lasers Imag Retina*. (2019) 50:639–48. doi: 10.3928/23258160-20191009-07

7. Ju L, Wang X, Zhao X, Bonnington P, Drummond T, Ge Z. Leveraging regular fundus images for training UWF fundus diagnosis models via adversarial learning and pseudo-labeling. *IEEE Trans Med Imaging*. (2021). doi: 10.1109/TMI.2021.3056395

8. Rasmussen ML, Broe R, Frydkjaer-Olsen U, Olsen BS, Mortensen HB, Peto T, et al. Comparison between Early Treatment Diabetic Retinopathy Study 7-field retinal photos and non-mydriatic, mydriatic and mydriatic steered widefield scanning laser ophthalmoscopy for assessment of diabetic retinopathy. *J Diabetes Complications*. (2015) 29:99–104. doi: 10.1016/j.jdiacomp.2014.08.009

9. Silva PS, Cavallerano JD, Tolls D, Omar A, Thakore K, Patel B, et al. Potential efficiency benefits of nonmydriatic ultrawide field retinal imaging in an ocular telehealth diabetic retinopathy program. *Diabetes Care*. (2014) 37:50–5. doi: 10.2337/dc13-1292

10. Silva PS, Cavallerano JD, Sun JK, Soliman AZ, Aiello LM, Aiello LP. Peripheral lesions identified by mydriatic ultrawide field imaging: distribution and potential impact on diabetic retinopathy severity. *Ophthalmology*. (2013) 120:2587–95. doi: 10.1016/j.ophtha.2013.05.004

11. Ting D, Cheung YL, Lim G, Tan G, Quang ND, Gan A, et al. Development and validation of a deep learning system for diabetic retinopathy and related eye diseases using retinal images from multiethnic populations with diabetes. *JAMA*. (2017) 318:2211. doi: 10.1001/jama.2017.18152

12. Sayres R, Taly A, Rahimy E, Blumer K, Coz D, Hammel N, et al. Using a deep learning algorithm and integrated gradients explanation to assist grading for diabetic retinopathy. *Ophthalmology*. (2018). doi: 10.1016/j.ophtha.2018.11.016

13. Foo A, Hsu W, Lee ML, Lim G, Wong TY. Multi-task learning for diabetic retinopathy grading and lesion segmentation. *Proc AAAI Conf Artif Intellig*. (2020) 34:13267–72. doi: 10.1609/aaai.v34i08.7035

14. Sun R, Li Y, Zhang T, Mao Z, Wu F, Zhang Y. Lesion-aware transformers for diabetic retinopathy grading. In: *Proceedings of the IEEE/CVF Conference on Computer Vision and Pattern Recognition*. (2021). p. 10938–10947.

15. Abdelmaksoud E, El-Sappagh S, Barakat S, Abuhmed T, Elmogy M. Automatic diabetic retinopathy grading system based on detecting multiple retinal lesions. *IEEE Access*. (2021) 9:15939–60. doi: 10.1109/ACCESS.2021.3052870

16. Zhou Y, He X, Huang L, Liu L, Zhu F, Cui S, et al. Collaborative learning of semi-supervised segmentation and classification for medical images. In: *Proceedings of the IEEE/CVF Conference on Computer Vision and Pattern Recognition*. (2019). p. 2079–2088.

17. Zhao Y, Zhang J, Pereira E, Zheng Y, Su P, Xie J, et al. Automated tortuosity analysis of nerve fibers in corneal confocal microscopy. *IEEE Trans Med Imaging*. (2020) 39:2725–37. doi: 10.1109/TMI.2020.2974499

18. Emma Dugas J, Jorge WC. *Diabetic Retinopathy Detection*. Kaggle (2015). Available online at: https://kaggle.com/competitions/diabetic-retinopathy-detection

19. Porwal P, Pachade S, Kamble R, Kokare M, Deshmukh G, Sahasrabuddhe V, et al. Indian diabetic retinopathy image dataset (IDRiD): a database for diabetic retinopathy screening research. *IEEE Dataport*. (2018) 3:25. doi: 10.21227/H25W98

20. Lim G, Bellemo V, Xie Y, Lee XQ, Yip MY, Ting DS. Different fundus imaging modalities and technical factors in AI screening for diabetic retinopathy: a review. *Eye and Vision*. (2020) 7:1–13. doi: 10.1186/s40662-020-00182-7

21. Oh K, Kang HM, Leem D, Lee H, Seo KY, Yoon S. Early detection of diabetic retinopathy based on deep learning and ultra-wide-field fundus images. *Sci Rep*. (2021) 11:1897. doi: 10.1038/s41598-021-81539-3

22. Liu R, Wang X, Wu Q, Dai L, Fang X, Yan T, et al. Deepdrid: Diabetic retinopathy grading and image quality estimation challenge. *Patterns*. (2022) 3:100512. doi: 10.1016/j.patter.2022.100512

23. Ahn E, Kumar A, Fulham M, Feng D, Kim J. Unsupervised domain adaptation to classify medical images using zero-bias convolutional auto-encoders and context-based feature augmentation. *IEEE Trans Med Imaging*. (2020) 39:2385–94. doi: 10.1109/TMI.2020.2971258

24. Chen C, Dou Q, Chen H, Heng PA. Semantic-aware generative adversarial nets for unsupervised domain adaptation in chest x-ray segmentation. In: *Machine Learning in Medical Imaging: 9th International Workshop, MLMI 2018, Held in Conjunction with*

MICCAI 2018, Granada, Spain, September 16, 2018, Proceedings 9. Cham: Springer. (2018). p. 143–151.

25. Du Z, Li J, Su H, Zhu L, Lu K. Cross-domain gradient discrepancy minimization for unsupervised domain adaptation. In: *Proceedings of the IEEE/CVF Conference on Computer Vision and Pattern Recognition*. (2021). p. 3937–3946.

26. Bai Y, Hao J, Fu H, Hu Y, Ge X, Liu J, et al. Unsupervised lesion-aware transfer learning for diabetic retinopathy grading in ultra-wide-field fundus photography. In: *Medical Image Computing and Computer Assisted Intervention-MICCAI 2022: 25th International Conference, Singapore, September 18-22, 2022, Proceedings, Part II*. Cham: Springer. (2022). p. 560–570.

27. Spaide RF. Peripheral areas of nonperfusion in treated central retinal vein occlusion as imaged by wide-field fluorescein angiography. *Retina*. (2011) 31:829–37. doi: 10.1097/IAE.0b013e31820c841e

28. Nagasato D, Tabuchi H, Ohsugi H, Masumoto H, Enno H, Ishitobi N, et al. Deep neural network-based method for detecting central retinal vein occlusion using ultrawide-field fundus ophthalmoscopy. *J Ophthalmol*. (2018) 2018:1–6. doi: 10.1155/2018/1875431

29. Cho M, Kiss S. Detection and monitoring of sickle cell retinopathy using ultra wide-field color photography and fluorescein angiography. *Retina*. (2011) 31:738–47. doi: 10.1097/IAE.0b013e3181f049ec

30. Giocanti-Aurégan A, Fajnkuchen F, Amari F, Bodaghi B, Giocanti-Aurégan A. Comparison between ultrawidefield and 7-standard field angiography for proliferative sickle cell retinopathy screening, follow-up and classification. *J Ophthalmol Clin Res*. (2019) 6:1–5.

31. Bonnay G, Nguyen F, Meunier I, Ducasse A, Hamel C, Arndt C. Screening for retinal detachment using wide-field retinal imaging. *J Francais Dophtalmologie*. (2011) 34:482–5. doi: 10.1016/j.jfo.2011.02.012

32. Ohsugi H, Tabuchi H, Enno H, Ishitobi N. Accuracy of deep learning, a machine-learning technology, using ultra wide-field fundus ophthalmoscopy for detecting rhegmatogenous retinal detachment. *Scient Rep*. (2017) 7:9425. doi: 10.1038/s41598-017-09891-x

33. Nagasawa T, Tabuchi H, Masumoto H, Enno H, Niki M, Ohara Z, et al. Accuracy of ultrawide-field fundus ophthalmoscopy-assisted deep learning for detecting treatment-naive proliferative diabetic retinopathy. *Int Ophthalmol*. (2019) 39:2153–9. doi: 10.1007/s10792-019-01074-z

34. Nagasawa T, Tabuchi H, Masumoto H, Morita S, Niki M, Ohara Z, et al. Accuracy of diabetic retinopathy staging with a deep convolutional neural network using ultra-wide-field fundus ophthalmoscopy and optical coherence tomography angiography. *J Ophthalmol*. (2021) 2021:6651175. doi: 10.1155/2021/6651175

35. Liu H, Teng L, Fan L, Sun Y, Li H. A new ultra-wide-field fundus dataset to diabetic retinopathy grading using hybrid preprocessing methods. *Comput Biol Med*. (2023) 157:106750. doi: 10.1016/j.compbiomed.2023.106750

36. Levenkova A, Sowmya A, Kalloniatis M, Ly A, Ho A. Automatic detection of diabetic retinopathy features in ultra-wide field retinal images. In: *Medical Imaging 2017: Computer-Aided Diagnosis. vol. 10134*. Bellingham: SPIE. (2017). p. 409–416.

37. You K, Long M, Cao Z, Wang J, Jordan MI. Universal domain adaptation. In: *2019 IEEE/CVF Conference on Computer Vision and Pattern Recognition (CVPR) (IEEE)*. Cham: Springer (2019). p. 2715–24.

38. Kundu JN, Venkat N, Rahul M, Babu RV. Universal source-free domain adaptation. In: *2020 IEEE/CVF Conference on Computer Vision and Pattern Recognition (CVPR) (IEEE)*. IEEE Computer Society (2020). p. 4543–52.

39. Chen M, Weinberger KQ, Blitzer JC. Co-training for domain adaptation. In: *Proceedings of the 24th International Conference on Neural Information Processing Systems*. Red Hook, NY: Curran Associates Inc. (2011). p. 2456–64.

40. Wang M, Deng W. Deep visual domain adaptation: a survey. *Neurocomputing*. (2018) 312:135–53. doi: 10.1016/j.neucom.2018.05.083

41. Ribani R, Marengoni M. A survey of transfer learning for convolutional neural networks. In: *2019 32nd SIBGRAPI Conference on Graphics, Patterns and Images Tutorials (SIBGRAPI-T)*. Rio de Janeiro: IEEE. (2019). p. 47–57.

42. Tan C, Sun F, Kong T, Zhang W, Yang C, Liu C. A survey on deep transfer learning. In: *Artificial Neural Networks and Machine Learning-ICANN 2018: 27th International Conference on Artificial Neural Networks, Rhodes, Greece, October 4-7, 2018, Proceedings, Part III 27*. Cham: Springer. (2018). p. 270–279.

43. Kang G, Jiang L, Yang Y, Hauptmann A. Contrastive adaptation network for unsupervised domain adaptation. In: *2019 IEEE/CVF Conference on Computer Vision and Pattern Recognition (CVPR)*. Long Beach, CA: IEEE Computer Society (2019). p. 4888–97.

44. Wang W, Ma L, Chen M, Du Q. Joint correlation alignment-based graph neural network for domain adaptation of multitemporal hyperspectral remote sensing images. *IEEE J Selected Topics Appl Earth Observat Remote Sens*. (2021) 14:3170–84. doi: 10.1109/JSTARS.2021.3063460

45. Pei Z, Cao Z, Long M, Wang J. Multi-adversarial domain adaptation. In: *Proceedings of the Thirty-Second AAAI Conference on Artificial Intelligence and Thirtieth Innovative Applications of Artificial Intelligence Conference and Eighth AAAI Symposium on Educational Advances in Artificial Intelligence*. Washington, DC: AAAI Press (2018). p. 3934–41.

46. Long M, Cao Z, Wang J, Jordan MI. Conditional adversarial domain adaptation. In: *Proceedings of the 32nd International Conference on Neural Information Processing Systems*. Red Hook, NY: Curran Associates Inc. (2018). p. 1647–57.

47. Zhuang F, Cheng X, Luo P, Pan SJ, He Q. Supervised representation learning: transfer learning with deep autoencoders. In: *Twenty-fourth International Joint Conference on Artificial Intelligence*. Washington, DC: AAAI Press (2015).

48. Zheng H, Fu J, Mei T, Luo J. Learning multi-attention convolutional neural network for fine-grained image recognition. In: *2017 IEEE International Conference on Computer Vision (ICCV)*. Venice: IEEE Computer Society (2017). p. 5219–27.

49. Yi Z, Zhang H, Tan P, Gong M. Dualgan: Unsupervised dual learning for image-to-image translation. In: *Proceedings of the IEEE International Conference on Computer Vision*. (2017). p. 2849–2857.

50. Kim T, Cha M, Kim H, Lee JK, Kim J. Learning to discover cross-domain relations with generative adversarial networks. In: *International Conference on Machine Learning*. New York: PMLR. (2017). p. 1857–1865.

51. Peng S, Zeng R, Cao L, Yang A, Niu J, Zong C, et al. Multi-source domain adaptation method for textual emotion classification using deep and broad learning. *Knowl-Based Syst*. (2023) 260:110173. doi: 10.1016/j.knosys.2022.110173

52. Hsu HK, Yao CH, Tsai YH, Hung WC, Tseng HY, Singh M, et al. Progressive domain adaptation for object detection. In: *Proceedings of the IEEE/CVF Winter Conference on Applications of Computer Vision*. IEEE Computer Society (2020). p. 749–57.

53. Cao J, Tang H, Fang HS, Shen X, Lu C, Tai YW. Cross-domain adaptation for animal pose estimation. In: *2019 IEEE/CVF International Conference on Computer Vision (ICCV)*. IEEE Computer Society (2019). p. 9497–506.

54. Kamnitsas K, Baumgartner C, Ledig C, Newcombe V, Simpson J, Kane A, et al. Unsupervised domain adaptation in brain lesion segmentation with adversarial networks. In: *International Conference on Information Processing in Medical Imaging*. Cham: Springer. (2017). p. 597–609.

55. Chai Z, Zhou K, Yang J, Ma Y, Chen Z, Gao S, et al. Perceptual-assisted adversarial adaptation for choroid segmentation in optical coherence tomography. In: *2020 IEEE 17th International Symposium on Biomedical Imaging (ISBI)*. Iowa City, IA: IEEE. (2020). p. 1966–1970.

56. Dong J, Cong Y, Sun G, Zhong B, Xu X. What can be transferred: Unsupervised domain adaptation for endoscopic lesions segmentation. In: *Proceedings of the IEEE/CVF Conference on Computer Vision and Pattern Recognition*. (2020). p. 4023–4032.

57. Kadambi S, Wang Z, Xing E, WGAN. domain adaptation for the joint optic disc-and-cup segmentation in fundus images. *Int J Comput Assist Radiol Surg*. (2020) 15:1205–13. doi: 10.1007/s11548-020-02144-9

58. Zhang Y, Wei Y, Wu Q, Zhao P, Niu S, Huang J, et al. Collaborative unsupervised domain adaptation for medical image diagnosis. *IEEE Trans Image Proc*. (2020) 29:7834–44. doi: 10.1109/TIP.2020.3006377

59. Zhou Y, Wang B, Huang L, Cui S, Shao L, A. benchmark for studying diabetic retinopathy: segmentation, grading, and transferability. *IEEE Trans Med Imaging*. (2020) 40:818–28. doi: 10.1109/TMI.2020.3037771

60. Cao P, Hou Q, Song R, Wang H, Zaiane O. Collaborative learning of weakly-supervised domain adaptation for diabetic retinopathy grading on retinal images. *Comput Biol Med*. (2022) 144:105341. doi: 10.1016/j.compbiomed.2022.105341

61. Song R, Cao P, Yang J, Zhao D, Zaiane OR. A domain adaptation multi-instance learning for diabetic retinopathy grading on retinal images. In: *2020 IEEE International Conference on Bioinformatics and Biomedicine (BIBM)*. Seoul: IEEE. (2020). p. 743–750.

62. He K, Zhang X, Ren S, Sun J. Deep residual learning for image recognition. In: *2016 IEEE Conference on Computer Vision and Pattern Recognition (CVPR)*. IEEE Computer Society (2016). p. 70–8.

63. Xiao X, Lian S, Luo Z, Li S. Weighted res-unet for high-quality retina vessel segmentation. In: *2018 9th International Conference on Information Technology in Medicine and Education (ITME)*. Hangzhou: IEEE. (2018). p. 327–331.

64. Hou Q, Lu CZ, Cheng MM, Feng J. Conv2former: a simple transformer-style ConvNet for visual recognition. *arXiv*. (2022) [Preprint]. arXiv:2211.11943. doi: 10.48550/arXiv.2211.11943

65. Petit O, Thome N, Rambour C, Themyr L, Collins T, Soler L. U-net transformer: self and cross attention for medical image segmentation. In: *Machine Learning in Medical Imaging: 12th International Workshop, MLMI 2021, Held in Conjunction with MICCAI 2021, Strasbourg, France, September 27, 2021, Proceedings 12*. Cham: Springer. (2021). p. 267–276.

66. Fu J, Liu J, Tian H, Li Y, Bao Y, Fang Z, et al. Dual attention network for scene segmentation. In: *Proceedings of the IEEE/CVF Conference on Computer Vision and Pattern Recognition*. (2019). p. 3146-3154.

67. Yushkevich PA, Gao Y, Gerig G. ITK-SNAP: An interactive tool for semi-automatic segmentation of multi-modality biomedical images. In: *2016 38th Annual International Conference of the IEEE Engineering in Medicine and Biology Society (EMBC)*. New York: IEEE (2016). p. 3342–3345.

68. Van Grinsven MJ, van Ginneken B, Hoyng CB, Theelen T. Sánchez CI. Fast convolutional neural network training using selective data

sampling: Application to hemorrhage detection in color fundus images. *IEEE Trans Med Imag.* (2016) 35:1273–84. doi: 10.1109/TMI.2016.2526689

69. Bousmalis K, Trigeorgis G, Silberman N, Krishnan D, Erhan D. Domain separation networks. In: *Advances in Neural Information Processing Systems*. Red Hook, NY: Curran Associates Inc. (2016). p. 29.

70. Tzeng E, Hoffman J, Saenko K, Darrell T. Adversarial discriminative domain adaptation. In: *2017 IEEE Conference on Computer Vision and Pattern Recognition (CVPR).* Honolulu, HI: IEEE (2017). p. 2962–71.

71. Saito K, Watanabe K, Ushiku Y, Harada T. Maximum classifier discrepancy for unsupervised domain adaptation. In: *2018 IEEE/CVF Conference on Computer Vision and Pattern Recognition*. IEEE (2018). p. 3723–32.

72. Xiao N, Zhang L. Dynamic weighted learning for unsupervised domain adaptation. In: *2021 IEEE/CVF Conference on Computer Vision and Pattern Recognition (CVPR).* Nashville, TN: IEEE (2021). p. 15237–46.

73. Simonyan K, Zisserman A. Very deep convolutional networks for large-scale image recognition. *arXiv.* (2014) [Preprint]. arXiv:1409.1556. doi: 10.48550/arXiv.1409.1556

frontiers | Frontiers in Medicine

TYPE Original Research
PUBLISHED 07 August 2024
DOI 10.3389/fmed.2024.1418048

OPEN ACCESS

EDITED BY
Shida Chen,
Sun Yat-sen University, China

REVIEWED BY
Jiàn xióng,
Second Affiliated Hospital of Nanchang University, China
Guoming Zhang,
Shenzhen Eye Hospital, China

*CORRESPONDENCE
Shengzhan Wang
✉ wangshengzhan886@163.com
Kai Jin
✉ jinkai@zju.edu.cn
Juan Ye
✉ yejuan@zju.edu.cn

RECEIVED 15 April 2024
ACCEPTED 23 July 2024
PUBLISHED 07 August 2024

CITATION
Wang S, Shen W, Gao Z, Jiang X, Wang Y, Li Y, Ma X, Wang W, Xin S, Ren W, Jin K and Ye J (2024) Enhancing the ophthalmic AI assessment with a fundus image quality classifier using local and global attention mechanisms.
Front. Med. 11:1418048.
doi: 10.3389/fmed.2024.1418048

Enhancing the ophthalmic AI assessment with a fundus image quality classifier using local and global attention mechanisms

Shengzhan Wang[1]*, Wenyue Shen[2], Zhiyuan Gao[2], Xiaoyu Jiang[3], Yaqi Wang[4], Yunxiang Li[5], Xiaoyu Ma[6], Wenhao Wang[1], Shuanghua Xin[1], Weina Ren[1], Kai Jin[2]* and Juan Ye[2]*

[1]The Affiliated People's Hospital of Ningbo University, Ningbo, Zhejiang, China, [2]Eye Center, School of Medicine, The Second Affiliated Hospital, Zhejiang University, Hangzhou, Zhejiang, China, [3]College of Control Science and Engineering, Zhejiang University, Hangzhou, China, [4]College of Media, Communication University of Zhejiang, Hangzhou, China, [5]College of Computer Science and Technology, Hangzhou Dianzi University, Hangzhou, China, [6]Institute of Intelligent Media, Communication University of Zhejiang, Hangzhou, China

Background: The assessment of image quality (IQA) plays a pivotal role in the realm of image-based computer-aided diagnosis techniques, with fundus imaging standing as the primary method for the screening and diagnosis of ophthalmic diseases. Conventional studies on fundus IQA tend to rely on simplistic datasets for evaluation, predominantly focusing on either local or global information, rather than a synthesis of both. Moreover, the interpretability of these studies often lacks compelling evidence. In order to address these issues, this study introduces the Local and Global Attention Aggregated Deep Neural Network (LGAANet), an innovative approach that integrates both local and global information for enhanced analysis.

Methods: The LGAANet was developed and validated using a Multi-Source Heterogeneous Fundus (MSHF) database, encompassing a diverse collection of images. This dataset includes 802 color fundus photography (CFP) images (302 from portable cameras), and 500 ultrawide-field (UWF) images from 904 patients with diabetic retinopathy (DR) and glaucoma, as well as healthy individuals. The assessment of image quality was meticulously carried out by a trio of ophthalmologists, leveraging the human visual system as a benchmark. Furthermore, the model employs attention mechanisms and saliency maps to bolster its interpretability.

Results: In testing with the CFP dataset, LGAANet demonstrated remarkable accuracy in three critical dimensions of image quality (illumination, clarity and contrast based on the characteristics of human visual system, and indicates the potential aspects to improve the image quality), recording scores of 0.947, 0.924, and 0.947, respectively. Similarly, when applied to the UWF dataset, the model achieved accuracies of 0.889, 0.913, and 0.923, respectively. These results underscore the efficacy of LGAANet in distinguishing between varying degrees of image quality with high precision.

Conclusion: To our knowledge, LGAANet represents the inaugural algorithm trained on an MSHF dataset specifically for fundus IQA, marking a significant milestone in the advancement of computer-aided diagnosis in ophthalmology. This research significantly contributes to the field, offering a novel methodology for the assessment and interpretation of fundus images in the detection and diagnosis of ocular diseases.

KEYWORDS

fundus photography, attention mechanism, image quality assessment, spatial information, multiscale feature extraction

Introduction

Fundus photography stands as a cornerstone in the diagnosis of diabetic retinopathy (DR), glaucoma, age-related macular degeneration (AMD), among various ocular disorders (1). With the advent of artificial intelligence (AI), the automation of disease screening through fundus imaging has emerged as a focal area of research and clinical application (2). Several algorithms have been explored, with a notable number being translated into clinical settings (3–5). The quality of fundus images is critical to the diagnostic accuracy of these models, necessitating a robust Image Quality Assessment (IQA) for automated systems.

Manual IQA, though reliable, places a significant burden on medical professionals which requires direct assessment of images to ensure pathological structures are discernibly visible. Conversely, automated IQA methods offer a less labor-intensive alternative, utilizing algorithms to evaluate image quality. These methods range from structure-analysis-based to generic image-statistics approaches (6). In the era of deep learning, innovations in IQA have significantly benefited from the advanced feature-extraction capabilities of convolutional neural networks (CNNs) (7–9), employing strategies such as hallucinated reference generation and distortion identification to enhance quality prediction and feature weighting through visual saliency (10). DeepFundus, a deep learning-based fundus image classifier, addresses the data quality gap in medical AI by offering automated, multidimensional image sorting, significantly enhancing model performance across various retinopathies and supporting a data-driven paradigm for the entire medical AI lifecycle (11).

Despite these advancements, challenges persist, particularly in the generalizability of algorithms across diverse imaging conditions and the integration of both local and global information critical for comprehensive quality assessment. Furthermore, the interpretability of deep learning models in this context remains uncertain. In order to fill these gaps, this study introduces the Local and Global Attention Aggregated Deep Neural Network (LGAANet), designed to leverage both local and global information in assessing the quality of fundus images. Most existing IQA datasets are single-center collections that overlook variations in imaging devices, eye conditions, and imaging environments. Our approach involves training on a multi-source heterogeneous fundus (MSHF) database (12), encompassing a broad spectrum of normal and pathological images captured through various imaging modalities, to enhance the model's generalizability and interpretability. This database was selected due to its diverse and representative nature, which allows for robust validation of the LGAANet model across various imaging conditions and sources.

Materials and methods

An overview of the study approach and methodology is presented in Figure 1. Our MSHF dataset consisted of various sub-databases collected from different devices and exhibited diverse appearance patterns. The dataset comprises 802 color fundus photography (CFP) images (302 from portable fundus cameras) and 500 ultrawide-field (UWF) images. These images originate from 904 patients, encompassing DR and glaucoma patients, in addition to normal individuals. Such samples collected via various domains are capable of providing more diversity during training of CNNs, which is beneficial for improving the generalization ability of models. Three critical dimensions of image quality: the illumination, clarity and contrast are selected based on the characteristics of human visual system, and indicates the potential aspects to improve the image quality. In order to validate the performance of our approach, we used an external dataset and noise dataset. A detailed description of each stage follows.

The spatial-information-retained multi-scale feature extractor

Multi-scale features and spatial attention mechanisms have shown potential for quality prediction (13–19). However, existing multi-scale-feature-incorporated quality-prediction studies tend to leverage Multi-Level Spatially Pooled (MLSP) strategy to aggregate features from various scales, i.e., using Global Average Pooling (GAP) to extract the multi-dimensional activations into a one-dimensional vector and concatenate vectors from various scales. The MLSP method yields one-dimensional vectors and inevitably leaves out much spatial information. Therefore, it is challenging to integrate spatial attention mechanisms into the one-dimensional feature.

In order to improve prediction accuracy and combine both multi-scale features and spatial mechanisms into our quality prediction model, we included a spatial-information-retained (SIR) multi-scale feature extractor to combine both local and global quality-aware features through an attention-incorporated perspective.

Specifically, let X denote the input image with size $[3, H, W]$, and denote the multi-scale feature (Scale#1 to Scale #3) extracted from ResNet50 as:

$$s_i = f(X|Stage_i), i \in \{1, 2, 3\} \tag{1}$$

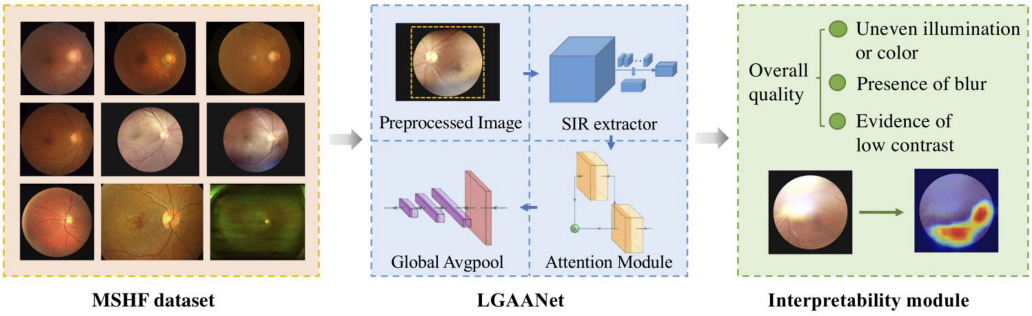

FIGURE 1
An overview of the study approach and methodology. The multi-source heterogeneous fundus (MSHF) dataset is collected, and then serves as an input to train the local and global attention aggregated deep neural network (LGAANet). The output is the image quality of each image based on three metrics, and a heap map is created to show the interpretability.

Where $f(\cdot|Stage_i)$ denotes the activations extracted from the last convolutional layer of ResNet50 in Stage#i. The s_i is rescaled channel-wise via a convolutional layer with kernel size 1x1 and followed by a batch-normalization and a RELU layer, i.e., $s'_i = g(s_i|T^{1,0}_{I_i,O_i})$, in which $g(\cdot|T^{k,p}_{C_{in},C_{out}})$ denotes the convolutional unit mentioned above with kernel size, padding, input channel size C_{in}, and output channel size C_{out}. In the architecture of ResNet50, $[I_1, I_2, I_3] = [256,\ 512,\ 1024]$, and we set $[O_1, O_2, O_3] = [16,\ 32,\ 64]$ to prevent the channel size after concatenation from being too large. Therefore, the size of s'_1, s'_2, s'_3 is $[16, W/4, H/4]$, $[32, W/8, H/8]$, $[64, W/16, H/16]$, respectively.

In order to maintain the detailed spatial information of features extracted from each scale and simultaneously rescale them to coordinate with features extracted from the last Stage of ResNet50 (i.e., Stage#4 with spatial size $[W/32, H/32]$), the s'_1, s'_2, s'_3 are non-overlapped and spatially split into several chunks with spatial size $[W/32, H/32]$, i.e.,:

$$chunk_i = split\left(s'_i\right) = \begin{bmatrix} c^{(i)}_{1,1} & \cdots & c^{(i)}_{1,k_i} \\ \vdots & \ddots & \vdots \\ c^{(i)}_{k_i,1} & \cdots & c^{(i)}_{k_i,k_i} \end{bmatrix} \tag{2}$$

Where $chunk_i$ denotes the set of chunks after spatial split from s'_i, and each of the chunks is denoted as $c^{(i)}_{m,n}$ (m and n denote the spatial index of the chunk) with a channel size coordinated with s'_i and a spatial size of $[W/32, H/32]$. In addition, $k_1 = 64, k_2 = 16, k_3 = 4$.

As for each $chunk_i$, its elements are concatenated channel-wise by,

$$s''_i = concat(\left\{c^{(i)}_{m,n} \middle| m \in k_i, n \in k_i\right\}, dim\ channel\_wise) \tag{3}$$

After this, the size of s''_1, s''_2, s''_3 is $[16{*}64, W/32, H/32]$, $[32{*}16, W/32, H/32]$, $[64{*}4, W/32, H/32]$. Finally, s''_1, s''_2, s''_3 and the activations extracted via $f(\cdot|Stage_4)$ are fed into $g(\cdot|T^{1,0}_{C_{in},128})$ and yield 4 multi-dimensional features with the same size, representing both local and global information. Channel-wise concatenation is then employed to obtain a local spatial-information-retained multi-scale feature with size $[128{*}4, W/32, H/32]$.

The above-described spatial-information-retained multi-scale feature extraction is also illustrated in Figure 2, taking Stage#1 as an example, and the pseudocode is listed in Table 1.

LGAANet

Based on the proposed SIR multi-scale feature extractor, we developed the LGAANet, as shown in Figure 3. Our LGAANet is comprised of a ResNet50-based SIR multi-scale feature extractor $f(\cdot;\theta)$, an attention module $Att(\cdot;\gamma)$, and a feature-aggregation module $g(\cdot;\delta)$. Let X denote the input image; the final quality prediction $\hat{q}$ is obtained via,

$$\hat{q} = g(f(X;\theta) \times att\left(f(X;\theta);\gamma\right);\delta) \tag{4}$$

Since the quality label q is binary, the loss to be optimized, denoted as L, is calculated by,

$$L = BCE(Sigmoid\left(\hat{q}\right), q) \tag{5}$$

Where $Sigmoid(\cdot)$ denotes the Sigmoid layer and $BCE(\cdot)$ denotes the binary cross-entropy.

The attention mechanism could be implemented via various CNN architectures. Here spatial attention [denoted as BaseLine (BL) + SpatialAtt + MultiScale (MS)] and self-attention (denoted as BL+SelfAtt+MS) are leveraged to learn the spatial weighting strategy for multi-scale quality-aware features. The spatial attention is implemented by several stacks of convolutional-batch normalization-RELU units while the self-attention is following (20). Also, we constructed a multi-scale excluded and attention-incorporated CNN framework for the ablation study, denoted as BL+SpatialAtt.

For the sake of comparison, we considered the BL in the performance comparison, in which the feature extracted from ResNet50 was directly fed into a GAP followed by stacks of the fully-connected layer. The MASK-incorporated model is also involved (denoted as BL+MASK) and has an overall pipeline similar to the BL, but the extracted features are multiplied elemental-wise with the MASK signal before being fed into the GAP layer.

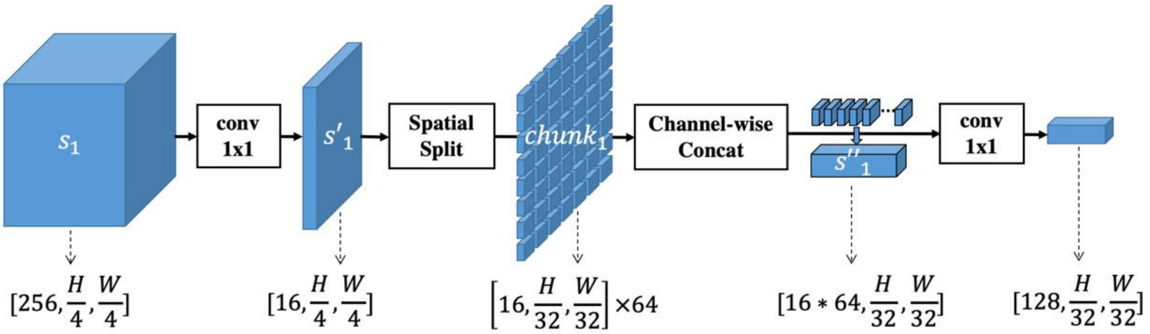

FIGURE 2
Illustration of spatial-information-retained (SIR) multi-scale feature extraction. The activations extracted from Stage#1 of ResNet50, denoted as s_1, are first rescaled into s'_1 by a convolutional layer with kernel size 1x1. Then s'_1 is spatially split into multiple chunks whose spatial size is coordinated with the features extracted from Stage#4 of ResNet50. The chunks are concatenated into s''_1 and rescaled to a size of [128, $H/32$, $W/32$]. In this way, the spatial information of multi-scale features is retained while the feature size within each scale is consistent.

Network hyperparameters: the minibatch size is 8, and the learning rate is 1e-3. The optimizer is Adam, and the weight-decay is 5e-4. The ratio of the learning rate of the ResNet model parameters to the subsequent newly added layer is 1:10; that is, the learning rate of the newly added layer is 1e-3, and of the ResNet layer is 1e-4. The training process traverses the training data in the database 20 times, which means the epoch = 20, and the highest test accuracy is selected as the final result. The division of training-test samples is randomly generated (a total of two, namely round = 2). The image index being used for training/testing is in the supplementary files teIdx01.mat (first test index), trIdx01.mat (first-time training index), teIdx02.mat (second test index), trIdx02.mat (second training index). The host configuration is i7-8700 CPU @3.2GHz & 32GB RAM + GTX1080@8GB.

To facilitate the development of deep learning models using the MSHF dataset, it was manually segmented into an 80% training set and a 20% test set. The training set facilitated model learning, while the test set served for performance evaluation. There was no overlap between these two sets, ensuring a fair distribution of image variety. Each set maintained an approximately equal proportion of high- and low-quality images.

Statistical methods

For statistical validation, we employed a stratified 5-fold cross-validation technique to ensure that each subset of data was representative of the overall distribution, thus mitigating any potential bias due to imbalanced data. This method involved dividing the data into 5 of folds, each containing an equal proportion of images from different categories and quality levels, ensuring that each fold was used once as a test set while the others served as the training set. We utilized the Receiver Operating Characteristic (ROC) curve to evaluate the sensitivity and specificity of LGAANet across different thresholds of classification.

TABLE 1 Pseudocode of spatial-information-retained multi-scale feature extractor.

```
Let $X$ denote the input image
Step1. Extract multi-scale feature $s_i$, $i = \{1, 2, 3\}$ from ResNet50 according to Equation 1
Step2. For each scale $i$:
    Rescale $s_i$ via $s'_i = g(s_i | T^{1,0}_{I_i, O_i})$ channel-wise
    Spatially split $s_i$ into $chunk_i$ according to Equation 2
    Concatenate elements in $chunk_i$ channel-wise according to Equation 3 and obtain $s''_i$
    Rescale $s''_i$ channel-wise via $g(\cdot | T^{1,0}_{C_{in},128})$ according to Equations 4, 5 and obtain $ft_i$
End
Step3. Get $ft_4$ by feeding $f(X | Stage_4)$ into $g(\cdot | T^{1,0}_{C_{in},128})$
Step4. Concatenate $\{ft_i | i \epsilon [1, 4]\}$ channel-wise and obtain the final spatial-information-retained multi-scale feature
```

Results

Experimental settings

We cropped blank areas of each image so that the width and height were equal and then scaled the cropped image to a resolution of 512 × 512. The eye-area mask was obtained through brightness and edge information, which was the alpha channel, denoted as MASK. The prediction model outputs a real value in the range of [0,1], outputs a 0/1 signal through the threshold judgment, and then compares it with the ground truth. In the experiment, the threshold (TH) was selected as 0.5.

Color fundus photography dataset

The dataset annotations are listed in Table 2. For the color fundus photography (CFP) dataset, images with good I/C accounted for 61.0%, while GLU contained 86.5% of the poor I/C images. As for 'blur', the CFP dataset had 58.6% images without

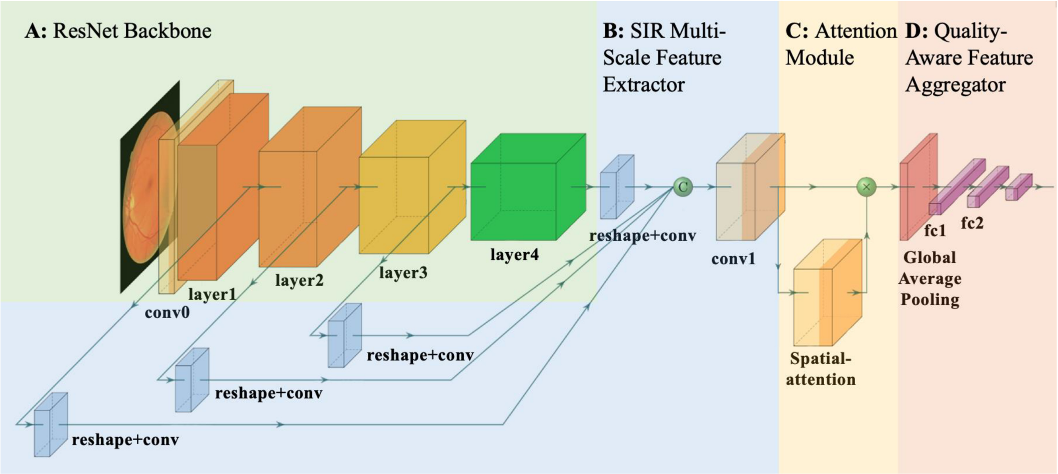

FIGURE 3
Overall pipeline of proposed local and global attention aggregated deep neural network (LGAANet) for quality prediction. **(A)** ResNet50 structure. **(B)** Spatial-information-retained (SIR) multi-scale feature extractor illustrated in Figure 2 and Section Methods-D. The green sphere labeled "C" denotes channel-wise concatenation of SIR features extracted at each scale. **(C)** The attention module is leveraged to learn the spatial weighting strategies and multiplied elemental-wise with the SIR multi-scale feature. **(D)** The global average pooling layer is incorporated and followed by several fully connected layers to aggregate the quality prediction.

TABLE 2 **Dataset annotations.**

Item	I/C		Blur		LC		Overall	
	0	1	0	1	0	1	0	1
LOCAL_1	158	41	94	105	85	114	142	57
LOCAL_2	78	25	59	44	41	62	77	26
DR_1	31	156	34	153	6	181	40	147
DR_2	36	199	120	115	78	157	117	118
GLU	45	7	48	4	42	10	50	2
NORMAL	2	24	0	26	0	26	0	26
DRIMDB	54	140	74	120	76	118	70	124
DRIVE	0	40	0	40	0	40	0	40
DR_UWF	215	285	163	337	50	450	168	332

noticeable blur conditions, where DRIVE and NORMAL datasets had no blurry images. The same thing happened with regard to LC, and 68.3% of the images in the CFP dataset showed eligible contrast. In each aspect, images from LOCAL_1 and LOCAL_2 were inferior to those from DR_1 and DR_2.

Except for the DRIVE database, 80% of the CFP databases were randomly selected as the training set and 20% as the test set. We calculated the average prediction accuracy of the test set, attaining an acceptable result for the baseline; and with the addition of MASK, the accuracy increased to over 0.9. Spatial attention, multiscale, and self-attention algorithms all improved accuracy: BL+SelfAtt+MS achieved the best I/C and blur results, with accuracies of 0.947 and 0.924, respectively, and BL+SpatialAtt+MS produced the best results for LC, with an accuracy of 0.947.

Also, we added Gaussian white noise (Gauss) with a mean of 0 and a variance of 0.05 to images in the CFP datasets to improve the competence of the human visual system (HVS) -based algorithm. We conducted the experiments on each model, and the results showed robust properties, with the best accuracy over 0.85.

ROC curves were drawn to further evaluate the performance of the models, as shown in Figure 4, and the areas under the ROC curves (AUCs) were calculated. For the CFP dataset, the AUC of each model on every item was over 0.95. Detailed information on accuracy and AUCs of the datasets is presented in Tables 3,4, respectively.

Visualization of the prediction is interpreted by heat map, as shown in Figure 5. For high-quality images, the activated area is even and covers the whole image. When an image is suspected of poor quality, such as an area of uneven illumination, the model will not activate the designated area.

Ultra-wide field fundus image dataset

In the UWF dataset, images with good quality accounted for 66.4%. Blurring was less common in UWF images, and the overall contrast was acceptable. The UWF dataset was not exploited for training, and we tested it with the proposed model as an external

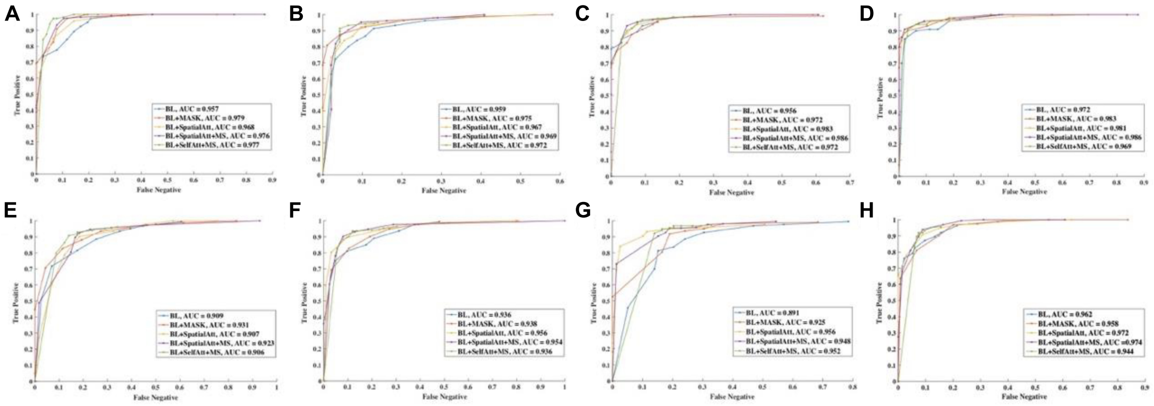

FIGURE 4
ROC curve of different items for **(A–D)** CFP datasets. **(E–H)** UWF datasets. **(A,E)** Detection of uneven illumination or color. **(B,F)** Detection of blur. **(C,G)** Detection of low contrast. **(D,H)** Overall quality.

TABLE 3 **Overall accuracy of different models on various datasets.**

Model	CFP dataset				UWF dataset				Noise dataset			
	I/C	Blur	LC	Overall	I/C	Blur	LC	Overall	I/C	Blur	LC	Overall
BL	0.886	0.874	0.874	0.897	0.826	0.839	0.852	0.876	0.802	0.802	0.819	0.809
+MASK	0.922	0.902	0.917	0.919	0.852	0.862	0.889	0.893	0.819	0.822	0.839	0.826
+SpatialAtt	0.927	0.914	0.929	0.932	0.869	0.899	0.903	0.909	0.832	0.813	0.852	0.849
+SpatialAtt+MS	**0.947**	0.919	**0.947**	**0.944**	0.883	0.909	0.916	**0.926**	0.852	0.856	**0.879**	**0.873**
+SelfAtt+MS	**0.947**	**0.924**	0.942	0.939	**0.889**	**0.913**	**0.923**	0.923	**0.862**	**0.869**	0.873	0.869

The bold values in the table represent the highest values in the respective columns.

TABLE 4 **The AUC of different models on various datasets.**

Model	CFP dataset				UWF dataset				Noise dataset			
	I/C	Blur	LC	Overall	I/C	Blur	LC	Overall	I/C	Blur	LC	Overall
BL	0.957	0.959	0.956	0.972	0.909	0.936	0.891	0.962	0.862	0.879	0.874	0.884
+MASK	**0.979**	**0.975**	0.972	0.983	0.931	0.938	0.925	0.958	0.874	0.877	0.878	0.854
+SpatialAtt	0.968	0.967	0.983	0.981	0.907	**0.956**	**0.956**	0.972	0.888	0.899	0.89	0.922
+SpatialAtt+MS	0.976	0.969	**0.986**	**0.986**	**0.923**	0.954	0.948	**0.974**	0.891	**0.915**	**0.928**	**0.931**
+SelfAtt+MS	0.977	0.972	0.972	0.969	0.906	0.936	0.952	0.944	**0.905**	0.894	0.88	0.917

The bold values in the table represent the highest values in the respective columns.

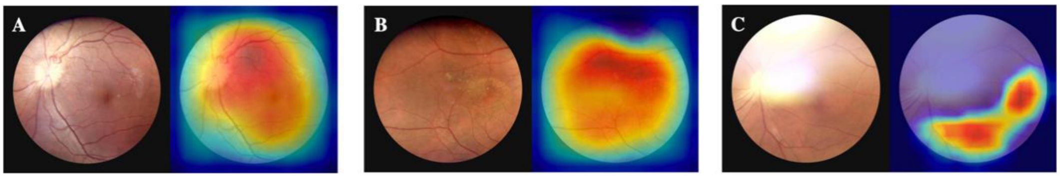

FIGURE 5
Heat map of the proposed model. **(A)** is a high-quality fundus image; the activated area is even and covers the whole image. **(B)** is a fundus image that contains a small area of uneven illumination, and therefore the top of the image is not activated. **(C)** contains a large area of strong light around the optic disk as well as the top of the image, and the rest area is properly activated.

dataset. Performance on the BL was moderate, and compared with the BL, the following models all achieved better results. BL+SelfAtt+MS attained accuracies of 0.889, 0.913, and 0.923 for I/C, Blur, and LC separately.

The ROC curves for UWF images exhibited similar performance. BL+SpatialAtt+MS attained an AUC of 0.923 for I/C. Nevertheless, the AUCs for Blur and LC reached their maximums (both 0.956) in the BL+SpatialAtt model.

TABLE 5 Appendix explains key technical terms and concepts.

Term and Concepts	Simple Explanation
Image Quality Assessment (IQA)	Evaluating how clear and useful an image is for medical purposes.
LGAANet	A smart system assessing eye images by analyzing both local details and the overall picture.
Multi-Source Heterogeneous Fundus (MSHF) Database	Collection of eye images from various sources and cameras.
Color Fundus Photography (CFP)	Standard color images of the retina.
Ultrawide-Field (UWF) Imaging	Wide-angle images capturing a broad view of the retina.
Attention Mechanisms	Focuses on significant parts of the image for analysis.
Saliency Maps	Highlights important image regions for decision-making in the neural network.
Multi-Level Spatially Pooled (MLSP)	Combines information from multiple levels of image analysis.
Global Average Pooling (GAP)	Computes the average of all feature maps in a neural network layer.
Spatial-Information-Retained (SIR)	Method preserving spatial details during image processing.
Receiver Operating Characteristic (ROC)	Graphical representation of a classifier's performance.
Human Visual System (HVS)	System responsible for processing visual information in humans.
Areas Under the ROC Curves (AUCs)	Measure of the overall performance of a classifier.

Table 5 provides a clear overview of the key technical terms and concepts used in the study, making it easier for readers from diverse backgrounds to understand the key aspects of the research.

Discussion

In the realm of IQA, much of the existing literature has concentrated on singular modalities, predominantly CFP. The incorporation of alternative imaging modalities, such as portable fundus photography and UWF fundus imaging, which may be preferable in certain clinical scenarios, has been relatively overlooked. Wang et al represented a notable exception, employing both portable fundus camera images and public CFP datasets, demonstrating the machine learning model's robust performance across these modalities (21).

To date, our research indicates a scarcity of research employing UWF images for fundus IQA, particularly studies that integrate CFP, portable fundus photography, and UWF imaging. Given that each imaging method addresses specific clinical requirements, developing an IQA system capable of accommodating this diversity is crucial. Furthermore, the challenge of 'domain variance' has been partially addressed in the prior research, which involved collecting images from both the source and target domains to train the network (22). Therefore, to fill these gaps, we compiled a multi-source heterogeneous fundus (MSHF) dataset, designed to meet the varied demands of clinical practice and mitigate the issue of domain variability.

Our Local and Global Attention Aggregated Deep Neural Network (LGAANet) was initially trained on images from portable and tabletop cameras, yet it demonstrated commendable adaptability and effectiveness when applied to UWF images. This underscores our model's potential and versatility across different clinical settings. Previous contributions have introduced several notable networks, focusing on segmentation or generic evaluation, leveraging both conventional machine learning techniques and advanced deep learning methodologies. Our LGAANet, aimed at enhancing algorithmic performance and accommodating multi-source heterogeneous data, integrates both local and global information, resulting in incremental improvements in accuracy and AUC with each enhancement.

The advent of AI in clinical practice has underscored the importance of medical imaging quality assessment. Li et al. introduced DeepQuality, a deep learning-based system for assessing and enhancing the quality of infantile fundus images to mitigate misdiagnosis risks in infant retinopathy screening, demonstrating significant improvements in diagnostic models' performance through analysis of over two million real-world images (23). This study introduces the innovative LGAANet for evaluating the quality of fundus images. Our MSHF dataset encompasses three primary types of retinal images: those captured by portable cameras, CFP images, and UWF images. These images were annotated by clinical ophthalmologists based on three distinct HVS characteristics and overall quality. The diversity of our dataset is visually represented through a spatial scatter plot. Developed on the sophisticated multi-level feature extractor SIR and incorporating an attention mechanism, the LGAANet was trained with images from portable cameras and CFP images. To evaluate the model's robustness, we also tested it with UWF images and noisy data, analyzing overall accuracy and generating ROC curves to calculate the AUC for each set. Additionally, we propose the use of a salience map as a post hoc interpretability tool. This model paves the way for further exploration into AI-driven diagnostics, especially in the field of ophthalmology.

While the LGAANet has demonstrated significant advancements in fundus IQA, there are notable limitations that must be addressed in future research. One such limitation is the current model's inability to enhance poor-quality images. Although LGAANet excels at assessing image quality, it does not yet possess the capability to improve subpar images to meet diagnostic standards. Future work should focus on developing algorithms that can transform low-quality images into high-quality ones, thereby increasing their diagnostic utility. Additionally, the reliance on a manually annotated dataset for model training and validation could introduce biases; thus, expanding the dataset and incorporating more diverse imaging conditions will be crucial for further validation. Finally, the generalizability of LGAANet to other imaging modalities and diseases outside of diabetic retinopathy and glaucoma remains to be explored. Addressing these limitations will be essential to fully realize the potential of LGAANet in clinical applications and to enhance the robustness and versatility of computer-aided diagnostic systems in ophthalmology.

Data availability statement

The datasets presented in this study can be found in online repositories. The names of the repository/repositories and accession number(s) can be found in the article/supplementary material.

Ethics statement

Ethical review and approval was not required for the study on human participants in accordance with the local legislation and institutional requirements. Written informed consent from the patients/participants was not required to participate in this study in accordance with the national legislation and the institutional requirements.

Author contributions

SW: Conceptualization, Formal analysis, Investigation, Validation, Writing—original draft. WS: Formal analysis, Validation, Writing—original draft, Methodology. ZG: Formal analysis, Methodology, Validation, Data curation, Writing—original draft. XJ: Methodology, Writing—review and editing, Visualization. YW: Formal analysis, Validation, Writing—review and editing, Resources. YL: Writing—review and editing, Validation, Visualization. XM: Formal analysis, Methodology, Software, Validation, Visualization, Writing—review and editing. WW: Formal analysis, Methodology, Validation, Writing—review and editing. SX: Formal analysis, Methodology, Validation, Writing—review and editing. WR: Formal analysis, Methodology, Validation, Writing—review and editing. KJ: Conceptualization, Formal analysis, Resources, Supervision, Writing—review and editing. JY: Conceptualization, Funding acquisition, Resources, Writing—review and editing.

Funding

The author(s) declare financial support was received for the research, authorship, and/or publication of the article. This research received financial support from the Natural Science Foundation of China (Grant number 82201195), Ningbo Clinical Research Center for Ophthalmology (2022L003), Ningbo Key Laboratory for neuroretinopathy medical research, Ningbo Clinical Research Center for Ophthalmology and the Project of NINGBO Leading Medical and Health Disipline (2016-S05), Technology Innovation 2025 Major Project of Ningbo (2021Z054), The project of Ningbo Medical Science and Technology (2018A27).

Conflict of interest

The authors declare that the research was conducted in the absence of any commercial or financial relationships that could be construed as a potential conflict of interest.

Publisher's note

References

1. Poplin R, Varadarajan A, Blumer K, Liu Y, McConnell M, Corrado G, et al. Prediction of cardiovascular risk factors from retinal fundus photographs via deep learning. *Nat Biomed Eng.* (2018) 2:158–64.

2. Ting D, Pasquale L, Peng L, Campbell J, Lee A, Raman R, et al. Artificial intelligence and deep learning in ophthalmology. *Br J Ophthalmol.* (2019) 103:167–75.

3. Ting D, Cheung C, Lim G, Tan G, Quang N, Gan A, et al. Development and Validation of a Deep Learning System for Diabetic Retinopathy and Related Eye Diseases Using Retinal Images From Multiethnic Populations With Diabetes. *JAMA.* (2017) 318:22. doi: 10.1001/jama.2017.18152

4. Gulshan V, Rajan R, Widner K, Wu D, Wubbels P, Rhodes T, et al. Performance of a Deep-Learning Algorithm vs Manual Grading for Detecting Diabetic Retinopathy in India. *JAMA Ophthalmology.* (2019) 137:9. doi: 10.1001/jamaophthalmol.2019.2004

5. Sayres R, Taly A, Rahimy E, Blumer K, Coz D, Hammel N, et al. Using a Deep Learning Algorithm and Integrated Gradients Explanation to Assist Grading for Diabetic Retinopathy. *Ophthalmology.* (2019) 126:552–64. doi: 10.1016/j.ophtha.2018.11.016

6. Raj A, Tiwari A, Martini M. Fundus image quality assessment: survey, challenges, and future scope. *IET Image Processing.* (2019) 13:1211–24.

7. Talebi H, Milanfar P. *NIMA: Neural Image Assessment*. Piscataway, NJ: IEEE (2018).

8. Liu X, Weijer J, Bagdanov A editors. RankIQA: Learning from Rankings for No-Reference Image Quality Assessment. *Proceedings of the 2017 IEEE International Conference on Computer Vision (ICCV)*. Piscataway, NJ: (2017). doi: 10.1109/TIP.2021.3084750

9. Bosse S, Maniry D, Muller K, Wiegand T, Samek W. Deep Neural Networks for No-Reference and Full-Reference Image Quality Assessment. *IEEE Trans Image Process.* (2018) 27:206–19.

10. Ma K, Liu W, Zhang K, Duanmu Z, Wang Z, Zuo W. End-to-End Blind Image Quality Assessment Using Deep Neural Networks. *IEEE Trans Image Process.* (2018) 27:1202–13.

11. Liu L, Wu X, Lin D, Zhao L, Li M, Yun D, et al. DeepFundus: A flow-cytometry-like image quality classifier for boosting the whole life cycle of medical artificial intelligence. *Cell reports Medicine.* (2023) 4:100912. doi: 10.1016/j.xcrm.2022.100912

12. Jin K, Gao Z, Jiang X, Wang Y, Ma X, Li Y, et al. MSHF: A Multi-Source Heterogeneous Fundus (MSHF) Dataset for Image Quality Assessment. *Scientific data.* (2023) 10:286. doi: 10.1038/s41597-023-02188-x

13. Lin K, Wang G. Hallucinated-IQA: No-Reference Image Quality Assessment via Adversarial Learning. *Proceedings of the 2018 IEEE/CVF Conference on Computer Vision and Pattern Recognition*. Piscataway, NJ: (2018). p. 732–41.

14. Li D, Jiang T, Lin W, Jiang M. Which Has Better Visual Quality: The Clear Blue Sky or a Blurry Animal? *IEEE Trans on Multimedia.* (2019) 21:1221–34.

15. Su S, Yan Q, Zhu Y, Zhang C, Ge X, Sun J, et al. Blindly Assess Image Quality in the Wild Guided by A Self-Adaptive Hyper Network. *Proceedings of the IEEE Conference on Computer Vision and Pattern Recognition*. Piscataway, NJ: (2020).

16. Zhang Y, Li H, Du J, Qin J, Wang T, Chen Y, et al. 3D Multi-Attention Guided Multi-Task Learning Network for Automatic Gastric Tumor Segmentation and Lymph Node Classification. *IEEE Trans Med Imaging.* (2021) 40:1618–31. doi: 10.1109/TMI.2021.3062902

17. Chen Q, Keenan T, Allot A, Peng Y, Agron E, Domalpally A, et al. Multimodal, multitask, multiattention (M3) deep learning detection of reticular pseudodrusen: Toward automated and accessible classification of age-related macular degeneration. *J Am Med Inform Assoc.* (2021) 28:1135–1118. doi: 10.1093/jamia/ocaa302

18. You J, Korhonen J. Transformer for Image Quality Assessment. *IEEE International Conference on Image Processing*. Piscataway, NJ: (2020).

19. Chen Q, Zhang W, Zhou N, Lei P, Xu Y, Zheng Y, et al. Adaptive Fractional Dilated Convolution Network for Image Aesthetics Assessment. *2020 IEEE/CVF Conference on Computer Vision and Pattern Recognition (CVPR)*. Piscataway, NJ: (2020).

20. Chen C, Gong D, Wang H, Li Z, Wong K. Learning Spatial Attention for Face Super-Resolution. *IEEE Trans Image Process.* (2021) 30:1219–31.

21. Wang S, Jin K, Lu H, Cheng C, Ye J, Qian D. Human Visual System-Based Fundus Image Quality Assessment of Portable Fundus Camera Photographs. *IEEE Trans Med Imaging.* (2016) 35:1046–55. doi: 10.1109/TMI.2015.2506902

22. Shen Y, Sheng B, Fang R, Li H, Dai L, Stolte S, et al. Domain-invariant interpretable fundus image quality assessment. *Medical image analysis.* (2020) 61:101654. doi: 10.1016/j.media.2020.101654

23. Li L, Lin D, Lin Z, Li M, Lian Z, Zhao L, et al. DeepQuality improves infant retinopathy screening. *NPJ Digit Med.* (2023) 6:192. doi: 10.1038/s41746-023-00943-3

frontiers | Frontiers in Medicine

TYPE Study Protocol
PUBLISHED 15 October 2024
DOI 10.3389/fmed.2024.1483930

EDITED BY
Jiong Zhang,
University of Southern California, United States

REVIEWED BY
André Ferreira,
Centro Hospitalar Universitário do Porto, Portugal
Hu Xiaoyang,
Chinese Academy of Sciences (CAS), China

*CORRESPONDENCE
Juan David Saldaña-Garrido
✉ jdsalga@hotmail.com

†These authors have contributed equally to this work

RECEIVED 20 August 2024
ACCEPTED 02 October 2024
PUBLISHED 15 October 2024

CITATION
Saldaña-Garrido JD, Cantó-Cerdán M, Gil-Guillén VF, Alfaro-Beltrá ML and Sivera F (2024) Association between central corneal thickness and systemic lupus erythematosus: a cross-sectional study protocol.
Front. Med. 11:1483930.
doi: 10.3389/fmed.2024.1483930

Association between central corneal thickness and systemic lupus erythematosus: a cross-sectional study protocol

Juan David Saldaña-Garrido[1,2*†], Mario Cantó-Cerdán[3], Vicente Francisco Gil-Guillén[2,4†], María Luisa Alfaro-Beltrá[1] and Francisca Sivera[2,5†]

[1]Department of Ophthalmology, General University Hospital of Elda, Elda, Spain, [2]Department of Clinical Medicine, School of Medicine, Miguel Hernández de Elche University, San Juan de Alicante, Spain, [3]Vissum Miranza, Alicante, Spain, [4]Department of Investigations, General University Hospital of Elda, Elda, Spain, [5]Department of Rheumatology, General University Hospital of Elda, Elda, Spain

Introduction: Systemic lupus erythematosus (SLE) is a chronic autoimmune disease affecting multiple systems and classified under connective tissue disorders. Ocular involvement occurs in up to 30% of SLE cases, with the cornea being particularly susceptible to thinning due to immune-complex deposits and its predominantly type I collagen composition. This corneal thinning is clinically significant in glaucoma, where patients with reduced central corneal thickness (CCT) may have up to a threefold increased risk of developing glaucoma, as well as in refractive surgery. However, existing studies on CCT in SLE are limited and marked by substantial heterogeneity in methodology, technology, criteria, and participant numbers, resulting in conflicting findings. Based in our hypothesis that SLE-related corneal lysis may result in decreased CCT, this study aims to determine and compare the mean CCT values between SLE patients and healthy controls to obtain a more precise understanding of the potential relationship.

Methods and analysis: A cross-sectional observational study will be conducted, enrolling SLE patients and age-and sex-matched healthy controls recruited from ophthalmology consultations. Exclusion criteria will be applied to rule out other corneal thinning risk factors. A pilot study estimated a minimum sample size of 34 participants per group. CCT measurements will be obtained using Zeiss HD Cirrus 5,000 optical coherence tomography (OCT) on a randomly selected eye, following concordance analysis using the Kappa index. Statistical analysis will include descriptive, bivariate, and multivariate methods. The study protocol was approved by the ethics committee.

Discussion: The cornea's vulnerability to thinning and lysis in SLE, which impacts CCT, is crucial for the accurate assessment of glaucoma, the leading cause of irreversible blindness worldwide and the second leading cause in Europe. Given that patients with reduced CCT are at a significantly higher risk of developing glaucoma, further research is necessary to understand the association between SLE and CCT. Our study aims to enhance methodological rigor compared to prior research by determining an appropriate sample size and exclusively enrolling SLE patients to increase participant homogeneity. If a significant difference in CCT between groups and an association between CCT and SLE are found, a prospective study will be considered.

KEYWORDS

systemic lupus erythematosus, central corneal thickness, pachymetry, optical coherence tomography, glaucoma, hydroxychloroquine

Introduction

Systemic lupus erythematosus (SLE) is a chronic autoimmune multisystemic disease of unknown etiology, classified under "connective tissue diseases." It is relatively rare, with a prevalence of 39 per 100,000 in Europe (1), and is more common among young women and individuals of Black, Asian, and Hispanic descent (2). The European League against Rheumatism (EULAR)/American College of Rheumatology (ACR) developed classification criteria for SLE, with a sensitivity and specificity of 96.1 and 93.4%, respectively (3). However, not all patients meet these criteria, complicating and delaying diagnosis.

Regarding SLE manifestations, most patients experience constitutional syndrome (fever, weight loss, and asthenia) at some point during the disease (1). The musculoskeletal system, skin and kidney are also commonly affected (4). However, the eye can also be involved, with ocular manifestations in up to 30% of patients (1, 5).

Most ocular alterations are not considered in the overall assessment of SLE, as recognized by the British Isles Lupus Assessment Group (BILAG) (1). However, these disorders often occur in the context of systemic disease activity, with many being asymptomatic (1, 6), delaying specific treatment and worsening visual prognosis. This suggests that ophthalmologic evaluation could be key for diagnosing and especially monitoring SLE activity.

These ocular manifestations vary widely and can affect nearly any ocular structure. Common changes include secondary dry eye syndrome—due to secondary Sjögren's syndrome (1, 5)—and bilateral small vessel retinal vasculitis (1, 4, 5, 7). Other manifestations include recurrent corneal erosions, stromal corneal infiltration, corneal opacity, peripheral ulcerative keratitis, corneal edema, interstitial keratitis (4), choroidal effusion, optic neuropathy (1), as well as orbital or eyelid inflammation, and various retinal vascular alterations such as vascular occlusions related to associated antiphospholipid syndrome (1).

The cornea, primarily composed of type I connective tissue (4, 5), is particularly vulnerable to thinning and lysis phenomena in SLE (4, 8) due to inflammation triggered by autoantibodies (specifically anti-double-stranded DNA antibodies—anti-dsDNA—and anti-Smith antibodies—anti-Sm) and immune complexes deposited in its basement membrane (4). Consequently, various research efforts have aimed to elucidate the relationship between SLE and the central corneal thickness (CCT). These investigations were conducted by Zang et al. (9), Çağlayan et al. (10), Yazici et al. (4), Mahendradas et al. (8), Eissa et al. (5), Kaya et al. (11) and Mahmoud et al. (6).

These previous studies examining CCT in SLE patients report conflicting results. Çağlayan et al. (10) and Zhang et al. (9) reported thicker CCT in SLE compared to controls. Conversely, Yazici et al. (4), Mahendradas et al. (8), Eissa et al. (5), Kaya et al. (11) and Mahmoud et al. (6), reported a reduced CCT in SLE compared to controls (4–6, 8, 11).

Additionally, these studies present certain limitations that hinder the extraction of definitive conclusions. The study by Zhang et al. (9) does not directly measure CCT, but rather evaluates corneal hysteresis and assumes an association with CCT based on previous studies. Regarding sample size, several investigations do not provide a sample size calculation and exhibit highly variable sizes. The studies by Mahendradas et al. (8) and Oğurel et al. (12) are notable for their particularly small samples 7 and 4 patients with SLE, respectively, sometimes only performing a descriptive statistical analysis of the SLE patients, as in the case of Mahendradas et al. (8), or analyzing both eyes, as in the case of Mahmoud et al. (6).

Furthermore, there are differences in the inclusion of patients with active or inactive SLE between the studies. While the studies by Yazici et al. (4), Zhang et al. (6), and Mahmoud et al. (9) do not mention the activity status of SLE, others, such as Mahendradas et al. (8), include patients with both active and inactive SLE. The study by Eissa et al. (5) includes only patients with active SLE, whereas the studies by Kaya et al. (10) and Çağlayan et al. (11) focus exclusively on patients with inactive SLE.

Measurement of CCT, a biomechanical property of the cornea, is essential for interpreting intraocular pressure (IOP) measurements (13) and it is considered one of the main sources of error in applanation tonometry (14). A thicker cornea (greater CCT) leads to artificially increased IOP measurements, whereas a thinner cornea (lower CCT) results in an underestimation of IOP (13). Therefore, evaluating CCT is crucial for diagnosing significant conditions such as glaucoma or keratoconus, as well as for assessing suitability for corneal refractive surgery techniques such as Laser Assisted *in Situ* Keratomileusis (LASIK) or photorefractive keratectomy (PRK) (14–16).

Glaucoma is the leading cause of irreversible blindness globally (17) and the second leading cause in Europe (18), with an estimated 111.8 million people projected to have glaucoma by 2040 (17). Glaucoma is typically asymptomatic until very advanced stages, with up to 50% of cases going undiagnosed (18). Despite its unknown etiology, elevated IOP is the primary risk factor for developing glaucoma (15, 18), making IOP and CCT evaluation essential in clinical practice. In SLE, this risk may be exacerbated by the disease's distinctive vascular characteristics, including retrobulbar artery narrowing and increased sensitivity to vasoconstriction (7).

Additionally, CCT measurements are crucial for predicting potential outcomes or complications of refractive surgery in SLE patients, who predominantly fall within the 30–50 age range and are therefore in their productive years (4). Misdiagnosis or inappropriate treatment strategies could significantly impact their quality of life and increase healthcare costs.

Apart from disease manifestations, it is important to consider the ocular toxicity and side effects of medications used to treat SLE. Commonly prescribed drugs include corticosteroids and hydroxychloroquine (HCQ). Corticosteroids can induce cortical or posterior subcapsular cataracts and secondary glaucoma (1). HCQ, meanwhile, can affect the cornea (19), leading to verticillate keratopathy (1), changes in endothelial cell density and may result in CCT thickening (10, 12). HCQ can also have an impact on the ciliary body and retinal pigment epithelium (RPE), causing maculopathy (1). These side effects necessitate regular ophthalmologic monitoring as they can pose a significant threat to vision (1).

Given the cornea's susceptibility to thinning and lysis phenomena in SLE (4, 8), and considering the limited number of studies on CCT and SLE relationship and their conflicting conclusions, further investigations to enhance our understanding of this association is crucial. Therefore, based on the hypothesis that CCT is reduced in SLE patients compared to healthy individuals, we are conducting this cross-sectional study with the main objective of determining whether there are differences in mean CCT between SLE patients and healthy controls.

Methods and analysis

Aims and objectives

The primary aim of this study is to determine and compare the mean CCT values between SLE patients and age-and sex-matched healthy controls using Zeiss HD Cirrus 5,000 optical coherence tomography (OCT). Additionally, the study aims to enhance methodological rigor relative to prior research by determining sample size and exclusively enrolling SLE patients to increase participant homogeneity.

Other secondary objectives are:

- To determine the agreement of CCT between the right eye and left eye in both the SLE group and the healthy control group.
- To describe the proportion of patients with decreased and normal CCT in both the SLE group and the healthy control group.
- To compare glaucoma-related variables – IOP, retinal nerve fiber layer (RNFL) thickness, and visual field (VF)—between the SLE group and the healthy control group.
- To identify the number of new glaucoma diagnoses in SLE group.
- To establish the association between patient and disease characteristics and CCT in patients with SLE.

Study design

Based on the hypothesis and the main objective, we are conducting a cross-sectional observational study at the Department of Ophthalmology at General University Hospital of Elda, in collaboration with the University of Miguel Hernández of Elche, Spain, where participants will be part of one of two groups:

- Group 1: patients with SLE diagnosis, without ocular or systemic pathology affecting CCT.
- Group 2: patients without SLE diagnosis, without ocular or systemic pathology affecting CCT.

Study subjects

Study population and sampling method

Catchment population includes all patients served by the Health Department of Elda (~200,000 patients). Study participants included both healthy control subjects and patients diagnosed with SLE, who meet all inclusion criteria, but none of the exclusion criteria. Patients will be recruited consecutively.

Sample size calculation

Given the limited available literature, with few studies, heterogeneous sample sizes and conflicting results, there is insufficient evidence to estimate the necessary sample size. Therefore, a pilot project was conducted with 20 patients (10 patients with SLE and 10 healthy patients) where the mean CCT value was 525 ± 25 μm for the group of patients with SLE and 510 ± 24 μm for the group of healthy patients. Establishing a bilateral hypothesis with a type 1 error or α of 5% and a type 2 error or β of 20% (equivalent to a power of 80%), the resulting effect size was 0.61. This calculation indicated a requirement of a minimum of 34 participants per group.

Inclusion criteria

- Patients 18 years of age or older.
- Patients diagnosed with and under follow-up for SLE by the Rheumatology Department of the Health Department of Elda, and not exhibiting disease activity according to the treating rheumatologist.
- Patients without SLE and without ocular or systemic pathology affecting the CCT (as specified in the exclusion criteria), from the Health Department of Elda.

Exclusion criteria

- Pregnancy or lactation.
- Patients of African descent.
- Previous ocular disease that may affect the CCT (keratoconus, corneal edema, uveitis) or previous diagnosis of glaucoma.
- Patients with systemic diseases that may affect the CCT (diabetes mellitus, chronic obstructive pulmonary disease—COPD).
- Severe astigmatism (> 3 diopters) or severe myopia [axial length (AL) > 26 mm or sphere ≥ -6 diopters].
- Patients undergoing topical ocular treatment, except for artificial tears or with a history of ophthalmic surgery and regular contact lens users.
- Patients treated with topical or inhaled corticosteroids in the last 3 months.
- Patients receiving periocular corticosteroids or systemic prednisone at doses ≥7.5 mg/day in the last 6 months.

Study variables

Qualitative dichotomous variables

- SLE (Yes/No)
- Hydroxychloroquine (Yes/No)
- Sex (Male/Female)
- Schirmer Test Type 2 (Normal/Abnormal): Considered abnormal when the test shows <10 mm wetting after 5 min.
- VF 24–2 (Glaucomatous/Non-glaucomatous): A glaucomatous VF will be considered when typical glaucoma defects are present: defects not respecting the vertical line but respecting the horizontal line, Rönne's nasal step, Bjerrum's arcuate defects, and centrocecal defects.

- Raynaud's Phenomenon (Yes/No)
- Constitutional Syndrome (fever, fatigue, and weight loss)
  - o Previous (Yes/No)
  - o Current (Yes/No)
- Mucocutaneous Involvement (malar rash, oral or nasal ulcers, photosensitivity)
  - o Previous (Yes/No)
  - o Current (Yes/No)
- Musculoskeletal Involvement (arthritis, arthralgia)
  - o Previous (Yes/No)
  - o Current (Yes/No)
- Renal Involvement (glomerulonephritis)
  - o Previous (Yes/No)
  - o Current (Yes/No)
- Cardiac Involvement (pericarditis)
  - o Previous (Yes/No)
  - o Current (Yes/No)
- Gastrointestinal Involvement (esophagitis, peritonitis, lupus hepatitis, pancreatitis)
  - o Previous (Yes/No)
  - o Current (Yes/No)
- Pulmonary Involvement (pleuritis, pneumonitis)
  - o Previous (Yes/No)
  - o Current (Yes/No)
- Neuropsychiatric Involvement (delirium, psychosis, depression, anxiety, epilepsy, motor disorder)
  - o Previous (Yes/No)
  - o Current (Yes/No)
- Hematologic Involvement (anemia, leukopenia, thrombocytopenia)
  - o Previous (Yes/No)
  - o Current (Yes/No)
- Ocular Involvement (dry keratoconjunctivitis, retinal vasculitis, scleritis/episcleritis)
  - o Previous (Yes/No)
  - o Current (Yes/No)
- Current use of Methotrexate (Yes/No)
- Current use of Mycophenolate (Yes/No)
- Current use of Azathioprine (Yes/No)
- Current use of Belimumab (Yes/No)
- Current use of Leflunomide (Yes/No)
- Current use of Tacrolimus (Yes/No)

Qualitative ordinal variables

- CCT: This is the main variable. It will be coded according to the following classification:
  - o Decreased: < 510 µm. CCT is classified as decreased when measurements fall below the threshold defined as normal by the European Glaucoma Society (EGS), specifically values less than 510 µm.
  - o Normal: > 510 µm. In categorizing CCT as "normal," all participants with CCT values falling within the normal range (510–570 µm) or higher (> 570 µm) are grouped together. CCT is considered normal or increased if measurements are equal to or greater than the thresholds established by the EGS, specifically starting from 510 µm.
- Color Code for Average RNFL Thickness of the Optic Nerve, measured by OCT:
  - o Normal: Green
  - o Abnormal: Yellow or Red
- Antinuclear Antibody Pattern

  - o Nuclear Dots
  - o Nucleolar
  - o Speckled
  - o Homogeneous
  - o Cytoplasmic
  - o Centromere

Quantitative discrete variables

- CCT (µm). Considered as the dependent variable, it is the main variable.
- IOP measured by Goldman applanation tonometry (GAT) (mmHg)
- Average RNFL Thickness of the Optic Nerve, measured by OCT (µm)
- Duration of SLE Disease (years)
- Time since last inflammatory flare-up (months)
- Age (years)
- Antinuclear Antibody Titers (fraction)
- Duration of hydroxychloroquine use (months)

Quantitative continuous variables

- Sphere (diopters)
- Cylinder (diopters)
- Spherical Equivalent (SE) (diopters): This simplifies and effectively represents the behavior of the optical system using an ideal spherical lens that represents the circle of least confusion where a clear image is produced in the patient, facilitating analysis. It is the result of the sum of the spherical refractive error and half of the cylindrical refractive error of the patient.
- AL (mm)
- Anti-dsDNA Antibodies (IU/mL). For statistical analysis, participants with values <9.8 IU/mL were assigned a value of 0, as values below 9.8 IU/mL are clinically considered "undetectable," allowing for clearer statistical analysis.
- Anti-Smith Antibodies (U/mL). For statistical analysis, participants with valued <3.3 U/mL were assigned a value of 0, as values below 3.3 U/mL are clinically considered "undetectable," allowing for clearer statistical analysis.
- Anti-Ro Antibodies (U/mL). For statistical analysis, participants with values <2.3 U/mL were assigned a value of 0, as values below 2.3 U/mL are clinically considered "undetectable," allowing for clearer statistical analysis.
- Anti-La Antibodies (U/mL). For statistical analysis, participants with values <3.3 U/mL were assigned a value of 0, as values below 3.3 U/mL are clinically considered "undetectable," allowing for clearer statistical analysis.
- Keratometry 1 (K1) -flat- (diopters): Measures the anterior curvature in the central 3 mm of the cornea in its flattest meridian. Normal value is 43–44 diopters.
- Keratometry 2 (K2) -steep- (diopters): Measures the anterior curvature in the central 3 mm of the cornea in its steepest meridian. Normal value is 43–44 diopters.

- Average Keratometry (KM) (diopters): Measures the average anterior curvature in the central 3 mm of the cornea. Normal value is 43–44 diopters.

Data analysis

Statistical analysis

The statistical analysis will be performed using the Statistical Package for the Social Sciences (SPSS) version 26.0 developed by IBM Corp. (Armonk, NY) for Windows. The study will be conducted, first considering the whole sample, and additionally, a sub-analysis will be carried out considering only patients with SLE.

To determine the concordance between the right eye and the left eye to decide whether both eyes or only one eye per participant will be analyzed, a concordance analysis using the Kappa index will be performed.

Descriptive analysis based on the type of variable

Proportions will be calculated for qualitative variables, while mean and standard deviation will be computed for quantitative variables. Additionally, 95% confidence intervals will be determined for the most pertinent variables.

Bivariate analysis

The normality of the variables will be determined using the Kolmogorov–Smirnov test. Parametric tests will be employed if the dependent variable conforms to a normal distribution: when comparing two qualitative variables (two proportions), the Chi-Square test will be used. When comparing a qualitative variable with a quantitative variable (two means), the Student's T-test will be used. For comparisons involving more than two means, analysis of variance (ANOVA) will be conducted. When comparing two quantitative variables, the measure of association used will be Pearson's linear correlation coefficient, and the statistical test will be the Student's T-test.

Non-parametric tests will be used if the dependent variable does not follow a normal distribution, tailored to the types of variables being compared.

Statistical significance will be set at $p < 0.05$ and the 95% confidence limits for the differences in proportions (qualitative variable) and mean differences (quantitative variable) between the two groups will be calculated.

Multivariate analysis

To minimize confounding bias in comparisons and to adjust and evaluate possible interactions, a multivariate analysis will be conducted. The most methodologically reasonable model based on the results will be selected and all necessary assumptions will be validated. Statistical significance will be defined as a p-value <0.05.

Data collection of study variables

Primary data collection (study variables) will be conducted through clinical interviews, review of computerized medical records, and complementary tests. Patients diagnosed with SLE, will be conducted by reviewing computerized medical records for the patients diagnosed with "Systemic Lupus Erythematosus" according to the 10th edition of the International Classification of Diseases (ICD-10), who are under follow-up by the Rheumatology Department of the Health Department of Elda.

For the selection of participants in group 1 (SLE), patients will be recruited consecutively from those attending follow-up appointments in the Rheumatology Department. Information from their medical records regarding the inclusion and exclusion criteria will also be considered to avoid including those who are not suitable candidates for the study. Potential candidates will be contacted by phone, informed about the study and invited to participate. Interested individuals will be scheduled for ophthalmology consultations where they will receive all necessary information (information sheet and informed consent) and initiate variable collection.

For the generation of group 2 (healthy controls), patients attending ophthalmology consultations for occupational check-ups, presbyopia evaluations or other minor eye issues not included in the study's exclusion criteria will be invited to participate. Additionally, companions of patients with SLE attending the consultation will also be invited, provided they meet the inclusion and exclusion criteria. Among these, patients without an SLE diagnosis and without ocular or systemic conditions affecting the CCT, who belong to the Health Department of Elda, will be selected.

Selected patients will be scheduled for ophthalmology consultations in the morning from 9:00 AM to 2:00 PM to avoid diurnal variations in measurements. After providing the information sheet and obtaining informed consent, a clinical interview and the following complementary tests will be conducted in a single visit. An ophthalmological examination will be performed on all subjects by a single observer, including refraction, visual acuity, anterior segment with slit-lamp, fundus examination, pachymetry using Zeiss Cirrus HD-OCT 5000, GAT, Schirmer 2 test, biometry (including keratometry), VF 24–2, and optic nerve OCT pupil dilation with tropicamide. In all cases, corneal OCT will be performed before the instillation of anesthetic and GAT to avoid alterations in the tear film and possible corneal deformations secondary to contact that could interfere with pachymetry. For pachymetry, a minimum of three images will be obtain with the best being selected for analysis. If none of the initial three images meet the quality standards specified by the device, which are indicated by a green signal, additional images will be taken as needed until a sufficiently high-quality image is acquired.

All data regarding the demographic and clinical characteristics of the participants will be recorded in a data collection form, which will serve as a database for statistical analysis using SPSS Statistics. This database will be managed by the principal investigator and will only be accessible to the supervisor, co-supervisor, and the statistical analyst.

Discussion

Error control and bias

To minimize random error, a representative sample size was calculated using a consecutive sampling method, as random or systematic sampling is not feasible in this patient population. A multivariate analysis will be conducted to minimize potential confounding bias and interactions.

Furthermore, to enhance the homogeneity, participants from both groups will be selected from the same population sample of the Health Department of Elda and matched based on controllable variables such as sex and age. Patients with conditions or diseases that could independently affect CCT, including keratoconus, corneal edema, diabetes mellitus and COPD, will be excluded from the sample. Regarding keratoconus, individuals with confirmed or suspected diagnosis will be excluded based on the identification of characteristic signs such as Vogt's striae or Fleischer's ring during slit-lamp examination, keratometry readings with K readings exceeding 47 diopters and high astigmatism, despite the absence of confirmatory topography.

It is important to note a potential selection bias among the healthy group, as participants are selected based on the absence of a SLE diagnosis without additional confirmation through complementary tests. However, according to the Spanish Society of Rheumatology's EPISER study, which included 4,900 participants to determine the prevalence of rheumatic diseases in Spain, 12 cases of SLE were identified through a telephone interview screening. Participants meeting positive screening criteria underwent further evaluation in rheumatology clinics for diagnostic confirmation, with 11 cases already diagnosed prior to screening (20). Therefore, given the estimated low prevalence of SLE, the likelihood of misclassifying patients without self-reported or documented SLE in their medical history is low (1/12).

To minimize measurement bias, data for the primary objective will be collected through clinical interviews using validated and calibrated instruments. Additionally, all participants will undergo standardized evaluations conducted by the same investigator, ensuring consistency between groups.

Limitations

The main study limitation is the lack of prior knowledge regarding the required sample size. Therefore, a pilot study was conducted to determine the minimum sample size necessary for representativeness. Furthermore, selecting participants consecutively, a form of non-probabilistic sampling, may not fully achieve the desired representativeness, thereby potentially limiting the generalizability of the findings.

The study design's cross-sectional nature presents a limitation in terms of temporality, as both disease and exposure data are collected simultaneously, precluding the establishment of a cause-and-effect relationship due to the absence of temporal sequencing. Additionally, it remains unknown whether CCT varies over the course of the disease or remains stable. Therefore, if a significant difference in CCT between groups and association between CCT and SLE are found upon study completion, a prospective study will be considered.

Finally, a limitation associated with CCT measurement using the Zeiss Cirrus HD-OCT 5000 is that measurements are taken from the tear film to the Descemet membrane (21), which may result in less precise measurements for patients with ocular surface pathology, such as reduced tear production or a decreased tear meniscus. To minimize potential measurement bias, artificial tears will be administered to all patients before performing pachymetry. While OCT is not considered the gold standard for CCT measurement compared to ultrasound pachymetry, both devices are considered interchangeable and quantification of CCT using corneal OCT offers several advantages over USP, including faster results acquisition, reduced need for patient cooperation and the elimination of topical anesthesia requirement, thereby minimizing risks of epithelial damage, corneal deformation and potential ocular contamination (21). Additionally, utilizing OCT for CCT measurement enables the use of a single device for multiple assessments, as OCT is already routinely employed for other evaluations in daily clinical practice. This streamlines the process, enhancing efficiency and reducing the need to transfer the patient between devices. Therefore, opting for OCT aligns with the increasing demand within the scientific community and among patients for faster and less invasive tests, without compromising measurement accuracy.

Ethics statement

The studies involving humans were approved by the Institutional Review Board (IRB) of the General University Hospital of Elda. The studies were conducted in accordance with the local legislation and institutional requirements. The participants provided their written informed consent to participate in this study.

Author contributions

JS-G: Conceptualization, Data curation, Funding acquisition, Investigation, Methodology, Writing – original draft, Writing – review & editing. MC-C: Formal analysis, Writing – review & editing. VG-G: Conceptualization, Methodology, Project administration, Supervision, Writing – review & editing. MA-B: Conceptualization, Project administration, Resources, Supervision, Writing – review & editing. FS: Conceptualization, Methodology, Project administration, Resources, Supervision, Writing – review & editing.

Funding

The author(s) declare that financial support was received for the research, authorship, and/or publication of this article. Navarro-Tripodi Foundation has provided financial support to the authors for publication of this article.

Acknowledgments

The authors thank all study participants for their interest and cooperation.

Conflict of interest

The authors declare that the research was conducted in the absence of any commercial or financial relationships that could be construed as a potential conflict of interest.

Publisher's note

References

1. Dammacco R. Systemic lupus erythematosus and ocular involvement: an overview. *Clin Exp Med.* (2018) 18:135–49. doi: 10.1007/s10238-017-0479-9

2. Lim SS, Drenkard C. Epidemiology of lupus: an update. *Curr Opin Rheumatol.* (2015) 27:427–32. doi: 10.1097/BOR.0000000000000198

3. Aringer M, Costenbader K, Daikh D, Brinks R, Mosca M, Ramsey-Goldman R, et al. 2019 European league against rheumatism/American College of Rheumatology classification criteria for systemic lupus erythematosus. *Arthritis Rheumatol.* (2019) 71:1400–12. doi: 10.1002/art.40930

4. Yazici A, Kara N, Yüksel K, Altinkaynak H, Baz O, Bozkurt E, et al. The biomechanical properties of the cornea in patients with systemic lupus erythematosus. *Eye (Lond).* (2011) 25:1005–9. doi: 10.1038/eye.2011.99

5. Eissa IM, Nassar GA, Arfeen SA, Dahab AA. Evaluation of central and peripheral corneal thicknesses in patients with systemic lupus erythematosus. *Clin Ophthalmol.* (2020) 14:589–95. doi: 10.2147/OPTH.S234568

6. Mahmoud MSE-D, Hamid MA, Abdelkader MF. Anterior segment optical coherence tomography of tear film and cornea in systemic lupus erythematosus patients. *Clin Ophthalmol.* (2021) 15:3391–9. doi: 10.2147/OPTH.S323673

7. Modrzejewska M, Ostanek L, Bobrowska-Snarska D, Karczewicz D, Wilk G, Brzosko M, et al. Ocular circulation in systemic lupus erythematosus. *Med Sci Monit.* (2009) 15:CR573-8.

8. Mahendradas P, Francis M, Vala R, Gowda P, Kawali A, Shetty R, et al. Quantification of ocular biomechanics in ocular manifestations of systemic autoimmune diseases. *Ocul Immunol Inflamm.* (2019) 27:1127–37. doi: 10.1080/09273948.2018.1501491

9. Zhang B, Shweikh Y, Khawaja AP, Gallacher J, Bauermeister S, Foster PJ. Associations with corneal hysteresis in a population cohort: results from 96 010 UK biobank participants. *Opththalmology.* (2019) 126:1500–10. doi: 10.1016/j.ophtha.2019.06.029

10. Çağlayan M, Akyol L, Balcı MA, Öncül H, Alakuş MF, Dağ U. Evaluation of corneal safety in systemic lupus erythematosus patients undergoing long-term hydroxychloroquine treatment. *Cutan Ocul Toxicol.* (2021) 40:21–5. doi: 10.1080/15569527.2020.1861003

11. Kaya H, Karasu U, Martin Ç, Taşçi M, Pekel G. Measurements of scleral thickness and corneal optic densitometry in patients with systemic lupus erythematosus. *Medicine.* (2020) 99:e21467. doi: 10.1097/MD.0000000000021467

12. Oğurel T, Özer MA, Akbulut Y, Gökçınar NB, Onaran Z, Ureten K. Corneal thickness and endothelial changes in long-term hydroxychloroquine use. *Cutan Ocul Toxicol.* (2019) 38:286–9. doi: 10.1080/15569527.2019.1608228

13. AAO O. Basic and clinical science course section 8 external disease and cornea. 2022–2023. San Francisco: American Academy of Ophthalmology (2022).

14. Pierro L, Iuliano L, Gagliardi M, Ambrosi A, Rama P, Bandello F. Central corneal thickness reproducibility among ten different instruments. *Optom Vis Sci.* (2016) 93:1371–9. doi: 10.1097/OPX.0000000000000974

15. Gaspar R, Abegão Pinto L, Cordeiro SD. Corneal properties and glaucoma: a review of the literature and meta-analysis. *Arq Bras Oftalmol.* (2017) 80:202–6. doi: 10.5935/0004-2749.20170050

16. Tranchina L, Lombardo M, Oddone F, Serrao S, Schiano Lomoriello D, Ducoli P. Influence of corneal biomechanical properties on intraocular pressure differences between an air-puff tonometer and the Goldmann applanation tonometer. *J Glaucoma.* (2013) 22:416–21. doi: 10.1097/IJG.0b013e31824cafc9

17. Tham Y-C, Li X, Wong TY, Quigley HA, Aung T, Cheng C-Y. Global prevalence of Glaucoma and projections of Glaucoma burden through 2040. A systematic review and Meta-analysis. *Ophthalmology.* (2014) 121:2081–90. doi: 10.1016/j.ophtha.2014.05.013

18. Society EG. Terminology and guidelines of Glaucoma. Savona: Publi Comm (2021).

19. Vural E, Hazar L, Erol K. The effect of long-term hydroxychloroquine use on the corneal endothelium in patients with systemic lupus erythematosus. *Int Ophthalmol.* (2020) 41:937–43. doi: 10.1007/s10792-020-01649-1

20. 2016 GdTdPE. Lupus Eritemasoso Sistémico In: R FED, editor. EPISER 2016: Estudio de prevalencia de las enfermedades reumáticas en población adulta en España. Madrid: Sociedad Española de Reumatología (2018). 79–88.

21. Calvo-Sanz JA, Ruiz-Alcocer J, Sánchez-Tena MA. Accuracy of cirrus HD-OCT and Topcon SP-3000P for measuring central corneal thickness. *J Optom.* (2018) 11:192–7. doi: 10.1016/j.optom.2016.12.004

frontiers | Frontiers in Medicine

TYPE Original Research
PUBLISHED 21 October 2024
DOI 10.3389/fmed.2024.1452756

OPEN ACCESS

EDITED BY
Jiong Zhang,
University of Southern California,
United States

REVIEWED BY
Endalkachew Belayneh Melese,
Johns Hopkins University, United States
Tae Keun Yoo,
Hangil Eye Hospital, Republic of Korea
Yao Tan,
Central South University, China

*CORRESPONDENCE
Xiang-Long Yi
✉ yixianglong1010@163.com

RECEIVED 21 June 2024
ACCEPTED 02 October 2024
PUBLISHED 21 October 2024

CITATION
Wang G and Yi X-L (2024) Development and construction of a cataract risk prediction model based on biochemical indices: the National Health and Nutrition Examination Survey, 2005–2008.
Front. Med. 11:1452756.
doi: 10.3389/fmed.2024.1452756

Development and construction of a cataract risk prediction model based on biochemical indices: the National Health and Nutrition Examination Survey, 2005–2008

Guoqing Wang[1,2] and Xiang-Long Yi[1,2]*

[1]Department of Ophthalmology, First Affiliated Hospital of Xinjiang Medical University, Urumqi, Xinjiang, China, [2]Xinjiang Medical University, Urumqi, Xinjiang, China

Purpose: The aim of this study is to develop and validate a novel multivariable prediction model capable of accurately estimating the probability of cataract development, utilizing parameters such as blood biochemical markers and age.

Design: This population-based cross-sectional study comprised 9,566 participants drawn from the National Health and Nutrition Examination Survey (NHANES) across the 2005–2008 cycles.

Methods: Demographic information and laboratory test results from the patients were collected and analyzed using LASSO regression and multivariate logistic regression to accurately capture the influence of biochemical indicators on the outcomes. The SHAP (Shapley Additive Explanations) scale was employed to assess the importance of each clinical feature, excluding age. A multivariate logistic regression model was then developed and visualized as a nomogram. To assess the model's performance, its discrimination, calibration, and clinical utility were evaluated using receiver operating characteristic (ROC) curves, 10-fold cross-validation, Hosmer-Lemeshow calibration curves, and decision curve analysis (DCA), respectively.

Results: Logistic regression analysis identified age, erythrocyte folate (nmol/L), blood glucose (mmol/L), and blood urea nitrogen (mmol/L) as independent risk factors for cataract, and these variables were incorporated into a multivariate logistic regression-based nomogram for cataract risk prediction. The area under the receiver operating characteristic (ROC) curve (AUC) for cataract risk prediction was 0.917 (95% CI: 0.9067–0.9273) in the training cohort, and 0.9148 (95% CI: 0.8979–0.9316) in the validation cohort. The Hosmer-Lemeshow calibration curve demonstrated a good fit, indicating strong model calibration. Ten-fold cross-validation confirmed the logistic regression model's robust predictive performance and stability during internal validation. Decision curve analysis (DCA) demonstrated that the nomogram prediction model provided greater clinical benefit for predicting cataract risk when the patient's threshold probability ranged from 0.10 to 0.90.

Conclusion: This study identified blood urea nitrogen (mmol/L), serum glucose (mmol/L), and erythrocyte folate (mmol/L) as significant risk factors for cataract. A risk prediction model was developed, demonstrating strong predictive accuracy and clinical utility, offering clinicians a reliable tool for early and effective diagnosis. Cataract development may be delayed by reducing levels of blood urea nitrogen, serum glucose, and erythrocyte folate through lifestyle improvements and dietary modifications.

KEYWORDS

cataract, blood biochemical indicators, prediction model, nomogram, machine learning

1 Introduction

Cataracts, characterized by the clouding of the lens, are a leading cause of vision impairment and blindness among older adults worldwide (1). In China, the prevalence of cataracts among individuals aged 45–89 exceeds 22% (2). Further research indicates that the cataract prevalence among individuals aged 60 and older ranges between 53 and 58% (3). With population growth and aging, the incidence of cataracts and the demand for cataract surgeries are expected to rise steadily (4). Although cataract surgery significantly improves vision, it remains prohibitively expensive, and many low-income countries face a shortage of skilled surgeons (5). Reducing cataract incidence is essential. Cataracts are associated with multiple factors, including smoking, diabetes, UV exposure, and blood metabolites (6). Identifying and targeting modifiable risk factors can substantially reduce the health and economic burden of cataracts.

Aging is the predominant factor influencing cataract development; however, additional factors also contribute to their onset (7). Numerous researchers have explored the impact of nutritional status on cataract formation and the potential use of biochemical markers to assess the risk of cataractogenesis, as these parameters can be modified by lifestyle changes (8, 9). Blood biochemical markers serve as key indicators of the body's overall metabolic state (10). Therefore, we aim to develop a logistic regression model incorporating blood biochemical markers and age to visualize the components contributing to cataract risk via a nomogram. However, to the best of our knowledge, no existing model currently predicts cataracts based on blood biochemical markers and age.

This article presents the findings of a cross-sectional study using data from the National Health and Nutrition Examination Survey (NHANES) conducted between 2005 and 2008. The aim of our study was to develop and validate a novel multivariate predictive model to accurately assess the probability of cataract onset based on blood biochemical markers and age. Additionally, we sought to explore the potential causes of cataracts.

2 Materials and methods

2.1 Data source and study population

NHANES is an extensive nationwide survey conducted by the National Center for Health Statistics. Its purpose is to evaluate the health and nutritional condition of the American people. It is a department of the U.S. Centers for Disease Control and Prevention. The survey data in NHANES were organized in a biennial style. We utilized data from two consecutive survey cycles (2005–2006 and 2007–2008) about cataracts. Of all 20,497 participants in NHANES 2005–2008, we excluded those without complete information on cataracts ($n = 9{,}592$). Further, we excluded participants under 20 years old without complete information on other covariates ($n = 1{,}339$). Finally, 9,566 subjects were included in the analytic population. The process of participant selection is summarized in Figure 1.

2.2 Cataract assessment

Consistent with other epidemiological research, a cataract operation was used as a surrogate for a cataract (11). The occurrence of a cataract operation was ascertained by inquiring participants about their history of undergoing a cataract operation. (VIQ071), with responses limited to "yes" or "no." If the response was affirmative, the subject was diagnosed with a cataract (12).

2.3 Covariates assessment

According to previous epidemiological studies concerning cataracts (13), potential confounding factors studied in the current work included sociodemographic factors (gender, age, race) and blood biochemical parameters. The sociodemographic characteristics were obtained using self-reported questionnaires, which included information on gender (male or female), age (continuous), and race (non-Hispanic white, non-Hispanic black, Mexican American, etc.). The source of the blood biochemical parameter specimen is serum. The serum specimens undergo processing, storage, and shipment to the Collaborative Laboratory Services for analysis. The NHANES Laboratory/Medical Technologists Procedures Manual (LPM) provides in-depth instructions on how to collect and prepare specimens. The NHANES QA/QC processes adhere to the requirements set by the 1988 Clinical Laboratory Improvement Act. The NHANES Laboratory/Medical Technologists Procedures Manual (LPM) provides comprehensive guidance for quality assurance and quality control (QA/QC) procedures. Refer to the General Documentation of the Laboratory Data file for comprehensive quality assurance and quality control techniques.

The subsequent blood biochemical values were gathered from patients with cataracts for further study. The laboratory examined the following values: albumin (g/L), alanine aminotransferase (ALT) (U/L), aspartate aminotransferase (AST) (U/L), alkaline phosphatase (U/L), and blood urea nitrogen (mmol/L). Blood calcium concentrations were measured in millimoles per liter (mmol/L), cholesterol levels in millimoles per liter (mmol/L), and bicarbonate, creatinine, and gamma glutamyltransferase concentrations in millimoles per liter (mmol/L), micromoles per liter (μmol/L), and units per liter (U/L), respectively. The serum's glucose concentration was measured in millimoles per liter (mmol/L), while the iron content was measured in micromoles per liter (umol/L) and needed to be kept in a refrigerator. The concentration of bilirubin in the blood is measured in micromoles per liter (umol/L). The following measurements are provided in the given units: total protein concentration (g/L), triglycerides (mmol/L), uric acid (mmol/L), sodium (mmol/L), potassium (mmol/L), chloride (mmol/L),

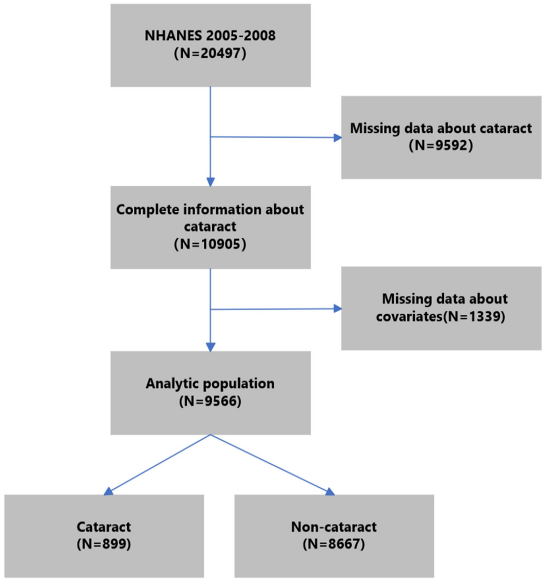

FIGURE 1
Flow chart of the study population.

osmolality (mmol/kg), globulins (g/L), C-reactive proteins (mg/dL), erythrocyte folate (mmol/L), serum folate (mmol/L), and glycated hemoglobin (%).

3 Statistical analysis

The median (interquartile range) was employed to represent continuous data, while categorical data were expressed as number (percentage) (14, 15). Comparisons between cataract and non-cataract groups were conducted using statistical tests such as the unpaired t-test, Wilcoxon rank-sum test, Pearson Chi-square test, or Fisher's exact test, as appropriate. Cases from the NHANES dataset were randomly allocated into a training set ($n = 6,696$) and a validation set ($n = 2,870$) in a 7:3 ratio. The outcome variable for this study was cataract status. To manage data dimensionality and predictor selection, the researchers employed the least absolute shrinkage and selection operator (LASSO) regression and multivariable logistic regression (16). Multivariable logistic regression analysis was used to develop a predictive model and a nomogram of cataract (17). The model's discriminative ability was assessed by calculating the area under the curve (AUC) (18). To enhance the estimation of model performance, 10-fold cross-validation was employed for evaluation. The model's calibration was assessed using the Hosmer-Lemeshow test and calibration curve, while its clinical utility was evaluated through decision curve analysis (DCA) (19). All statistical analyses were performed using R software (version 4.3.2; R Foundation for Statistical Computing, Vienna, Austria) and Python (version 3.12). A significance threshold of $p < 0.05$ was applied to determine statistical significance.

LASSO regression (Least Absolute Shrinkage and Selection Operator) efficiently integrates variable selection with regularization, enhancing both the predictive accuracy and interpretability of statistical models. Through the introduction of an L1 penalty, LASSO reduces specific coefficients to zero, thus enabling efficient variable selection. The optimal lambda (λ) is typically determined via 10-fold cross-validation, aiming to minimize prediction error while balancing model complexity and fit. In this study, 20-fold cross-validation was employed, which, despite the higher computational costs, produces more stable and accurate model evaluations.

The analysis commenced with data preprocessing, wherein categorical variables such as sex, diagnosis, and race were transformed into factor variables to ensure appropriate handling during modeling. Numerical variables were subsequently normalized using a min-max scaling function, which transformed each variable into a range of [0,1]. This normalization is critical in LASSO regression, as the model is sensitive to the scale of the input variables. The transformation was applied to all numeric variables within the dataset using the mutate_if function within a pipeline, and the resultant dataset was converted into a data frame for further processing. To ensure reproducibility, a random seed was set [set. seed (123)], and the preprocessed data was partitioned into a matrix of predictors (x) and a response vector (y). The response vector y was further converted to numeric form to be compatible with the modeling functions. The LASSO regression was executed using the glmnet function, specifying a binomial family to accommodate the binary nature of the outcome variable. The function was configured to evaluate 1,000 distinct values of the regularization parameter lambda (n lambda = 1,000), enabling the model to thoroughly explore the regularization path. This extensive range of lambda values ensures that the model can identify the optimal level of penalization, balancing model complexity with predictive performance. Following the initial fitting of the LASSO model, the regularization path was visualized using a plot of the model coefficients against the logarithm of lambda. This plot facilitates understanding of how the coefficients shrink as the penalization increases, and which variables remain significant across varying levels of lambda. To validate the model and prevent overfitting, a 20-fold cross-validation was conducted using the cv. glmnet function. This process involves partitioning the data into 20 subsets, fitting the model on 19 subsets, and validating it on the remaining one. This procedure is repeated 20 times, ensuring that each subset serves as a validation set once. The cross-validation results were plotted to visualize the relationship between lambda and the cross-validated error, aiding in the selection of the most appropriate lambda value. Two key lambda values were identified from the cross-validation results: Lambda. min: The lambda value that minimizes the cross-validated mean squared error (MSE), representing the point at which the model achieves the best predictive accuracy. Lambda.1se: The lambda value that is one standard error above the minimum MSE. This value typically results in a more parsimonious model, as it provides a simpler model with fewer predictors, while still maintaining a reasonable level of accuracy. Finally, the model coefficients corresponding to lambda. 1se were extracted using the coef function. These coefficients indicate which variables are most influential in predicting the outcome, offering insights into the underlying relationships within the data.

For multivariable logistic regression:variable selection criteria are based on significance testing ($p < 0.05$). LASSO-screened variables were included in the multivariable logistic regression, and variables with p less than 0.05 were selected for the prediction model.

TABLE 1 **Demographic and clinical characteristics of study participants.**

Characteristic	Total (*n* = 9,566)	Cataract (*n* = 899)	Non-cataract (*n* = 8,667)	*p*
Gender, *n* (%)				0.089
Male	4,637 (48)	411 (46)	4,226 (49)	
Female	4,929 (52)	488 (54)	4,441 (51)	
Age, Median (Q1,Q3)	48 (34, 64)	78 (70, 80)	46 (33, 61)	< 0.001
Ethnicity, *n* (%)				< 0.001
Mexican American	1821 (19)	72 (8)	1749 (20)	
Other Hispanic	719 (8)	56 (6)	663 (8)	
Non-Hispanic White	4,678 (49)	633 (70)	4,045 (47)	
Non-Hispanic Black	1957 (20)	112 (12)	1845 (21)	
Other Race - Including Multi-Racial	391 (4)	26 (3)	365 (4)	
Albumin (g/L), Median (Q1,Q3)	42 (40, 44)	41 (39, 44)	42 (40, 44)	< 0.001
alanine aminotransferase (ALT) (U/L), Median (Q1,Q3)	21 (16, 28)	19 (15, 24)	21 (17, 29)	< 0.001
Asparate aminotransferase (AST) (U/L), Median (Q1,Q3)	23 (20, 28)	24 (21, 28)	23 (20, 28)	0.001
Alkaline phosphotase (U/L), Median (Q1,Q3)	67 (55, 82)	71 (59, 86)	67 (55, 82)	< 0.001
Blood urea nitrogen (mmol/L), Median (Q1,Q3)	4.28 (3.21, 5.36)	6.07 (4.28, 7.85)	4.28 (3.21, 5.36)	< 0.001
Total calcium (mmol/L), Median (Q1,Q3)	2.35 (2.3, 2.42)	2.35 (2.3, 2.42)	2.35 (2.3, 2.42)	0.319
Cholesterol (mmol/L), Median (Q1,Q3)	5.04 (4.37, 5.82)	4.89 (4.19, 5.77)	5.07 (4.4, 5.82)	< 0.001
Bicarbonate (mmol/L), Median (Q1,Q3)	25 (23, 26)	25 (24, 27)	25 (23, 26)	< 0.001
Creatinine (μmol/L), Median (Q1,Q3)	76.91 (63.65, 89.28)	88.4 (72.49, 106.08)	74.26 (63.65, 88.4)	< 0.001
Gamma glutamyl transferase (U/L), Median (Q1,Q3)	21 (15, 32)	20 (15, 30)	21 (15, 32)	0.18
Glucose, serum (mmol/L), Median (Q1,Q3)	5.16 (4.72, 5.77)	5.61 (5, 6.61)	5.11 (4.66, 5.72)	< 0.001
Iron, refigerated (umol/L), Median (Q1,Q3)	14.3 (10.7, 18.75)	13.6 (10.6, 18.1)	14.5 (10.7, 18.8)	0.003
Lactate dehydrogenase LDH (U/L), Median (Q1,Q3)	128 (113, 146)	140 (122, 160)	127 (112, 144)	< 0.001
Phosphorus (mmol/L), Median (Q1,Q3)	1.23 (1.1, 1.32)	1.23 (1.1, 1.32)	1.23 (1.1, 1.32)	0.595
Bilirubin, total (umol/L)(umol/L), Median (Q1,Q3)	11.97 (8.55, 15.39)	11.97 (10.26, 15.39)	11.97 (8.55, 15.39)	< 0.001
Total protein (g/L), Median (Q1,Q3)	71 (68, 74)	70 (68, 74)	71 (68, 75)	< 0.001
Triglycerides (mmol/L), Median (Q1,Q3)	1.42 (0.94, 2.2)	1.55 (1.05, 2.23)	1.41 (0.93, 2.2)	< 0.001
Uric acid (umol/L), Median (Q1,Q3)	315.2 (261.7, 374.7)	333.1 (279.6, 395.55)	315.2 (261.7, 374.7)	< 0.001
Sodium (mmol/L), Median (Q1,Q3)	139 (138, 141)	140 (138, 141)	139 (138, 140)	< 0.001
Potassium (mmol/L), Median (Q1,Q3)	3.95 (3.7, 4.2)	4.1 (3.8, 4.3)	3.9 (3.7, 4.1)	< 0.001
Chloride (mmol/L), Median (Q1,Q3)	104 (102, 106)	104 (101, 105)	104 (102, 106)	< 0.001
Osmolality (mmol/Kg), Median (Q1,Q3)	278 (275, 281)	281 (277, 284)	278 (275, 281)	< 0.001
Globulin (g/L), Median (Q1,Q3)	29 (26, 32)	29 (26, 32)	29 (27, 32)	0.125
C-reactive protein(mg/dL), Median (Q1,Q3)	0.21 (0.08, 0.49)	0.25 (0.1, 0.56)	0.21 (0.08, 0.49)	< 0.001
RBC folate (nmol/L), Median (Q1,Q3)	840.3 (586.6, 1,220)	1112.1 (758.8, 1,620)	820 (576, 1184.6)	< 0.001
Serum folate (nmol/L), Median (Q1,Q3)	31.5 (21.5, 45.9)	43.9 (29.5, 71.05)	30.6 (21, 44)	< 0.001
Glycohemoglobin (%), Median (Q1,Q3)	5.4 (5.2, 5.8)	5.7 (5.4, 6.2)	5.4 (5.1, 5.7)	< 0.001

4 Results

4.1 Patient characteristics

Out of the individuals involved in the study, 9.4% (899 out of 9,556) were diagnosed with cataracts. Table 1 displays the demographic and clinical characteristics of the individuals who participated in the study. Out of the 30 variables obtained from patients, 5 were chosen based on non-zero coefficients produced by LASSO regression analysis (Figure 2).

4.2 Identification of the risk factors for cataract

The variables consisted of blood urea nitrogen (mmol/L), blood glucose (mmol/L), erythrocyte folate (mmol/L), serum folate (mmol/L), and age. The logistic regression prediction model was created using a multivariable method, incorporating the five factors chosen by LASSO regression as independent variables. The research's findings demonstrate that blood urea nitrogen (mmol/L), glucose (mmol/L), serum

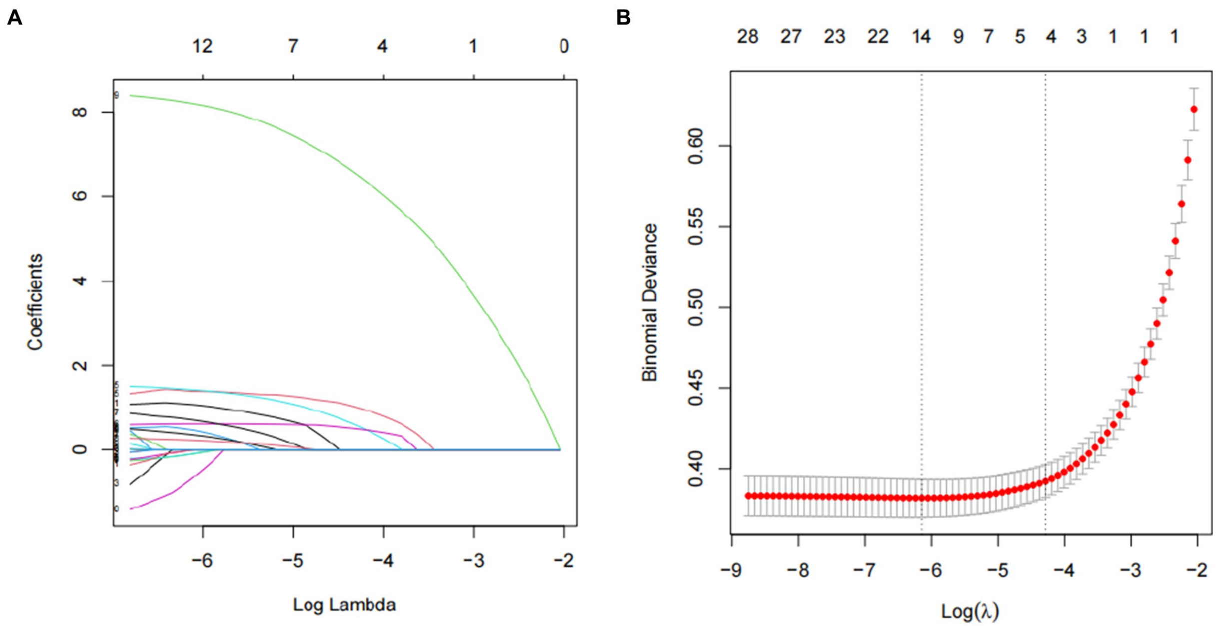

FIGURE 2
Predictor selection using the LASSO regression analysis with twenty fold cross-validation. (A) Tuning parameter (lambda) selection of deviance in the LASSO regression based on the minimum criteria (left dotted line) and the 1-SE criteria (right dotted line). (B) A coefficient profile plot was created against the log (lambda) sequence. In the present study, predictor's selection was according to the 1-SE criteria (right dotted line), where 5 nonzero coefficients were selected. LASSO, least absolute shrinkage and selection operator; SE, standard error.

(mmol/L), erythrocyte folate (nmol/L), and age have been identified as risk factors for cataract. These results are presented in Table 2.

4.3 Comparison of predictive influence

It is crucial to compare the impact of biochemical indicators with the influence of age, given that age remains the most significant predictor of cataracts. When age was used as the sole predictor in this study's dataset, the area under the ROC curve (AUC) was 0.9167 (95% CI: 0.9066–0.9267) in the training set and 0.904 (95% CI: 0.8853–0.9228) in the validation set. While age alone demonstrated robust predictive performance, incorporating models identified through LASSO and multivariate logistic regression further enhanced predictive accuracy. In this study, the AUC for the training set was 0.917 (95% CI: 0.9067–0.9273), and for the validation set, the AUC was 0.9148 (95% CI: 0.8979–0.9316).

4.4 Utilizing SHAP to highlight variable importance

To facilitate the visual interpretation of the selected variables, we employed SHAP (20) to elucidate the specific contributions of these variables to the model's prediction of cataract formation. Figure 8 highlights the 19 most significant features in the logistic regression model, which was developed using 29 variables. Each feature's contribution to the outcome is represented by colored dots along the significance line, with red indicating high-risk values and blue representing low-risk values. Among the top five features, elevated levels of blood urea nitrogen, serum folate, erythrocyte folate, osmolality, and potassium were associated with an increased risk of age-related cataract formation. Figure 9 presents the ranking of the 19 risk factors, evaluated by the mean absolute SHAP value, with the SHAP value on the *X*-axis reflecting each factor's importance in the predictive model. Without variable screening, the ROC curve for the test set was 0.8 when all variables were included in the model, and 0.73 when only blood urea nitrogen was included. After applying the stacked formula sequentially, model performance did not improve with the inclusion of the third variable, erythrocyte folate. The area under the ROC curve for the test set was 0.77, decreasing slightly to 0.76 following the inclusion of erythrocyte folate. Two variables, blood urea nitrogen and erythrocyte folate, were consistently selected through LASSO and multivariate logistic regression screening, indicating their significant impact on cataract prognosis. However, based on the SHAP scores, blood urea nitrogen, serum folate, and erythrocyte folate were ranked 1st, 2nd, and 3rd, respectively, while serum glucose was ranked 11th in terms of importance. In summary, the model constructed using variables identified through LASSO and multivariate logistic regression screening proved to be feasible.

4.5 Construction of predictive model for cataract

Based on the four variables indicated above that were chosen using the LASSO regression approach and the logistic regression technique, multivariable logistic regression analysis was carried out to create a predictive model for cataract. The differentiation of the cataract risk prediction model was assessed using the ROC curve. The training group's AUC was 0.917 (95%CI = 0.9067–0.9273) and the validation group's was 0.9148 (95%CI = 0.8979–0.9316), according to

TABLE 2 **Multivariate logistic regression was used to analyze the influencing factors of cataract.**

variable	β	SE	*z* value	OR	2.5–97.5%CI	*p* value
Blood urea nitrogen (mmol/L)	0.041	0.016	2.563	1.042	1.009–1.074	<0.001
Glucose, serum (mmol/L)	0.069	0.017	4.168	1.072	1.036–1.107	0.01
RBC folate (nmol/L)	0.0003	0	3.281	1	1.0001–1.0004	<0.001
Serum folate (nmol/L)	0.0016	0.001	1.054	1.002	0.998–1.004	0.291
Age	0.134	0.005	28.811	1.143	1.133–1.152	<0.001

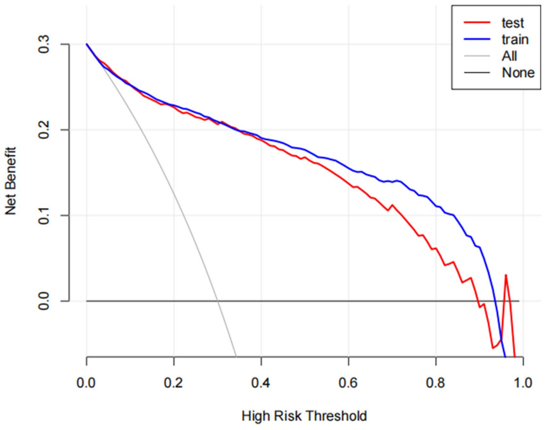

FIGURE 3
The benefit curve represented by the prediction model. The *y*-axis indicates the overall net benefit, which is calculated by summing the benefits (true positive results) and subtracting the harms (false positive results). The *x*-axis indicates the threshold that used to decide whether it is high risk to have cataracts. All: net benefit curve when all cataract patients are treated. None: net benefit curve when all cataract patients are not treated.

the data (Figure 4). A nomogram was created in order to depict the predictive model, offering a useful customized tool for assessing the probability of cataract development (Figure 5). The suggested model (Figure 6) has good calibration. For the Hosmer-Lemeshow test, a *p*-value of less than 0.05 is typically seen as indicating a poor model fit and a significant discrepancy between the predicted and true values. However, this study's huge sample size is associated with the HL test results (21). With bigger and larger sample sizes, it is more likely that simply uncorrelated disparities between estimated and true probability will result in the rejection of the perfect fit hypothesis since the power of classic goodness-of-fit tests grows with sample size (22). As a result, an HL test *p*-value of less than 0.05 does not always signify a poor model fit. In this study, the relatively small deviation of the calibration curves from the reference line indicates that the fit between predicted and observed values is not statistically significantly biased and is therefore highly credible. To further assess model calibration, we computed the Brier score (23), a metric that evaluates the accuracy of probabilistic predictions, particularly for binary outcomes. A Brier score of 0.057 in the training set indicates strong model calibration, reflecting the model's accurate probabilistic performance. We utilized 10-fold cross-validation for model evaluation, and the resulting performance metrics are presented in Figure 7. Based on these results, our 10-fold cross-validation analysis confirms that the logistic regression model exhibits moderate-to-strong predictive ability and is likely to perform robustly in external validation studies.

DCA was also carried out to evaluate its clinical utility (Figure 3). In decision curve analysis (DCA), the model optimizes true positive rates while minimizing false positives, confirming its capacity to improve clinical decision-making by delivering considerable net benefit across a range of threshold probabilities. The decision curve consistently remains above the "None" line (representing no intervention) across a broad spectrum of threshold probabilities, demonstrating a positive net benefit. This illustrates the model's clinical utility in identifying high-risk patients likely to benefit from intervention. Conversely, red and blue curves falling below the "None" line at higher threshold probabilities suggest that treating all patients results in unnecessary interventions, thereby diminishing net benefit.

Decision curve analysis demonstrates that the nomogram provides optimal predictive performance for cataract risk within high-risk thresholds of 0.10 to 0.90, delivering superior net benefit compared to treating all patients or none. At a threshold of 0.4, where patients with a 40% predicted probability are classified as high-risk and receive treatment, the model yields a net benefit of 0.2. This signifies that 20 out of every 100 patients benefit from treatment without undergoing unnecessary interventions. At a threshold of 0.5, the net benefit decreases to 0.15, indicating that 15 out of every 100 patients benefit from the model's recommendations.

5 Discussion

This study employed LASSO regression alongside multivariate logistic regression to identify key factors associated with cataract risk and to construct a predictive model. Four predictors were evaluated: age, erythrocyte folate (nmol/L), blood glucose (mmol/L), and blood urea nitrogen (mmol/L). Additionally, a logistic regression model was developed using the identified factors. The predictive model demonstrated excellent discriminatory power, calibration, and clinical utility, and was visualized through a nomogram, allowing easy interpretation of the predicted probability.

The LASSO regression technique was used to select independent risk factors for the purpose of modeling and predicting variables of various types. The application of penalized regression reduced the coefficients of less significant independent variables to zero, thereby enhancing model stability. Numerous studies have also employed machine learning techniques to improve and train nomogram-based prediction models for accurately predicting the survival outcomes of patients with breast and colon cancer (24, 25). Multiple factors have been reported to influence cataract development, including socio-demographic and lifestyle factors (4), nutrient intake (12), blood components (26), and genetic predispositions (27). The primary objective of this study was to investigate the influence of

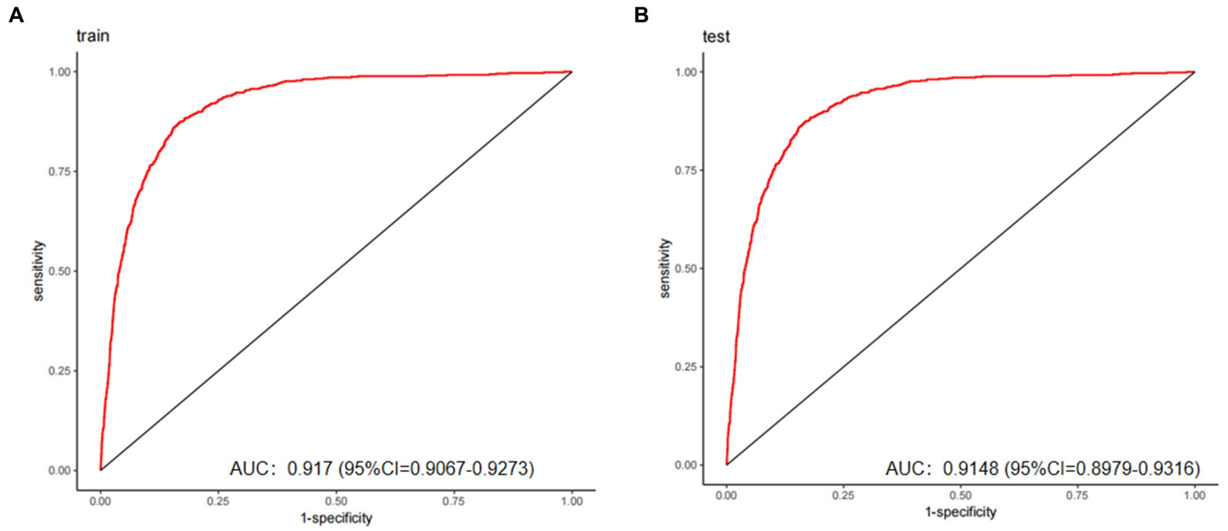

FIGURE 4
The predictive model's performance was assessed using ROC curves for both the training (A) and validation (B) groups, yielding AUC values of 0.917 and 0.9148, respectively. These results demonstrate good discriminative capacity and excellent generalizability.

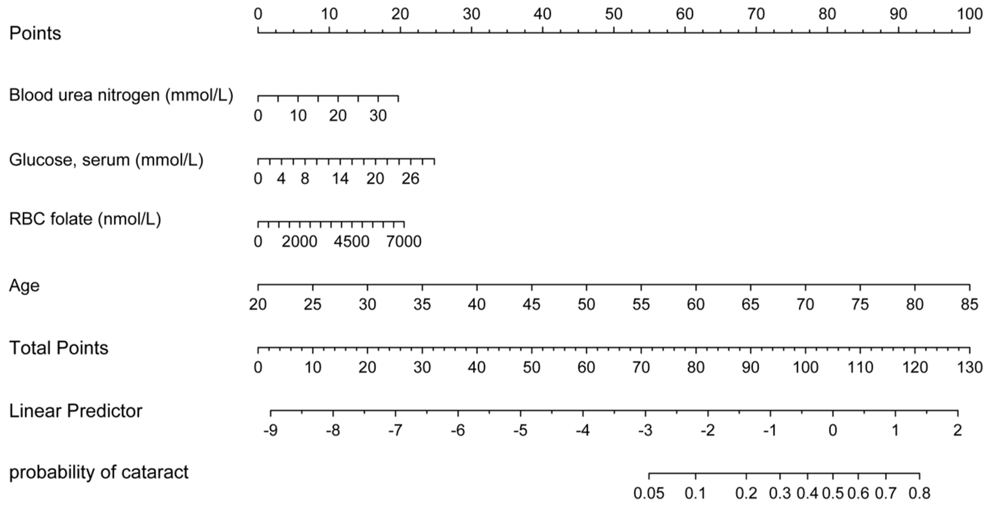

FIGURE 5
Nomogram for predicting cataract risk and its algorithm. First, a point was found for each variable of a people who may have cataracts on the uppermost rule; then all scores were added together and the total number of points were collected. Finally, the corresponding predicted probability of people who may have cataracts was found on the lowest rule.

blood components and age on cataract formation, visualizing the results through a nomogram. To our knowledge, this is the first study to utilize a nomogram to illustrate cataract risk. Multivariate logistic regression analysis in this study revealed statistically significant differences across four variables: blood urea nitrogen (mmol/L), serum glucose (mmol/L), RBC folate (nmol/L), and age. Each of these factors will be discussed in detail in the subsequent sections. The study by C. Y. Huan et al. identified a significant correlation between chronic kidney disease (CKD) and an increased incidence of both prevalent and incident cataracts (28). B. E. Klein et al. suggested that elevated serum blood urea nitrogen (BUN) and creatinine levels are associated with the development of posterior subcapsular cataracts in continuous models (29). These findings, consistent with those of the present study, suggest that elevated blood urea nitrogen is a risk factor for cataract development, with an odds ratio of 1.042 and a 95% confidence interval of 1.009–1.074. Several potential mechanisms are outlined below. The initial hypothesis suggests that chronic hypocalcemia in patients with chronic kidney disease may disrupt glucose metabolism in the lens (30). The interplay between calcium levels, glucose metabolism, and lens health is complex. Nevertheless, in this study, blood urea nitrogen exerted a more pronounced influence on cataract formation compared to calcium and glucose, likely due to its impact on lens osmolarity, thus promoting cataract development. The second hypothesis proposes that elevated blood urea nitrogen levels disrupt enzymes critical to lens metabolism. Oxidative stress is widely

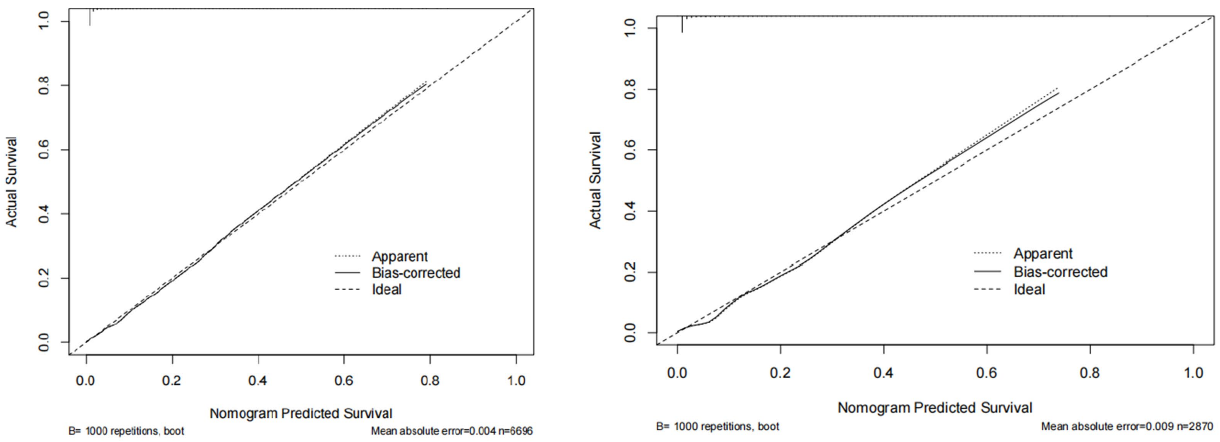

FIGURE 6
The calibration curve of predictive nomograms for predicting cataracts. The nomogram shows the predicted probability on the *x*-axis and the actual probability on the *y*-axis.

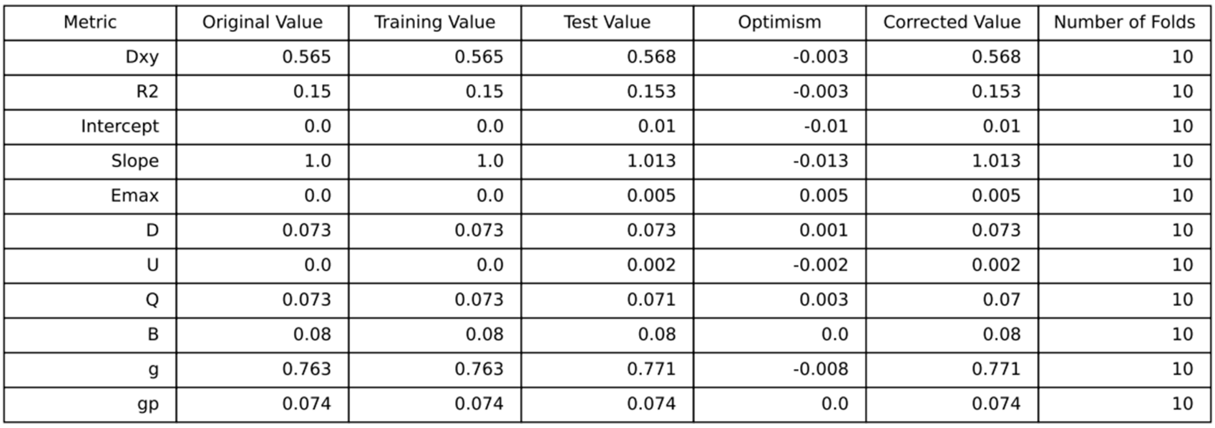

Metric	Original Value	Training Value	Test Value	Optimism	Corrected Value	Number of Folds
Dxy	0.565	0.565	0.568	-0.003	0.568	10
R2	0.15	0.15	0.153	-0.003	0.153	10
Intercept	0.0	0.0	0.01	-0.01	0.01	10
Slope	1.0	1.0	1.013	-0.013	1.013	10
Emax	0.0	0.0	0.005	0.005	0.005	10
D	0.073	0.073	0.073	0.001	0.073	10
U	0.0	0.0	0.002	-0.002	0.002	10
Q	0.073	0.073	0.071	0.003	0.07	10
B	0.08	0.08	0.08	0.0	0.08	10
g	0.763	0.763	0.771	-0.008	0.771	10
gp	0.074	0.074	0.074	0.0	0.074	10

FIGURE 7
Provides a summary of the results from 10-fold cross-validation.

acknowledged as a major contributor to cataract formation, with antioxidant enzymes like glutathione synthase, thioredoxin reductase, glutathione reductase, and thioltransferase playing pivotal roles in slowing cataract progression (31). Elevated blood urea nitrogen may impair the activity of these antioxidant enzymes, thereby accelerating cataract progression. These potential mechanisms require experimental validation. Kang K H, Shin D, Ryu I H, et al. found that fatty liver disease (FLD) may serve as an independent risk factor for cataracts (32), likely due to its role in systemic metabolic disorders. These systemic disorders, often resulting from dyslipidaemia and chronic inflammation linked to FLD, can disrupt metabolic processes throughout the body. One such disruption involves altered biochemical indices, including elevated blood urea nitrogen (BUN) (33). Elevated BUN levels may indicate impaired renal function or increased protein catabolism, both of which could contribute to cataract pathophysiology by promoting oxidative stress and osmotic imbalances in the lens. Therefore, our findings suggest that the heightened risk of cataracts observed in patients with FLD may be mediated, at least in part, by elevated blood urea nitrogen levels. This underscores the need for further investigation into the specific mechanisms connecting FLD, abnormal biochemical markers, and cataract formation, as well as the potential for targeted interventions to mitigate these metabolic disruptions. L. Li et al. identified a significant increase in the likelihood of cataract development among individuals diagnosed with type 2 diabetes mellitus (34). According to this study, elevated glucose levels were associated with an increased likelihood of cataract development. The role of folic acid as a risk factor for cataracts remains debatable. A. Tan et al. showed the 5-year PSC incidence with no significant associations with homocysteine, B12, and folate (35). But C. Ma et al. showed lower serum folate levels in cataract patients compared to controls (36). In addition, W. G. et al. found that in a randomized, double-masked, placebo-controlled trial, combined folic acid, vitamin B6, and vitamin B12 supplementation may increase the risk of cataract extraction surgery (37). The results of W. G. et al. are similar to ours in that folate (nmol/L) was higher in cataract patients compared to non-cataracts, and higher RBC folate (nmol/L) may be a risk factor for cataracts,

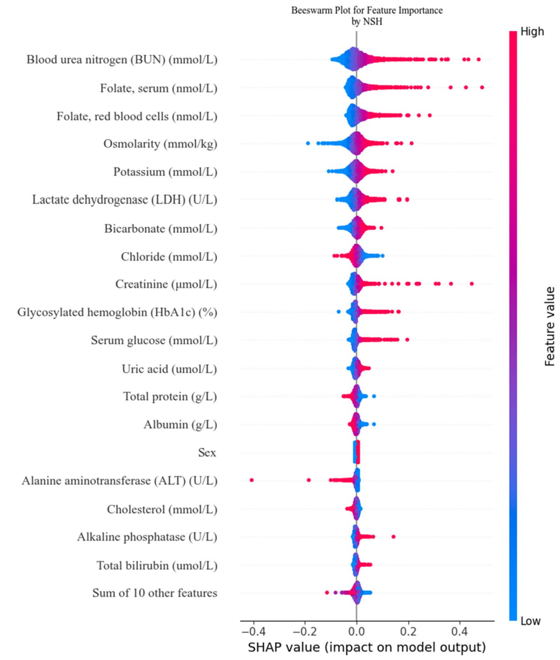

FIGURE 8
Feature contributions in SHAP: each line represents a feature, with the SHAP value plotted on the *x*-axis. Red dots indicate higher feature values, while blue dots indicate lower feature values. The spread of the dots along the x-axis illustrates the impact of each feature on the model's prediction.

but to a lesser extent with an OR close to one. Among the previous studies, folic acid supplementation was considered protective against cataracts (38). Tan, A. and colleagues utilized posterior subcapsular cataract (PSC) as the outcome measure in a 5-year follow-up study, revealing that elevated homocysteine levels (per SD; OR 1.17; 95% CI 1.00–1.37) and reduced folic acid levels (per SD; OR 1.24; 95% CI 0.99–1.56) were associated with a higher prevalence of PSC36. Ma, C., Liu, Z., Yao, S., Hei, L., and Guo, W. prospectively recruited 60 patients with senile cataracts and 58 age-matched healthy controls, finding that blood folate levels were significantly lower in cataract patients than in healthy controls. Kuzniarz, M. and Mitchell, P. conducted a cross-sectional study with 2,873 participants, categorizing cataract types and concluding that folic acid supplementation had a protective effect against cortical cataracts. Despite differences in methodology, all three research teams consistently found that cataract patients had lower folic acid levels and that folic acid supplementation may confer a protective effect against cataracts. However, the findings of Christen, W. G. and colleagues were unexpected. In contrast to the previous three studies, Christen, W. G. and colleagues conducted a randomized, double-blind, placebo-controlled trial under more stringent conditions, involving 3,925 participants and yielding more robust results over a follow-up period of up to 7.3 years. In this large-scale randomized trial of women at high risk for cardiovascular disease, daily supplementation with folic acid, vitamin B6, and vitamin B12 had no significant impact on cataract incidence but may have increased the risk of cataract extraction. The findings of Christen, W. G. and colleagues, which aligned with our results that also focused on cataract removal, indicated a facilitating effect of folic acid with an OR close to 1 (95% CI 1.0001–1.0004). The aforementioned studies varied considerably in design, encompassing both observational studies and randomized controlled trials (RCTs). The study populations also differed in demographics, baseline health conditions, and genetic predispositions, all of which may have influenced the observed association between folic acid levels and cataract risk. For example, both this study and the work by C. Ma et al., which used cataract surgery as the outcome measure, reached the same conclusion: higher folic acid levels increased the risk of cataract extraction. These findings underscore the need for longitudinal studies with extended follow-up periods to comprehensively assess the role of folic acid in cataract development. Given the findings of this study, we recommend exercising caution when considering folic acid supplementation as a means to delay the onset of cataracts. It is well established that age is a major determinant of cataract development and requires little further discussion (6).

This study has several limitations. In the absence of direct lens assessments in the NHANES dataset, cataract surgery was used as a surrogate marker for cataract occurrence. A similar approach has been employed in previous epidemiological studies11. However, the distinctions between the two approaches should not be overlooked. The decision to undergo cataract surgery is influenced by a multitude of factors, including cataract severity, visual acuity, ocular measurements, the surgeon's clinical expertise, and patient preferences (39). The decision to opt for cataract surgery is heavily contingent upon financial resources (40), which also shape health literacy and behavioral patterns, subsequently influencing blood biochemical markers (41). When cataract surgery is employed as an outcome measure, this economic disparity introduces significant selection bias (42). Individuals with higher disposable income and better access to healthcare are more likely to undergo regular ophthalmologic evaluations, facilitating early cataract detection and timely intervention. Conversely, individuals from lower socioeconomic backgrounds frequently delay or forgo surgery due to financial barriers, leading to pronounced disparities in health outcomes. Furthermore, health literacy—the capacity to access, interpret, and comprehend essential health information—tends to be higher in wealthier populations. Wealthier individuals are generally more proactive in managing their health, frequently engaging in preventive behaviors such as regular medical check-ups and strict adherence to medical advice. This often results in more favorable biochemical profiles (e.g., better glycemic control), potentially influencing study outcomes. The direct correlation between socioeconomic status and improved access to nutrition, healthcare, and healthier lifestyles is well-documented (43). Populations of lower socioeconomic status typically present with more abnormal biochemical markers and a higher prevalence of severe cataracts (44). Failure to account for these socioeconomic factors may lead to an overestimation of the impact of biochemical markers on cataract risk. This overestimation may partly arise from the fact that individuals of lower socioeconomic status are more likely to adopt unhealthy lifestyles, such as poor diets and lack of exercise, and face limited access to quality healthcare. Consequently, the observed association between biochemical indicators and cataract risk may be confounded by underlying socioeconomic conditions. Additionally, cataract surgery reflects a relatively advanced stage of the disease, and the relationship between early

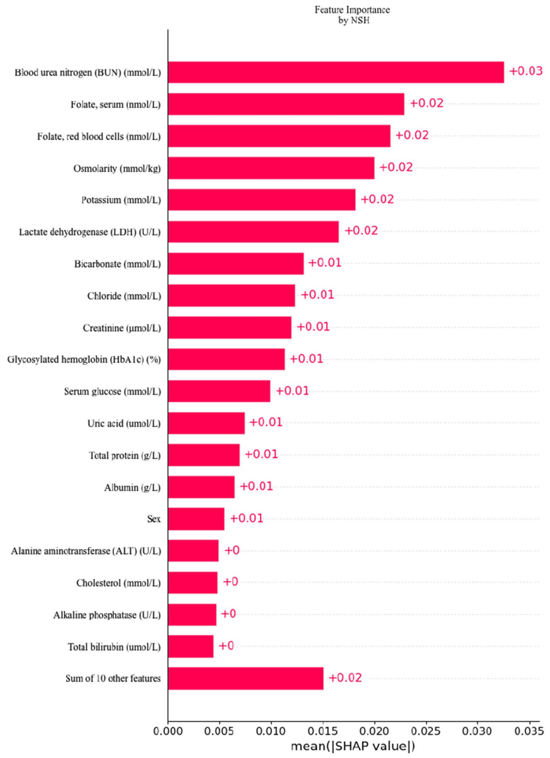

FIGURE 9
Feature importance ranking by SHAP: this matrix diagram ranks the importance of each covariate in the development of the final predictive model, highlighting which features contribute most significantly to the model's output.

lens opacity and biochemical markers could not be assessed using NHANES data. Furthermore, the data derived from cataract surgery do not allow for differentiation between distinct types of cataracts in individual patients.

Nevertheless, several limitations exist in this study. The risk factor analysis did not account for potential variables such as patients' daily living environments and dietary habits, which were not integrated into the predictive model. Incorporating these factors would likely enhance the model's predictive accuracy and overall performance. This study was conducted retrospectively at a single center, and the predictive validity of the model was not assessed through external validation. This study was a retrospective analysis conducted at a single center. The predictive validity of the model was established using internal validation methods; however, external validation was not performed. It is important to note that while the model shows promise based on its internal validation, the lack of external validation limits our ability to generalize the findings to other settings or populations. Future research will focus on validating the model using large datasets from multiple regions and centers to enhance its predictive accuracy and broader applicability.

6 Conclusion

This study identified blood urea nitrogen (mmol/l), serum glucose (mmol/l), erythrocyte folate (mmol/l), and age as significant risk factors for cataracts, and subsequently developed a cataract risk prediction model. This model demonstrated strong predictive accuracy and clinical applicability, offering clinicians a valuable tool for early and accurate diagnosis. Cataract progression may be delayed by lowering blood urea nitrogen, serum glucose, and erythrocyte folate levels through lifestyle modifications and dietary improvements.

Data availability statement

The datasets presented in this study can be found in online repositories. The names of the repository/repositories and accession number(s) can be found here: https://www.cdc.gov/nchs/nhanes/ and in the article/Supplementary material.

Ethics statement

The studies involving humans were approved by the National Centre for Health Statistics (NCHS) Research Ethics Review Board. The studies were conducted in accordance with the local legislation and institutional requirements. The human samples used in this study were acquired from Institutional Review Board Statement: The National Centre for Health Statistics (NCHS) Research Ethics Review Board (protocol 2005–06) granted approval for this investigation. Extensive information can be found at the following website: https://www.cdc.gov/nchs/nhanes/irba98.htm (accessed on February 16, 2024). Informed consent was obtained from all subjects involved in the study. Written informed consent for participation was not required from the participants or the participants' legal guardians/next of kin in accordance with the national legislation and institutional requirements.

Author contributions

GW: Conceptualization, Data curation, Funding acquisition, Investigation, Methodology, Resources, Software, Supervision, Validation, Visualization, Writing – original draft, Writing – review & editing. X-LY: Conceptualization, Data curation, Formal analysis, Funding acquisition, Project administration, Supervision, Investigation, Resources, Writing – review & editing.

Funding

The author(s) declare that financial support was received for the research, authorship, and/or publication of this article. The Natural Science Foundation of Xinjiang Uygur Autonomous Region, China, is funding the key project with the reference number 2022D01D68.

Acknowledgments

The authors express their gratitude to all the participants and personnel involved in the National Health and Nutrition Examination

Survey for their significant contributions to the collection, management, and release of data. In the course of preparing this manuscript, we employed OpenAI's ChatGPT (version GPT-4.0) as a tool to aid in refining and enhancing the linguistic clarity and coherence of the article. We gratefully acknowledge the valuable contributions of this technology in improving the overall textual quality and presentation.

Conflict of interest

The authors declare that the research was conducted in the absence of any commercial or financial relationships that could be construed as a potential conflict of interest.

Publisher's note

Supplementary material

The Supplementary material for this article can be found online at: https://www.frontiersin.org/articles/10.3389/fmed.2024.1452756/full#supplementary-material

References

1. Steinmetz JD, Bourne RRA, Briant PS, Flaxman SR, Taylor HRB, Jonas JB, et al. Causes of blindness and vision impairment in 2020 and trends over 30 years, and prevalence of avoidable blindness in relation to VISION 2020: the right to sight: an analysis for the global burden of disease study. *Lancet Glob Health*. (2021) 9:e144–60. doi: 10.1016/s2214-109x(20)30489-7

2. Song P, Wang H, Theodoratou E, Chan KY, Rudan I. The national and subnational prevalence of cataract and cataract blindness in China: a systematic review and meta-analysis. *J Glob Health*. (2018) 8:010804. doi: 10.7189/jogh.08.010804

3. Singh S, Pardhan S, Kulothungan V, Swaminathan G, Ravichandran JS, Ganesan S, et al. The prevalence and risk factors for cataract in rural and urban India. *Indian J Ophthalmol*. (2019) 67:477–83. doi: 10.4103/ijo.IJO_1127_17

4. Purola PKM, Nättinen JE, Ojamo MUI, Rissanen HA, Gissler M, Koskinen SVP, et al. Prevalence and 11-year incidence of cataract and cataract surgery and the effects of socio-demographic and lifestyle factors. *Clin Ophthalmol*. (2022) 16:1183–95. doi: 10.2147/opth.S355191

5. Yan W, Wang W, van Wijngaarden P, Mueller A, He M. Longitudinal changes in global cataract surgery rate inequality and associations with socioeconomic indices. *Clin Experiment Ophthalmol*. (2019) 47:453–60. doi: 10.1111/ceo.13430

6. Liu YC, Wilkins M, Kim T, Malyugin B, Mehta JS. Cataracts. *Lancet*. (2017) 390:600–12. doi: 10.1016/s0140-6736(17)30544-5

7. Hashemi H, Pakzad R, Yekta A, Aghamirsalim M, Pakbin M, Ramin S, et al. Global and regional prevalence of age-related cataract: a comprehensive systematic review and meta-analysis. *Eye (Lond)*. (2020) 34:1357–70. doi: 10.1038/s41433-020-0806-3

8. Bunce GE, Kinoshita J, Horwitz J. Nutritional factors in cataract. *Annu Rev Nutr*. (1990) 10:233–54. doi: 10.1146/annurev.nu.10.070190.001313

9. Leske MC, Wu SY, Hyman L, Sperduto R, Underwood B, Chylack LT, et al. Biochemical factors in the lens opacities. Case-control study. The Lens opacities case-control study group. *Arch Ophthalmol*. (1995) 113:1113–9. doi: 10.1001/archopht.1995.01100090039020

10. Lee YW, Lin YY, Weng SF, Hsu CH, Huang CL, Lin YP, et al. Clinical significance of hepatic function in graves disease with type 2 diabetic mellitus: a single-center retrospective cross-sectional study in Taiwan. *Medicine (Baltimore)*. (2022) 101:e30092. doi: 10.1097/md.0000000000030092

11. García-Layana A, Ciufo G, Toledo E, Martínez-González M, Corella D, Fitó M, et al. The effect of a Mediterranean diet on the incidence of cataract surgery. *Nutrients*. (2017) 9:453. doi: 10.3390/nu9050453

12. Zhou J, Lou L, Jin K, Ye J. Association between healthy eating Index-2015 and age-related cataract in American adults: a cross-sectional study of NHANES 2005-2008. *Nutrients*. (2022) 15:98. doi: 10.3390/nu15010098

13. Theodoropoulou S, Theodossiadis P, Samoli E, Vergados I, Lagiou P, Tzonou A. The epidemiology of cataract: a study in Greece. *Acta Ophthalmol*. (2011) 89:e167–73. doi: 10.1111/j.1755-3768.2009.01831.x

14. Wan X, Wang W, Liu J, Tong T. Estimating the sample mean and standard deviation from the sample size, median, range and/or interquartile range. *BMC Med Res Methodol*. (2014) 14:135. doi: 10.1186/1471-2288-14-135

15. Rosner B, Glynn RJ. Power and sample size estimation for the Wilcoxon rank sum test with application to comparisons of C statistics from alternative prediction models. *Biometrics*. (2009) 65:188–97. doi: 10.1111/j.1541-0420.2008.01062.x

16. Green MA. Use of machine learning approaches to compare the contribution of different types of data for predicting an individual's risk of ill health: an observational study. *Lancet*. (2018) 392:S40. doi: 10.1016/s0140-6736(18)32877-0

17. Sun S, Wang J, Yang B, Wang Y, Yao W, Yue P, et al. A nomogram for evaluation and analysis of difficulty in retroperitoneal laparoscopic adrenalectomy: a single-center study with prospective validation using LASSO-logistic regression. *Front Endocrinol*. (2022) 13:1004112. doi: 10.3389/fendo.2022.1004112

18. de Hond AAH, Steyerberg EW, van Calster B. Interpreting area under the receiver operating characteristic curve. *Lancet Digit Health*. (2022) 4:e853–5. doi: 10.1016/s2589-7500(22)00188-1

19. Van Calster B, Wynants L, JFM V, Verbakel JY, Christodoulou E, et al. Reporting and interpreting decision curve analysis: a guide for investigators. *Eur Urol*. (2018) 74:796–804. doi: 10.1016/j.eururo.2018.08.038

20. Lundberg SM, Lee S-I. A unified approach to interpreting model predictions. *Adv Neural Inf Proces Syst*. (2017) 30:arXiv:1705.07874.

21. Paul P, Pennell ML, Lemeshow S. Standardizing the power of the Hosmer-Lemeshow goodness of fit test in large data sets. *Stat Med*. (2013) 32:67–80. doi: 10.1002/sim.5525

22. Nattino G, Pennell ML, Lemeshow S. Assessing the goodness of fit of logistic regression models in large samples: a modification of the Hosmer-Lemeshow test. *Biometrics*. (2020) 76:549–60. doi: 10.1111/biom.13249

23. Rufibach K. Use of brier score to assess binary predictions. *J Clin Epidemiol*. (2010) 63:938–9. doi: 10.1016/j.jclinepi.2009.11.009

24. Lin S, Mo H, Li Y, Guan X, Chen Y, Wang Z, et al. Development and validation of a nomogram for predicting survival of advanced breast cancer patients in China. *Breast*. (2020) 53:172–80. doi: 10.1016/j.breast.2020.08.004

25. Wang Z, Wang Y, Yang Y, Luo Y, Liu J, Xu Y, et al. A competing-risk nomogram to predict cause-specific death in elderly patients with colorectal cancer after surgery (especially for colon cancer). *World J Surg Oncol*. (2020) 18:30. doi: 10.1186/s12957-020-1805-3

26. Mirsamadi M, Nourmohammadi I. Correlation of human age-related cataract with some blood biochemistry constituents. *Ophthalmic Res*. (2003) 35:329–34. doi: 10.1159/000074072

27. Zou X, Wang H, Zhou D, Liu Z, Wang Y, Deng G, et al. The polymorphism rs2968 of LSS gene confers susceptibility to age-related cataract. *DNA Cell Biol*. (2020) 39:1970–5. doi: 10.1089/dna.2020.5872

28. Huang CY, Lee JI, Chang CW, Liu YH, Huang SP, Chen SC, et al. Chronic kidney disease and its association with cataracts-a cross-sectional and longitudinal study. *Front Public Health*. (2022) 10:1029962. doi: 10.3389/fpubh.2022.1029962

29. Klein BE, Knudtson MD, Brazy P, Lee KE, Klein R. Cystatin C, other markers of kidney disease, and incidence of age-related cataract. *Arch Ophthalmol*. (2008) 126:1724–30. doi: 10.1001/archophthalmol.2008.502

30. Berlyne G, Danovitch G, Ari JB, Blumenthal M. Cataracts of chronic renal failure. *Lancet*. (1972) 299:509–11. doi: 10.1016/S0140-6736(72)90175-4

31. Bejarano E, Weinberg J, Clark M, Taylor A, Rowan S, Whitcomb EA. Redox regulation in age-related cataracts: roles for glutathione, vitamin C, and the NRF2 signaling pathway. *Nutrients*. (2023) 15:3375. doi: 10.3390/nu15153375

32. Kang KH, Shin D, Ryu IH, Kim JK, Lee IS, Koh K, et al. Association between cataract and fatty liver diseases from a nationwide cross-sectional study in South Korea. *Sci Rep*. (2024) 14:77. doi: 10.1038/s41598-023-50582-7

33. Liu X, Zhang H, Liang J. Blood urea nitrogen is elevated in patients with non-alcoholic fatty liver disease. *Hepato-Gastroenterology*. (2013) 60:343–5.

34. Li L, Wan XH, Zhao GH. Meta-analysis of the risk of cataract in type 2 diabetes. *BMC Ophthalmol*. (2014) 14:94. doi: 10.1186/1471-2415-14-94

35. Tan AG, Mitchell P, Rochtchina E, Flood VM, Cumming RG, Wang JJ. Serum homocysteine, vitamin B12, folate and the prevalence of age-related cataract. *Invest Ophthalmol Vis Sci*. (2009) 50:510–0.

36. Ma C, Liu Z, Yao S, Hei L, Guo W. Correlation between serum homocysteine, folate, vitamin B6 and age-related cataract. *Pteridines*. (2019) 30:142–5. doi: 10.1515/pteridines-2019-0017

37. Christen WG, Glynn RJ, Chew EY, Albert CM, Manson JE. Folic acid, vitamin B6, and vitamin B12 in combination and age-related cataract in a randomized trial of women. *Ophthalmic Epidemiol*. (2016) 23:32–9. doi: 10.3109/09286586.2015.1130845

38. Kuzniarz M, Mitchell P, Cumming RG, Flood VM. Use of vitamin supplements and cataract: the Blue Mountains eye study. *Am J Ophthalmol*. (2001) 132:19–26. doi: 10.1016/s0002-9394(01)00922-9

39. Mailu EW, Virendrakumar B, Bechange S, Jolley E, Schmidt E. Factors associated with the uptake of cataract surgery and interventions to improve uptake in low-and middle-income countries: a systematic review. *PLoS One*. (2020) 15:e0235699. doi: 10.1371/journal.pone.0235699

40. Wang W, Yan W, Müller A, He M. A global view on output and outcomes of cataract surgery with National Indices of socioeconomic development. *Invest Ophthalmol Vis Sci*. (2017) 58:3669–76. doi: 10.1167/iovs.17-21489

41. Slopen N, Goodman E, Koenen KC, Kubzansky LD. Socioeconomic and other social stressors and biomarkers of cardiometabolic risk in youth: a systematic review of less studied risk factors. *PLoS One*. (2013) 8:e64418. doi: 10.1371/journal.pone.0064418

42. Fang R, Yu YF, Li EJ, Lv NX, Liu ZC, Zhou HG, et al. Global, regional, national burden and gender disparity of cataract: findings from the global burden of disease study 2019. *BMC Public Health*. (2022) 22:2068. doi: 10.1186/s12889-022-14491-0

43. Svendsen MT, Bak CK, Sørensen K, Pelikan J, Riddersholm SJ, Skals RK, et al. Associations of health literacy with socioeconomic position, health risk behavior, and health status: a large national population-based survey among Danish adults. *BMC Public Health*. (2020) 20:565. doi: 10.1186/s12889-020-08498-8

44. Sonron EA, Tripathi V, Hariharan S. The impact of sociodemographic and socioeconomic factors on the burden of cataract in Small Island developing states (SIDS) in the Caribbean from 1990 to 2016. *Ophthalmic Epidemiol*. (2020) 27:132–40. doi: 10.1080/09286586.2019.1700534

frontiers | Frontiers in Medicine

TYPE Original Research
PUBLISHED 24 October 2024
DOI 10.3389/fmed.2024.1494659

OPEN ACCESS

EDITED BY
Jiong Zhang,
University of Southern California, United States

REVIEWED BY
Da Sun,
Wenzhou University, China
Guolin Sun,
University of Electronic Science and Technology of China, China

*CORRESPONDENCE
Zhentao Zhu
✉ jshayyzzt@163.com
Meiting Yu
✉ 15657005637@163.com
Yuhua Tong
✉ tyh331359797@126.com

†These authors have contributed equally to this work and share first authorship

RECEIVED 11 September 2024
ACCEPTED 15 October 2024
PUBLISHED 24 October 2024

CITATION
Lu Y, Fang R, Xu B, Feng C, Zhu Z, Yu M and Tong Y (2024) A semantic segmentation method to analyze retinal vascular parameters of diabetic nephropathy. *Front. Med.* 11:1494659. doi: 10.3389/fmed.2024.1494659

A semantic segmentation method to analyze retinal vascular parameters of diabetic nephropathy

Youlv Lu[1]†, Ruolin Fang[1]†, Bolun Xu[2], Chunyun Feng[2], Zhentao Zhu[3]*, Meiting Yu[2]* and Yuhua Tong[2]*

[1]Second Clinical Medical College, Zhejiang Chinese Medical University, Hangzhou, China, [2]Department of Ophthalmology, The Quzhou Affiliated Hospital of Wenzhou Medical University, Quzhou People's Hospital, Quzhou, China, [3]Department of Ophthalmology, Huaian Hospital of Huaian City, Huaian, China

Introduction: By using spectral domain optical coherence tomography (SD-OCT) to measure retinal blood vessels. The correlation between the changes of retinal vascular structure and the degree of diabetic nephropathy is analyzed with a full-pixel Semantic segmentation method.

Methods: A total of 120 patients with diabetic nephropathy who were treated in the nephrology department of Quzhou People's Hospital from March 2023 to March 2024 were selected and divided into three groups according to the urinary albumin creatinine ratio (UACR). The groups included simple diabetes group (UACR < 30 mg/g), microalbuminuria group (30 mg/g ≤ UACR <300 mg/g) and macroalbuminuria group (UACR ≥300 mg/g). SD-OCT was used to scan the arteries and veins in the superior temporal area B of the retina. The semantic segmentation method built into the SD-eye software was used to automatically identify the morphology and structure of the vessels and calculate the parameters of arteriovenous vessels. The parameters of arteriovenous vessels are as follows: outer diameter of the retinal artery (RAOD); inner diameter of the retinal artery (RALD); arterial wall thickness (AWT); arterial wall to lumen ratio (AWLR); cross sectional area of arterial wall (AWCSA); retinal vein outer diameter (RVOD); retinal vein inner diameter (RVLD); vein wall thickness (VWT); vein wall to lumen ratio (VWLR); cross sectional area of vein wall (VWCSA). Statistical analysis software was used to compare and analyze the parameters of retinal arteriovenous vessels of the three groups.

Results: The study revealed statistically significant differences in RAOD and RALD among the three groups ($p < 0.05$) with the RAOD and RALD of the macroalbuminuria group and microalbuminuria group being lower than those of the simple diabetes group. Conversely, there were no significant differences in AWT, AWLR and AWCSA among the three groups ($p > 0.05$). Additionally, the differences in RVOD and RVLD among the three groups were found to be statistically significant ($p < 0.05$) with the RVOD and RVLD of the simple diabetes group being lower than those of the microalbuminuria group and macroalbuminuria group. No significant differences were observed in VWT and VWL among the groups. Additionally, RVOD and RVLD were weakly associated with UACR ($R = 0.247$, $p = 0.007$; $R = 0.210$, $p = 0.021$). Full-pixel semantic segmentation method combined with OCT images is a new retinal vascular scanning technology, which can be used as a new method for early diagnosis of diabetic nephropathy. The structural changes of retinal vessels can be used to predict the severity of diabetic nephropathy during the development of diabetic nephropathy.

KEYWORDS

optical coherence tomography, urinary protein creatinine ratio, full pixel semantic segmentation method, diabetic nephropathy, vascular structure

1 Introduction

Diabetic nephropathy (DN) is a severe complication of diabetes (DM) resulting from poor blood sugar control over an extended period. It is characterized by tiny vascular lesions. At the same time, diabetic nephropathy causing renal failure is the important cause leading to the terminal uremia. In early diabetic nephropathy patients, hyperlipidemia and high blood sugar are accompanied by an increased abnormal glomerular filtration rate, proteinuria, serum creatinine, blood urea nitrogen index and progressive changes in renal function. In recent years, the diagnosis of diabetic nephropathy has advanced significantly with various methods such as the serology detection of proinflammatory factors (1–5), inflammatory factors (6), and gene diagnosis (7). However, accurately diagnosing the lesions of diabetic nephropathy remains challenging. Retinal and renal vessels share anatomical, physiological and pathological traits. Diabetes-induced hyperglycemia harms microvessels including those in the retina and kidneys. Retinal vessels which are visible without invasive methods can indicate diabetic microangiopathy severity. Many studies (8–10) show a strong link between retinal microangiopathy and diabetic nephropathy progression. Therefore, by measuring changes in retinal blood vessels, the progression of diabetic nephropathy can be indirectly assessed. This study utilizes the full pixel semantic segmentation method to identify individuals with diabetic nephropathy based on retinal vascular parameters. It also examines the various stages of diabetic nephropathy by analyzing retinal vascular structures, abnormal changes in retinal blood vessel structure and the correlation between the severity of diabetic nephropathy.

2 Subjects and methods

2.1 Ethical approval

A cohort of 120 patients diagnosed with diabetic nephropathy and admitted to the Department of Nephrology at Quzhou People's Hospital between March 2023 and March 2024, all of whom were aged 50 years or older, were selected for this study. The research protocol was approved by the Research Ethics Committee of Quzhou People's Hospital and conducted in compliance with the guidelines outlined in the Helsinki Declaration. Informed written consent was obtained from all participants.

2.2 General information and grouping

The inclusion criteria of subjects in this study needed to meet the diagnostic criteria for diabetes nephropathy in the 2021 version of the Chinese Guidelines for the Prevention and Treatment of diabetes Nephropathy, exclude kidney diseases caused by other reasons and meet one of the following conditions: (1) two out of three times over a six-month period, the UACR was found to be at least 30 mg/g; (2) GFR less than 60 mL/min/1.73 m^2 lasts for more than 3 months. Exclusion criteria: (1) type 1 diabetes, gestational diabetes and special type diabetes; (2) acute complications of diabetes (such as diabetic ketoacidosis); (3) chronic nephritis or kidney combined with other diseases that could lead to proteinuria and hematuria; (4) recent use of hormones, immunosuppressants or diuretics; (5) intraocular pressure over 21 mmHg; (6) eye blinding disease history (such as: optic nerve diseases, senile cataracts, history of closure angle glaucoma, open angle glaucoma, anterior uveitis and retinal vascular disease) and poor vision correction operation difficulties; (7) other causes of proteinuria including acute infection, hypertension and obesity. According to the urinary albumin creatinine ratio (UACR), 120 patients with diabetic nephropathy were divided into diabetic non-nephropathy group (35 subjects), diabetic microalbuminuria group (49 subjects) and diabetic macroalbuminuria group (36 subjects). The UACR of patients in the diabetic non-nephropathy group was less than 30 mg/g and the UACR of patients in the diabetic macroalbuminuria group was greater than or equal to 30 mg/g when the UACR of the patients in diabetic microalbuminuria group was greater than or equal to 30 mg/g and less than 300 mg/g.

2.3 Routine inspection items

All participants underwent blood pressure, fasting blood glucose, glycated hemoglobin, triglycerides, cholesterol, liver and kidney function, urine routine, ophthalmic intraocular pressure (IOP) measurement, anterior slit-lamp examination and fundus retinal examination.

2.4 OCT image acquisition and parameter measurement of retinal vessels

All the study objects of OCT imaging were checked by skilled and highly qualified doctors of ophthalmology through SD-OCT scanning. The subject's head was fixed on the SD-CT operating table and they were asked to maintain the correct sitting posture during the operation. At the same time, the subject was asked to fixate on the blue fixation light in the lens. The SD-OCT scanner was used to scan the retinal arteries and accompanying retinal veins in the superior temporal region of the right eye of each subject. Zone B was defined as the superotemporal range extending 1–2 disc diameters from the edge of the optic disc. A linear scan with a corresponding depth image was selected for scanning and the scanning line was maintained perpendicular to the vascular axis (Figure 1A). Each eye was scanned three times to select the clearest images of blood vessel walls for the next study. After the scan was completed, the first OCT images of the vertical level ratio was adjusted to 1:1 microns. After 8x magnification,

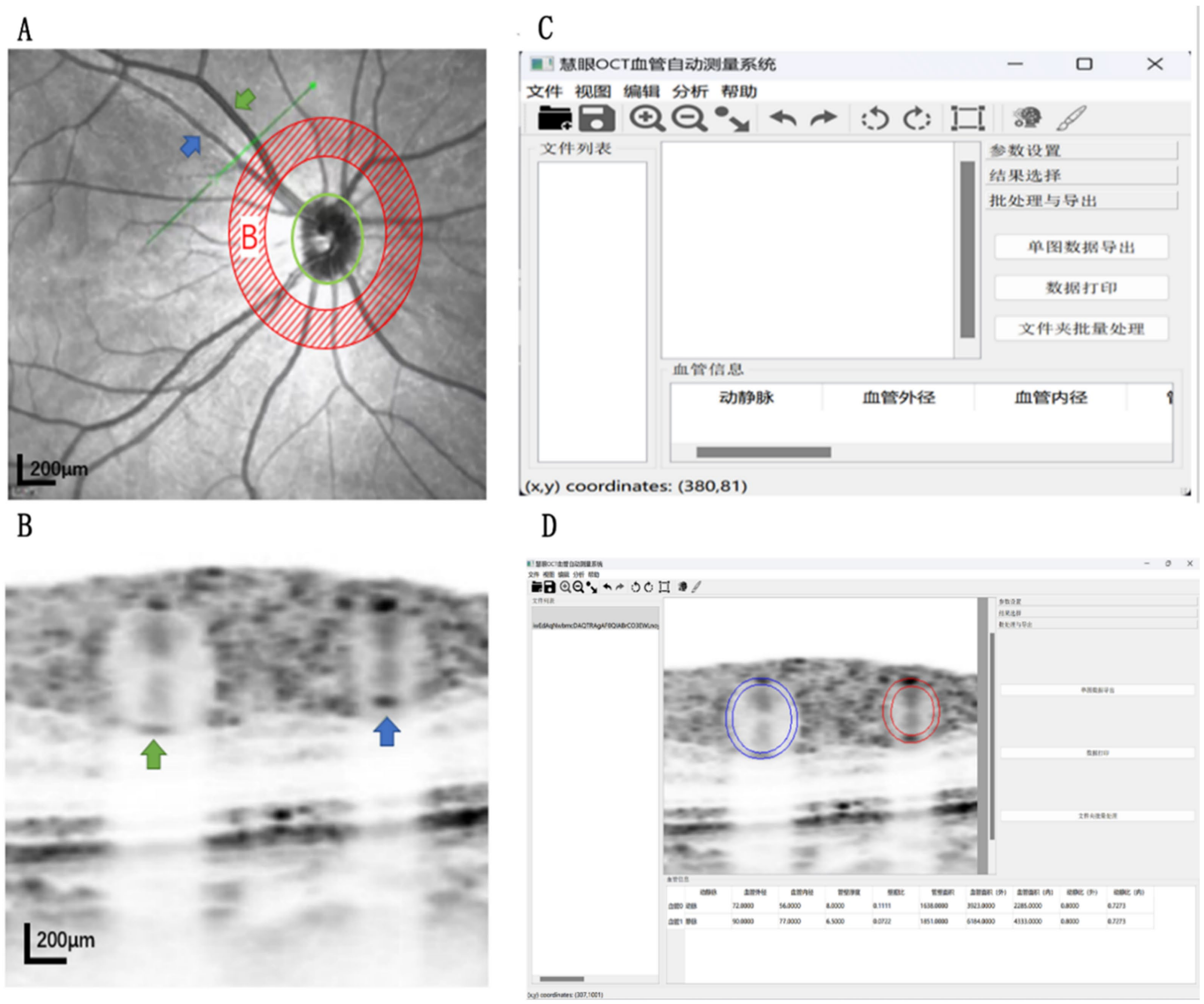

FIGURE 1
operation process **(A)**: The green straight line represents the OCT linear scan line. the shaded **(B)** area is the linear scan area. When the blue arrow marks the artery, the green arrow marks the vein. B: The image shows the corresponding cross-sectional area image of the arterial and venous vessels in Figure A. **(C)**: The interface is displayed after the initial startup of the Huiyan OCT vascular automatic measurement system **(D)**: the corresponding arterial and venous parameters are measured after importing into the Huiyan software OCT vascular automatic measurement system.

it was saved as a vascular cross-section of a 512 × 512 pixel image (Figure 1B). The image was fed into Eye Recognition Software to identify and measure blood vessels (Figures 1C,D). The software calculated the retinal artery diameter (RAOD) and inner diameter (RALD); vein diameter (RVOD) and inner diameter (RVLD); arterial blood wall thickness (AWT) = (RAOD − RALD)/2; arterial vessel wall to lumen ratio (AWLR) = (RAOD − RALD)/2/RALD; Venous blood wall thickness (VWT) = (RVOD − RVLD)/2; the artery wall cross sectional area (AWCSA) = ($RAOD^2 - RALD^2$) × 3.14/4; wall to lumen ratio of venous vessels (VWLR) = (RVOD − RVLD)/2/RVLD; venous wall cross-sectional area (VWCSA) = ($RVOD^2$-$RVLD^2$) × 3.14/4.

2.5 A new type of image segmentation method

The semantic segmentation method is a method of image processing based on computer vision and deep learning. It is able to classify each pixel in an image into a specific category or region, which enables detailed parsing and recognition of the image content. This method uses a model of training to learn and understand the semantic information in the medical image, specifically the meaning or object representing different areas and applies this understanding to the categorization of each pixel in the image. In the process of semantic segmentation method analysis, each pixel in the image is analyzed according to its features such as color, texture and shape to determine its category and area. In this way, the different objects in the image of the semantic segmentation method can realize accurate positioning and recognition for subsequent image analysis, scene understanding and various applications providing strong support. The application of semantic segmentation method in the recognition and measurement of retinal vascular parameters is a new technology in the field of medical image processing. The recognition software uses the full-pixel semantic segmentation method to identify the image contour of retinal blood vessels. The artery and vein structures in each image can be captured by the software at the same time and the parameters of blood vessels can be automatically calculated and the vascular structural parameters of multiple images can be exported in batches.

2.6 Statistical analysis

SPSS 26.0 statistical software was used for data processing and analysis. The measurement data of the three groups exhibited a normal distribution with the mean ± standard deviation utilized to depict the central tendency and variability. Analysis of variance (ANOVA) was employed to compare the groups while frequency (%) was utilized for categorical data. Correlation analysis was conducted to investigate the relationship between urinary albumin creatinine ratio and retinal vascular parameters in patients with diabetic nephropathy when statistical significance was defined as $p < 0.05$.

3 Results

3.1 Comparison of general data among the three groups

Single factor analysis of variance showed that there were no significant differences in gender, age, systolic blood pressure, diastolic blood pressure, body mass index, glycosylated hemoglobin, uric acid, triglyceride and total cholesterol among the three groups ($p > 0.05$) (Table 1).

3.2 Comparison of arterial vascular parameters among the three groups

Table 2 showed the comparison results of retinal artery vascular parameters in the three groups. The statistical results showed that WLR, AWT, and WSCA of the three groups had no statistical significance ($p > 0.05$). The RAOD and RALD of the diabetic non-nephropathy group were 103.69 ± 9.10 μm and 80.34 ± 6.48 μm, which were the largest in the three groups. When the RAOD and RALD of diabetic microalbuminuria group had values of 96.12 ± 11.16 μm and 75.24 ± 10.13 μm, those of diabetic macroalbuminuria group had values of 90.23 ± 9.66 μm and 70.38 ± 13.13 μm. The RAOD and RALD among the three groups were statistically significant ($p < 0.05$).

3.3 Comparison of venous vascular parameters among the three groups

Table 3 presented a comparison of retinal vein parameters across the three groups. The findings indicated that there was no statistically significant difference in terms of WLR, VWT, and WSCA among the groups ($p > 0.05$). Specifically, the RVOD and RVLD measurements for the diabetic non-nephropathy group were 114.17 ± 11.00 μm and 99.69 ± 12.74 μm representing the smallest values among the three groups. In contrast, the RVOD and RVLD measurements for the diabetic microalbuminuria group were 123.73 ± 18.33 μm and 107.05 ± 17.88 μm while those for the diabetic macroalbuminuria group were 130.80 ± 11.70 μm and 115.18 ± 14.25 μm. The differences in RVOD and RVLD among the three groups were found to be statistically significant ($p < 0.05$).

3.4 Correlation between parameters of the retinal arteriole and urine creatinine, microalbumin and UACR in the three groups

Table 4 illustrated the weak association between AWT, WSCA ($R = 0.190$, $p = 0.037$; $R = 0.210$, $p = 0.021$) and Urinecreatinine. Additionally, RAOD ($R = 0.174$, $p = 0.058$), RALD ($R = 0.125$, $p = 0.174$), and WLR ($R = 0.079$, $p = 0.391$) showed no significant correlation with Urinecreatinine. Furthermore, there was no relationship between RAOD, RALD, WLR, AWT, WSCA, Microalbumin, and UACR ($p > 0.05$). The AWT ($R = 0.020$, $p = 0.827$), WLR ($R = 0.119$, $p = 0.194$), WSCA ($R = 0.089$, $p = 0.334$) also did not exhibit a clear correlation with UACR.

3.5 Correlation between parameters of the retinal vein and urine creatinine, microalbumin and UACR in the three groups

Table 5 presented the correlation analysis results indicating that RVOD, RVLD, VWT, WLR and WSCA did not show significant correlations with Urinecreatinine. However, RVOD and RVLD exhibited a significant positive correlation with Microalbumin levels

TABLE 1 Clinical baseline characteristics of the three groups.

Variables	Non-nephrotic	Microalbuminuria	Macroalbuminuria	X^2/F	*P*
Age (y)	61.57 ± 7.34	64.67 ± 10.34	66.61 ± 13.26	2.05	0.181
Sex, male/female	18/17	25/24	25/21	3.42	0.134
Total cholesterol (mmol/L)	4.11 ± 1.01	4.39 ± 1.12	4.41 ± 1.35	0.76	0.471
uric acid (μmol/L)	323.25 ± 79.50	320.86 ± 86.89	350.16 ± 108.76	1.20	0.305
Triglyceride (mmol/L)	2.29 ± 1.62	2.44 ± 1.11	2.51 ± 2.48	0.15	0.862
body mass index (kg/m^2)	25.25 ± 3.35	25.12 ± 1.96	24.80 ± 2.42	0.29	0.747
diastolic pressure (mmHg)	80.63 ± 9.97	79.86 ± 12.75	82.69 ± 9.92	0.69	0.505
Systolic pressure (mmHg)	141.71 ± 14.76	143.45 ± 12.96	143.45 ± 12.96	1.51	0.226
Glycosylated hemoglobin (HbAlc %)	7.74 ± 2.42	8.59 ± 3.09	13.67 ± 31.28	1.27	0.285

TABLE 2 Comparison of retinal arteriole parameters among the three groups.

Parameters	RALD	RAOD	WLR	AWT	WSCA
Non-nephrotic	80.34 ± 6.48	103.69 ± 9.10	0.09 ± 0.03	8.81 ± 3.29	3507.11 ± 1203.17
Microalbuminuria	75.24 ± 10.13	96.12 ± 11.16	0.08 ± 0.01	8.07 ± 0.97	3295.85 ± 557.08
Macroalbuminuria	70.38 ± 13.13	90.23 ± 9.66	0.09 ± 0.01	8.32 ± 0.93	3189.40 ± 626.95
F	8.30	15.67	2.53	1.50	1.40
P	<0.05	<0.05	0.084	0.227	0.251

RALD, Rentinal arteriolar lumen diameter; RAOD, Rential arteriolar outer diameter; WLR, wall-to-lumen ratio; AWT, Arteriolar wall thickness; WCSA, Wall cross-sectional area.

TABLE 3 Comparison of retinal vein parameters among the three groups.

Parameters	RVLD	RVOD	WLR	VWT	VWSCA
Non-nephrotic	99.69 ± 12.74	114.17 ± 11.00	0.06 ± 0.01	6.37 ± 0.78	3468.73 ± 616.71
Microalbuminuria	107.05 ± 17.88	123.73 ± 18.33	0.05 ± 0.01	6.57 ± 0.84	3668.00 ± 673.86
Macroalbuminuria	115.18 ± 14.25	130.80 ± 11.70	0.05 ± 0.01	6.69 ± 0.89	3511.99 ± 772.71
F	8.92	11.56	2.64	1.35	0.99
p	<0.05	<0.05	0.076	0.263	0.373

RVLD, Rentinal venular lumen diameter; RVOD, Rential venular outer diameter; WLR, wall-to-lumen ratio; VWT, Vein wall thickness; WCSA, Wall cross-sectional area.

($R = 0.207$, $p = 0.024$; $R = 0.194$, $p = 0.034$). Conversely, VWT, WLR, and WSCA did not show significant correlations with Microalbumin. Additionally, RVOD and RVLD were weakly associated with UACR ($R = 0.247$, $p = 0.007$; $R = 0.210$, $p = 0.021$) while VWT, WLR, and WSCA did not exhibit significant correlations with UACR.

4 Discussion

Suboptimal glycemic controlin diabetic patients can lead to chronic vascular complications including diabetic retinopathy and diabetic nephropathy. Chronic high blood sugar causes diabetic microangiopathy damaging the kidney and retina's small blood vessels. In the kidneys, it alters blood flow, increases filtration pressure and harms glomerular cells and membranes. In the retina, it disrupts the link between capillary cells and the pigment layer, causing vascular leakage and microaneurysms. The emergence of diabetic nephropathy is often associated with changes in the choroid (11–14), retina (15), and optic nerve (16, 17). One study showed that with the increase of UACR, the mean vessel density of the deep retinal capillary plexus decreased significantly in DN (8). In addition, according to a study (9), as the DN lesion degree deepened, not only the deep retinal capillary density decreased, but the shallow retinal capillary density was also significantly reduced. At the same time, Yao and Li (10) also measured the avascular area of the macular fovea and the choroidal vessel density in DN patients and found that the fundus structure of DN changed significantly. They suggested that the enlargement of the avascular area in the fovea might be due to abnormalities in the choroidal vessels and proposed the possibility of macular ischemia While the decrease in choroidal vessel density suggested retinal and choroidal ischemia. High sugar (18), oxidative stress (19), and inflammation factors (20) only aggravate vascular reactions which are thought to be caused by retinal ischemia and hypoxia and the important reason for the change in the structure of the retina. Through checking the retinal blood vessels, fundus and systemic microvascular changes can be more directly and objectively observed in DN patients.

In this study, RAOD and RALD of the diabetic macroalbuminuria group and diabetic microalbuminuria group were significantly lower than those of the diabetic non-nephropathy group. This may be related to damage to the arterial endothelium caused by hyperglycemia (21). Oxidative stress induced by hyperglycemia is believed to cause vascular endothelial damage to retinal arteries in the fundus through the secretion of inflammatory cytokines by infiltrating macrophages (22) leading to vascular blood supply and relaxation dysfunction. At the same time, inflammation promotes fibrosis of the vascular wall and further narrowing of the blood vessels. Microalbuminuria is an early marker of endothelial injury (23). The increase in microalbuminuria not only indicates serious changes in renal pathological structure in patients, but also indicates the continuous increase of endothelial damage to microvessels throughout the body. Feng et al. (24) measured the diameter of retinal microvessels in 690 diabetic patients through an automatic retinal image analysis system and found that narrow retinal arteriolar diameter was positively correlated with the risk of DN in type 2 diabetic patients. This is consistent with the results of this study.

In this study, a large amount of proteinuria was observed in the diabetic microalbuminuria group with RVOD and RVLD being significantly higher than in the diabetic non-nephropathy group. Additionally, the albuminuria group had the highest levels of RVOD and RVLD. This may be related to the increased secretion of vascular endothelial growth factor (VEGF). VEGF (25–27) plays a positive role in promoting vascular endothelial proliferation. Multiple factors (28–32) mediated endothelial damage and VEGF levels increased significantly. These lead to increased permeability of retinal blood vessels, an increase in endovascular blood volume, and an increase in the diameter and flexibility of blood vessels. A high glucose environment leads to decreased deformability of red blood cells in the blood and enhanced aggregation ability (33). Meanwhile, vascular endothelial damage further activates platelets and the physiological mechanism of coagulation (34), thus keeping blood in a hypercoagulable state. This may be another important reason for the increase in retinal vein diameter. Nusinovici et al. (35) measured the vascular diameters of retinal arterioles and venules in 703 white

TABLE 4 Correlation analysis between parameters of the retinal arteriole and urine creatinine, microalbumin and UACR in the three groups.

Parameters	RAOD	RALD	AWT	WLR	AWSCA
Urinecreatinine					
R	0.174	0.125	0.190	0.079	0.210
P	0.058	0.174	0.037	0.391	0.021
Microalbumin					
R	−0.1390	0.066	0.020	0.099	0.085
P	0.129	0.472	0.827	0.282	0.353
UACR					
R	−0.177	−0.002	0.020	0.119	0.089
P	0.053	0.985	0.827	0.194	0.334

RALD, Rentinal arteriolar lumen diameter; RAOD, Rential arteriolar outer diameter; WLR, wall-to-lumen ratio; AWT, Arteriolar wall thickness; WCSA, Wall cross-sectional area.

TABLE 5 Correlation analysis between parameters of the retinal vein and urine creatinine, microalbumin and UACR in the three groups.

Parameters	RVOD	RVLD	VWT	WLR	VWSCA
Urinecreatinine					
R	0.021	0.049	−0.134	−0.091	0.117
P	0.824	0.594	0.144	0.322	0.202
Microalbumin					
R	0.207	0.194	0.041	−0.141	0.058
P	0.024	0.034	0.654	0.125	0.532
UACR					
R	0.247	0.210	0.135	−0.113	0.011
P	0.007	0.021	0.142	0.219	0.905

RVLD, Rentinal venular lumen diameter; RVOD, Rential venular outer diameter; WLR, wall-to-lumen ratio; VWT, Vein wall thickness; WCSA, Wall cross-sectional area.

diabetic patients and found that a higher RVOD in white diabetic patients was positively correlated with the risk rate of DN. The findings of this study align closely with those of previous research.

Optical coherence tomography (SD-OCT) combined with semantic segmentation can quickly scan and analyze the parameters of retinal blood vessels. Semantic segmentation is a newly emerging automatic recognition algorithm for identifying, measuring image structure and analyzing vascular parameters. The semantic segmentation method uses deep learning technology to train a large number of retinal blood vessel image data. So that the model can automatically identify and segment the blood vessel regions in the image. During the segmentation process, the algorithm will classify each pixel and label it as a vascular or non-vascular category in order to obtain an accurate blood vessel segmentation result. Based on the segmented vascular regions, the semantic segmentation method can further extract and measure the vascular parameters. By calculating the pixel width of the vessel area, the diameter information of the vessel can be obtained. At the same time, the algorithm can also analyze the direction and tortuosity of blood vessels to evaluate the morphological characteristics of blood vessels. Through the analysis of the overall structure of the network of blood vessels, we can also understand the vascular distribution density and complexity. In practice, semantic segmentation method can be combined with other medical image processing techniques to further improve the accuracy and reliability of retinal vascular parameter measurement.

4.1 Advantages and disadvantages

Compared to traditional manual measurement and semi-automatic FWHM image segmentation methods (36, 37), the semantic segmentation method (38) facilitates the automated measurement through artificial intelligence (39–42) mitigating manual errors and enhancing both efficiency and accuracy relative to the semi-automatic FWHM image segmentation method. In practical applications, semantic segmentation method can be integrated with other medical image processing techniques to further augment the accuracy and reliability of retinal vascular parameter measurements (43–45).

The semantic segmentation method can understand the eye lesions more comprehensively. Semantic segmentation method of ophthalmic images allows for a more detailed analysis of lesion areas, which aids in accurate disease evaluation. However, there are some shortcomings. Firstly, the semantic segmentation method is based on artificial intelligence to learn the blood vessel structure parameters and then recognize the blood vessel structure. Manual calculation of blood vessel parameters will inevitably have errors which will directly affect the effectiveness of artificial intelligence learning. Secondly, The semantic segmentation method accurately identifies the vascular structure and measures the vascular parameters by analyzing the pixel differences in the image. Image quality significantly impacts the measurement precision of the segmentation software Thirdly, semantic segmentation method for complex analytical ability of eye disease is limited. Serious eye diseases often have complex pathological mechanisms and intricate texture images. Segmentation based solely on gray level information may not be accurate. This can lead to errors in the segmentation process affecting subsequent analysis and diagnosis. Fourthly, semantic segmentation method has achieved substantial advancements in the domains of image recognition and segmentation. However, it often lacks the sensitivity required to accurately delineate fine boundaries and intricate details in complex images. Conversely, Optical Coherence Tomography Angiography (OCTA) exhibits superior capability in rendering detailed structures and boundaries with greater clarity attributable to its high resolution and significant penetration depth. Furthermore, unlike OCTA which is a non-invasive imaging modality grounded in physical principles and does not necessitate supplementary labeled data, semantic segmentation techniques typically demand extensive pixel-level labeled datasets for effective training. Semantic segmentation method is not only time-consuming and labor-intensive, but also affected by the error of labeling data. Therefore, further improvement of Huiyan software in the later stages requires time to supervise artificial intelligence learning and select a large number of high-definition pictures for artificial intelligence training in order to realize the automatic measurement of vascular structure parameters in a true sense. Considering the aforementioned limitations, there exists substantial potential for future research in the domain of semantic segmentation for the measurement of retinal vessels in patients with diabetic nephropathy. Initially, efforts can be directed toward optimizing the algorithmic model to enhance the accuracy and efficiency of vessel segmentation, thereby facilitating the detection of more nuanced vascular lesions. Secondly, integrating clinical data like renal function and blood glucose is examined to create a comprehensive disease monitoring model. Finally, the study will be converted into clinical tools to aid early diagnosis, disease monitoring, and personalized treatment plans for diabetic nephropath.

In this study, advanced semantic segmentation technology was employed to conduct an in-depth analysis of fundus images from diabetic patients. Retinal blood vessels were automatically segmented and various vascular parameters were successfully extracted. The findings indicate that abnormal changes in these vascular parameters are significantly associated with an elevated risk of diabetic nephropathy. In addition, these studies also show a significant correlation between changes in vascular parameters and progressive progression of diabetic nephropathy. This provides a novel and objective method for the early diagnosis and risk assessment of diabetic nephropathy. This study applies the semantic segmentation method in deep learning to the domain of medical image processing, addressing the limitations inherent in traditional manual measurement techniques and enhancing the accuracy and efficiency of analysis. A notable limitation of this study is the relatively small sample size, which constrains the generalizability and reliability of the findings. This limited sample size may undermine the representativeness of the sample, thereby impeding the extrapolation of the results to the broader population. To address this limitation, future research should consider increasing the sample size to encompass a more diverse cohort of patients with varying backgrounds and degrees of illness severity. Such an approach would enhance the study's credibility and applicability. Despite the need for further research in model optimization and the exploration of pathophysiological mechanisms, this investigation offers valuable insights and guidance for clinical research and therapeutic practices related to diabetic nephropathy. Furthermore, it underscores the significant potential and promising applications of semantic segmentation method within the medical field.

Data availability statement

The datasets presented in this study can be found in online repositories. The names of the repository/repositories and accession number(s) can be found in the article/Supplementary material.

Ethics statement

The studies involving humans were approved by the Medical Ethics Review Committee of Quzhou People's Hospital. The studies were conducted in accordance with the local legislation and institutional requirements. The participants provided their written informed consent to participate in this study.

Author contributions

YL: Writing – original draft, Conceptualization. RF: Data curation, Writing – review & editing. BX: Data curation, Writing – review & editing. CF: Software, Writing – review & editing. ZZ: Supervision, Writing – review & editing. MY: Funding acquisition, Writing – review & editing. YT: Validation, Writing – review & editing.

Funding

The author(s) declare that financial support was received for the research, authorship, and/or publication of this article. This work was supported by the Zhejiang Province Traditional Chinese Medicine Science and Technology Project (No. 2024ZL1212) and Quzhou Key Science and Technology Project (No. 2023K136).

Conflict of interest

The authors declare that the research was conducted in the absence of any commercial or financial relationships that could be construed as a potential conflict of interest.

Publisher's note

Supplementary material

The Supplementary material for this article can be found online at: https://www.frontiersin.org/articles/10.3389/fmed.2024.1494659/full#supplementary-material

References

1. Dejenie TA, Abebe EC, Mengstie MA, Seid MA, Gebeyehu NA, Adella GA, et al. Dyslipidemia and serum cystatin C levels as biomarker of diabetic nephropathy in patients with type 2 diabetes mellitus. *Front Endocrinol.* (2023) 14:14. doi: 10.3389/fendo.2023.1124367

2. Opazo-Ríos L, Mas S, Marín-Royo G, Mezzano S, Gómez-Guerrero C, Moreno JA, et al. Lipotoxicity and diabetic nephropathy: novel mechanistic insights and therapeutic opportunities. *Int J Molecularsci.* (2020) 21:2632. doi: 10.3390/ijms21072632

3. Calle P, Hotter G. Macrophage phenotype and fibrosis in diabetic nephropathy. *Int J Mol Sci.* (2020) 21:2806. doi: 10.3390/ijms21082806

4. Dean YE, Elawady SS, Shi W, Salem AA, Chotwatanapong A, Ashraf H, et al. Progression of diabetic nephropathy and vitamin D serum levels: a pooled analysis of 7722 patients. *Endocrinol Diab Metab.* (2023) 6:e453. doi: 10.1002/edm2.453

5. Kawada T. Serum Irisin and diabetic nephropathy in patients with diabetes mellitus. *Horm Metab Res.* (2021) 53:825. doi: 10.1055/a-1676-4118

6. Chang TT, Chen JW. The role of chemokines and chemokine receptors in diabetic nephropathy. *Int J Mol Sci.* (2020) 21:3172. doi: 10.3390/ijms21093172

7. Szostak J, Gorący A, Durys D, Dec P, Modrzejewski A, Pawlik A. The role of MicroRNA in the pathogenesis of diabetic nephropathy. *Int J Mol Sci.* (2023) 24:6214. doi: 10.3390/ijms24076214

8. Cankurtaran V, Inanc M, Tekin K, Turgut F. Retinal microcirculation in predicting diabetic nephropathy in type 2 diabetic patients without retinopathy. *Ophthalmologica.* (2020) 243:271–9. doi: 10.1159/000504943

9. Surawatsatien N, Pongsachareonnont PF, Kulvichit K, Varadisai A, Somkijrungroj T, Mavichak A, et al. Optical coherence tomography angiography biomarkers in Thai patients with diabetic nephropathy: a diabetic eye and kidney

diseases (DEK-D) study. *Transl Vis Sci Technol*. (2023) 12:19. doi: 10.1167/tvst.12.4.19

10. Yao H, Li Z. Is preclinical diabetic retinopathy in diabetic nephropathy individuals more severe? *Front Endocrinol*. (2023) 14:14. doi: 10.3389/fendo.2023.1144257

11. Han X, du NN, Li S, Diao ZL, Fu L, Liu WH. Choroidal vascularity index assessment: a potential noninvasive technique for diagnosing diabetic nephropathy. *J Ophthalmol*. (2022) 2022:3124746. doi: 10.1155/2022/3124746

12. Kocasarac C, Yigit Y, Sengul E, Sakalar YB. Choroidal thickness alterations in diabetic nephropathy patients with early or no diabetic retinopathy. *Int Ophthalmol*. (2018) 38:721–6. doi: 10.1007/s10792-017-0523-5

13. da Silva MO, do Carmo Chaves AEC, Gobbato GC, Lavinsky F, Lavinsky D. Early choroidal and retinal changes detected by swept-source oct in type 2 diabetes and their association with diabetic kidney disease: a longitudinal prospective study. *BMC Ophthalmol*. (2024) 24:85. doi: 10.1186/s12886-024-03346-4

14. Choi MG, Kim JT. Strong correlation of renal function with choroidal thickness in patients with type 2 diabetes: retrospective cross-sectional study. *J Clin*. (2020) 9:2171. doi: 10.3390/jcm9072171

15. Tarkkonen A, Claesson TB, Eriksson MI, Forsblom C, Thorn LM, Summanen P, et al. Atrophy of the optic chiasm is associated with microvascular diabetic complications in type 1 diabetes. *Front Endocrinol*. (2023) 14:14. doi: 10.3389/fendo.2023.1134530

16. Jung S, Bosch A, Ott C, Kannenkeril D, Dienemann T, Harazny JM, et al. Retinal neurodegeneration in patients with end-stage renal disease assessed by spectral-domain optical coherence tomography. *Sci Rep*. (2020) 10:1–10. doi: 10.1038/s41598-020-61308-4

17. Yan Y, Yu L, Sun C, Zhao H, Zhang H, Wang Z. Retinal microvascular changes in diabetic patients with diabetic nephropathy. *BMC Endocr Disord*. (2023) 23:101. doi: 10.1186/s12902-022-01250-w

18. Ashrafi Jigheh Z, Ghorbani Haghjo A, Argani H, Sanajou D. Sodium-glucose co-transporters and diabetic nephropathy: is there a link with toll-like receptors? *Clin Exp Pharmacol Physiol*. (2020) 47:919–26. doi: 10.1111/1440-1681.13261

19. Li R, Shi T, Xing E, Qu H. Atorvastatin calcium tablets on inflammatory factors, hemorheology and renal function damage indexes in patients with diabetic nephropathy. *Pak J Med Sci*. (2021) 37:1392–6. doi: 10.12669/pjms.37.5.4045

20. Jin Q, Liu T, Qiao Y, Liu D, Yang L, Mao H, et al. Oxidative stress and inflammation in diabetic nephropathy: role of polyphenols. *Front Immunol*. (2023) 14:14. doi: 10.3389/fimmu.2023.1185317

21. Yang J, Liu Z. Mechanistic pathogenesis of endothelial dysfunction in diabetic nephropathy and retinopathy. *Front Endocrinol*. (2022) 13:13. doi: 10.3389/fendo.2022.816400

22. GH T. Macrophages and diabetic nephropathy. *Semin Nephrol*. (2010) 30:290–301. doi: 10.1016/j.semnephrol.2010.03.007

23. Ceccarelli Ceccarelli D, Paleari R, Solerte B, Mosca A. Re-thinking diabetic nephropathy: microalbuminuria is just a piece of the diagnostic puzzle. *Clin Chim Acta*. (2022) 524:146–53. doi: 10.1016/j.cca.2021.11.009

24. Feng J, Xie X, Teng Z, Fei W, Zhen Y, Liu J, et al. Retinal microvascular diameters are associated with diabetic kidney disease in patients with type 2 diabetes mellitus. *Diab Metab Syndromeandob*. (2023) 16:1821–31. doi: 10.2147/DMSO.S415667

25. Liu Y, Hong K, Weng W, Huang S, Zhou T. Association of vascular endothelial growth factor (VEGF) protein levels and gene polymorphism with the risk of chronic kidney disease. *Libyan J Med*. (2023) 18:2156675. doi: 10.1080/19932820.2022.2156675

26. Yang B, Zhao XH, Ma GB. Role of serum β2-microglobulin, glycosylated hemoglobin, and vascular endothelial growth factor levels in diabetic nephropathy. *World J Clin Caces*. (2022) 10:8205–11. doi: 10.12998/wjcc.v10.i23.8205

27. Liang T, Qian Z, Tao Y, Peng Y, Cui Y, Zhang C, et al. The relationship between the aqueous VEGF level and the severity of type 1 retinopathy of prematurity. *J Clin Med*. (2022) 11:5361. doi: 10.3390/jcm11185361

28. Zhang J, Wu Y, Zhang J, Zhang R, Wang Y, Liu F. ABCA1 deficiency-mediated glomerular cholesterol accumulation exacerbates glomerular endothelial injury and dysfunction in diabetic kidney disease. *Metab Clin Exp*. (2023) 139:155377. doi: 10.1016/j.metabol.2022.155377

29. Huang JC, Chen SC, Chang WA, Hung WW, Wu PH, Wu LY, et al. KITLG promotes glomerular endothelial cell injury in diabetic nephropathy by an autocrine effect. *Int J Mol Sci*. (2022) 23:11723. doi: 10.3390/ijms231911723

30. Li M, Deng L, Xu G. METTL14 promotes glomerular endothelial cell injury and diabetic nephropathy via m6A modification of α-klotho. *Mol Med*. (2021) 27:106. doi: 10.1186/s10020-021-00365-5

31. Zheng F, Ma L, Li X, Wang Z, Gao R, Peng C, et al. Neutrophil extracellular traps induce glomerular endothelial cell dysfunction and Pyroptosis in diabetic kidney disease. *Diabetes*. (2022) 71:2739–50. doi: 10.2337/db22-0153

32. Wang X, Su W, Ma M, Zhu L, Gao R, Qin C, et al. The KLF4-p62 axis prevents vascular endothelial cell injury via the mTOR/S6K pathway and autophagy in diabetic kidney disease. *Endokrynol Pol*. (2022) 73:837–45. doi: 10.5603/EP.a2022.0072

33. Abdel-Moneim A, Mahmoud B, Nabil A, Negeem Z. Correlation between oxidative stress and hematological profile abnormalities in diabetic nephropathy. *Diab Metab Syndr*. (2019) 13:2365–73. doi: 10.1016/j.dsx.2019.06.014

34. Wei S, Pan X, Xiao Y, Chen R, Wei J. The unique association between the level of plateletcrit and the prevalence of diabetic kidney disease: a cross-sectional study. *Front Endocrinol*. (2024) 15:1345293. doi: 10.3389/fendo.2024.1345293

35. Nusinovici S, Sabanayagam C, Lee KE, Zhang L, Cheung CY, Tai ES, et al. Retinal microvascular signs and risk of diabetic kidney disease in Asian and white populations. *Sci Rep*. (2021) 11:4898. doi: 10.1038/s41598-021-84464-7

36. Xu BL, Zhou WL, Zhu TP, Cheng KY, Li YJ, Zhan HJ, et al. A full-width half-maximum method to assess retinal vascular structural changes in patients with ischemic heart disease and microvascular anginga. *Sci Rep*. (2019) 9:11019. doi: 10.1038/s41598-019-47194-5

37. Huang C, Wang Z, Yuan G, Xiong Z, Hu J, Tong Y. PKSEA-net: a prior knowledge supervised edge-aware multi-task network for retinal arteriolar morphometry. *Comput Biol Med*. (2024) 172:108255. doi: 10.1016/j.compbiomed.2024.108255

38. Tong YH, Zhu TP, Zhao ZL, Zhan HJ, Jiang FZ, Lian HL. Retinal arteriolar morphometry based on full width at half maximum analysis of spectral-domain optical coherence tomography images. *PLoS One*. (2015) 10:e0144437. doi: 10.1371/journal.pone.0144437

39. Yang W-H, Shao Y, Xu Y-W. Guidelines on clinical research evaluation of artificial intelligence in ophthalmology (2023). *Int J Ophthalmol*. (2023) 16:1361–72. doi: 10.18240/ijo.2023.09.02

40. Zheng B, Zhang M, Zhu S, Wu M, Chen L, Zhang S, et al. Research on an artificial intelligence-based myopic maculopathy grading method using EfficientNet. *Indian J Ophthalmol*. (2024) 72:S53–9. doi: 10.4103/IJO.IJO_48_23

41. Xu Y, Yang W. Editorial: artificial intelligence applications in chronic ocular diseases. *Front Cell Dev Biol*. (2023) 11:1295850. doi: 10.3389/fcell.2023.1295850

42. Liu Y-H, Li L-Y, Liu S-J, Gao L-X, Tang Y, Li Z-H, et al. Artificial intelligence in the anterior segment of eye diseases. *Int J Ophthalmol*. (2024) 17:1743–51. doi: 10.18240/ijo.2024.09.23

43. Jiang Y, Gong D, Chen X-H, et al. Analysis and comparison of retinal vascular parameters under different glucose metabolic status based on deep learning. *Int J Ophthalmol*. (2024) 17:1581–91. doi: 10.18240/ijo.2024.09.02

44. Wang J, Wang SZ, Qin XL, Chen M, Zhang HM, Liu X, et al. Algorithm of automatic identification of diabetic retinopathy foci based on ultra-widefield scanning laser ophthalmoscopy. *Int J Ophthalmol*. (2024) 17:610–5. doi: 10.18240/ijo.2024.04.02

45. Chen N, Zhu Z, Yang W, Wang Q. Progress in clinical research and applications of retinal vessel quantification technology based on fundus imaging. *Front Bioeng Biotechnol*. (2024) 12:1329263. doi: 10.3389/fbioe.2024.1329263

frontiers | Frontiers in Medicine

TYPE Original Research
PUBLISHED 06 November 2024
DOI 10.3389/fmed.2024.1460779

OPEN ACCESS

EDITED BY
Jiong Zhang,
University of Southern California,
United States

REVIEWED BY
Xiang Li,
University of Electronic Science and
Technology of China, China
Thangal Yumnamcha,
Wayne State University, United States

*CORRESPONDENCE
Shanjun Cai
✉ caishanjun@163.com

RECEIVED 07 July 2024
ACCEPTED 14 October 2024
PUBLISHED 06 November 2024

CITATION
Wang Q and Cai S (2024) Exploring the relationship between cathepsin and age-related macular degeneration using Mendelian randomization.
Front. Med. 11:1460779.
doi: 10.3389/fmed.2024.1460779

Exploring the relationship between cathepsin and age-related macular degeneration using Mendelian randomization

Qiuyuan Wang[1,2] and Shanjun Cai[1]*

[1]Guizhou Branch of the Affiliated Hospital of Zunyi Medical University, National Clinical Research Center of the Eye Hospital of Guizhou Province, Key Laboratory of Eye Disease Characteristics of Guizhou Province, Zunyi, China, [2]Department of Clinical Medicine, The First Clinical College, Zunyi Medical University, Zunyi, China

Purpose: Age-related macular degeneration (AMD) is the leading cause of low vision and even blindness in the elderly population worldwide. However, no studies have been conducted to analyze the causal relationship between the cathepsin family and AMD. The present study aimed to explore and analyze this potential association using Mendelian randomization (MR).

Methods: In this study, AMD was classified into two types: exudative AMD and atrophic AMD. Inverse-variance weighting (IVW) was used as the main analysis method. The association between nine cathepsins and the two classifications of AMD were analyzed using multivariable Mendelian randomization (MVMR). Sensitivity analysis included Cochran's Q-test and the MR-Egger intercept test.

Results: Two-sample MR analysis showed that higher levels of cathepsin L2 were associated with a delay in the development of atrophic AMD (IVW: $p = 0.017$; OR = 0.885; 95% CI = 0.799–0.979). Reverse MR analysis indicated that cathepsin E levels were increased in individuals with atrophic (IVW: $p = 0.023$; OR = 1.058; 95% CI = 1.007–1.111) and exudative AMD (IVW: $p = 0.018$; OR = 1.061; 95% CI 1 = 1.010–1.115). MVMR analysis indicated a causal relationship between cathepsin G (IVW: $p = 0.025$; OR = 1.124; 95% CI = 1.014–1.245), cathepsin O (IVW: $p = 0.043$, OR = 1.158, 95% CI = 1.004–1.336), and exudative AMD after coordinating for other types of cathepsin.

Conclusion: This study demonstrated a potential link between the cathepsin family and the onset of AMD. Elevated serum concentrations of cathepsin L2 may serve as a protective factor for atrophic AMD, while increased levels of serum cathepsin G and O concentrations may promote the development of exudative AMD. Besides, the development of AMD may be associated with elevated serum concentrations of cathepsin E.

KEYWORDS

cathepsins, age-related macular degeneration, Mendelian randomization, causal analysis, multivariable Mendelian randomization

1 Introduction

Age-related macular degeneration (AMD) is the leading cause of low vision and blindness in the elderly population (1). Currently, the global prevalence of AMD is approximately 8.69% (age range: 45–85 years), with the number of affected patients projected to increase to 288 million by 2040 (2). Therefore, preventing AMD risk factors has become an important area of research in clinical practice. AMD-related risk factors include age, immune system-related genetic variants, smoking, obesity, excessive cholesterol intake, and various known cardiovascular metabolic factors (3). In addition, some studies have shown that hyperglycemia can affect the development of AMD through the accumulation of highly stable advanced glycation end products, oxidative stress, and hemodynamic perturbations related to inflammatory responses, such as mitochondrial dysfunction (4). Cathepsins represent a group of lysosomal proteolytic enzymes that play an important role in maintaining cellular homeostasis (5). Common cathepsins belong to the papain superfamily of cysteine proteases (6). They are integral to almost all physiological and pathophysiological cellular processes, such as protein and lipid metabolism, autophagy, antigen presentation, growth factor receptor recycling, cellular stress signaling, extracellular matrix degradation, and lysosome-mediated cell death (7). The cathepsin family is closely involved in regulating proinflammatory signaling pathways, and cathepsin D and S can promote the degradation of the photoreceptor outside the retina (8). Moreover, Thomas (9) found a causal relationship between cathepsin F and early AMD.

However, no study has explored the mechanism further. Some scholars believe that the abnormal regulation of cathepsin activity may be related to the occurrence and development of AMD. However, no previous study in China has been conducted to analyze systematically whether a potential link exists between cathepsins and the occurrence and development of AMD (2). An increasing number of studies have revealed the role of genetics in disease etiology with the advancement of genomics. Mendelian randomization (MR) relies on genome-wide association studies (GWAS) using one or more genetic variants as instrumental variables (IVs) for causal analysis. These variables are strongly associated with the exposure and are unaffected by confounding factors. MR studies can infer the causal effect of exposure on outcomes (10). In this context, this study analyzed the potential causal associations between different types of tissue proteins and both AMD classifications using two-sample and multivariate MR methods.

2 Materials and methods

2.1 Instrumental variables (IVs)

The IV for tissue proteins (μg/L) was obtained from the INTERVAL study, which included 3,301 Europeans (11). The data source is https://questions.mrcieu.ac.uk. The cathepsin-related IV screening conditions for MR analysis are as follows: $p < 5\times10^{-8}$, linkage disequilibrium (LD, $r^2 \leq 0.001$), satisfying Hardy–Weinberg balance, and a genetic distance of <10,000 kb (12).

2.2 Outcome data source

Based on clinical presentation, the Age-related Eye Disease Study team classified AMD into AMD-free, early, middle, and advanced stages. Two distinct manifestations emerged in the late stages of AMD (13). One is the development of confluent areas of atrophy involving photoreceptors and retinal pigment epithelium, known as geographic atrophy (atrophic AMD). The other is the growth of abnormal blood vessels in the macular region, referred to as neovascular AMD (exudative AMD) (13). Thus, the AMD data were obtained from the FinnGen database. This study divided the outcome (AMD) into previous studies of exudative AMD (4,848 case group, 252,277 controls; European population) and atrophic AMD (6,065 case group, 251,042 controls; European population). Table 1 shows the details.

3 Analytical methods

MR refers to an analytic approach to assess the causality of an observed association between a modifiable exposure or risk factor and a clinically relevant outcome (14). It uses genetic variation as an IV to analyze whether exposure would have a causal effect on the outcome (14). For two-sample MR, the causal effect of the exposure (X is cathepsins) on the outcome (Y is AMD) via the GIV (G) can then be estimated by $\beta_{MR} = \beta_{Y\sim G}/\beta_{x\sim G}$; β_{MR} (known as the Wald ratio estimate) represents the causal effect estimate obtained from $\beta_{Y\sim G}$ and $\beta_{x\sim G,}$ the regression coefficients obtained from the regression of the outcome on the GIV and the regression of the exposure on the GIV, respectively (15) (Figure 1). MVMR is an extension of MR that allows for the causal effects of multiple exposures on an outcome to be estimated (16).

MVMR estimates the "direct" causal effects of each exposure included in the estimation of the outcome, conditional on the other exposures included in the model (17). It is particularly useful where two or more potentially related exposures are of interest, and the researcher wishes to understand whether both exposures exert a causal effect on the outcome or, as described later, where one exposure is potentially a mediator of another exposure. With individual-level data, MVMR is implemented through two-stage least-squares regression of the model: $Y = \beta_0 + \beta_1 X_1 + \beta_2 X_2 + V_{y,}$ where Y is the outcome of interest; X_1 and X_2 are the exposures of interest; β0, β1, and β2 are the intercept and effects of X_1 and X_2 on the outcome, respectively. V_y is a random error term that is assumed to be normally distributed (18) (Figure 2).

The selected IVs must meet three criteria. First, they should be highly correlated with the exposure. Second, the SNP should not confound the relationship between exposure and outcome. Finally, the SNP cannot be associated with the outcome through any pathway other than exposure. When the last two conditions are violated, the SNP is considered to exhibit horizontal pleiotropy (19).

In previous studies, inverse variance weighting (IVW) has been used as the primary method for estimating the overall effect size (20). In particular, the causal effect estimates from each genetic variant are combined using an IVW meta-analysis framework. Thus, the IVW method is a weighted average of the causal effects derived from the genetic variants. This approach is akin to fitting a weighted linear regression of the associations between the instruments and the

TABLE 1 Two-sample forward MR analysis.

Database	Data name	The first author	Sample capacity	The year of publication	Race	Sex	Website
IEU	Cathepsins	Jialin Li	3301	2023	European	Men and women	https://gwas.mrcieu.ac.uk
FinnGen	Dry age-related macular degeneration	NA	257107	2023	European	Men and women	https://storage.googleapis.com/finngen-public-data-r9/summary_stats/finngen_R9_DRY_AMD.gz
	Wet age-related macular degeneration	NA	257125	2023	European	Men and women	https://storage.googleapis.com/finngen-public-data-r9/summary_stats/finngen_R9_WET_AMD.gz/

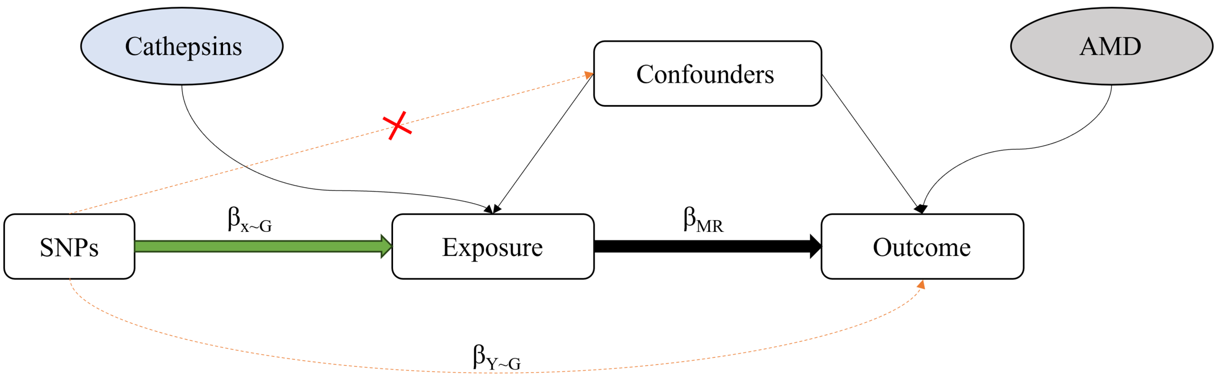

FIGURE 1
Diagram of the approach used by Mendelian randomization studies, which compare the observed genotype-outcome association with the expected genotype-outcome association: $\beta_{X\sim G}$: regression coefficient of the genetic variant-exposure association. $\beta_{Y\sim G}$: regression coefficient of the genetic variant-outcome association. β_{MR}: regression coefficient of the exposure-outcome association.

outcome, with the intercept term set to zero. Notably, this method assumes that all instruments are valid and that no pleiotropic effects exist, meaning the genetic variants are not associated with multiple exposures. Thus, any differences in the causal estimates derived from each genetic variant can be attributed to sampling variability, adhering to the homogeneity assumption (21, 22). Supplementary methods such as MR-Egger (23) and weighted median (WM) (24) were used to verify the robustness of the MR results.

In short, in the presence of pleiotropy, one could fit a weighted linear regression of the associations between the instruments and the outcome while assuming an unconstrained intercept term (in contrast to the IVW approach, where the intercept term is constrained and set to zero), resulting in the MR-Egger regression method (20). The slope of the MR-Egger regression is a robust estimate of the causal effect accounting for potential horizontal pleiotropy. An estimator of the WM method (15) is a median, where the individual MR estimates are weighted proportionally according to their precision. When up to 50% of genetic variants are invalid instruments, a causal effect can be estimated as the median of the weighted ratio estimates using the reciprocal of the variance of the ratio estimate as weights (24). MR analysis (including IVW, MR-Egger, and WM) was performed using the R TwoSampleMR package.

Sensitivity analysis and statistical tests were performed in this study to evaluate the validity of the hypotheses. The heterogeneity of SNPs was judged using Cochran's Q test, with a p-value of >0.05, indicating a lack of heterogeneity (12). The MR-PRESSO global test and the MR-Egger intercept were used to identify outliers and horizontal pleiotropic effects (25).

The MR-Egger intercept represents the average multidirectional effect (intercept $p < 0.05$), and the slope can produce robust multidirectional MR estimates.

The MR-PRESSO outliers test was used to correct for pleiotropy by removing or lowering outliers when pleiotropy was significant (tested here using $p < 0.05$) (25).

Multivariate MR is an extension of the two-sample MR (19). This study not only included the causal relationship between individual cathepsins and AMD but also explored the association between nine cathepsins and AMD through multivariate MR. In addition, this study included two AMD classifications as exposure factors by using cathepsins as the outcome to assess reverse causality and demonstrate the existence of bidirectional causality. These reverse MR analyses used the same GWAS dataset described above.

4 Results

4.1 Two-sample MR analysis clarified the causal relationship between nine cathepsins and different subtypes of AMD

As detailed in Figure 3, a two-sample MR analysis of nine cathepsins (B, E, F, G, H, L2, O, S, and Z) and both AMD classifications was performed to assess the effect of nine cathepsins on AMD subtypes. The results showed that for atrophic AMD, the increased concentrations of serum cathepsin L2 delayed its progression (IVW: $p = 0.017$; OR = 0.885; 95% CI = 0.799–0.979).

However, a weak association existed between cathepsin O and atrophic AMD, with elevated serum cathepsin O concentrations protecting against it (WM: $p = 0.038$; OR = 0.882; 95% CI = 0.783–0.993). For exudative AMD, none of the nine cathepsins showed a significant correlation with them. None of the above studies showed pleiotropy or heterogeneity. All the analyses are detailed in Table 2.

Reverse MR analysis was performed in this study to explore whether reverse causality existed. The occurrence of atrophic AMD caused increased cathepsin E (IVW: $p = 0.023$; OR = 1.058; 95% CI = 1.007–1.111), and the MR-Egger intercept and the MR-PRESSO analysis showed no significant pleiotropy (0.757 and 0.811,

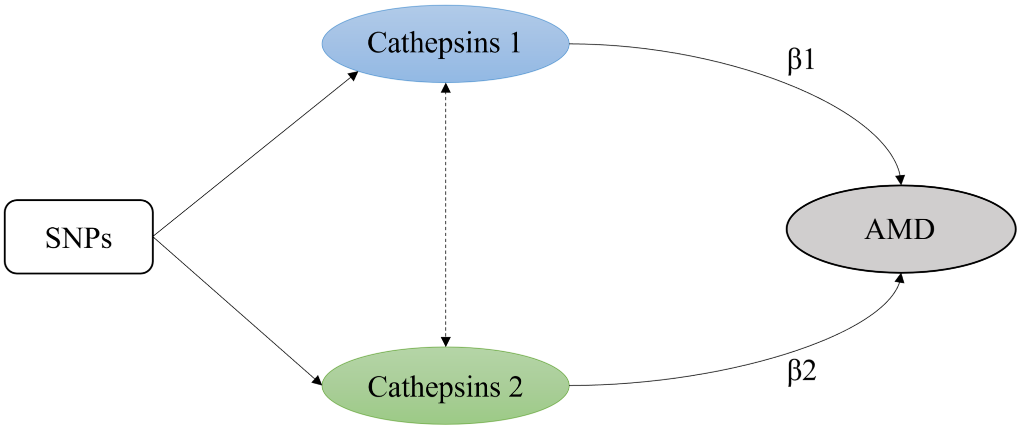

FIGURE 2
A simple multivariable Mendelian randomization model with two exposures. β1 and β2 are the intercept and effects of exposure on the outcome.

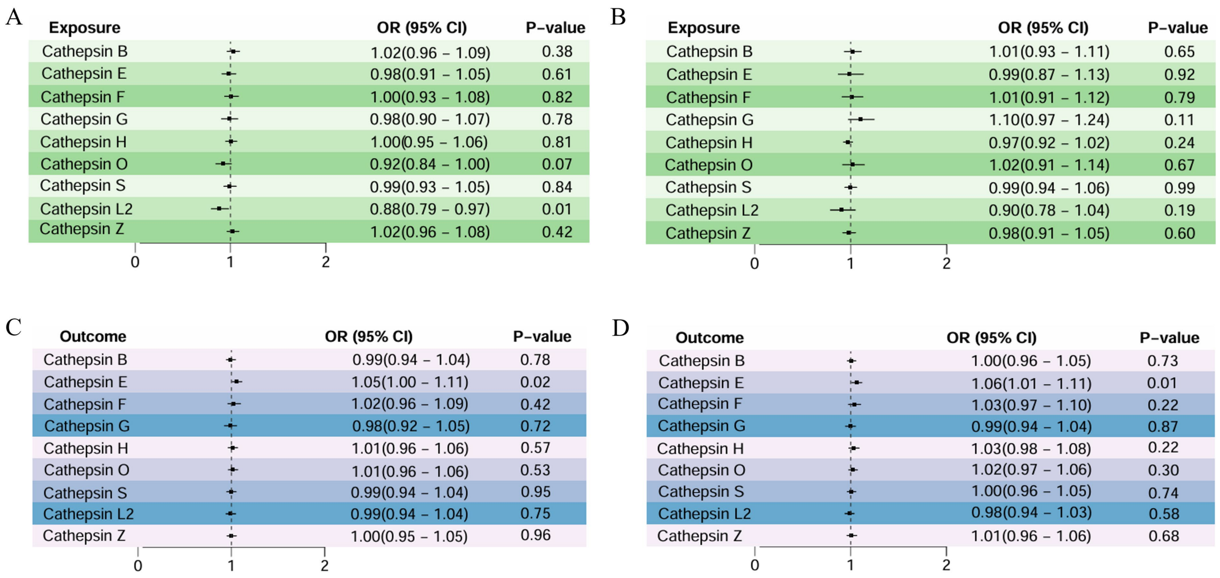

FIGURE 3
Two-sample MR analysis: **(A)** forward analysis of atrophic AMD, **(B)** forward analysis of exudative AMD, **(C)** reverse analysis of atrophic AMD, and **(D)** reverse analysis of exudative AMD.

TABLE 2 Two-sample forward MR analysis.

Cathepsin	SNPs	Inverse variance weighted		MR-Egger		Weighted median	
		OR (95%CI)	*p*	OR (95%CI)	*p*	OR (95%CI)	*p*
Cathepsin B							
Atrophic AMD	18	1.02 (0.96–1.09)	0.38	1.01 (0.87–1.17)	0.85	0.97 (0.89–1.07)	0.65
Exudative AMD	18	1.01 (0.93–1.11)	0.65	1.07 (0.87–1.31)	0.48	1.03 (0.93–1.14)	0.45
Cathepsin E							
Atrophic AMD	9	0.98 (0.91–1.05)	0.61	0.99 (0.88–1.12)	0.95	0.96 (0.86–1.06)	0.46
Exudative AMD	9	0.99 (0.87–1.13)	0.92	0.90 (0.72–1.12)	0.39	0.94 (0.84–1.05)	0.28
Cathepsin F							
Atrophic AMD	10	1.00 (0.93–1.08)	0.82	1.03 (0.86–1.24)	0.73	1.00 (0.91–1.10)	0.91
Exudative AMD	10	1.01 (0.91–1.12)	0.79	1.19 (0.91–1.55)	0.22	0.96 (0.86–1.07)	0.48
Cathepsin G							
Atrophic AMD	11	0.98 (0.90–1.07)	0.78	1.05 (0.87–1.26)	0.57	0.99 (0.88–1.12)	0.97
Exudative AMD	11	1.10 (0.97–1.24)	0.11	1.18 (0.90–1.54)	0.24	1.12 (0.97–1.28)	0.10
Cathepsin H							
Atrophic AMD	10	1.00 (0.95–1.06)	0.81	0.97 (0.90–1.04)	0.47	0.99 (0.94–1.04)	0.77
Exudative AMD	10	0.97 (0.92–1.01)	0.24	0.92 (0.86–0.98)	0.04	0.95 (0.90–1.00)	0.07
Cathepsin L2							
Atrophic AMD	11	0.88 (0.79–0.97)	0.01	0.77 (0.59–1.01)	0.09	0.93 (0.81–1.07)	0.34
Exudative AMD	11	0.90 (0.78–1.04)	0.19	1.39 (1.03–1.88)	0.05	0.92 (0.79–1.08)	0.34
Cathepsin O							
Atrophic AMD	12	0.92 (0.84–1.00)	0.07	1.04 (0.85–1.28)	0.64	0.88 (0.78–0.99)	0.03
Exudative AMD	12	1.02 (0.91–1.14)	0.67	1.02 (0.78–1.33)	0.86	0.99 (0.87–1.13)	0.95
Cathepsin S							
Atrophic AMD	23	0.99 (0.93–1.05)	0.84	0.89 (0.80–0.98)	0.03	0.91 (0.84–0.99)	0.03
Exudative AMD	23	0.99 (0.94–1.06)	0.99	0.93 (0.84–1.03)	0.22	0.94 (0.86–1.03)	0.20
Cathepsin Z							
Atrophic AMD	13	1.02 (0.96–1.08)	0.42	0.95 (0.87–1.05)	0.38	0.98 (0.90–1.06)	0.66
Exudative AMD	13	0.98 (0.91–1.05)	0.60	0.96 (0.86–1.06)	0.49	0.96 (0.88–1.04)	0.37

AMD, age-related macular degeneration; CI, confidence interval; OR, odds ratio.

respectively). Exudative AMD also led to elevated cathepsin E (IVW: $p = 0.018$; OR = 1.061; 95% CI = 1.010–1.115).

Moreover, the MR-Egger intercept and the MR-PRESSO analysis showed that the results did not show significant pleiotropy (0.291 and 0.248, respectively). The rest of the analysis did not demonstrate a causal link between the two AMD classifications and other cathepsins (Table 2).

4.2 MVMR analysis clarified the causal relationship between nine cathepsins and different subtypes of AMD

In this study, the relationship between the genetic propensity of multiple cathepsins and different subtypes of AMD was assessed by multivariate MR. The results showed that after the coordination of other types of cathepsin enzymes, serum cathepsin G (IVW: $p = 0.025$; OR = 1.124; 95% CI = 1.014–1.245) and the increased concentration of cathepsin O (IVW: $p = 0.043$; OR = 1.158; 95% CI = 1.004–1.336) could promote the occurrence of exudative AMD. For atrophic AMD, no significant cathepsins were found after the coordination of other types of cathepsins (Figure 4 and Table 3). The above analysis results do not have pleiotropy and heterogeneity.

5 Discussion

This study revealed a potential causal relationship between the cathepsin family and the occurrence of AMD through MR analysis, thereby providing a favorable reference for further studies.

AMD is the major cause of low vision and even blindness in the elderly population (1). The number of patients with AMD worldwide is expected to reach 288 million in 2040 (2). The prevalence of AMD in people older than 70 years in China is 20.2% (2). The number of patients with AMD continues to increase with the aging of China's population. The authors of the previous studies believe that the onset

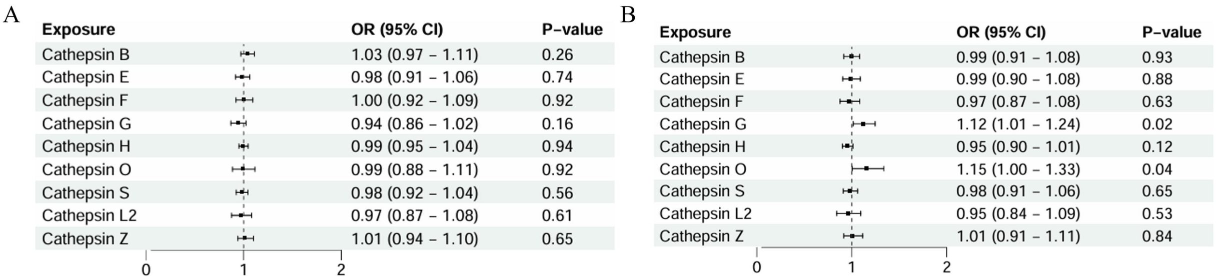

FIGURE 4
Multivariate MR analysis: **(A)** atrophic AMD analysis and **(B)** exudative AMD analysis.

TABLE 3 **Two-sample reverse MR analysis.**

Cathepsin	SNPs	Inverse variance weighted		MR-Egger		Weighted median	
		OR (95%CI)	*p*	OR (95%CI)	*p*	OR (95%CI)	*p*
Cathepsin B							
Atrophic AMD	21	0.99 (0.94–1.04)	0.78	0.99 (0.91–1.07)	0.92	1.00 (0.93–1.08)	0.86
Exudative AMD	20	1.00 (0.96–1.05)	0.73	0.97 (0.90–1.04)	0.44	1.00 (0.94–1.07)	0.84
Cathepsin E							
Atrophic AMD	21	1.05 (1.00–1.11)	0.02	1.03 (0.95–1.12)	0.35	1.05 (0.98–1.11)	0.12
Exudative AMD	20	1.06 (1.01–1.11)	0.01	1.00 (0.93–1.08)	0.89	1.04 (0.98–1.10)	0.11
Cathepsin F							
Atrophic AMD	21	1.02 (0.96–1.09)	0.42	0.96 (0.87–1.07)	0.56	1.00 (0.93–1.08)	0.84
Exudative AMD	20	1.03 (0.97–1.10)	0.22	0.97 (0.88–1.07)	0.61	1.02 (0.95–1.08)	0.49
Cathepsin G							
Atrophic AMD	21	0.98 (0.92–1.05)	0.72	0.99 (0.89–1.11)	0.92	1.02 (0.95–1.09)	0.47
Exudative AMD	20	0.99 (0.94–1.04)	0.87	0.98 (0.90–1.07)	0.68	1.01 (0.96–1.07)	0.49
Cathepsin H							
Atrophic AMD	21	1.01 (0.96–1.06)	0.57	0.97 (0.89–1.05)	0.54	1.00 (0.93–1.08)	0.86
Exudative AMD	20	1.03 (0.98–1.08)	0.22	0.98 (0.90–1.06)	0.71	1.05 (0.98–1.12)	0.12
Cathepsin L2							
Atrophic AMD	21	0.99 (0.94–1.04)	0.75	0.96 (0.88–1.04)	0.39	0.98 (0.91–1.05)	0.61
Exudative AMD	20	0.98 (0.94–1.03)	0.58	0.99 (0.91–1.07)	0.82	1.00 (0.94–1.06)	0.91
Cathepsin O							
Atrophic AMD	21	1.01 (0.96–1.06)	0.53	0.98 (0.90–1.06)	0.71	1.01 (0.94–1.09)	0.64
Exudative AMD	20	1.02 (0.97–1.06)	0.30	1.00 (0.93–1.08)	0.81	1.03 (0.96–1.10)	0.31
Cathepsin S							
Atrophic AMD	21	0.99 (0.94–1.04)	0.95	1.04 (0.96–1.13)	0.30	0.99 (0.92–1.05)	0.76
Exudative AMD	20	1.00 (0.96–1.05)	0.74	1.02 (0.95–1.10)	0.44	1.01 (0.95–1.07)	0.68
Cathepsin Z							
Atrophic AMD	21	1.00 (0.95–1.05)	0.96	0.96 (0.88–1.04)	0.36	1.02 (0.94–1.09)	0.58
Exudative AMD	20	1.01 (0.96–1.06)	0.68	0.95 (0.88–1.03)	0.31	1.01 (0.95–1.07)	0.70

AMD, age-related macular degeneration; CI, confidence interval; OR, odds ratio.

of AMD, a multifactorial disease, is associated with many risk factors, such as age, immune system-related genetic variants, smoking, obesity, excessive cholesterol intake, and known cardiovascular and metabolic factors (3). In addition, a study showed that the development of AMD is closely associated with numerous activated microglia and macrophages (2). However, no study has proposed definite observations related to the onset of AMD. Given the high blindness rate of the disease, exploring and analyzing the surveillance indicators of AMD pathogenesis is valuable for early diagnosis and treatment.

Previous studies have found that oxidative stress may affect the occurrence and development of AMD through microglia. In normal retinal tissue, continuous monitoring of harmful stimuli is performed by microglia, which are mostly confined to the plexiform layer, where they exhibit complex branching processes to sense the local retinal microenvironment (26).

These cells play an important role in retinal homeostasis and contribute to neuroprotection against transient pathophysiological insults. However, when stress is permanent, persistent microglial inflammatory responses may cause changes in retinal integrity and induce neuronal death. These changes lead to retinal degeneration and may also be caused by direct damage to glial cells by stress (27). Active microglia phagocytose retinal myelin debris and promote retinal regeneration. However, the ability of microglia to maintain immune surveillance and tissue repair decreases with age (28). Microglial senescence is associated with the production and release of proinflammatory cytokines, which are involved in the pathogenesis of AMD and other retinal neurodegenerative diseases (29). In addition, under oxidative stress, with the occurrence of aging retinal pigment epithelium (RPE), the production and accumulation of advanced glycation end products (AGEs) and the activation of AGE receptors (RAGE) are enhanced (30). AGE receptors are present in cells, such as endothelial cells, pericytes, microglia, monocytes, and macrophages (30). Experimental studies have shown that exposure of RPE cells to the RAGE ligand AGEsorS100B can cause retinal tissue damage through RPE-mediated VEGF expression, leading to pathological angiogenesis (31). Therefore, abnormal microglial function plays an important role in the occurrence and development of AMD.

The cathepsin family is involved in protein and lipid metabolism, autophagy, and antigen presentation and has great value for cell homeostasis (7). In the absence of external stimuli, cathepsins are generally affected by transcription, translation, and epigenetic regulation, and extracellular cathepsins can accumulate in the extracellular environment by activating immune cells, osteoclasts, fibroblasts, glial cells, endothelial cells, and smooth muscle cells (32). Cathepsin release plays a role when pathological conditions, such as cancer, inflammation, and immune imbalance, occur (32). Previous studies showed that cathepsins are important in the activation of microglia during chronic neuroinflammation (33, 34). This finding proves that cathepsins promote the development of AMD by activating microglia in response to external stimulation. As one of the characteristics of exudative AMD, the production mechanism of retinal neovascularization is also the focus of the current research. Wang (34) found that cathepsins can effectively affect the expression of proteins closely related to angiogenesis, such as phosphorylated endothelial-type nitrogen oxide synthase and phospho-glycogen synthase kinase-3 protein. Moreover, cathepsins can promote angiogenesis in response to hypoxia and ischemic stress.

Moreover, Jan (35) found that dysregulation of cystatin (cathepsin inhibitors) in humans may increase susceptibility to exudative AMD. This finding also provides further evidence for the potential role of cathepsins in exudative AMD.

Based on previous studies, the present study used multiple MR methods to comprehensively analyze the potential causal relationship between the cathepsin family and atrophic and exudative AMD.

The findings suggest that cathepsin L 2 may be a protective factor for atrophic AMD, while cathepsin G and O are risk factors for exudative AMD. In addition, atrophic and exudative AMD may be accompanied by increased cathepsin E concentrations. Previous studies have found that the cathepsin E-sTRAIL axis is involved in communication between microglia and neurons during the progression of Alzheimer's disease (36). Given that Alzheimer's disease and AMD are diseases of aging, this indirectly suggests that cathepsin E may also play an important role in the pathogenesis of AMD and is closely associated with the cathepsin E-sTRAIL axis (36). When other types of cathepsins were adjusted in multivariate analysis, no causal relationship existed between cathepsins and atrophic AMD. This result may be due to the functional compensation of other cathepsins, and multivariate MR analysis helped mitigate these potential biases that may affect traditional observational studies (12). This study explored and analyzed the possible causal relationship between the cathepsin family and AMD pathogenesis through MR, thereby providing a reference for the subsequent exploration of the effective monitoring indicators of AMD pathogenesis. Given that the pathogenesis of AMD is mediated by multiple factors and the cathepsin family is involved in many cellular physiological processes, further research is needed to analyze the specific link between the two.

With the continuous development of medical technology and science, the early screening, diagnosis, and treatment of AMD have become the focus of ophthalmologists. The results of this study provide new monitoring indicators for the early screening of AMD.

This study demonstrated a potential link between the cathepsin family and AMD pathogenesis, where elevated serum cathepsin L 2 concentration may be a protective factor for atrophic AMD.

Moreover, elevated serum concentrations of cathepsin G and O may promote the development of exudative AMD. However, the development of AMD may be accompanied by elevated serum cathepsin E concentrations.

Given the high blindness rate of AMD, recognizing and controlling the risk factors for AMD are crucial for reducing its prevalence and enabling early diagnosis and treatment.

Although this MR-designed investigation has several strengths that complement traditional epidemiological studies, it also has some limitations to be considered. First, the study was limited to individuals of European ancestry, which suggests that our findings should not be directly extrapolated to other populations. Second, while we did not observe evidence of pleiotropy for the causal association using different MR approaches, there remains a possibility that the variants used in the MR confer a risk of AMD through a pleiotropic pathway. Therefore, further MR analysis using individual-level data should be conducted to evaluate the potential causal relationship between the cathepsin family and the risk of AMD. In addition, further studies, such as ablation experiments, should be conducted to elucidate the underlying mechanism, which will help verify these findings.

Data availability statement

The original contributions presented in the study are included in the article/supplementary material, further inquiries can be directed to the corresponding author.

Author contributions

QW: Conceptualization, Data curation, Methodology, Validation, Writing – original draft. SC: Supervision, Writing – review & editing.

Funding

The author(s) declare financial support was received for the research, authorship, and/or publication of this article. This study was supported by the Guizhou Science and Technology Cooperation Foundation under Grant ZK[2021] General 423, ZK[2021] General 428, ZK[2022] General 647, and Guizhou Science and Technology Cooperation Support [2023] General 265.

Conflict of interest

The authors declare that the research was conducted in the absence of any commercial or financial relationships that could be construed as a potential conflict of interest.

Publisher's note

References

1. Flaxel CJ, Adelman RA, Bailey ST, Fawzi A, Lim JI, Vemulakonda GA, et al. Age-related macular degeneration preferred practice pattern®. *Ophthalmology*. (2020) 127:P1–P65. doi: 10.1016/j.ophtha.2019.09.024

2. Chinese Vitreo-Retina Society of Chinese Medical Association; Fundus Disease Group of Chinese Ophthalmologist Association. [Evidence-based guidelines for diagnosis and treatment of age-related macular degeneration in China (2023)]. *Zhonghua Yan Ke Za Zhi*. (2023) 59:347–66. doi: 10.3760/cma.j.cn112142-20221222-00649

3. Lambert NG, ElShelmani H, Singh MK, Mansergh FC, Wride MA, Padilla M, et al. Risk factors and biomarkers of age-related macular degeneration. *Prog Retin Eye Res*. (2016) 54:64–102. doi: 10.1016/j.preteyeres.2016.04.003

4. Lee H, Han KD, Shin J. Association between glycemic status and age-related macular degeneration: a nationwide population-based cohort study. *Diabetes Metab*. (2023) 49:101442. doi: 10.1016/j.diabet.2023.101442

5. Reiser J, Adair B, Reinheckel T. Specialized roles for cysteine cathepsins in health and disease. *J Clin Invest*. (2010) 120:3421–31. doi: 10.1172/JCI42918

6. Fonović M, Turk B. Cysteine cathepsins and extracellular matrix degradation. *Biochim Biophys Acta*. (2014) 1840:2560–70. doi: 10.1016/j.bbagen.2014.03.017

7. Conus S, Simon HU. Cathepsins: key modulators of cell death and inflammatory responses. *Biochem Pharmacol*. (2008) 76:1374–82. doi: 10.1016/j.bcp.2008.07.041

8. Cipriani V, Tierney A, Griffiths JR, Zuber V, Sergouniotis PI, Yates JRW, et al. Beyond factor H: the impact of genetic-risk variants for age-related macular degeneration on circulating factor-H-like 1 and factor-H-related protein concentrations. *Am J Hum Genet*. (2021) 108:1385–400. doi: 10.1016/j.ajhg.2021.05.015

9. Julian TH, Cooper-Knock J, MacGregor S, Guo H, Aslam T, Sanderson E, et al. Phenome-wide Mendelian randomisation analysis identifies causal factors for age-related macular degeneration. *eLife*. (2023) 12:e82546. doi: 10.7554/eLife.82546

10. Burgess S, Davey Smith G, Davies NM, Dudbridge F, Gill D, Glymour MM, et al. Guidelines for performing Mendelian randomization investigations: update for summer 2023. *Wellcome Open Res*. (2023) 4:186. doi: 10.12688/wellcomeopenres.15555.3

11. Sun BB, Maranville JC, Peters JE, Stacey D, Staley JR, Blackshaw J, et al. Genomic atlas of the human plasma proteome. *Nature*. (2018) 558:73–9. doi: 10.1038/s41586-018-0175-2

12. Li L, Ren Q, Zheng Q, Bai Y, He S, Zhang Y, et al. Causal associations between gastroesophageal reflux disease and lung cancer risk: a Mendelian randomization study. *Cancer Med*. (2023) 12:7552–9. doi: 10.1002/cam4.5498

13. Fleckenstein M, Schmitz-Valckenberg S, Chakravarthy U. Age-related macular degeneration: a review. *JAMA*. (2024) 331:147–57. doi: 10.1001/jama.2023.26074

14. Taylor AE, Davies NM, Ware JJ, VanderWeele T, Smith GD, Munafò MR. Mendelian randomization in health research: using appropriate genetic variants and avoiding biased estimates. *Econ Hum Biol*. (2014) 13:99–106. doi: 10.1016/j.ehb.2013.12.002

15. Sekula P, Del Greco MF, Pattaro C, Köttgen A. Mendelian randomization as an approach to assess causality using observational data. *J Am Soc Nephrol*. (2016) 27:3253–65. doi: 10.1681/ASN.2016010098

16. Burgess S, Thompson SG. Multivariable Mendelian randomization: the use of pleiotropic genetic variants to estimate causal effects. *Am J Epidemiol*. (2015) 181:251–60. doi: 10.1093/aje/kwu283

17. Sanderson E, Davey Smith G, Windmeijer F, Bowden J. An examination of multivariable Mendelian randomization in the single-sample and two-sample summary data settings. *Int J Epidemiol*. (2019) 48:713–27. doi: 10.1093/ije/dyy262

18. Sanderson E. Multivariable Mendelian randomization and mediation. *Cold Spring Harb Perspect Med*. (2021) 11:a038984. doi: 10.1101/cshperspect.a038984

19. Li J, Tang M, Gao X, Tian S, Liu W. Mendelian randomization analyses explore the relationship between cathepsins and lung cancer. *Commun Biol*. (2023) 6:1019. doi: 10.1038/s42003-023-05408-7

20. Burgess S, Thompson SG. Interpreting findings from Mendelian randomization using the MR-egger method. *Eur J Epidemiol*. (2017) 32:377–89. doi: 10.1007/s10654-017-0255-x

21. Burgess S, Scott RA, Timpson NJ, Davey Smith G, Thompson SGEPIC- InterAct Consortium. Using published data in Mendelian randomization: a blueprint for efficient identification of causal risk factors. *Eur J Epidemiol*. (2015) 30:543–52. doi: 10.1007/s10654-015-0011-z

22. Greco MFD, Minelli C, Sheehan NA, Thompson JR. Detecting pleiotropy in Mendelian randomisation studies with summary data and a continuous outcome. *Stat Med*. (2015) 34:2926–40. doi: 10.1002/sim.6522

23. Bowden J, Davey Smith G, Burgess S. Mendelian randomization with invalid instruments: effect estimation and bias detection through egger regression. *Int J Epidemiol*. (2015) 44:512–25. doi: 10.1093/ije/dyv080

24. Bowden J, Davey Smith G, Haycock PC, Burgess S. Consistent estimation in Mendelian randomization with some invalid instruments using a weighted median estimator. *Genet Epidemiol*. (2016) 40:304–14. doi: 10.1002/gepi.21965

25. Verbanck M, Chen CY, Neale B, Do R. Detection of widespread horizontal pleiotropy in causal relationships inferred from Mendelian randomization between complex traits and diseases. *Nat Genet*. (2018) 50:693–8. doi: 10.1038/s41588-018-0099-7

26. Karlstetter M, Scholz R, Rutar M, Wong WT, Provis JM, Langmann T. Retinal microglia: just bystander or target for therapy? *Prog Retin Eye Res*. (2015) 45:30–57. doi: 10.1016/j.preteyeres.2014.11.004

27. Rashid K, Akhtar-Schaefer I, Langmann T. Microglia in Retinal Degeneration. *Front Immunol*. (2019) 10:1975. doi: 10.3389/fimmu.2019.01975

28. Blasiak J, Sobczuk P, Pawlowska E, Kaarniranta K. Interplay between aging and other factors of the pathogenesis of age-related macular degeneration. *Ageing Res Rev*. (2022) 81:101735. doi: 10.1016/j.arr.2022.101735

29. Guzman-Martinez L, Maccioni RB, Andrade V, Navarrete LP, Pastor MG, Ramos-Escobar N. Neuroinflammation as a common feature of neurodegenerative disorders. *Front Pharmacol*. (2019) 10:1008. doi: 10.3389/fphar.2019.01008

30. Alves CH, Fernandes R, Santiago AR, Ambrósio AF. Microglia contribution to the regulation of the retinal and choroidal vasculature in age-related macular degeneration. *Cells*. (2020) 9:1217. doi: 10.3390/cells9051217

31. Ma W, Lee SE, Guo J, Qu W, Hudson BI, Schmidt AM, et al. RAGE ligand upregulation of VEGF secretion in ARPE-19 cells. *Invest Ophthalmol Vis Sci*. (2007) 48:1355–61. doi: 10.1167/iovs.06-0738

32. Yadati T, Houben T, Bitorina A, Shiri-Sverdlov R. The ins and outs of cathepsins: physiological function and role in disease management. *Cells*. (2020) 9:1679. doi: 10.3390/cells9071679

33. Nakanishi H. Microglial cathepsin B as a key driver of inflammatory brain diseases and brain aging. *Neural Regen Res*. (2020) 15:25–9. doi: 10.4103/1673-5374.264444

34. Wang H, Inoue A, Lei Y, Wu H, Hong L, Cheng XW. Cathepsins in the extracellular space: focusing on non-lysosomal proteolytic functions with clinical implications. *Cell Signal*. (2023) 103:110531. doi: 10.1016/j.cellsig.2022.110531

35. Zurdel J, Finckh U, Menzer G, Nitsch RM, Richard G. CST3 genotype associated with exudative age-related macular degeneration. *Br J Ophthalmol*. (2002) 86:214–9. doi: 10.1136/bjo.86.2.214

36. Xie Z, Meng J, Kong W, Wu Z, Lan F, Narengaowa , et al. Microglial cathepsin E plays a role in neuroinflammation and amyloid β production in Alzheimer's disease. *Aging Cell*. (2022) 21:e13565. doi: 10.1111/acel.13565

Frontiers in Medicine

Translating medical research and innovation into improved patient care

A multidisciplinary journal which advances our medical knowledge. It supports the translation of scientific advances into new therapies and diagnostic tools that will improve patient care.

Discover the latest Research Topics

See more →


frontiers

Frontiers in
Medicine

Frontiers

Avenue du Tribunal-Fédéral 34
1005 Lausanne, Switzerland
frontiersin.org

Contact us

+41 (0)21 510 17 00
frontiersin.org/about/contact